Behaviour of nickel, iron and copper by application of inert anodes in aluminium production

by

Odd-Arne Lorentsen

Thesis submitted in partial fulfilment of the
requirements for the degree
Doktoringeniør

Norwegian University of Science and Technology
Department of Materials Technology and Electrochemistry

Trondheim, December 2000

URN:NBN:no-6347

Doktoringeniøravhandling 2000:104

IME-rapport : 2000:20

Author : Odd-Arne Lorentsen

Address : Department of Materials Technology and Electrochemistry
Sem Sælandsvei 6, Kjemiblokk 4 / 4. etg.
N-7491 TRONDHEIM
NORWAY

E-mail : aktroean@online.no

ISBN : 82-7984-133-4

ISSN : 0809-103X

Print : Reprosentralen, Bygg 4, nivå 3, N-7491 Trondheim, Norway

URN:NBN:no-6347

Acknowledgement

This work was carried out at the Department of Materials Technology and Electrochemistry at NTNU, in close co-operation with the personnel at the SINTEF Materials Technology, Electrolysis Group. This work has been a part of a research project under the PROSMAT program.

First of all, I want to acknowledge the Norwegian Aluminium Industry and The Research Council of Norway (NFR) for their financial support.

I would like to thank my supervisor Professor Jomar Thonstad for support and helpful discussions during this work.

I want to express my sincere thanks to Dr. Ernest W. Dewing for excellent guidance and encouraging discussions regarding the interpretation of the solubility measurements.

I would also like to thank Espen Olsen, Egil Skybakmoen and Henrik Gulbrandsen for practical guidance, especially in the laboratory. Thanks are also extended to the staff and the dr. ing. students at the Department of Electrochemistry and the staff at SINTEF's Electrolysis Group for a positive working environment, interesting discussions, practical help and memorable moments together.

I want to thank my co-worker and "room-mate" Trond Eirik Jentoftsen for all the fruitful discussions we had and our growing friendship.

I thank my parents who taught me that as long as I did my very best I should be satisfied.

Last, but not least, I want to thank Anne Kari for encouraging support during these years working with this thesis. You made it a lot easier for me to cope with difficult and time consuming experiments, unsolved problems and long working nights.

I dedicate this work to my daughter, Sigrid, who put life into its right perspective.

Trondheim, December 2000

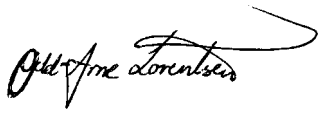

Odd-Arne Lorentsen

URN:NBN:no-6347

Experiment!

Make it your motto day and night.

Experiment,

And it will lead you to the light.

The Apple on the top of the tree

Is never too high to achieve,

So take an example from Eve…

Experiment!

Be curious,

Though interfering friends may frown.

Get furious

At each attempt to hold you down.

If this advice you only employ,

The future can offer you infinite joy

And merriment…

Experiment

And you'll see!

Cole Porter

URN:NBN:no-6347

Table of Contents

URN:NBN:no-6347

List of symbols and abbreviations

Symbol/ Abbrivation	Meaning	Units
a	Activity	-
A_a	Anode Area	cm^2
A_c	Cathode Area	cm^2
α-Al_2O_3	Al_2O_3	-
a_α	Activity of α-Al_2O_3	-
a_β	Activity of β-Al_2O_4	-
AC	Anodic concentration	mol/l
Alumina	Al_2O_3	-
AR	Anodic reaction	-
B	Constant = $(k_a*c_{sat}*A_a) / ((k_c*A_c)+(k_a*A_a))$	mol/m^3
β-Al_2O_3	$Na_2O \cdot 11Al_2O_3$	-
Bath	Electrolyte = Melt	-
C	Constant	-
c	Number of particles	-
c(o)	Initial concentration	mol/m^3
c(oo)	Steady state concentration	mol/m^3
c(t)	Time dependent concentration of species in the electrolyte	sec.
CC	Cathodic concentration	mol/l
CE	Current efficiency	%
CIP	Cold Isostatic Pressure	-
C_p	Molar heat capacity	$J/K \cdot mol$
CR	Cryolite ratio (NaF/AlF_3 molar ratio)	-
Cryolite	Na_3AlF_6	-
c_{sat}	Saturation concentration	mol/m^3
diss.	Dissolved	-
ΔT	Temperature difference T_2-T_1	K
E	Voltage	V
e^-	electron	-
Emf	Electromotive force	V
ext.	External	
F	Faraday's constant, *i.e.* 96487	C/mol
Fe(II)	Fe^{2+} ion	-
g	Gas	-

URN:NBN:no-6347

Symbol/ Abbrivation	Meaning	Units
γ	Activity coefficient (*i.e.* a/x)	-
G^o	Standard Gibbs energy	J/mol
η	Overvoltage	V
Hematite	Fe_2O_3	-
Hercynite	$FeAl_2O_4$	-
H^o	Standard entalphy	J/mol
ICP	Ionic Coupling Plasma	-
K	Equilibrium constant	-
k_a	mass transfer coeff. anode-electrolyte	m/s
k_c	mass transfer coeff. Electrolyte-metal pad	m/s
l	Liquid	-
Liq.	Liquidus	-
Magnetite	Fe_3O_4	-
n	Number of electrones transferred in the reaction	-
n	# mol	mol
Nat.	Natural cryolite	-
p	Partial pressure	atm.
R	Ideal gas constant , *i.e* 8.3143	J/K·mol
R	Reaction	-
rev.	Reversible	-
s	Solid	-
SEM	Scanning Electronic Microscopy	-
S^o	Standard entrophy	J/K·mol
Synt.	Synthetic cryolite made of NaF and AlF_3	-
t	Time	h
T	Temperature	K or ^oC
τ	Time constant	s
tpy	Tonnes per year	-
U	Cell voltage	V
V	Electrolyte volume	m^3
Wustite	$Fe_{0.947}O$	-
x_i	Molar ratio of species "i"	-
XRD	X-ray diffration	-
XRMA	X-ray microanalysis	-

URN:NBN:no-6347

Summary

A thorough investigation was performed on the behaviour of Ni, Fe and Cu oxides dissolved in cryolite melts, and the solubility of these species was measured as a function of alumina content, NaF/AlF_3 molar ratio (CR) and temperature. Predominance area diagrams showing the solid phases containing Ni, Fe and Cu, respectively, as a function of the partial oxygen pressure and the alumina activity at 1020 ^oC were constructed. These diagrams were based on present emf and solubility measurements.

The interpretations of the solubility measurements for the oxides of Ni and Fe gave conclusive and consistent results. The oxides of Ni and Fe exhibit decreasing solubility with decreasing temperature and with increasing alumina concentration. The Ni(II) concentration decreased from 0.32 wt% in cryolite to 0.003 wt% in alumina-saturated melts, while that of Fe(II) decreased from 4.17 to 0.32 wt% in similar melts. FeO and NiO are stable solid phases at low alumina concentrations, while $FeAl_2O_4$ and $NiAl_2O_4$ are stable at high concentrations. The alumina concentrations corresponding to the points of coexistence between FeO and $FeAl_2O_4$ and between NiO and $NiAl_2O_4$ were determined to be 5.03 and 3.0 wt% Al_2O_3, respectively, corresponding to the following Gibbs energy of formation from the oxide compounds, $\Delta G^o_{f\ NiAl_2O_4} = -28.6 \pm 2$ kJ/mol and $\Delta G^o_{f\ FeAl_2O_4} = -17.6 \pm 0.5$ kJ/mol.

The solubilities of $FeAl_2O_4$ and $NiAl_2O_4$ as a function of the CR were investigated in alumina-saturated melts at 1020 ^oC. For both compounds a maximum solubility was found at CR ~5, being 0.008 wt% Ni(II) and 0.62 wt% Fe(II). The results are discussed with respect to the species present in solution. Both Fe(II) and Ni(II) dissolve as fluorides with different numbers of associated "NaF's". Ni(II) seems to form Na_3NiF_5 in melts with molar ratios 2 to 12, while Fe(II) is present as $NaFeF_3$ in acidic (CR 3–10) melts and as Na_3FeF_5 and probably some Na_4FeF_6 in basic melts (CR > 3).

The solubility of both Cu oxidation states Cu(I) and Cu(II) decreases with decreasing temperature. The solubilities of Cu(I) initially decreased with increasing alumina concentration, showing a minimum at a certain alumina concentration followed by an increase. The solubilities were 0.36 wt% Cu(I) and 0.92 wt% Cu(II) in cryolite, and 0.30 wt% Cu(I) and 0.45 wt% Cu(II) in alumina-saturated cryolite at 1020 ^oC.

At 1020 ^oC the solubilities of Cu_2O and CuO were little influenced when changing the CR from 3 to 8 in alumina-saturated melts (~0.30 wt% Cu(I) and ~0.45 wt% Cu(II)), but there was an upward trend for CR < 3. Solubility measurements for CuO in alumina-saturated melts at CR 3.0 to 1.2 clearly showed that the saturation concentration is dependent on both temperature and melt composition.

Copper ions in solution show a complex behaviour, since they form fluorides and oxy-complexes simultaneously. The extent of co-existence of Cu(I) and Cu(II) in the same melt is also considerable, and it is depending on the alumina activity in the melt. According to thermodynamics the stable copper oxide phases at high alumina activities are the

URN:NBN:no-6347

aluminates $CuAlO_2$ and $CuAl_2O_4$. However, no clear changes in the solubilities were found for the points of coexistence between Cu_2O and $CuAlO_2$ and CuO and $CuAl_2O_4$, respectively, as was the case for Ni(II) and Fe(II). Although there are uncertainties regarding the thermodynamic data available for the formation of copper aluminates, models for the dissolution mechanisms and for the species present in the melt are suggested. Cu(I) seems to form mainly CuF at low alumina contents, while Na_5CuO_3 dominates at higher alumina concentrations. Likewise, Cu(II) seems to form CuF_2, but the concentration of CuF_2 decreases with increasing alumina content. The species that gave the best fit for the cupric oxy-complexes was $Na_{16}CuO_9$, and the amount increased with increasing alumina content.

Cermet anodes were prepared with a $NiFe_2O_4$-based oxide phase mixed with a ~20 wt% copper-rich metal phase. The electrical conductivity for these materials was measured as a function of temperature, showing semiconductor behaviour in the temperature range from room temperature to 1050 ^oC. The highest electrical conductivity measured was ~30 S/cm at 1000 ^oC, which is on the low side for use as an anode material for aluminium production.

Three cermet anodes were tested by electrolysis for 48 hours. After the experiments the anodes were examined with SEM. There was no metal phase present in the outer 100 μm of the anode, not even pores were observed that could indicate where the metal grains had been. A copper-rich phase was found in one case ~2 mm from the outer surface, and it is believed that copper diffuses out of the anode.

The cermet anodes dissolved slowly in the electrolyte during electrolysis. The steady state concentrations of Fe and Cu in the electrolyte were below the saturation concentrations, while the concentration of Ni was 3 - 4 times above saturation. The dissolution of the anode does not fit a first order mass-transport model, but it can probably be explained by a controlled dissolution mechanism with some additional disintegration/spalling of the anode material. Further work is needed to draw a firm conclusion. In general, correct solubility data for the anode constituents are needed to make a proper evaluation of various anode materials. Perhaps the first order mass-transport model agrees for some materials, but based on the present results it seems untenable for cermet materials made of $NiFe_2O_4$ with a copper-rich metal phase.

The solubilities of the oxides of Ni(II) and Fe(III) are very low for the alumina-saturated melt used during electrolysis, which make them promising candidates for inert anodes. However, if nickel aluminate, which is an insulator, is formed and deposited on the anode surface, it is a cause of concern. Fe(II) aluminate is not expected to form on the anode surface, since Fe(III) is the stable oxidation state in the presence of oxygen gas. However, solid Fe(II) aluminate may be formed in the bulk of the electrolyte where the partial oxygen pressure is lower.

URN:NBN:no-6347

1 Introduction

Aluminium is the most abundant metallic element (8.1 mass percent) in the earth's crust. Due to its strong affinity to oxygen, aluminium does not occur in nature in its pure elemental state, and is only found in combined forms such as oxides and silicates. However, the discovery of naturally occurring aluminium (1), (2) in various geological districts in Siberian platforms and in Southern Ural in Russia, as well as in the Guangxi and Guizhou Provinces in China, may be in contradiction to the above-mentioned statement. Even though the soil only contained traces of elementary aluminium, the discovery may reveal interesting formation mechanisms.

1.1 The Hall-Héroult process

The fist commercial aluminium was produced in the middle of the 19th from sodium aluminium chloride, reacting with metallic sodium by an expensive thermal reduction process century. The melting point of *alumina* (Al_2O_3) is close to 2030 ^oC, which generally is too high for commercial production (ex. lining material problems and costs). In order to produce aluminium more efficiently, *i.e*. at a lower operating temperature, scientists in the 19th century sought to identify a chemical compound that acted as a solvent for alumina. In 1886 Paul Louis Toussaint Héroult of France and Charles Martin Hall of USA independently of each other discovered and patented the process which is still in use today, *i.e.* the electrolysis of alumina dissolved in cryolite melts. The operating temperature of their melts was approximately 1010 ^oC, which is the melting point of cryolite.

To carry out electrolysis in the 1880's most people had to use batteries as power source. Hall (3) made cells of zinc in dilute sulphuric acid and graphite in concentrated nitric acid (Bunsen batteries). Due in part to inefficiencies in the process, about 30 grams of zinc would be consumed in making 30 grams of aluminium metal. The aluminium electrolysis process could, therefore, not have become such a success if not the motor dynamo had been invented (1867) and improved so it could be used in industrial cells (1880) (4).

The Hall-Héroult process has successfully withstood the many attempts to replace it. The *Hall-Héroult Process* is the only method by which aluminium is produced industrially today, drastic improvements have been made over the years, ranking from cell design, cell size, developing new cell construction materials, additives, to different kinds of feeding strategies and cell control.

In the Hall-Héroult Process liquid aluminium is produced by electrolytic reduction of alumina dissolved in an electrolyte (bath) mainly containing cryolite (Na_3AlF_6). Oxygen from the alumina is discharged electrolytically onto the anode as C_xO intermediate product at the carbon surface. However, these intermediates reacts with the carbon anode and thus gradually consumes it by formation of mainly gaseous carbon dioxide (CO_2) and small amounts of carbon monoxide (CO). Below the electrolyte there is a pool of liquid aluminium, contained in a performed carbon lining with insulation materials inside a steel shell. The aluminium is formed at the bath/metal interface, which acts as the cathode. Thus the overall chemical reaction can be written:

URN:NBN:no-6347

$$2Al_2O_3 + 3C = 4Al + 3CO_2 \quad [1\text{-}1]$$

There are two types of cells used in the smelter industry today, *i.e.* Søderberg (Fig. 1.1) and prebake (Fig. 1-2) Cells. New plants use prebake cells exclusively. The main difference between these two cell types is the anode and the feeding mechanism. Søderberg cells use one, continuous anode while prebake cells use several individual anodes. For Søderberg cells, the anode bakes continuously using heat from the cell, while prebake cells use pre-manufactured anodes.

The electrolyte (bath) which mainly contains cryolite (Na_3AlF_6) and some aluminium fluoride (AlF_3) in excess, is used because of its unique and unmatched capacity as a solvent for alumina. The bath is not consumed as such during the electrolytic process, but some losses occur, mainly by vaporisation.

Prebaked anodes have to be removed at regular intervals, usually after 22-26 days (4), when they have reached down to one third or one fourth of their original size. Prebaked anodes has the advantage that they give a better quality product compared to Søderberg anodes, and they significantly reduce anode carbon consumption (400 kg C/tonne prebake anode versus 550 kg/tonne anode paste for a Søderberg cell). Søderberg anodes are continuous and self-baking, which in principle is advantageous since no process and heat balance interruption is introduced to the cell. The anode raw materials are petroleum coke and tar pitch, but Søderberg paste contain more pitch, typically more than 25 mass percent, while prebaked anode paste usually contains between 13 and 18 mass percent pitch (4). Anode paste briquettes are added on top of the Søderberg anode, and while the paste passes slowly downwards through a rectangular steel casing, it is baked into a solid composite by pyrolysis of the pitch by the heat generated in the bath of the cell. Electric current enters the Søderberg anode usually through vertical spikes or studs connected to the anode beam, while horizontal studs are still used in some older Søderberg cells. These spikes are pulled at intervals of approximately 20 days, and cleaned spikes are reset at a higher level when they approach the bottom surface of the anode.

During recent decades, environmental considerations have been taken very seriously in aluminium production, and in Norway an “Effect Study” (6) was performed from 1990 to 1994 to investigate the effect of pollution from the aluminium smelters on the local communities in the vicinity of the plants. Earlier, these small communities experienced environmental destruction, particularly from fluoride emission. To overcome this problem, the ability of alumina to absorb fluoride gas was utilised to remove fluorides from the emissions. By driving cell fumes (gas and particles) counter current to alumina in big dry scrubbing units, fluoride emission to the environment dropped to an acceptable level. The absorption process also had another positive effect because of the recycling of fluoride-absorbed alumina to the cells. This process (6) recycles 80-90 percent of the fluoride escaping from the cell-line.

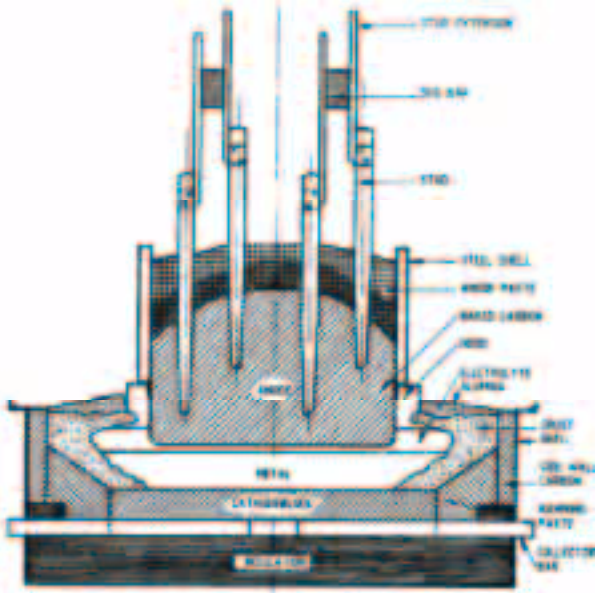

Figure 1-1: A Søderberg cell (5).

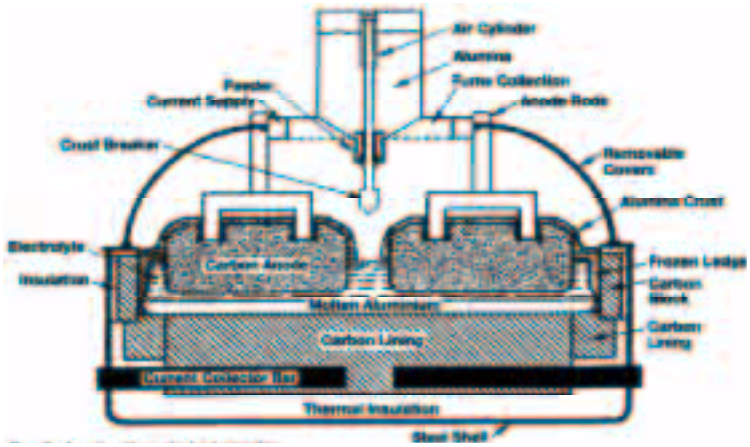

Figure 1-2: A prebake cell(5).

1.2 Aluminium producers today

The largest aluminium producers today (7) are found in USA, EU, Russia, Canada, Australia Norway, China and Brazil. From the nineteen seventies, the producers in South East Asia, South America and Africa have become more and more important. The competition, especially in Norway's primary export market, EU, is strong. The production capacity in the western part of the world is expected (7) to increase with 4.2 million tons from 1999 to 2006, in addition to a net export from the Eastern States. Russia will still be a important exporter. The net export from the Eastern States is, however, expected to decrease from 2.3 million tons in 1997 to 1.5 million tons in 2006.

The Norwegian aluminium industry is the largest single producer in Western Europe with a production of approximately 900.000 metric tonnes per year. The Norwegian aluminium producers are localised in Lista, Mosjøen, Høyanger, Årdal, Sunndalsøra, Karmøy and Husnes. Norsk Hydro (Hydro Aluminium Metal Products) owns four of the aluminium producers, Elkem and Alcoa[1] (50/50) own two of them, while Sør-Norge Aluminium (Søral) is owned by Norsk Hydro and Alusuisse (49/50, others 1 percent). The main export from Norway is semi-finished, but some domestic aluminium refining occur (7).

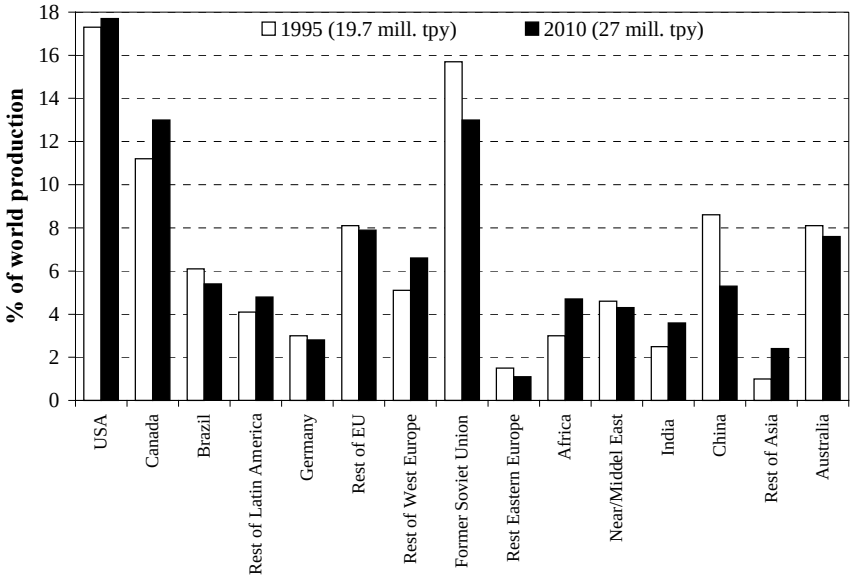

Figure 1-3: Percentage distribution of the world production of aluminium in 1995 and estimates for 2010, data from (8).

Over 17 million tons of primary aluminium is used in the Western World (9) every year. Western Europe accounts for approximately one third of the primary aluminium consumed (10) here.

The manufacturing and converting industries in Western Europe presently use about 3.0 million tons of rolled products, 1.9 million tons of extruded products, 0.5 million tons of other semi-fabricated products and 0.5 million tons of aluminium foil per year (9). In addition approximately 1.6 million tons of casting alloys were used from the secondary aluminium industry.

Consuming about 5 million tons and producing only 3 million tons, Western Europe imports about 2 million tons of primary aluminium per year. Semi-fabricated rolled products have a net export position of approximately 0.5 million tons. Extrusions produced are all consumed in Europe, with very small quantities being net import (9).

[1] Alcoa = Former "Aluminum Company of America"

The transport, building and packaging sectors are the most important markets for aluminium products. The remaining part goes into applications such as electrical and mechanical engineering, office equipment, domestic appliances, lighting, chemistry and even pharmaceuticals.

The aluminium and automotive industries have a history of collaboration on developing the use of the most common lightweight metal in cars. As a result an average European car currently contains about 65 kg of aluminium (9).

Because of its low density combined with high strength, extensive use of aluminium contributes considerably to weight-saving. Weight reduction helps car manufacturers to reduce fuel consumption and thereby lowering gas emissions from fuel combustion, without sacrificing safety, comfort and reliability. 95% of the aluminium in cars is collected and recycled and accounts for over 50% of the material value at the end of its life; Car manufacturers and aluminium producers are working closely together on a whole range of new aluminium parts: from various mass-produced components to an entire aluminium body.

Over the past few years (9), there has been a strong upward trend in the use of aluminium in automotive applications. Ten years ago, engine blocks and cylinder heads, heat exchangers, transmission housings, engine parts and wheels accounted for most of the 60 kg or so of aluminium used in an average passenger car. This Figure has risen today to more than 85 kg, an increase of more than 30%.

In the modern Eco-society, consumers ask for an efficient use of natural resources, limited health risks, high quality and convenience at low cost. Lightweight aluminium packaging, with its wide range of beneficial properties, meets these demands: aluminium packaging provides an impermeable barrier to protect food, beverages, pharmaceuticals and cosmetics and minimises wastage: aluminium packaging is highly corrosion-resistant and for most fillings chemically neutral (9). It is hygienic, non-toxic and non-tainting; the high economic value of used aluminium packaging produces an incentive that results in a high level of recovery and recycling.

Aluminium building products have long service life and little maintenance. Aluminium products offer engineers and architects design flexibility. Its strength-to-weight ratio allows architects to meet required performance specifications. Aluminium alloys ensure durability, weatherproofness and corrosion resistance. Finally, aluminium-building products can be totally recycled retaining its high-performance properties and offering major savings in energy and natural resources (9).

The European aluminium industry offers jobs to about 200.000 people (7). The total turnover of the 3000 companies of the European aluminium industry is about 25 billion ECU. According to *The Norwegian Bureau of Statistics*, 5252 were employed in the Norwegian aluminium industry in 1995, and the value added was 5143 million NOK.

From 1950 to 1970 the consumption of primary aluminium in the western part of the world grew 10-15 percent per year. During the eighties the production levelled out, with an average of 2.3 percent growth per year between 1980 and 1991 (7). This was caused by a

change in production towards less material intensive industries like data, telecommunication systems and electronics. Aluminium has in many ways substituted other materials for special applications, but has also met competitions from plastics and other newer materials like composites. More and more aluminium is also recycled, which reduces the demand for primary aluminium.

.

There is still a growing demand for aluminium, which is also expected to continue in the future. The greatest demand for aluminium is from the transport sector (cars, airplanes, trains *etc.*), building projects and packaging. The low weight is also thought to be beneficial in the future, but it will probably be lesser demand for aluminium used for packaging. Simple calculations (7) indicate the aluminium consumption to grow from 17.8 million tons in 1996 to 23.5 million tons in 2006 in the western part of the world.

According to Norges Offentlige Utredinger (NOU) (7), only a small increase in the aluminium prices is expected the next few years, but reduced prices towards 2004 because of increasing production. The history of aluminium production has, however, shown that predicting the aluminium prices is very difficult, and it is influenced by the overall macro economy development and the relations between supply and demand.

EU has 6 % duty for import of primary aluminium from countries outside EFTA or members of the Lomé Convention. This is beneficial for the Norwegian aluminium producers, since Norway is a member of EFTA and exports over 90 percent of the aluminium produced to EU (7).

1.3 Comparison of the traditional and the potential new technology

The *chemical* difference between the old traditional *Hall-Héroult Process* and the new inert technology is mainly the anode processes, probably combined with a wetted TiB_2 cathode (4). Instead of being consumed, producing CO_2, the new inert anodes serve as a catalyst to oxidise oxygen ions in the melt to oxygen gas. If one could use inert anodes instead of carbon anodes, the overall reduction reaction can be written,

$$2Al_2O_3 = 4Al + 3O_2 \qquad [1\text{-}2]$$

for which (12),

$$\Delta G_T^o = 1697.7 + 14 \cdot 10^{-3} T \ln T - 0.386T \quad (kJ) \qquad [1\text{-}3]$$

and,

$$\Delta H_T^o = 1671.2 + 8.85 \cdot 10^{-3} T \ln T + 3.46 \cdot 10^{-6} T^2 - 2865.5\ T \quad (kJ) \qquad [1\text{-}4]$$

At the temperature of 950°C, the theoretical consumption of electrical energy is 8555.6 kWh/t Al at the reversible potential of alumina decomposition of –2.19 V (11). The overall reduction reaction for reduction of alumina with carbon anodes has a standard decomposition voltage of only –1.17 V. The types of anodes used cause the difference between these two technologies. One of the advantages of the present process is therefore the reduction of the decomposition voltage with approximately one volt, due to the reaction

of the carbon anode to form CO_2 (see comparison in Figure 1-4). In this way one saves electric energy in the electrolysis process by consuming carbon.

However, a new inert anode could probably not replace an ordinary carbon anode. A complete new cell design is probably needed to get a stable production with a proper heat balance.

A **B**

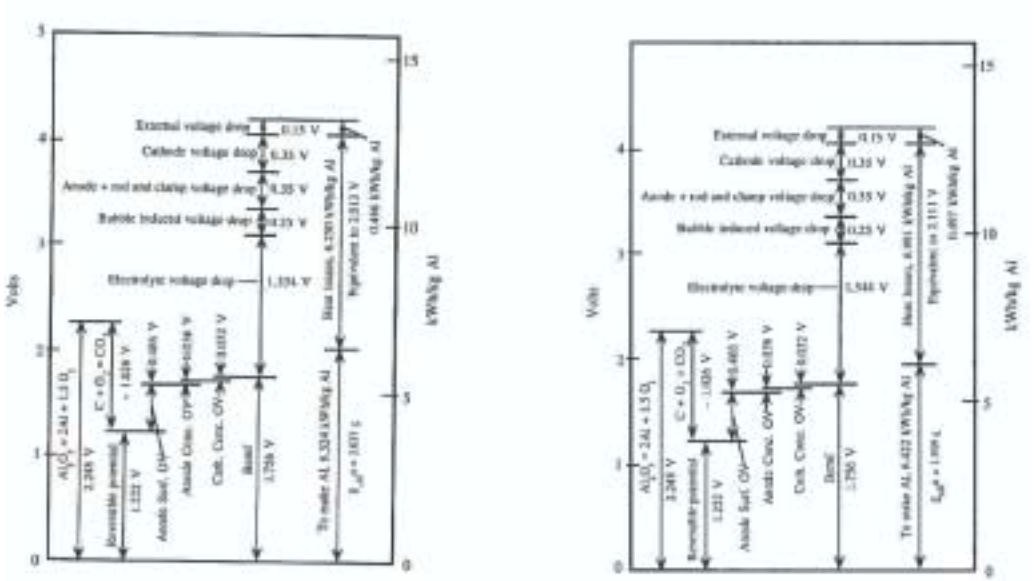

A) Cell voltage and Power @ 96% CE, 4.19 V, 13.0 kWh/kg Al, 960 °C, Alumina-10% α- 33% saturation.

B) Cell voltage and Power @ 90% CE 4.20 V, 13.91 kWh/kg Al, 960 °C, Alumina-10% α- 33% saturation.

Figure 1-4: Typical voltage distribution and energy balance for an average Hall-Héroult cell with carbon anodes with varying current efficiency (CE), from (13).

The overall cell voltage consists of both ohmic and non-ohmic terms.

$$U_{cell} = \sum_{i} U_{ohmic,i} + \sum_{j} U_{non-ohmic,j} \qquad [1\text{-}5]$$

The non-ohmic part consists of the reversible voltage E_{rev} and other non-ohmic potentials represented as overvoltages (η) (see Figure 1.4). The definition of anodic overvoltage is the extra voltage required for the anode to occur with a sufficient rate of reaction (14). The main anodic overvoltage is the so-called anodic reaction overvoltage, with a typical value of about 0.5 V for carbon anodes. A non-ohmic cell potential[2], $E_{reaction}$, may therefore be defined as,

[2] Includes a potential due to the bubble layer underneath the anodes, U_{bubble}

$$E_{reaction} = |E_{rev}| + \eta_{AR} + \eta_{AC} + \eta_{CC} \quad [1\text{-}6]$$

where AR = *anodic reaction*, AC = *anodic concentration and CC = cathodic concentration*. The overall cell voltage, U_{cell} then becomes,

$$U_{cell} = U_{reaction} + U_{ext} + U_{bath} \quad [1\text{-}7]$$

where U_{ext} is the voltage drop of the external electrical busbar system and E_{bath} is the ohmic resistance of the electrolyte.

The higher energy requirement that inert anodes represent is not beneficial for using this technology, but one cannot consider the reversible potential alone. The overvoltages η_{aa} and η_{ac} are under normal operation approximately 0.5 volts for the traditional Hall-Héroult process with carbon anodes(Figure 1.4), but only 0.1 volts for inert anodes (fig 1.5). By changing the cell design it is also possible to reduce the distance between the anode and cathode, called the *interpolar distance* or *AC distance*, and thereby reducing the ohmic drop in the bath considerably. Kvande (14) estimates (see Figure 1-5) that the total voltage increase will be about 0.6 V in cells with inert anodes and a conventional carbon cathode. A further reduction of the interpolar distance may be possible because of a more even anode surface and easier gas escape in combination with a drained cathode (4), (15).

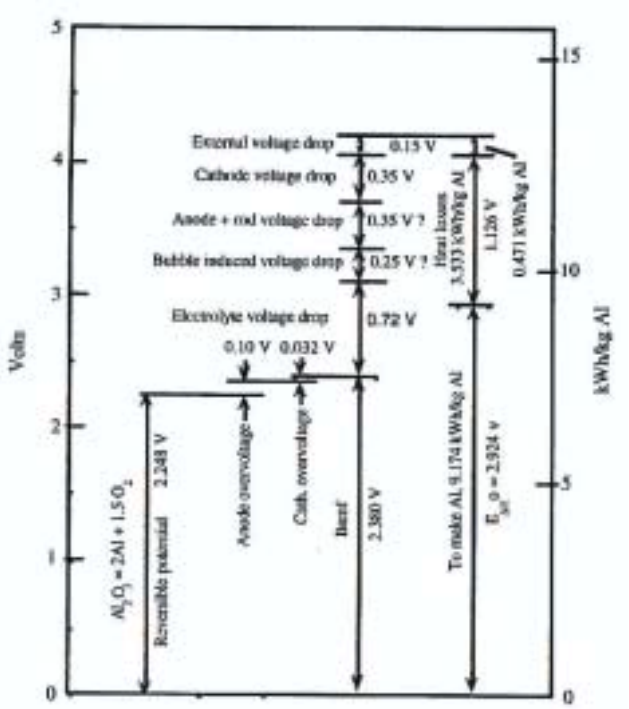

Figure 1-5: Typical voltage distribution and energy balance using inert anodes, Cell Voltage & Power Distribution @ 95% CE, 4.20 V, 13.2 kWh/kg Al, 960°C, Alumina-10% alpha- 33% saturation, from (13).

The overvoltage at the electrodes gives useful heat production in the cell. If the anodic overvoltages did not exist, the heat balance of the cell must have been maintained by a higher electrolyte voltage drop, and thereby a higher interpolar distance. Another possibility is a better conservation of the heat inside the cell by increasing the thermal insulation of the cell or by a radical new cell design with improved thermal insulation. The energy efficiency would be 47.5 % for cells with carbon anodes and 69.6 % for cells with inert anodes provided that the anode-cathode distance in the latter is reduced and/or increasing the electrode areas (13). Because more of the electric power in these cells goes into making aluminium and less into producing heat, maintaining the electrolyte temperature will be difficult (13).

1.4 The development of inert anodes

In the chemistry class Charles Martin Hall heard Professor Jewett's talk about aluminium and the challenge to find an economical method for preparing this element. Jewett said, "*Any person who discovers a process by which aluminium can be made on a commercial scale will bless humanity and make a fortune to himself*". 3 years later, on February the 23rd 1886 Hall succeeded in producing globules of aluminium metal by the electrolysis of aluminium oxide dissolved in cryolite- aluminium fluoride mixture. He used carbon rods as anodes, but tried to develop a superficially oxidised inert copper anode (16). However, he never succeeded using copper-based inert anodes and gave up in 1912.

Belyaev investigated the feasibility of tin oxide and other ceramic oxide electrodes as early as in the thirties (17), (18). At Alusuisse, oxygen-ion conductors and tin oxide were tested, and then nickel ferrite and cermets as further possibilities (19).

An extensive amount of work has been done (19), (20), (21) to try to find a suitable inert anode material since Hall gave up almost hundred years ago. In 1987 McLeod *et al.* (22): "*The search for inert anode materials has proved to be one of the most difficult challenges for modern materials science*." Great efforts have still not yet led to any acceptable material, and the work may perhaps best be characterised as a long and mostly unfruitful struggle (14). The development of a non-consumable anode is, however, presently claimed (24) to be one of the highest research priorities among primary aluminium producers. A concerted effort to develop an inert anode by 2020 could play a key role in expanding the demand for aluminium products (14).

1.5 Inert anode patents and literature review

Technologies that are potential replacements for the conventional Hall-Héroult technology must be assessed in light of their technical, economic and environmental attributes. The Technical Working Group (23) ran a literature search on inert anode technologies related to aluminium production. From present time back to 1985 they found 119 patens, and from 1945 to 1985 another 229 patents. The list of the patents and literature on inert anode technology is found in (23). Topics reviewed in the patent literature included cell design, cathode development, connection schemes, alternative electrolytes, ideas of solid oxide fuels cells, and inert anode materials. From the number of patents they selected, it is apparent that a good deal of work on inert anodes has been carried out. However, a review

of the state-of the-art within the industry indicates that little of this work has been deployed. To date, no fully acceptable inert anode materials have been found published or patented.

Insight gained from evaluation of numerous unsuccessful attempts to develop an inert anode suggests that this past work addressed only part of the task. The Technical Working Group concluded that the best ways of improve cell efficiency and attain economic and environmental responsibility is by studying the whole system instead of only the anode. The most workable solution to develop a successful inert anode involve what they call a "system approach" which requires the development of a wide range of new technologies involving the anode material, cell design and cell operation.

"Even if a successful inert anode is not developed in the near future, research that employs the systems approach may foster the development of spin-off technologies that could be applied to conventional Hall-Héroult cells. These technologies would be expected to achieve the industry goals of reduced energy consumption, low environmental impact, and improved domestic industrial competitiveness." (23)

1.5.1 Refractory hard metals

When a metallic anode is used, there is normally an oxidation reaction of the anode material, which may be written as:

$$xM + \frac{y}{2}O_2 \rightarrow M_xO_y \qquad [1\text{-}8]$$

The concept involves the formation of a dense and stable electronically conducting oxide layer at the surface of the anode, which protects the metal phase from further oxidation. The oxides formed on the anode must also have a very low solubility in the melt. The high melting point metals such as Mo, W, Zr, Hf, Ti, Cr, Ta, and Nb possess adequate electronic conductivity and possibly low solubilities (25). However, in tests at Alcoa Laboratories (25) all of them oxidised to non-conducting, volatile and/or soluble species. Many of the dissolved oxides are reduced at the cathode and leads to aluminium contamination.

1.5.2 Borides, nitrides and carbides

Some of these refractories have attractive semiconducting properties and low solubilities in the electrolyte and should not react with oxygen to a great extent. In tests as anodes at Alcoa Laboratories (25), they were all oxidised under the conditions of electrolysis and lost conducting properties.

1.5.3 Noble metals

Metals such as Pt, Au, Ag, Pd and Rh are good electronic conductors and form no stable oxides. However, in contact with aluminium metal, they form alloys of aluminium. When oxygen was continuously discharged on the platinum in tests at Alcoa Laboratories (25) the

anodes were more stable than anode made of nickel, iron or copper, but such metals are excluded because of the cost.

1.5.4 High temperature corrosion resistant metal alloys

The metal anode is designed to form a protective oxide layer that under cell operating conditions maintain thick enough to prevent chemical attack of underlaying matal, yet thin enough to allow electronic current to pass without a substantial increase in cell voltage (26). High temperature corrosion resistant alloys possess adequate electronic conductivity and a number of them have low solubility in a Hall- Héroult cell electrolyte.

In tests at Alcoa Laboratories (25) various commercial high temperature alloys invariably oxidised, degraded and lost conducting properties. "Slow consumable" metal based anodes comprise an alloy of iron with at least one of the metals nickel, copper, cobalt or zinc has, however, recently been patented (27), (28),(29). During use these anodes form an oxide surface layer mainly containing hematite and (nickel) ferrite. These anodes showed a wear rate of 1.2 micron/day after 100 hour of electrolysis. Cells using these anodes have also been patented (30).

1.5.5 Mixed oxides

The oxides belong to a class of materials that cover a wide range of stability, resistance to further oxidation, solubility in the electrolyte, resistance to fluoride formation and electronic conductivity. If the oxide is soluble in the melt, there is a possibility of the soluble species reacting with the metal pad, *i.e.* Al,

$$M_xO_y + \frac{2}{3}y \cdot Al = \frac{y}{3}Al_2O_3 + x \cdot M_{\text{dissolved in metal}} \qquad [1\text{-}9]$$

This reaction is thermodynamically favourable if the free energy of formation of the oxide per gram atom of oxygen is less negative than that of alumina. For a compound less stable than alumina to function as an inert anode, its rate of dissolution under electrolysis should be small. Further more, many oxides form fluorides (31) by reaction with cryolite, *e.g.*,

$$\frac{1}{y}M_xO_y + \frac{2}{3}Na_3AlF_6 = \frac{x}{y}MF_{2\frac{y}{x}} + \frac{1}{3}Al_2O_3 + 2NaF \qquad [1\text{-}10]$$

$$\frac{1}{y}M_xO_y + 4AlF_3 = \frac{x}{y}MF_{2\frac{y}{x}} + \frac{1}{3}Al_2O_3 \qquad [1\text{-}11]$$

Ray (31) reported the tendency for the formation of fluorides to increase with increasing activity of AlF_3, and these oxides should be avoided. There is also a possibility of other components of the electrolyte, *e.g.* Al_2O_3, CaF_2 reacting with the anode. In practice the activity of the components have to be considered. The stability of individual oxides may be improved by compound formation.

The oxide may be stable in the presence of aluminium, but the fluoride of the same metal can be less stable than aluminium fluoride (32). The result is aluminiothermic reduction of this compound,

$$MF_n + \frac{n}{3}Al = \frac{n}{3}AlF_3 + \underline{M} \qquad [1\text{-}12]$$

where the underline on the metal product, M, denotes its dissolution in the molten aluminium cathode to form a liquid metal alloy (32).

Those oxides that are more stable than Al_2O_3, *i.e.* BaO, BeO, CaO, MgO, etc., are generally quite soluble in molten cryolite, while some transition metal oxides in their highest valence state are relatively insoluble in the molten fluoride bath. Fe_2O_3 and NiO have relatively low solubility in cryolite melts, and each oxide is more stable than its fluoride.

Nickel ferrite ($NiFe_2O_4$) is one of the spinel type materials, AB_2O_4, and may contain two types of cations (A and B) (see Chapter 8.2). The A cations occupy the tetrahedral positions and the B cations the octahedral positions. The spinel structure has a possibility to substitute a variety of cations and alter properties. Further, the stability of the mixed oxides is likely to be reflected in lower solubilities.

1.5.6 Cermet anodes and alloys

Cermets are a class of materials in which both metallic and ceramic components are present. Ideally these would have the desirable properties of metallic materials as well as those of the ceramics. The matrix is made of oxide/oxides, and need to have the desirable low corrosion properties, while the metallic materials/alloys have satisfactory electrical conductivity and thermal shock resistance. By a proper combination of the different materials, the scope is to produce an oxide anode with enhanced electrical conductivity while retaining the desired degree of inertness.

Many patents have been published in the last 20 years (33), and one promising anode material was recently patented by Alcoa (34). Their anode contains at least one metal oxide (preferably iron oxide and nickel oxide) and a mixture or alloy of copper and silver. The alloy or mixture of copper and silver preferably comprises particles having an interior portion containing more copper than silver, and an exterior portion containing more silver than copper.

1.5.7 Coating and conducting materials

Attempts have been made at the Alcoa Laboratories (25) to use suitable coatings on steel, copper or graphite. The coating material included electroplated metals and some oxides. However, such attempts have not been successful mainly because the deposited material did not satisfy the stringent material requirements in a Hall- Héroult bath.

The feasibility of protecting electrodes by *in situ* formation of a ceric oxide layers, designated by ELTECH as CEROX$^{TM\ 3)}$-coatings has also been investigated (33), (35).

[3)] CEROX is a trademark of MOLTECH Invent S.A.

1.5.8 Plasma spraying

Plasma spraying is a process whereby powdered material introduced into a plasma stream becomes molten and is projected against the surface, which is being coated. Owing to "splat-quenching" of the molten particles on the cool substrate, a coating is built up which consists of many layers of overlapping lenticular particles. As a result of this mode of formation, three important properties must be considered:

- coating-to substrate adhesion
- interconnected porosity
- accumulating stress factors as the coating thickness is increased

1.6 Obstacles for the inert anode technology

The major cost-related hurdle for deploying new greensite Hall-Héroult aluminium smelters is the required capital investment of 1-2 billion USD (23). A smelter based on an inert anode technology will not be an attractive investment unless the projected costs of investing in and operating it are less than, or equivalent to, the costs of a conventional smelter. Projections must also show the potential of the new technology to be environmentally sustainable.

The efficiency of a system using inert anodes should meet or exceed the energy performance of a conventional system using carbon anodes. The minimum theoretical energy requirements for an inert anode process (producing Al and O_2) are about 47 % higher than those for the Hall-Héroult process (producing Al and CO_2). While the present state-of-the-art reduction cells run on the order of 49 % energy efficiency, the operating efficiencies of corresponding inert anode cells will have to be of the order of 71.5 % or higher (23).

Replacing consumable carbon anodes with non-consumable anodes would totally eliminate CO_2 , SO_2, COS, H_2S, CS_2, CF_4 and C_2F_6 emissions from the Hall-Héroult cell. However, if the energy efficiency of the inert anodes is less than that of the conventional carbon anode, increased CO_2 emissions will be shifted to fossil fuel fired power plants where they are used instead. On a world-wide basis, only 56 % of the electricity for the present aluminium smelting capacity is supplied by hydro-power.

Since the reduction potential is more than 1.0 V higher when inert anodes are used, compared to traditional carbon anodes, one has to reduce the anode-to-cathode distance. However, this change requires that a wettable cathode, which is probably TiB_2 based, is in place so that the aluminium metal pad will be stable enough to prevent shorting. The side-walls or the cell top must also be insulated more efficiently. If more insulation is used, the cell will probably operate without a frozen ledge, and an inert side-wall material must be developed.

An inert anode material and an encompassing cell that produces aluminium that fails to meet existing quality standards will not be successful unless there is a reliable, cost-effective method for adequately remove the relevant impurities (23). Industry is likely to prefer using inert anodes that cost more and produce relatively pure metal, rather than inert anodes that cost less but corrode and produce impurities that must be removed in a

secondary process at a cost equivalent to the higher-priced anodes (23). Any additional process adds its own set of potential complications and unexpected costs, which might not be economical feasible. Add-on refining steps would be considered on an element basis, in terms of the amount of impurities to be extracted and the maximum degree of refining that can be achieved. The Technical Working Group (23) concluded that industry is likely to prefer using inert anodes that are slightly more costly but that produce relatively pure metal, rather than inert anodes that costs less but corrode and produce impurities that must then be removed in a secondary process.

Despite all these obstacles Credit Suisse First Boston Corporation (CSFB) recently published a note (36) where they wrote the following: "*…we think two revolutionary smelting technologies -inert anodes and wettable cathodes – under development will be introduced for commercial scale aluminium production within the next two years. We believe they will begin to be adopted broadly by the industry in the middle of the next decade. Each technology would lower production costs…Further with the development of inert anodes, aluminium smelting would generate oxygen, not greenhouse gases. Indeed it would help provide sunlight in our universe."*

1.7 Motivation for the present work

The classical Hall-Héroult process was invented in 1886, and has progressively been improved ever since. Why then, should someone want to change a process that is well understood and that works?

Inert electrodes would mean a technical revolution of the Hall-Héroult process (14). They could yield significant cost, energy and environmental benefits (14). The primary aluminium production cost may be reduced by 15-20 % by using inert anodes, and the energy consumption may be lowered by up to 25 % if inert anodes could be coupled with a wettable cathode (14). Presently (1999) the net consumption of anode carbon is 400-500 kg/tonne aluminium produced. Introduction of inert anodes, meaning no carbon consumption, amounts to 12-15 % reduction of the production costs (14).

Another economic gain can be the oxygen gas developed at the anode, which may be collected as a valuable by-product from the process. It has been assumed that the sales price of the oxygen gas can amount to about 3 % of the value of the aluminium produced (20).

No need for changing of inert anodes in the cells saves manual work, and will give less cell operational disturbances, too.

1.7.1 New and more effective technology

So far carbon has been the only applicable anode material in Hall-Héroult cells. For a long time one has been aware of the inherent disadvantage of the carbon anode (14). The production of these anodes is expensive, with a price of about 400 USD/tonne carbon, which correspond to about 200 USD/tonne of aluminium produced. The production process, with the raw materials petroleum coke and pitch, is energy consuming (about 1 kWh/kg Al), and it gives considerable pollution by emitting an amount of $CO_{2(g)}$ that

correspond to about 10 % of the CO_2 emissions from the electrolysis process per tonne of aluminium produced.

The greatest disadvantage of carbon anodes is the fact that they are consumable. Prebake anodes must be changed at regular intervals, usually after 22-27 days (14), and this corresponds to about one anode change per cell-day. The anode change is labour intensive, and the insertion of a new and cold anode now represents the greatest operational disturbance to the heat balance of the cell. Uneven wear of the anode working surface can give poor anodic current distribution, unstable cell voltage and formation of carbon dust in the electrolyte. The anode consumption requires frequent anode beam adjustments to maintain constant cell voltage. In addition the anode beam raising procedure is required about every three weeks. The reduced need for anode handling will have important benefits related to improved safety and industrial hygiene for the workers.

1.7.2 Energy requirements in a cell with inert anodes

The only meaningful way of comparing the energy requirements for the traditional Hall-Héroult process with a process where inert electrodes are being used is by comparing the *total* energy requirement to produce the same amount of liquid aluminium. The theoretical minimum energy consumption for the decomposition of alumina to aluminium and oxygen at 960 ^{o}C is 9.26 kWh/kg aluminium, as compared to 6.34 kWh/kg aluminium with carbon anodes and CO_2 formation. In addition one must also account for the energy saved by not producing carbon anodes. By assuming that this amounts to be about 17 percent of the energy consumption by the electrolysis process (14), one calculates that the total energy consumption will be reduced by about 4 percent by changing technology if the same interpolar distance (~4.5 cm) is used in the two calculations.

The only practical way to obtain additional reduction in energy consumption is to reduce the interpolar distance. If it could be lowered from 4.5 to 1.9 cm, the energy consumption would be reduced by about 23 percent. This will require a different thermal insulation in the cell than we have today, and suitable materials must be developed before this may be possible in practice. For an extremely low interpolar distance of only 0.6 cm, which would require an inert *cathode*, the energy consumption for the electrolysis process would be about 12.1 kWh/kg aluminium (37), with a calculated cell voltage of 3.69 V. The total energy savings would then be about 32 percent, when the carbon anode production is included (14). This is a very significant energy reduction! For comparison, one could mention that the maximum energy saving with bipolar cells (see (4) (15) for further details), with inert electrodes, could be as much as 35 percent lower than the best present Hall-Héroult cell.

1.7.3 Environmental perspective

The European aluminium industry is committed to sustainable development (9). The environmental performance is continuously improved by:

- efficient use of resources and energy
- reduction of emissions to air and water
- improvement and development of process technology
- reduction of waste and increased recycling

The environmental advantages with inert anodes will mainly be the strongly reduced process-related emissions of greenhouse gases. By introducing inert anodes, all CO_2, CF_4 and C_2F_6 gas emissions from the cell could be eliminated. Hydrogen Fluoride (HF) is formed by reactions between fluorides in the cell and moisture or hydrogen as a component of anode carbon. Replacing consumable carbon anodes with inert anodes would totally eliminate the second source of hydrogen and should significantly reduce the first source because the inert anode cells must be kept more tightly sealed to minimise heat losses. The PAH components from the production of carbon anodes and Søderberg anode paste will also be eliminated, although a small amount of PAH would still be produced in the manufacture of cathode blocks and cell-lining. Replacing consumable carbon anodes with inert anodes would totally eliminate sulphur emissions from the aluminium production cells.

The environmental aspects of primary aluminium production are considered so important that they are given a comprehensive treatment in appendix A to give a broader perspective of the global climate and how the aluminium producers influence the global warming.

1.8 Objectives of the present work

Solubility data for the various anode components are scarce and partly in contradiction of each other. Since the dissolution of inert anodes strongly depends on the solubility of the anode constituents, determination of the solubility of the anode components nickel (Ni(II)), iron (Fe(II) and some Fe(III)) and copper (Cu(I) and Cu(II)) in various melt compositions were, consequently, considered to be very important. Based on the solubility measurements, models for dissolution mechanisms were made.

Cermet nickel ferrite anodes with different amounts of excess NiO were produced and tested electrochemically. Their electrical conductivity was also measured as a function of the temperature. Investigations of the mechanisms of degradation of the anode and the transport of the anodic impurities from the anode to the cathode were compared with the results from the solubility measurements.

1.9 References

(1) Zhuxian,Q., Qiu, Z., Grjotheim, K. and Kvande, H., *Naturally occurring Aluminium?*, The International Terje Østvold Symposium, Røros, Nov.2-3, Dept. of Chemistry, NTNU, Norway, pp. 149-154, 1998.

(2) Zhuxian, Q., Qiu, Z., Grjotheim, K. and Kvande, H., *Naturally occurring Aluminium?*, Aluminium, 75. Jahrgang, Vol 7/8, pp. 619-625, 1999.

(3) Craig, N.C., *Charles Martin Hall – The Young Man, His Mentor, and His Metal*, Journal of Chemical Education, 63, 557, 1986.

(4) Grjotheim, K., Krohn, C., Malinovský, M., Matiašovský, K. and Thonstad, J., A*luminium Electrolysis. Fundamentals of the Hall-Héroult Process,* 2nd ed., Aluminium-Verlag, Düsseldorf, ISBN 3-87017-155-3, 1982.

(5) Grjotheim, K., and Kvande, H., *Introduction to Aluminium Electrolysis*, 2nd ed., Aluminium-Verlag, ISBN 3-87017-233-9, 1993.

(6) Hydro Aluminium a.s., Elkem Aluminium ANS, Sør-Norge Aluminium A/S, *Norsk Aluminiumindustri og Miljø*, Hydro Media, ISBN 82-90861-25-5, Sep. 1994.

(7) Norges Offentlige Utredninger (NOU), *Kraftkrevende Industri og treforedling. Hovedtrekk og perspektiver*, No. 11, Chap. 20, C/O Norsk Hydro, Norway, 1998.

(8) Schwartz, H.-G., Kruger, B., and Kuckshinrichs, W., *Studies of global material flow of primary aluminium,* Aluminium, vol. 76, no. 1/2, pp. 60-64, 2000.

(9) European Aluminium Association, http://www.aluminium.org/eaa.htm, 99.02.09.

(10)Moomaw, W.R., *Industrial emissions of greenhouse gases*, Energy Policy, vol. 24, no. 10/11, pp. 951-968, 1996.

(11) Galasiu, R. and Galasiu, I., *Procedings VII Al Symposium, Donovaly,* Slovakia, p. 69, 1993.

(12) Oprea, F., Taloi, I., Constantin, I., and Roman, R., *Metallurgical Process Theory*, E.T.P., Bucuresti, pp. 336,381 and 533, 1978.

(13) Haupin, W. and Kvande, H., *Thermodynamics of Electrochemical Reduction of Alumina,* Light Metals 2000, pp. 379-385, 2000.

(14) Kvande, H., *Inert Electrodes in Aluminium Electrolysis Cells*, Light Metals 1999, pp. 369-376, 1999.

(15) Beck T.R., Rousar, I. and Thonstad, J., *Energy Efficiency Considerations on Monopolar Versus Bipolar Fused Salt Electrolysis Cells*, Light Metals 1993, TMS, pp. 485-491, 1993.

(16) Haupin, W., *History of Electrical Energy Consumption by Hall-Héroult Cells*, Hall-Héroult Centennial Volume, The Metallurgical Soc., Inc., Warrendale, PA, 1986.

(17) Belyaev, A.I. and Studentsov, Y.E., *Electrolysis of Alumina with Oxide Anodes,* Legkie Metal, no.6, vol. 3, pp. 17–22, 1937.

(18) Belyaev, A.I., *Electrolysis of Alumina using Ferrite Anodes,* Legkie Metal, vol. 1, no. 7, pp. 7–20, 1938.

(19) Billehaug, K, Øye, H.A., *Inert Anodes for Aluminium Electrolysis in Hall-Héroult Cells (I)*, Aluminium, vol. 57 no. 2, pp. 146-150, 1981.

(20) Pawlek, R.P., *Inert Anodes for the Primary Aluminium Industry*: *An Update,* Light Metals 1996, pp. 243-248, 1996.

(21) Billehaug, K, Øye, H.A., *Inert Anodes for Aluminium Electrolysis in Hall-Héroult Cells (II)*, Aluminium, no. 57 (3), pp. 228-231, 1981.

(22) McLeod, A.D., Lihrman, J.M., Haggerty, J.S., Sadoway,D., *Selection and Testing of Inert Anode Materials for Hall Cells*, Light Metals 1987, pp. 357-365, 1987.

(23) *Technical Working Group on Inert Anode Technology*, American Society of Mechanical Engineers', CRTD - vol. 53, under contract to The U.S. Department of Energy Office of Industrial Technologies, ASME International, July, 1999.

(24) Margolis, N., Eisenhauger, J., *Inert Anode Roadmap, A Framework for Technology Development*, Colombia Maryland: The Aluminium Association Inc., pp. 1-29, Feb. 1998.

(25) Weyand, J.D., DeYoung, D.H., Ray, S.P., Tarcy, G.P. and Baker, F.W., *Inert Anodes for Aluminium Smelting. Final Report*, Alcoa Technical Center, DOE/CS/40158-20, 1986.

(26) Hryn, J.H. and Sadoway, D.R., *Cell Testing of Metal Anodes for Aluminium Electrolysis*, Light Metals 1993, TMS, pp. 475-483, 1993.

(27) Moltech Invent S.A., *Nickel-Iron Alloy Based Anodes for Aluminium Electrowinning Cells,* Patent no. WO 00/06804, 10.Feb. 2000.

(28) Moltech Invent S.A., *Slow Consumable Non-Carbon Metal-Based Anodes for Aluminium Production Cells,* Patent no. WO 00/06805, 10.Feb. 2000.

(29) Moltech Invent S.A., *Nickel-Iron Alloy Based Anodes for Aluminium Electrowinning Cells,* Patent no. WO 00/06803, 10.Feb. 2000.

(30) Moltech Invent S.A., *Cells for the Electrowinning of Aluminium Having Dimensionally Stable Metal-Based Anodes,* Patent no. WO 00/06802, 10.Feb. 2000.

(31) Ray, S.P., *Effect of Cell Operating Parameters on Performance of Inert Anodes in Hall Cells*, Light Metals 1987, TMS, pp. 367-380, 1987.

(32) Sadoway, D.R., *A Material Systems Approach to Selection and Testing of Nonconsumable Anodes for the Hall Cell*, Ligt Metals 1990, pp. 403-407, 1990.

(33) Gregg, J.S., Frederick, H.L., King, L.H. and Vaccaro,A.J., *Testing of cerium oxide coated cermet anodes in a laboratory cell,* Light Metals 1993, pp. 455-464, 1993.

(34) Dowless, R.K., LaCamera, A.F., Troup, R.L., Ray, S.P and Hosler, R.B., *Molten Salt Bath Circulation Design for an Electrolytic Cell*, Alcoa, US Patent no. 5.938.914, Aug. 17th, 1999.

(35) Gregg, J.S., Frederick, H.L., Vaccaro, A.J., Alcorn, T.R., Tabereaux, A.T., and Richards, N.E., *Pilot cell demonstration of cerium oxide coated anodes,* Light Metals 1993, pp. 465-473, 1993.

(36) Van Leeuwen, T.M., *An Aluminum Revolution*, Desk notes, Credit Suisse First Boston Corporation, Dept. U.S./Nonferrous Metals/Aluminium, June 23rd, 2000.

(37) Jarrett, N., *Future Developments in the Bayer-Hall-Héroult Process*, in Production of. Aluminium and Alumina, Chap.13, pp. 188-207, John Wiley & Sons, 1987.

2 Behaviour of nickel ferrite cermet anodes

The scope of this work was to investigate the reaction mechanisms at the surface of the anode, and to try to understand the corrosion mechanisms involved during electrolysis. Knowledge about the mechanisms of degradation may give valuable information about how inert anodes should be made and under which conditions they will run optimally.

2.1 Thermodynamical considerations regarding the chemistry at the surface of the anode and in the melt

There are several chemical reactions that can take place during sintering of anode materials. Some of them can be avoided, but others are just a fact. Based on a thermodynamical database (1) with data from JANAF (2), Barin (3) and Knacke *et al*. (4), chemical stability has been considered. The standard Gibbs energy was calculated for the reactions at 1000 ^{o}C when not otherwise stated.

It is important to note that all the thermodynamic calculations for the oxides and fluorides are based on standard state data for pure substances, and not data for the specific species present in cryolite melts. The calculations will hopefully still give an indication of the stability of the different coexisting phases.

If one uses the Gibbs energy of formation (ΔG^{o}) for the species present in the cermet and in the melt, it is possible to calculate the stability of different coexisting species by calculating ΔG^{o}. If it is negative, it means that the reaction in question is spontaneously going to the right if reactants and products are in their standard states.

Cermet with excess nickel oxide (NiO) has shown promising low corrosion rates during electrolysis (5), (6), (7), (8). It is therefor important to consider the stability of the cermet phases, which are $NiFe_2O_4$, NiO, Ni, Cu, Fe and the cell components NaF, AlF_3, Al_2O_3, CaF_2 and Al.

Although the solubility of aluminium in cryolite is low, the cryolite melt contains dissolved aluminium or AlF^{-} and Na species, which can reduce the anode material or the metal fluoride. For metal oxides, the typical reactions can be expressed as (9):

$$MO_{\frac{n}{2}} + \frac{n}{3}Al = M + \frac{n}{6}Al_2O_3 \qquad [2\text{-}1]$$

$$MF_n + \frac{n}{3}Al = \frac{n}{3}AlF_3 + M \qquad [2\text{-}2]$$

If aluminium is present in contact with the cermet, most of the oxides in the cermet will be reduced.

2.1.1 Stability of nickel ferrite

Nickel ferrite will according to thermodynamics not dissociate:

$$NiFe_2O_4 = NiO + Fe_2O_3 \qquad \Delta G_R^0 = 24.1 \text{ kJ/mol} \qquad [2\text{-}3]$$

Neither will nickel ferrite react with alumina according to,

$$NiFe_2O_{4(s)} + Al_2O_{3(s)} = NiAl_2O_{4(s)} + Fe_2O_{3(s)} \quad \Delta G_R^0 = 5.669 \text{ kJ/mol} \qquad [2\text{-}4]$$

These calculations assume that all the reactants and products are in their standard states. This will, however, not always be the case during electrolysis. The equilibrium constant, K, for equation [2-4] can be expressed as,

$$K = \left(\frac{a_{Fe_2O_3}}{a_{Al_2O_3}} \right) = 0.59 \text{ at } 1020\,^{o}C \qquad [2\text{-}5]$$

since the activities of $NiFe_2O_4$ and $NiAl_2O_4$ are equal to 1.

Based on the equilibrium constant, a stability diagram for $NiFe_2O_4$ and $NiAl_2O_4$ can be constructed as a function of the activities of Al_2O_3 and Fe_2O_3, and the result is shown in Figure 2-1.

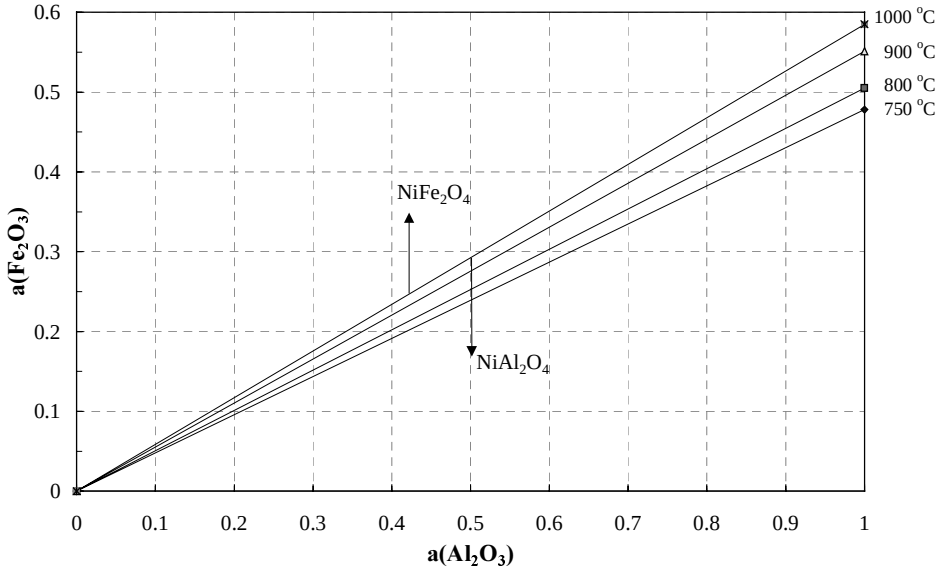

Figure 2-1: Stability regions of $NiFe_2O_{4(s)}$ and $NiAl_2O_{4(s)}$ as a function of the activities of Al_2O_3 and Fe_2O_3 at 750 - 1000 ^{o}C.

As one can see from Figure 2-1, as long as K is below 0.59, $NiAl_2O_4$ can be formed. What it means in terms of the practicality of this "non-consumable" anode is that the Fe_2O_3 activity has to be kept high, or the anode material will convert to aluminate, which is an electrical insulator. This also implies that one will get a transfer of iron into the produced aluminium and contaminate the metal.

2.1.2 Stability of iron compounds

If metallic iron (Fe) is present in the cermet, the following reactions are possible according to the thermodynamics for Fe:

$$Fe + 0.528O_{2(g)} = 1.056Fe_{0.947}O \qquad \Delta G_R^0 = -193.744 \text{ kJ/mol} \qquad [2\text{-}6]$$

$$Fe + \frac{3}{4}O_{2(g)} = \frac{1}{2}Fe_2O_3 \qquad \Delta G_R^0 = -246.304 \text{ kJ/mol} \qquad [2\text{-}7]$$

$$Fe + \frac{2}{3}O_{2(g)} = \frac{1}{3}Fe_3O_4 \qquad \Delta G_R^0 = -236.721 \text{ kJ/mol} \qquad [2\text{-}8]$$

$$Fe + \frac{1}{2}O_{2(g)} + \frac{2}{3}AlF_3 = FeF_2 + \frac{1}{3}Al_2O_3 \qquad \Delta G_R^0 = -168.885 \text{ kJ/mol} \qquad [2\text{-}9]$$

$$Fe + \frac{3}{4}O_{2(g)} + AlF_3 = FeF_3 + \frac{1}{2}Al_2O_3 \qquad \Delta G_R^0 = -212.454 \text{ kJ/mol} \qquad [2\text{-}10]$$

All the reactions have a negative ΔG^o value, and will spontaneously go to the right.

The following reaction will not occur *when the species are in their standard states*:

$$FeO + \frac{2}{3}AlF_3 = FeF_2 + \frac{1}{3}Al_2O_3 \qquad \Delta G_R^0 = 11.972 \text{ kJ/mol} \qquad [2\text{-}11]$$

Since neither the activities of AlF_3 nor Al_2O_3 are unity in melts unsaturated with respect to alumina, FeF_2 can be formed as shown in Chapter 5.

Iron aluminates may be formed according to the following two reactions,

$$FeF_2 + \frac{4}{3}Al_2O_3 = FeAl_2O_4 + \frac{2}{3}AlF_3 \qquad \Delta G_R^0 = -55.202 \text{ kJ/mol} \qquad [2\text{-}12]$$

$$FeO + Al_2O_3 = FeAl_2O_4 \qquad \Delta G_R^0 = -43.230 \text{ kJ/mol} \qquad [2\text{-}13]$$

Iron aluminate can, however, react with oxygen and aluminium fluoride (AlF_3) to form FeF_3 *below* approximately 750 °C, but at 1000 °C ΔG^o is positive:

$$FeAl_2O_4 + AlF_3 + \frac{1}{4}O_{2(g)} = FeF_3 + \frac{3}{2}Al_2O_3, \quad \Delta G_R^0 = \quad 11.633 \text{ kJ/mol} \qquad [2\text{-}14]$$

$FeAl_2O_4$ is, however, not stable in coexistence with Fe_2O_3:

$$FeAl_2O_4 + \frac{1}{4}O_{2(g)} = \frac{1}{2}Fe_2O_3 + Al_2O_3, \qquad \Delta G_R^0 = -22.217 \text{ kJ/mol} \qquad [2\text{-}15]$$

Iron can exist with two oxidation states, *i.e.* Fe(II) and Fe(III), and the solid states of the different iron species present in an electrolysis cell are depending on the partial pressure of oxygen and the activity of alumina. The following equilibria were expressed to construct the predominance area diagram showing the solid iron phases as a function of the partial oxygen pressure and alumina activity at 1020 ^oC.

$$4Fe_3O_{4(s)} + O_{2(g)} = 6Fe_2O_{3(s)} \qquad \Delta G_R^0 = -120.441 \text{ kJ/mol} \qquad [2\text{-}16]$$

$$2.252Fe_2O_{3(s)} = 4.756Fe_{0.947}O_{(s)} + O_{2(g)} \qquad \Delta G_R^0 = \quad 231.654 \text{ kJ/mol} \qquad [2\text{-}17]$$

$$Fe_{0.947}O_{(s)} = 0.947Fe_{(s)} + \frac{1}{2}O_{2(g)} \qquad \Delta G_R^0 = \quad 182.196 \text{ kJ/mol} \qquad [2\text{-}18]$$

$$37.736Fe_{0.947}O_{(s)} + 35.736Al_2O_{3(l)} \rightarrow 35.736FeAl_2O_{4(s)} + O_{2(g)}$$
$$\Delta G_R^0 = -1074.782 \text{ kJ/mol} \qquad [2\text{-}19]$$

$$2FeAl_2O_{4(s)} = 2Fe_{(s)} + 2Al_2O_{3(l)} + O_{2(g)} \qquad \Delta G_R^0 = \quad 407.344 \text{ kJ/mol} \qquad [2\text{-}20]$$

$$6FeAl_2O_{4(s)} + O_{2(g)} = 2Fe_3O_{4(s)} + 6Al_2O_{3(s,\alpha)} \qquad \Delta G_R^0 = -189.289 \text{ kJ/mol} \qquad [2\text{-}21]$$

According to thermodynamics, Gibbs energy of formation can be expressed as,

$$\Delta G^o = -RT \cdot \ln(K) \qquad [2\text{-}22]$$

the partial oxygen pressures for equations [2-16] to [2-21] were expressed as a function of the alumina activity and the equilibrium constant K. To give an example, equation [2-21] can be expressed as,

$$\log\left(p_{O_2(g)}\right) = 6 \cdot \log\left(a_{Al_2O_3}\right) - 7.646 \qquad [2\text{-}23]$$

Based on the thermodynamic data collected by Dewing and Thonstad (10), the predominance area diagram was constructed (see Figure 2-2) at 1020 ^oC.

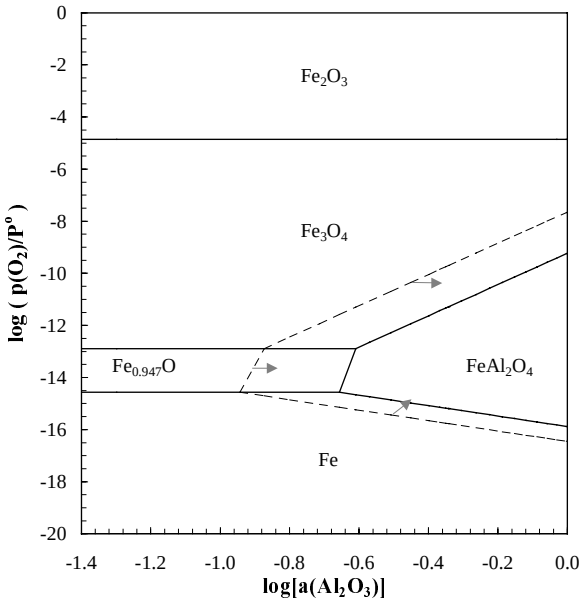

Figure 2-2: The predominance area diagram showing the solid iron phases as a function of the partial oxygen pressure and the alumina activity at 1020 °C. The dotted lines are given by data from Dewing and Thonstad (10), and the non-horizontal solid lines are calculated from the results in Chapter 5.

Figure 2-2 shows the stability region of the solid iron states as a function of the partial oxygen pressure and the alumina activity. As one can see, it is important to control both oxygen pressure and the alumina activity parameters to stabilise a certain species.

2.1.3 Stability of nickel compounds

According to thermodynamics NiO is a stable phase in the absence of aluminium, and reaction [2-23] will not occur *when the species are in their standard states*:

$$NiO + \frac{2}{3}AlF_3 = NiF_2 + \frac{1}{3}Al_2O_3 \qquad \Delta G_R^0 = 27.174 \text{ kJ/mol} \qquad [2\text{-}24]$$

$NiFe_2O_4$ based cermet anodes are best protected in alumina-saturated melts. According to thermodynamics, aluminates form readily from anode metals, oxides and fluorides under electrolytic conditions. For nickel this means that the following reactions are possible,

$$NiF_2 + \frac{4}{3}Al_2O_3 = NiAl_2O_4 + \frac{2}{3}AlF_3 \qquad \Delta G_R^0 = -45.578 \text{ kJ/mol} \qquad [2\text{-}25]$$

$$NiO + Al_2O_3 = NiAl_2O_4 \qquad \Delta G_R^0 = -18.586 \text{ kJ/mol} \qquad [2\text{-}26]$$

Based on thermodynamic data given for NiO and Al_2O_3 by Barin (3), for $NiAl_2O_4$ by Knacke (4), and activities for Al_2O_3 by Dewing and Thonstad (11), a predominance area diagram showing the solid nickel phases as a function of the partial oxygen pressure and the alumina activity has been constructed. Figure 2-3 is constructed in the same way as Figure 2-2 by expressing [2-22] for equilibria [2-26] to [2-28] at 1020 °C:

$$Ni_{(s)} + Al_2O_{3(s,\alpha)} + \frac{1}{2}O_{2(g)} = NiAl_2O_{4(s)} \quad \Delta G_R^0 = -142.744 \text{ kJ/mol, from (1)} \qquad [2\text{-}27]$$

$$Ni_{(s)} + \frac{1}{2}O_{2(g)} = NiO_{(s)} \quad \Delta G_R^0 = -124.158 \text{ kJ/mol, from (1)} \qquad [2\text{-}28]$$

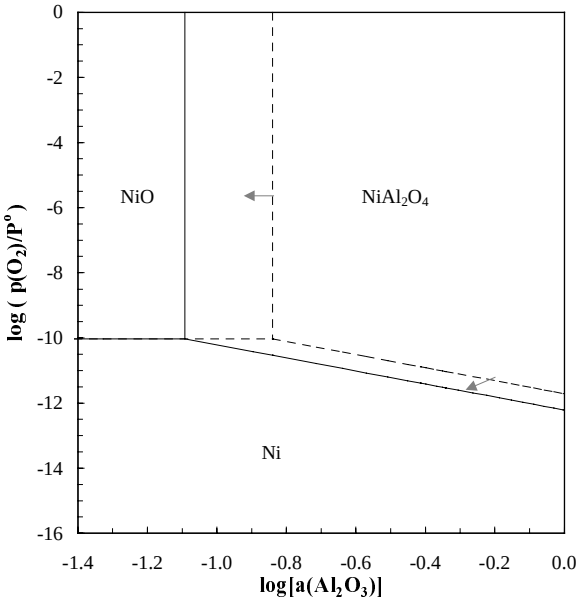

Figure 2-3: The predominance area diagram showing the solid nickel phases as a function of the partial oxygen pressure and the alumina activity. Temperature = 1020 °C. The dotted lines are given by (1), and the non-horizontal solid lines are based on the present results in Chapter 4.

As one can see, only NiO and $NiAl_2O_4$ are the stable solid phases involved under normal operating conditions.

2.1.4 Stability of copper compounds

Copper (Cu) is according to thermodynamics a stable phase in coexistence with $NiFe_2O_4$, but it will react with oxygen according to,

$$Cu + \frac{1}{4}O_{2(g)} = \frac{1}{2}Cu_2O \quad \Delta G_R^0 = -37.929 \text{ kJ/mol} \qquad [2\text{-}29]$$

$$Cu + \frac{1}{2}O_{2(g)} = CuO \qquad \Delta G_R^0 = -43.507 \text{ kJ/mol} \qquad [2\text{-}30]$$

Copper fluoride may form in cryolite-based melts. Strachan *et al*. (12) detected no CuF in the reaction product, but their AC impedance data supported a reaction of this type. CuF will not be formed according to,

$$\frac{1}{2}Cu_2O + \frac{1}{3}AlF_3 = CuF + \frac{1}{6}Al_2O_3 \qquad \Delta G_R^0 = 15.083 \text{ kJ/mol} \qquad [2\text{-}31]$$

CuF is, however, not a stable phase at room temperature (13), (14) and questions can be raised regarding the stability and the existence of CuF at elevated temperatures. The thermodynamic data given for CuF in JANAF (2) and in Barin (3) may even be questionable.

Neither will CuO react to CuF_2 over 900 ^oC by the following mechanism,

$$CuO + \frac{2}{3}AlF_3 = CuF_2 + \frac{1}{3}Al_2O_3 \qquad \Delta G_R^0 = 45.939 \text{ kJ/mol} \qquad [2\text{-}32]$$

The following reactions produce copper aluminates,

$$CuF + \frac{2}{3}Al_2O_3 = CuAlO_2 + \frac{1}{3}AlF_3 \qquad \Delta G_R^0 = -21.353 \text{ kJ/mol} \qquad [2\text{-}33]$$

$$CuF_2 + \frac{4}{3}Al_2O_3 = CuAl_2O_4 + \frac{2}{3}AlF_3 \qquad \Delta G_R^0 = -52.905 \text{ kJ/mol} \qquad [2\text{-}34]$$

$$\frac{1}{2}Cu_2O + \frac{1}{2}Al_2O_3 = CuAlO_2 \qquad \Delta G_R^0 = -6.270 \text{ kJ/mol} \qquad [2\text{-}35]$$

CuO will react to aluminate when the temperature above approximately 550 ^oC:

$$CuO + Al_2O_3 = CuAl_2O_4 \qquad \Delta G_R^0 = -6.966 \text{ kJ/mol} \qquad [2\text{-}36]$$

Since copper can exist with both valence one and two, and exchange reactions between Cu(II) and Cu are possible.

$$CuF_2 + Cu = 2CuF \qquad \Delta G_R^0 = -48.126 \text{ kJ/mol} \qquad [2\text{-}37]$$

Although no CuF could be detected in the reaction products by Strachan (12), their ac impedance data supported reaction [2-38] which was mass transport controlled.

$$Cu + F^- = CuF + e^- \qquad [2\text{-}38]$$

Their explanation was that the unstable CuF compound reacted with alumina according to

$$CuF + \frac{1}{2}O^{2-} = \frac{1}{2}Cu_2O + F^- \qquad [2\text{-}39]$$

which was supported by the large amounts of Cu_2O found on pure copper electrodes (12).

Cu_2O can, however also be produced according to [2-29] or,

$$CuF_2 + \frac{1}{3}Al_2O_3 + Cu = Cu_2O + \frac{2}{3}AlF_3 \qquad \Delta G_R^0 = -78.291 \text{ kJ/mol} \qquad [2\text{-}40]$$

Based on the thermodynamic equations given by Jacob and Alcock (15), the following 7 reactions were expressed as a function of oxygen partial pressure and alumina activity:

$$4Cu_{(s)} + O_{2(g)} \rightarrow 2Cu_2O_{(s)} \qquad \Delta G_R^0 = -150.187 \text{ kJ/mol} \qquad [2\text{-}41]$$

$$2Cu_2O_{(s)} + O_{2(g)} \rightarrow 4CuO_{(s)} \qquad \Delta G_R^0 = -18.010 \text{ kJ/mol} \qquad [2\text{-}42]$$

$$4Cu_{(s)} + O_{2(g)} + 2Al_2O_{3(s,\alpha)} = 4CuAlO_{2(s)} \qquad \Delta G_R^0 = -170.731 \text{ kJ/mol} \qquad [2\text{-}43]$$

$$Cu_2O_{(s)} + Al_2O_{3(s,\alpha)} = 2CuAlO_{2(s)} \qquad \Delta G_R^0 = -10.251 \text{ kJ/mol} \qquad [2\text{-}44]$$

$$4CuAlO_{2(s)} + 2Al_2O_{3(s,\alpha)} + O_{2(g)} = 4CuAl_2O_{4(s)} \qquad \Delta G_R^0 = -31.427 \text{ kJ/mol} \qquad [2\text{-}45]$$

$$4CuAlO_{2(s)} + O_{2(g)} = 4CuO_{(s)} + 2Al_2O_{3(s,\alpha)} \qquad \Delta G_R^0 = 2.492 \text{ kJ/mol} \qquad [2\text{-}46]$$

$$CuO_{(s)} + Al_2O_{3(s,\alpha)} = CuAl_2O_{4(s)} \qquad \Delta G_R^0 = -8.468 \text{ kJ/mol} \qquad [2\text{-}47]$$

With the use of equations [2-41] to [2-47] and alumina activity data from Dewing and Thonstad (11), 7 equations similar to [2-23] were expressed as a function of the alumina activity and the corresponding equilibrium constants. The following predominance area diagram was then constructed showing the stability regions of the different copper phases as a function of $\log[a(Al_2O_3)]$ and $\log[(p_{O_2}) / p^o]$.

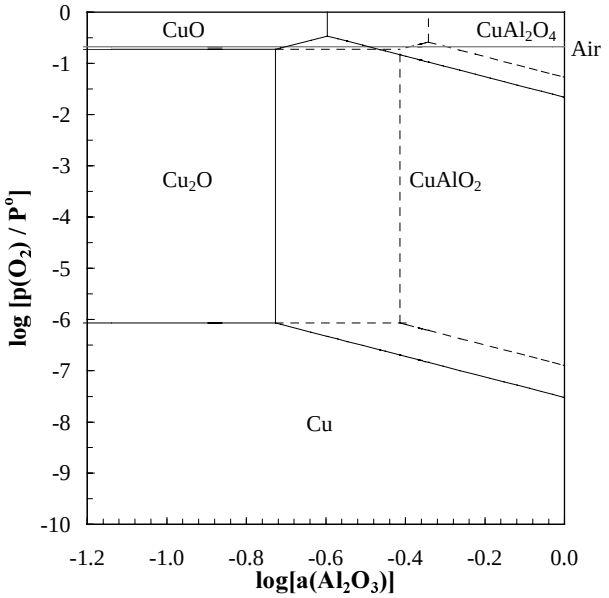

Figure 2-4: The predominance area diagram showing the stability regions for Cu, Cu_2O, CuO, $CuAlO_2$ and $CuAl_2O_4$ at 1020 °C. The gray line is the partial pressure of oxygen in air. The dotted lines are given by Jacob and Alcock (15) and the non-horizontal lines are based on the present results (see Chapter 6).

As one can see from Figure 2-4, only CuO and $CuAl_2O_4$ are stable under an atmosphere of oxygen at 1020 °C. In air, the phase diagram predicts that one is operating at a partial pressure of oxygen very close to several phase boundaries. There is a risk of getting both Cu_2O and $CuAlO_2$ in the solutions depending on the alumina activity. if one changes the temperature from 1020 °C to 1025 °C, the dotted line coincides with the CuO/Cu_2O line, and it goes through the triple-point where CuO, $CuAl_2O_4$ and $CuAlO_2$ coexist at 1000 °C (see Appendix B). The window showing the stability region for CuO increases at the expense of Cu_2O and $CuAl_2O_4$ with decreasing temperature.

Low ratio bath with an operating temperature of only 750 °C has been suggested (16), (17), and the phase diagram is shown in Appendix B for this temperature. As one can see, the stability region for CuO has increased tremendously. CuO is known to have a higher solubility than Cu_2O and is also a poorer ionic conductor than Cu_2O, which may disfavour using low melting baths when copper is used.

As one can see, there are several different reactions that may occur at the surface of the cermet during electrolysis. There is, however, not possible to give more than a qualitative discussion regarding the mechanisms without knowing anything about the kinetics of the various reactions. X-ray and SEM analysis of the anode materials may give some information about the mechanisms involved, but it is not possible to run such analysis during similar conditions as during electrolysis, so these results may give a incorrect picture of the conditions *in situ*. This will be discussed thoroughly later.

2.2 Oxidation of the metal phase under an oxygen atmosphere

The inert anodes produce oxygen, which causes oxidation of the metal phase. Since the electrical conductivity of the metal phase is so much higher than for the oxide phases, especially if the metal phase is continuos in the oxide matrix, at least in the first period of operation much of the current flows through the metal phase giving unit oxygen pressure at the surface of the metal phase. After a while a depletion of the metal phase occurs in the outer layer of the anode. In the areas where the metal is oxidised and dissolved in the melt transport pores may develop into the interior of the anode if the melt is under-saturated with alumina. The partial pressure of oxygen is probably close to 1 atmosphere inside these pores, and the oxidation of the metal phase inside these pores may act similarly to what a pure metal phase will do in an atmosphere of oxygen at the same temperature.

Eletrochemical and spectroscopic methods for determining electrochemical reaction were found by Hart *et al*. (18) to give the best results or show the most potential when applied to all-metal anodes. They therefore recommended that studies on the electrochemical reactions mechanisms of candidate cermet anodes in molten cryolite should be focused on metal/alloys with compositions similar to the metal phases in these anodes.

In the presence of metallic copper Cu_2O is the stable phase:

$$CuO_{(s)} + Cu_{(s)} \rightarrow Cu_2O_{(s)} \qquad \Delta G_R^0 = -32.352 \text{ kJ/mol} \qquad [2\text{-}48]$$

which indicates that Cu_2O forms on the metallic copper substrate, and CuO is formed on top of the Cu_2O layer. The quantities of the two oxides will be a function of the partial oxygen pressure, and of the kinetics of the two reactions.

Haugsrud (19) investigated the oxidation of copper in oxygen atmosphere. He found brake away oxidation of copper to CuO caused by pores and lattice tension at below 1000 ^oC in oxygen atmosphere, while a dense and stable layer of Cu_2O with only a very thin layer of CuO on top of this layer was formed above 1000 ^oC. Haugsrud recommended using a nickel-rich copper-nickel alloy, ex. a Cu80%Ni alloy, to form a protective outer layer of NiO.

If one assumes that reaction [2-29] and [2-30] are taking place under the oxidising conditions near the anode, reaction [2-30] may be shifted to the left under slightly reducing conditions near the cathode, giving Cu_2O. The final result may be that metallic copper precipitate near the cathode according to:

$$Cu_2O_{(s)} + \frac{2}{3}Al_{(s)} = 2Cu_{(s)} + \frac{1}{3}Al_2O_{3(s,\alpha)} \qquad \Delta G_R^0 = -347.359 \text{ kJ/mol} \qquad [2\text{-}49]$$

Chin reported (20), (21) a “skim layer” of metallic copper in the melt near the surface of the aluminium (cathode) after the experiment was terminated and the melt was solidified. This discovery supports the assumption of such mechanisms, but might also indicate reaction between copper ion and the less noble ions of iron and nickel.

Haugsrud and Kofstad (22) investigated the oxidation of high purity Cu and copper-nickel alloys at 900-1050 ^{o}C under oxygen pressures from $5 \cdot 10^{-4}$ to 0.21 atmosphere for Cu and from $5 \cdot 10^{-4}$ to 1 atmosphere for Cu-Ni-alloys. The oxidation rate, as measured by thermogravimetry, was parabolic. At oxygen pressures where only Cu_2O is formed, the oxygen pressure dependence gradually changed from being proportional to $P_{O_2}^{1/7}$ at low pressures, to $P_{O_2}^{1/4}$ at near-atmospheric oxygen pressure. Cu30Ni15Fe did, however, oxidise linearly in 1 atmosphere of oxygen, *i.e.* a constant rate of oxidation and no formation of a protecting oxide layer (23). The reaction kinetics and oxygen pressure dependence was interpreted to reflect that the oxidation is governed by diffusion of copper predominantly via singly charged vacancies at the lower oxygen pressures and neutral vacancies at the near-atmospheric oxygen pressures. Depending on the temperature and the partial pressure of oxygen, the oxide scale either consisted of Cu_2O or Cu_2O + CuO. As the diffusion of Cu in CuO is much slower than in Cu_2O, the main part of the double-layered Cu_2O + CuO scale consisted of Cu_2O. Oxygen tracer measurements have shown that oxygen diffusion increases with increasing oxygen pressure, and from this pressure dependence it is concluded that defects in the oxygen lattice are singly charged oxygen interstitials. Haugsrud and Kofstad reported that lattice diffusion of oxygen vacancies probably does not significantly influence the oxidation process at elevated oxygen pressures.

If grain boundary diffusion contributes significantly to the diffusional transport through the oxide layer, it would probably lead to a higher oxidation rate than that predicted for the oxidation limited by lattice diffusion at low oxygen pressures and temperatures. This could therefore be a possible alternative explanation of the observed gradual change in the oxygen pressure dependence (22).

In a copper- nickel alloy with 1-20 wt% Ni, the rate of oxidation gradually increased and exceeded that of unalloyed copper (24). For Cu-rich alloys, the oxide scales consisted of a thin outer layer of CuO in 1 atmosphere of oxygen, a relatively thick and dense layer of Cu_2O, and next to the metal a porous layer of Cu_2O and NiO. The copper oxides and NiO are usually considered to be virtually immiscible, but the solubility of NiO in Cu_2O has been suggested to be about 0.2 wt% at 800 ^{o}C (24). The NiO is dispersed as particles in a matrix of Cu_2O, and the NiO particles are essentially immobile relative to the Cu_2O matrix. Nickel is internally oxidised to NiO particles. The porosity for a 5 wt% Ni-Cu alloy was slightly higher than for the 2% alloy. The porosity is reported (24) to be largest at reduced oxygen pressures and it decreases gradually with increasing oxygen pressure and temperature and, thus with increasing rate of oxidation. The relative thickness of the inner region increases with increasing oxygen pressure and nickel content, but decreases with increasing temperature. The oxygen pressure dependence is very similar to that for unalloyed copper. The parabolic rate constant is larger than that for unalloyed copper at 1000 ^{o}C and 1050 ^{o}C, while the rate constants are approximately the same at 900 ^{o}C. It was concluded (24) that the oxidation of the Cu-2%Ni and Cu-5%Ni is closely related to that of unalloyed copper. The presence of relatively small amounts of nickel additions to copper dramatically changes the morphology and microstructure of the oxide scales.

The very initial oxide layer that is formed by oxidation (24) of Cu-Ni alloys at 800 ^{o}C has the same composition as that of the surface layer of the alloy, and it consists of lateral grains of Cu_2O and NiO. As the diffusion of copper through the Cu_2O grains is several orders of magnitude faster than the corresponding diffusion of nickel through NiO, the Cu_2O rapidly overgrows the NiO grains. This is the reason why the outer scale consists of Cu_2O and CuO only. The oxygen self-diffusion in Cu_2O is two to three orders of magnitude slower than the self-diffusion of copper, so inward oxygen-lattice diffusion is not important in the growth of Cu_2O. At sufficiently high oxygen pressures the Cu_2O is slowly oxidised to CuO, but this latter oxide only accounts for a minor fraction of the outer copper oxide layer.

At the scale-metal interface the Cu_2O dissociates and atomic oxygen dissolves and diffuses into the alloy where it reacts with the nickel component in the alloy to form NiO precipitates (24). The copper from the dissociation diffuses outward through the Cu_2O phase to the scale surface where it reacts with oxygen to form additional Cu_2O. Because of this internal oxidation of the nickel alloy component, the metal phase at the scale-metal interface essentially consists of copper only.

As oxidation proceeds, a steady state growth of the oxide scale is gradually established. Copper diffuses outward through the scale by solid state diffusion through the Cu_2O phase. However, the NiO particles can be considered to be relatively immobile in the oxide layer. They practically block the outward diffusion since they reduce the cross-sectional area for diffusion. Furthermore, the NiO dispersed in the oxide and metal phases impede the plastic deformation of both the inner layer of the scale and the initially oxidised layer of the metal. The copper and the Cu_2O phases between the NiO particles diffuse outwards during oxidation. Because NiO particles are present, copper is depleted and porosity develops between the NiO particles. At steady state the inner layer consists of Cu_2O, NiO particles and porosity.

Even though the NiO particles may block the outward copper diffusion, this does not necessarily mean that the oxidation rate is reduced under all conditions, since oxygen may be transported inward across the pores or voids due to dissociative transport. As the metal ions move outward, oxygen is liberated as gas in the voids according to,

$$\frac{1}{2}Cu_2O_{(\text{in oxide layer})} = Cu_{(\text{in oxide layer})} + \frac{1}{2}O_{2(g)} \qquad [2\text{-}50]$$

The oxygen gas is transported inward across the void and reacts with new copper ions arriving at the void surface facing the metal. In this way oxidation continuos and the inward oxygen transport can be considered to partially short-circuit the outward diffusion of copper and thereby reduce the effective solid state diffusion distance.

In considering gaseous transport across voids and porosity it is also important to consider the possibility of evaporation of copper from the metal phase and outward gaseous transport of copper atoms through the porosity next to the metal phase. The vapour pressure of copper is $7.2 \cdot 10^{-10}$ atmosphere at 1000 ^{o}C, and by using (24) the Hertz-Langmuir equation this yields an evaporation rate of about $7 \cdot 10^{-7}$ g/cm^2·s^{-1}. Thus copper evaporation from the substrate metal and from Cu_2O near the metal phase is not considered

(24) important under most reduction consideration except for temperatures higher than 1000 ^{o}C.

For further details, Kofstad (25) and (26) has made a thorough evaluation of defect chemistry and transport properties in metal oxides.

During preliminary oxidation of a Cu30Ni15Fe alloy, all the alloying elements will oxidise giving NiO FeO and Cu_2O (19). The growth of Cu_2O is, however, fastest and copper metal diffuses through this preliminary oxide layer and produces a continuous layer of Cu_2O covering all the other oxides. Under this new Cu_2O layer FeO and NiO are produced. Oxygen diffuses into the alloy and reacts with iron forming an inner layer of FeO. The oxidation mechanisms previously mentioned cause the alloy to be copper depleted and enriched with iron and nickel. When the oxide layer thickness increases, tensions occur in the layer, which may cause cracking and peeling of the oxide layer.

Autopsies of similar metal anodes used in electrolysis with eutectic (acidic) melt at 750 ^{o}C for 4 hours (27) did not show the outer formation of CuO. The oxide layer seemed to crack, and melt constituents were found in interfacial zones inside the oxide layers.

Windisch and Marschman (28) have presented cyclic voltammograms for Cu metal in alumina-saturated molten cryolite (molar ratio (CR) = 2.2) at 980 ^{o}C. They suggested the primary anode reaction at a Cu electrode to be the oxidation of Cu_2O to CuO.

$$Cu_2O_{(s)} + Al_2O_{3(s,\alpha)} \overleftarrow{=} 2CuO_{(s)} + O_{2(g)} + 2Al_{(s)} \qquad E^{o}_{R} = -2.187\ V \qquad [2\text{-}51]$$

No sign of oxidation of pure Cu metal was identified, indicating the presence of Cu_2O on the surface of the Cu metal at the start of the polarisation. The open circuit potential for the Cu electrode was 1.80 V, which indicates (28) the reaction:

$$Cu_2O_{(s)} + 2Al_{(s)} \overleftarrow{=} 6Cu_{(s)} + Al_2O_{3(s,\alpha)} \qquad E^{o}_{R} = -1.796\ V \qquad [2\text{-}52]$$

No significant traces of copper fluorides and only minor amounts of aluminium species were detected (28), indicating that the predominant electrochemical transformations involved copper oxides. XRD analysis did, however indicate the formation of $CuAlO_2$, but this layer was reported to be formed on the outside of the copper oxide deposits and not on the metal surface. Only Cu_2O was identified adjacent to the Cu metal. This observation suggests that the copper aluminate was a product of a reaction between Cu_2O and alumina and/or molten cryolite at the Cu metal surface. The formation of Cu(III) species at potentials above the decomposition potential of alumina was suggested.

Cyclic voltammograms obtained (28) for Cu in a cryolite melt unsaturated with alumina suggested that the Cu_2O layer is not completely formed or is unstable at low alumina concentrations. Cu metal was oxidised directly under these conditions, and both the formation of CuO and Cu_2O were detected at 1.98 V and 1.77 V, respectively.

Cyclic voltammograms of a cermet consisting of $NiFe_2O_4$ and 17 % Cu were also conducted (28) in alumina-saturated molten cryolite (molar ratio (CR) = 2.2) at 960 ^oC at "low" current densities. A broad peak at 2.16 V and an even broader peak below 2.00 V may indicate the same oxidation reactions as obtained for Cu metal in alumina-saturated melts, but their results obtained for the cermet is very hard to interpret. The formation of Cu_2O and CuO and their transformation may play a role for the cermet corrosion rate.

2.3 Oxidation of the metal phase under an oxygen atmosphere with halogens present

It is important to emphasise that the oxidation processes might be influenced by the presence of fluorides, and it might change and speed up the oxidation processes tremendously. McNallan (29) showed that the presence of small amounts of halides in air, and especially fluorine and chlorine, caused the formation of volatile metal halides in the metallic oxide layer and increased the deterioration of the metal. Fluorides may also enter into solid copper (30) and nickel (31), (32). If F^- ions substitute O^{2-} ions in the metal ion lattice, vacancies will be formed and F^- ions can diffuse through the oxide scale and attack the metal inside.

Many fluoride corrosion products will be volatile at elevated temperatures (29), and Table 2-1 lists the melting point and vaporisation temperature for important metal fluorides.

Table 2-1: Melting and Vaporisation Temperatures of Metal Fluorides (^oC), from (29).

Fluoride	Melting Point ^oC	Temperature for $T = 10^{-4}$ atm.
FeF_2	1020	906
FeF_3	1027	673
NiF_2	1450	939
CuF_2	770	-
CuF	747 [from (1), (4)]	-

When the vapour pressure of a species exceeds 10^{-6} atm., volatilisation can contribute to the corrosion mechanism, and if the vapour pressure exceeds 10^{-4} atm., volatilisation can be the dominant mechanism (29). In this case, corrosion can occur by the formation of volatile species which diffuse away from the reaction site without the formation of a protective oxide scale (29). Reaction kinetics are linear under these conditions, and the corrosion rates often can be predicted from mass transfer considerations (29).

Halogens have been reported (29) to penetrate through the oxide layer to the regions of low oxygen potential at the scale-metal interface, and produce volatile metal halogens. These volatile halogens diffuse out through the pores in the oxide and come into contact with the oxygen outside the scale. There the metal halogens are converted to metal oxide, which forms with a powdery, non-protective morphology. Internal attack along the grain boundaries penetrating into the metal has also been reported for nickel. Strachan *et al.* (33)

indicated the possibility that volatilisation of copper and nickel from the outer region of cermet anodes, also above the melt surface, occur. SEM analysis showed that most severe was the depletion of nickel from the metal phase above the melt surface.

Oxidation of metals in a gas phase probably does not produce the same effects as electrolytic oxidation, largely because the effects of surface dissolution and internal electrolytic transport are missing and fluoride doping of the oxide materials might also change the ionic transport numbers.

2.4 Failure due to oxide deficiency of the electrolyte

In the electrolysis of aluminium oxide from fluoride melts, complex oxygen-containing ions react at the anode to form oxygen (34), (35),

$$Al_2O_2F_4^{2-} + 2AlF_6^{3-} = 4AlF_4^- + O_2 + 4e^- \qquad [2\text{-}53]$$

If the rate at which the oxygen-containing ions reach the electrode is insufficient, another electrode reaction can occur. In the traditional Hall-Héroult process using carbon anodes, carbon fluoride compounds form and lead to the well-known anode effect. Changes in wetting of the anode by electrolyte initiates the formation of a continuous gas layer on the electrode that causes the characteristic voltage rise of 20 volts, or more. However, the continuous gas film does not appear to occur at oxide or cermet anodes (36). A different electrochemical reaction also takes place, but in this case the oxide of the anode material may participate, as, *e.g.*, according to:

$$2NiO = 2Ni(II) + O_2 + 4e^- \qquad [2\text{-}54]$$

In this case, the positive nickel ions migrate actively away from the anode and destruction of the anode is rapid, possibly approaching faradaic rates. Similar reactions may take place with other oxides such as FeO and SnO_2. Wang and Thonstad (37) have however, reported SnO_2 anodes to suffer from a catastrofic form of corrosion called “disintegration” under certain process conditions, *i.e.* for example high current densities and high NaF contents. They concluded that the anodes dissolved very quickly, but SEM studies showed the presence of SnO_2 particles that were too large to occur only during electrolysis. Alumina depletion and change in the cryolite ratio at the surface of the anode were given as explanation for the rapid deterioration.

Alumina depletion is, of course, an unwanted situation, which has to be avoided in practice. Unfortunately, a large voltage rise as a warning signal does not occur as it does for ordinary carbon anodes. Severe anode corrosion has been observed (36) to occur without obvious change in the current/voltage characteristics both in laboratory-scale tests and in a pilot cell. Perhaps the observation of gas bubble size, direct or indirect, may serve to detect the undesirable condition. Reliable management of the alumina dissolution to maintain a high alumina content, will eliminate this source of anode deterioration. Beck and Brooks (38) have patented a slurry cell that will keep the electrolyte alumina-saturated. The finely divided alumina particles introduced into the cell are, according to the patent,

kept in suspension by the anode gas bubbles generated at the bottom and elsewhere on the interior metal lining in the cell when the latter is part of the anode arrangement.

2.5 Concentration gradients in the vicinity of the anode and their effect on anode degradation

The corrosion of the anode constituents is depending on the conditions at the surface of the anode, and the dissolution of all the oxides from the nickel ferrite cermet increases with decreasing alumina concentration. The bulk concentrations may give an indication of the conditions at the surface of the anode, but concentration gradients play an important role when it comes to dissolution kinetics and anode chemistry.

The solubility measurements of NiO in cryolite melts indicate increasing solubility with decreasing alumina concentration and increasing temperature (see Chapter 4) and it has a very low solubility in alumina-saturated melts. Present electrolysis experiments (Chapter 7) and results by other workers (5), (8) gave, however, Ni(II) concentrations 4-5 times higher than the solubility concentrations *presently* obtained (see Chapter 4). This discrepancy might indicate the presence of alumina concentration gradients near the anode surface and poor convection in the cells. The melt viscosity increases slightly with increasing alumina concentration, and thereby reduces the melt circulation. Another explanation is that the anode disintegrates or small anode flakes spall during electrolysis, forming very small dispersed particles in the melt (see Chapter 7).

Since the anode consists of a highly conductive copper-rich metal phase and a ceramic phase which is practically an electrical insulator, there might *initially* be a non-uniform current distribution at the electrode surface where the metal phase may carry most of the current. If a protective oxide/fluoride layer does not form at the metallic surface, anodic dissolution of the metallic phase will occur. Not so many solubility data for Cu(I) and Cu(II) have been found in the literature, but the present results (see Chapter 6) indicate a rather high saturation concentration in cryolite-based melts. High alumina activity at the surface of the anode seems even more important for a Ni-rich metal phase than for the ceramic phase, since the cermet needs the metal phase intact to keep proper electrical conductivity. Many workers (5), (8), (39), (40) and (41) have reported a depletion of the metal phase in the outer region of the anode after 5 to 50 hours of electrolysis, which may be a result of the copper oxide/fluoride dissolution from the surface of the anode.

2.6 How temperature variations in the cell affect the anode dissolution

If one assumes the highest temperature in the system to be at the anode, anode constituents can precipitate in the melt or in the aluminium. The so-called entropy effect (42) predicts an electrochemical cooling effect of a few degrees at the surface of the anode. An overheated anode can, however, occur if ohmically induced heat is generated because of high resistance in the anode or in the joints between the anode and the electrical connections (lead). A high resistance may occur if the cermet is depleted of the highly conductive metal phase by corrosion or dissolution into the melt. The result of a warmer anode will be higher mass transfer coefficients for the anode constituents at the anode than

for the corresponding reduction into the cathode metal. If the concentrations of the anode constituents are close to saturation at the surface of the anode, precipitation of these components in a colder area between the electrodes may occur. Chin (20), (21) has reported a "skim layer" of copper near the surface of the aluminium pad in an autopsied cell. If, however, the convection in the cell is poor, there will be a more stagnant region of the bulk electrolyte where the concentration of alumina is higher than near the surface of the anode. The solubility measurements for Ni(II) (43), Fe(II) (44) and Fe(III) (43), (45) show that the solubility of these constituents decrease with increasing alumina content, and a precipitation can therefore be explained simply by an alumina gradient in the inter-electrode space.

DeYoung (43) reports the solubility equation for Ni(II) and Fe(III) from the cermet anode to be:

$$\log(\text{wt\%Ni(II)}) = 7.25 - \frac{11700}{T} \qquad [2\text{-}55]$$

$$\log(\text{wt\%Fe(III)}) = 1.26 - \frac{3100}{T} \qquad [2\text{-}56]$$

regardless of the alumina concentration and molar ratio in the melt, which is a rather coarse assumption (see Chapter 4 and 5). DeYoung concluded that the effect of changing temperature was larger than that of changing alumina concentration and NaF/AlF_3 molar ratio. DeYoung reported, however, the correlation coefficient to be poor. He also reported the solubility of Ni(II) and Fe(III) from $NiFe_2O_4$ to be lower than the solubility of the simple oxides NiO and Fe_2O_3. DeYoung reported the solubility of the simple oxides to be,

$$\log(\text{wt\% Ni(II)}) = 6.27 - \frac{9740}{T} \qquad [2\text{-}57]$$

$$\log(\text{wt\%Fe(III)}) = 4.71 - \frac{7080}{T} \qquad [2\text{-}58]$$

DeYoung's solubility data for Ni(II) and Fe(III) are similar to the presently obtained data for Ni(II) and Diep's (45) data for Fe(III) at *low* alumina concentrations.

2.7 How surface conditions at the anode affect the anode dissolution

Many aluminates are stable in contact with cryolite-based melts. Aluminates are, however, stable only at alumina activities higher than a critical value. The critical alumina concentrations vary with the species involved (see Chapters 4 and 5 regarding Ni(II) and Fe(II) solubility). Whether the alumina concentrations at the surface of the anode are above the critical value is depending on the bulk concentration, the convection near and at the surface and the current density at the surface. If one assumes that the alumina concentration is high enough at the surface, a layer of aluminate(s) with low electrical conductivity may be the result. The result might be a redistribution of the current, and locally high current densities at aluminate-free spots. High local current density may cause

disintegration of the oxide layer present at the surface (46), giving a non-protected surface as a result. Since the metal phase has a higher electrical conductivity, it is believed that this mechanism will be more severe for a *continuous* metal phase and will be detrimental to the anode because a continuous depletion of the metal phase will occur (47). A uniform formation of layer(s) at the anode with equal electric conductivity and thickness are believed to be optimal for a long lasting anode if the anode layer constituents at the same time have low solubilities in the melt.

2.8 How pores in the anode influence the corrosion mechanisms

The problem of manufacturing effective electrodes naturally falls into three major parts. The fist includes the tasks of selecting the most suitable electrode materials and studying the electrochemical kinetics involving all the important reactants. The second part of the problem reduces to the study of the macrokinetics of the processes operating in porous media, which should take into account the transport stages and the known microkinetics.

The cermet anodes produced in the present work contained 3-5 percent porosity. In addition, as electrolysis time passes the surface of the cermet anodes is depleted of metal phase (6), which may give a porous outer structure as a result if the alumina concentration at the electrode surface is unsaturated. The porosity has been shown to increase during electrolysis, and most severely in melts unsaturated with alumina (8). Figure 2-5 shows an example of how badly a cermet anode can corrode in unsaturated melts.

The transport processes, such as flow, diffusion, heat transfer, and passage of electrical current, may severely limit the electrochemical reaction rates in the porous electrode (48). If the pore radius varies from point to point, *i.e*. the pore is corrugated, the effective electrical conductivity is lower than that for pores of constant cross section. The pore intersections significantly influence the effective electrical conductivity, as does their corrugated nature.

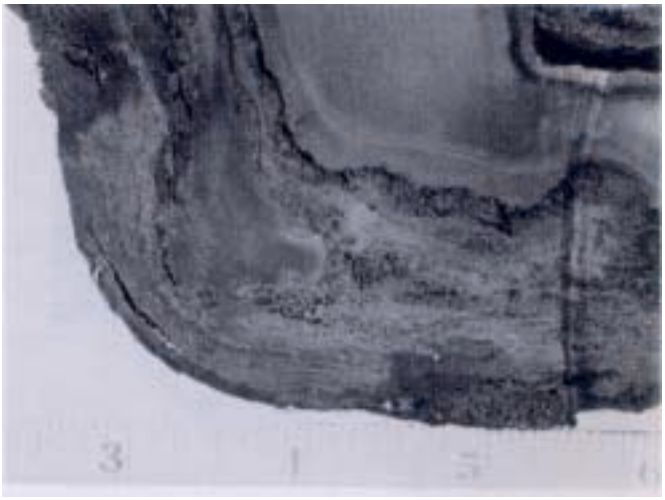

Figure 2-5: Outer corrosion zone of a cermet $NiFe_2O_4$ anode used for 260 hours (49), (50). The scale unit is inches.

The anode shown in Figure 2-5 was used in a pilot cell, and the average data for the test period are CR=2.7 / 5.9 wt% Al_2O_3 / 4.1 wt% CaF_2 / 976 ^oC / 1 $A \cdot cm^{-2}$. As one can see, the outer 3-4 cm has corroded severely, and has become very porous.

When an electrical current passes through a porous electrode, the current distribution is not equipotential, *i.e*. the potential in the solution/gas filling the pores of the electrode is not equipotential. The current passing through the pores gradually shunts into the electrode's matrix as a result of the electrochemical reactions. The presence of the ohmic, activational, and concentrational resistance in the electrode changes the potential distribution in the pores in such a way that, in practice, the electrochemical reaction penetrates only to a limited depth of the anode.

In a *two-phase system* (48), the pores are completely filled with an electrolyte in which the reactants and the reaction products are dissolved. Such pores may exist in parts of the electrode where the anode is poorly conducting or covered with an electrochemically passive phase. The process of electrical current generation in such pores comprises a number of stages. In the first stage, the reactants are transported through the solution to the outer surface of the porous electrode. This stage, which is called the external diffusion stage, depends first of all on the conditions of mixing. The next stage is the transport of the reactants through the porous space of the active electrode filled with electrolyte. Finally adsorption, the electrochemical reaction, and the generation of an ionic current take place. The electrochemical reaction proceeds both in the outer and inner surfaces of the electrode. If the electrode material is highly active, so that the exchange current exceeds the limiting current of external diffusion, then at sufficiently high potentials the reactant concentration at the outer surface tends to zero. As a result, the reactants do not penetrate into the porous electrode and the electrical current is largely generated at the outer surface. (The two-phase system deals with very porous systems, and is, therefore, not relevant to the behaviour of inert anodes.)

The pores can be filled with non-conducting medium, *i.e.* oxygen. In porous media partly filled with electrolyte (*three-phase systems)*, all of the electrolyte-filled pores may be divided into two categories: "blind" pores which are filled with electrolyte at one end only and "through-going" pores which are filled with electrolyte at both ends. It is clear that only the through-going pores can contribute to the electrical conductivity of the medium. The number of the through-going pores is preliminary determined by the structure of the porous space in the electrode.

2.9 Anodic surface layers found at cermet $NiFe_2O_4$ anodes after electrolysis

Investigating the surface layer of a cermet anode used for aluminium production is not an easy task. The electrolysis is conducted at approximately 960 ^oC, and is not possible to observe the anode surface directly. Electrochemical measurements may give some indications of the ongoing reactions, but some of the reactions may be masked, and no good electrochemical results have been found in the literature. An investigation of the anodes after electrolysis is completed after the anodes are cooled down is possible, but the

phases found at room temperature may not be the same as the phases actual present during electrolysis.

Olsen (5) reported a depletion of iron from both the oxide phases NiO and $NiFe_2O_4$, while nickel was preferentially depleted from the Cu-Ni metal phase after 4 hours of electrolysis. The stoichiometric nickel ferrite materials developed a smoother surface than the nickel ferrite materials with excess NiO. Olsen explained it with a more uniform distribution of the stoichiometric oxide phase, which is denser than the material with excess NiO. The ferrite phase seemed to dissolve quicker than the NiO phase, leaving grains of NiO protruding into the electrolyte, which also has been observed by Windisch *et al.* (39) (see Figure 2-6).

Hart *et al.* (18) proposed that Cu_2O formation is an important reaction in molten cryolite. At high alumina concentration, Cu_2O forms or is stabilised under open circuit conditions, and only its oxidation to CuO is observed in the cyclic voltammograms.

Tarcy (47) reported a surface layer containing approximately 60-70 % $CuAlO_2$ and 30-40 % Cu_2O film on top of the metallic copper surface of a cermet $NiFe_2O_4$ anode after electrolysis. The formation of $CuAlO_2$ can be explained by reaction [2-35]. Since Cu_2O is present in the layer, $CuAlO_2$ is most likely produced according to this reaction.

Tarcy (47) proposed that CuO is formed electrochemically according to:

$$Cu_2O + O^{2-} \rightarrow 2CuO + 2e^- \qquad [2\text{-}59]$$

Tarcy (47) reported $CuAlO_2$ to be an electrically passivating layer, indicated by a low passivating current. He also reported a selective oxidation of nickel from the metal phase, leaving almost pure copper. The depth of this oxidising zone was reported to be less than 1 mm, and it was not observed to increase on extended electrolysis tests up to 264 hours.

In contradiction to the proposals by Weyand *et al.* (8), Strachan *et al.* (12) claimed that $CuAl_2O_4$ is not a passivating reaction product and claimed that it forms as a result of the decomposition of the primary Cu(II)-containing products.

Windisch *et al.* (51) investigated the effect of microstructure on the corrosion of 4 cermet anodes after 6 hours of electrolysis. They concluded that small grains are detrimental to the inert anode because the mode of attack appeared to be along grain boundaries. It was characterised by changes in the physical and electrical properties of the anode as well as by changes in the composition and distribution of the phases. Increased current density at the anode increased the corrosion of the metal phase as well as the dissolution/reaction of the oxide phases. These anodes also bloated, and the metallic phase was depleted/ vanished in the outer surface region for all the anodes investigated. During electrolysis the porous outer layer became saturated with molten electrolyte, with an accompanying increase in conductivity. The porosity affected the corrosion rate, and the more porous the anode was, the more severe the corrosion was and the deeper the attack entered into the anode.

The current paths may play a role in the deterioration mechanisms. Just after the electrolysis is started, the outer metal phases probably transport most of the current because of the high electrical conductivity, and the result is high local current densities and anodic dissolution of the metal phase or production of a Cu_2O (51) and/or a CuO phase. Anodic overvoltage and gas coverage of the anode surface will, however, even-out the current distribution. Diffusion of copper through its own oxide layers is fast, forming even more copper oxide(s). Haugsrud (19) reports that "break-away oxidation" can be formed when CuO is formed on top of a Cu_2O layer because of stress components within the CuO oxide layer. If this happens, the oxide layers formed do not protect the inner copper metal phase, and this continuous corrosion mechanism is known as "linear" as opposed to the desired "parabolic" where the corrosion kinetics slows down as a function of time.

The $NiFe_2O_4$ phase dissolves faster than NiO, according to Windisch *et al.* (39), (which is in conflict with the results reported by Weyand *et al.* (8)). However, if one assumes that NiO particles fall out from the $NiFe_2O_4$ matrix when the $NiFe_2O_4$ is dissolving away, one can explain why several workers (5), (8) report Ni(II) concentrations in the melt during electrolysis which are 4-5 times higher than the corresponding solubility limit presently measured. This phenomenon was reported by Windisch *et al.* (39) to happen after one hour of electrolysis (see Figure 2-6).

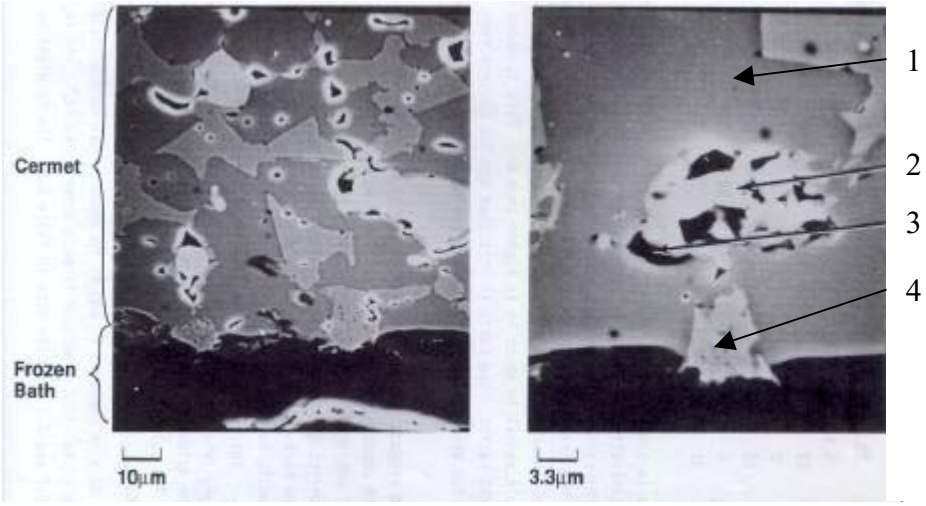

Figure 2-6: SEM Micrographs of a surface region of a cermet anode after 1 hour of electrolysis using 0.51 A/cm^2 in alumina-saturated bath (CR = 2.29, 5.5 wt% CaF_2 and 1.0 wt% MgF_2) at 983 ^oC, from (39). 1 = $NiFe_2O_4$, 2 = reacted Cu, 3 = cryolite and 4 = NiO.

Copper ions are also more soluble than Ni(II) (see Chapter 4) and Fe(III) ions (45), in a cryolite based melt. The copper phases will, therefore, dissolve relatively fast into the melt, and the outer metal phase will disappear as a result. The absence of copper in the outer region of the nickel ferrite cermet was shown in various reports (19), (39), (40) and (41). Copper ions coming from metal "globules" (see Chapter 3 for further details about the cermet phases) from within the cermet will probably diffuse through the oxide phases too,

causing more copper depletion of the outer region of the cermet anode. The disappearance of the NiO grains will roughening the surface, giving higher surface area and lower current density as a result if the pits produced are not passivated (electroactive).

Nickel and iron aluminates can be formed (41), (39) (51) in melts containing high alumina concentrations at a certain oxygen pressure. This observation is consistent with thermodynamics. The current paths will then be driven through other phases because of the low electrical conductivity of the aluminate phases. The oxygen coverage of the anode surface will depend on where oxygen is produced, and consequently on the current paths. When the current is no longer passing through the growing aluminate layers, the anodic resistance will increase and temperature will increase accordingly. Windisch *et al.* (39) reported a non-continuous depletion of iron and an enrichment of aluminium in the outer region of the spinel phase.

At low current densities (anode potentials lower than 2.1 volts), impedance measurements reported by Windisch *et al.* (52) indicated Warburg type diffusion controlled corrosion of the cermet. For porous electrodes, the phase angle will be less than 45 degrees at low frequencies (53). Windisch *et al.* reported their measured phase angle to be 32 degrees, which is consistent with the presence of a porous electrode.

Potential-step tests run by Windisch *et al*. (52) at anode potentials higher than 2.1 volts indicated the anodic reactions to be less diffusion controlled than below 2.1 volts. Instead, semicircular Nyquist plots indicated charge-transfer processes above 2.2 volts and lack of the Warburg-like character seen at lower anode potentials. They concluded that above 2.2 volts the main anode reaction to be activation controlled two-step production of oxygen.

Weyand *et al.* (8) postulated the formation of a passivating and protective layer of $CuAl_2O_4$ on the surface of the NiO-$NiFe_2O_4$-Cu cermet. By introducing aluminium metal to the cermet before sintering, Hart *et al.* (18) did not succeed in producing $CuAl_2O_4$ *in-situ* during sintering, but the resulting cermet material obtained at least 4 times higher electrical conductivity than other NiO-$NiFe_2O_4$-Cu cermets. However, these anodes were obviously not a success since they were not mentioned in later PNL[1]-reports.

Strachan *et al*. (54) reported that the metal phase in a cermet anode was completely oxidised in the rim area above the electrolyte surface after 100 hours of electrolysis. X-ray analysis of material well within the oxidised zones showed that the NiO and $NiFe_2O_4$ phases were still present, but the Cu had been oxidised to CuO. The material was slightly richer in Ni than the interior of the anode, and the material in this zone had undergone some structural reorganisation that resulted in an increased porosity. Oxidation of the cermet above the electrolyte appeared to be quite excessive and probably resulted in some spalling of the material. Cu- and Ni-containing species seemed to be volatilised (54), probably as fluorides, leaving behind relatively Fe-rich material. An X-ray diffraction pattern of the surface material showed the presence of NaF, Na_3AlF_6, CaF_2, Al_2O_3 (both alpha and beta), and two copper aluminate phases, i.e. $CuAl_2O_4$ and $CuAlO_2$ besides the typical anode phases. The Cu was oxidised to CuO above the electrolyte surface and to

[1] PNL = Pacific Northwest Laboratories

Cu_2O below the electrolyte surface. A red-ox reaction between Ni and Cu_2O from the metal phase in the cermet formed pure Cu and NiO (54).

The 100 hours electrolysis test were reported by Strachan *et al.* (55) to oxidise the metal phase to a depth of around 10 mm. Even though Cu_2O has a higher electrical resistance than copper metal, their test indicated that the oxide at least does not hinder electrical conduction, and may be a good conductor at 950 ^oC since it is a defect semiconductor.

2.10 CEROX coating of inert anodes

In 1982 it was discovered that a fluoride-containing CeO_2 coating could be anodically deposited from a molten cryolite electrolyte when CeO_2 was added to the melt (56), (57). The coating, known as CEROX$^{TM\ 2)}$, was found to reduce corrosion of inert anodes.

Dewing *et al.* (58) showed that it is Ce(III), and not Ce(IV) that is dissolved in cryolite and reported the solubility of Ce(III). The CEROX deposition can be described as an electrochemical oxidation deposition (56):

Anode: $$2CeF_3 + \frac{4}{3}Al_2O_3 = 2AlF_3 + 2CeO_2 + \frac{2}{3}Al(III) + 2e^- \quad [2\text{-}60]$$

Cathode: $$\frac{2}{3}Al(III) + 2e^- = \frac{2}{3}Al \quad [2\text{-}61]$$

Net reaction: $$2CeF_3 + \frac{4}{3}Al_2O_3 = 2AlF_3 + 2CeO_2 + \frac{2}{3}Al \quad [2\text{-}62]$$

Or as a chemical deposition,

$$2CeF_3 + Al_2O_3 + \frac{1}{2}O_2 = 2CeO_2 + 2AlF_3 \quad [2\text{-}63]$$

Both the electrochemical and chemical reactions (57) are possible when there is a low activity of AlF_3.

Gregg *et al*. (56) added CeF_3 hourly to their melts where they tested cermets composed of $NiFe_2O_4$, NiO and 17% Cu metal. They reported that high molar cryolite ratio (CR = 3.2) and current densities around 1.4 A/cm^2 led to thick and dense CEROX coatings, while a CR of 2.4 and current density of 1.0 A/cm^2 led to thin and discontinuous layers. A horizontal electrode arrangement with a hanging anode with a flat bottom got thicker coatings on the sides and outer bottom edges, than the coating on the bottom of the anode. They assumed that oxygen accumulation under the anode was the reason for this since a rounded anode did not show the same behaviour. The anode corrosion seemed to increase slightly with increasing current density. The CEROX coating reduced the total corrosion

[2)] CEROX is a trademark of MOLTECH Invent S.A.

resistance to 1/7 that of the uncoated anode under the same conditions, and the best 100 hours tests with rounded bottom showed no macroscopic tapering of the material. SEM pictures did, however, reveal areas were the corrosion had been more severe. Since a thin layer of CEROX coating had re-deposited at the corroded areas, it might indicate that peeling of the coating had occurred. Tests were performed in melt unsaturated with alumina, with higher concentration of CeF_3 added to the melt than in the alumina-saturated experiments. The higher levels of Ce in the melt led to thicker CEROX coatings (1 – 5 mm) on these anodes. In these coatings the inner 1 to 2 mm were dense, while the outer region was porous. Even though the CEROX coating protected the anode, the corrosion increased with decreasing alumina content in the melt.

The Cu-rich cermet substrates tested in melts both saturated and unsaturated with respect to alumina underwent microstructural changes during the testing (57). Next to the CEROX coating there was a Cu depleted layer that consisted of NiO and $NiFe_2O_4$. Adjacent to the oxidised region with Cu oxide, Cu was still present together with NiO and $NiFe_2O_4$. The boundary between the Cu metal region and the oxidised region was always distinct. In anodes with extensive oxidation, alternating Cu oxide-rich and Cu oxide-poor bands were developed within the oxidised region. In addition, porosity was increased in the oxidised areas relative to the untested cermet, and porosity was even higher in the Cu oxide-poor bands. The oxidised region increased in thickness with increasing current density and the electrical conductivity decreased accordingly. The conductivity of the CEROX coating was reported to be 0.20 ± 0.05 S/cm (56), which resulted in a voltage penalty compared to a non-covered anode.

In the tested anodes, the Cu metal and the Cu oxide phases were enriched in Cu and depleted in Ni relative to the Cu metal in the untested material. The NiO in the tested samples was enriched in Cu and Ni and depleted in Fe compared to the untested material. In the untested cermet the $NiFe_2O_4$ was slightly Fe-enriched compared to the stoichiometric ferrite, but the composition of the ferrite appeared to become more stoichiometric in the tested anode, particularly in the oxidised region.

According to Gregg *et al.* (57), the cermet anodes cracked during testing, and only small areas within the cracks had a CEROX coating. The cracks were attributed to thermal shock caused by immersing the anode in the melt or mismatch between the thermal coefficient of expansion between the cermet and the connector rod (Inconel 601) (57). They (57) concluded that it was not possible to attribute the reduced corrosion to the CEROX coating because the extent of cracking may not have been the same for the tests with and without the CEROX coating. Walker *et al*. (59) did, however, not observe this type of cracking.

Another problem with CeF_3 addition to the melt is the aluminium metal contamination. Gregg *et al*. (57) report a contamination of 3-5 weight % Ce in the aluminium produced. It will have to be refined before the foundry can use this metal. A way of purifying the metal has been patented by Alcan (60) and Moltech Invent SA (61). Their concept is to reduce the Ce content in the aluminium metal by mixing the metal with AlF_3 or $AlCl_3$. The following reaction will take place:

$$Ce_{\text{in Al}} + AlF_3 \rightarrow CeF_3 + Al \qquad [2\text{-}64]$$

The oxidation of Ce according to equation [2-65] has its equilibrium corresponding to Ce concentration between 0.1-0.3 wt% depending on the temperature. Solid CeF_3 wets aluminium poorly, and can easily be skimmed off the surface of the metal below 800 ^oC (61). Further reduction of the Ce content can be obtained by bubbling clorine gas through the aluminium already purified with AlF_3. The following reaction will take place (58):

$$Ce_{\text{in Al}} + \frac{3}{2}Cl_{2(g)} \rightarrow CeCl_3 \qquad [2\text{-}65]$$

The Ce content in aluminium can easily be reduced to 50 ppm by using chlorine gas.

2.11 References

(1) Outokumpu Research Oy, *HSC Chemistry*, computer program, ver. 3.0, Info Service, P.O. Box 60, FIN-28101 PORI, Finland.

(2) JANAF, *Thermochemical Tables*, 3rd ed., National Bureau of Standards, Washington D.C., 1985.

(3) Barin, I., *Thermodynamical Data of Pure Substances*, 3rd ed., VCH Verlags-gesellschaft mb-H, D-69451, Weinheim, Germany, 1995.

(4) Knacke, O., Kubaschewski, O., Hesselmann, K., *Thermochemical Properties of Inorganic Substances*, 2nd ed., Springer-Verlag, Verlag Stahleisen, 1991.

(5) Olsen, E., *Nickel Ferrite and Tin Oxide as Anode Materials for Aluminium Electrolysis,* doktoringeniøravhandling (Ph.D. thesis), NTH, Trondheim, ISBN 82-7119-850-5, no.100, 1995.

(6) Olsen, E. and Thonstad, J., *Nickel ferrite as inert anodes in aluminium electrolysis: Part I. Material fabrication and preliminary testing*, J. Appl. Electrochem., vol. 29, pp. 293-299, 1999.

(7) Weyand, J.D., *Manufacturing processes used for the production of inert anodes*, Light Metals 1986, pp. 321-339, 1986.

(8) Weyand, J.D., DeYoung, D.H., Ray, S.P., Tarcy, G.P., and Baker, F.W., *Inert Anodes for Aluminium Smelting. Final Report*, Alcoa Centre, DOE/CS/40158-20, Feb., 1986.

(9) Sekhar, J.A., Liu, J. and Deng, H., *Reduction Conditions Encountered in Cryolite Baths*, Light Metals 1999, pp. 383-387, 1999.

(10) Dewing, E.W. and Thonstad, J., *Solutions of Iron Oxides in Molten Cryolite,* Metall. Mater. Trans. B, vol. 31B, pp. 609–613, 2000.

(11) Dewing, E.W. and Thonstad, J., *Activities in the System Cryolite-Alumina*, Metall. Mater. Trans. B, Vol 28 B, pp. 1089-1093, Dec. 1997.

(12) Strachan, C.M, Koski, O.H., Marschman, S.C., Benden, B.B. and Davis, N.C., *Fiscal Year 1987 Annual Report,* Pacific Northwest Laboratory, PNL-6746 UC-95f, Dec., 1988.

(13) Aldrich – Chemie GmbH & Co., *Catalogue Handbook of Fine Chemicals*, Steinheim, Germany, 1994-1995.

(14) CRC Press, Handbook of Chemistry and Physics, 71st ed., B-93, 1990-1991.

(15) Jacob, K.T. and Alcock, C.B., *Thermodynamics of $CuAlO_2$ and $CuAl_2O_4$ and Phase Equilibria in the System Cu_2O-CuO-Al_2O_3,* J. Am. Cer. Soc., vol. 58, no 5-6, pp. 192-195, May-June, 1975.

(16) Beck, T.R., *Production of Aluminium With Low Temperature Fluoride Melts*, Light Metals 1994, pp. 417-423, 1994.

(17) Beck, T.D., *A Non-Consumable Anode for Production of Aluminium With Low-Temperature Fluoride Melts*, Light Metals 1995, pp. 355-360, 1995.

(18) Hart, P.E., Brenden, B.B., Davis, N.C., Koski, O.H. and Marschman, S.C., *Fiscal Year 1986 Annual Report*, Pacific Northwest Laboratory, PNL-6247 UC-95f, June, 1987.

(19) Haugsrud, R., *On the High Temperature Oxidation of Copper-Nickel Based Alloys*, Ph.D. thesis, University of Oslo, Norway, 1999.

(20) Chin, P.C.Y., *The Behaviour of Impurity Species in Hall-Heroult Aluminium Cells*, Ph.D. thesis, Carnagie Mellon University, Pittsburgh, 1992.

(21) Chin, P.C.Y., Sides, P.J. and Keller, R., *The Transfer of Nickel, Iron and Copper from Hall Cell Melts to Molten Aluminum*, Can. Metall. Quart., vol. 35, no.1, pp. 61-68, 1996.

(22) Haugsrud, R. and Kofstad, P., *On the Oxygen Pressure Dependence of High Temperature Oxidation of Copper*, Materials Sci. Forum, Trans Tech Publications, Switzerland, vol. 251-254, pp. 65-72, 1997.

(23) Tveten, B. and Kofstad, P, *Inerte Anoder i Aluminiumelektrolysen,* Report no. 29721, Program of EXPOMAT, University in Oslo, Norway, May 1995.

(24) Haugsrud, R. and Kofstad, P., *On the High-Temperature Oxidation of Cu-Rich Cu-Ni Alloys*, Oxidation of Metals, vol. 50, Nos. 3-4, pp. 189-213, 1998.

(25) Kofstad, P., *Defect Chemistry in Metal Oxides*, Phase Transitions, vol. 58, pp. 75-93, 1996.

(26) Kofstad, P., *Defect and Transport Properties of Metal Oxides*, Oxidation of Metals, vol. 44, Nos 1-2, pp. 3-27, 1995.

(27) Osvold, K. and Kofstad, P., *Inerte Anoder i Aluminiumelektrolysen,* Report no. 29721, Program of EXPOMAT, University in Oslo, Norway, Jan. 1996.

(28) Windish, C.F. and Marchman, S.C., *Electrochemical Polarization Studies on Cu and Cu-containing Cermet Anodes for the Aluminium Industry*, Light Metals 1987, TMS, pp. 351-355, 1987.

(29) McNallan, M., *High-Temperature Corrosion in Halogen Environments*, Material Performance, pp. 54-57, Sept. 1994.

(30) Reddy, S.N.S. and Rapp, A., *The Solubility and Diffusivity of Fluorine in Solid Copper from Electrochemical Measurements*, Metall. Trans. B, vol. 9B, pp. 559-565, 1978.

(31) Reddy, S.N.S. and Rapp, A., *The Solubility and Diffusivity of Fluorine in Solid Nickel from Electrochemical Measurements*, Metall. Trans. B, vol. 11B, pp. 99-106, 1980.

(32) Reddy, S.N.S. and Rapp, A., *Internal Fluorination of Ni-5.6 Pct Cr Alloy*, Metall. Trans. B, vol. 11B, pp. 533-534, 1980.

(33) Strachan, D.M., Windisch Jr., C.F., Koski, O.H., Morgan, L.G., Peterson, R.D., Richards, N.E., Tabereaux, A.T., *Results from electrolysis test of a prototype inert anode*, Pacific Northwest Laboratory, PNL-7345, UC-313, May, 1990.

(34) Grjotheim, K., Krohn, C., Malinovský, M., Matiašovský, K. and Thonstad, J., A*luminium Electrolysis. Fundamentals of the Hall-Héroult Process,* 2nd ed., Aluminium-Verlag, Düsseldorf, ISBN 3-87017-155-3, 1982.

(35) Grjotheim, K., and Kvande, H., *Introduction to Aluminium Electrolysis*, 2nd ed., Aluminium-Verlag, ISBN 3-87017-233-9, 1993.

(36) Keller, R., Rolseth, S. and Thonstad, J., *Mass transport considerations for the development of oxygen-evolving anodes in aluminium electrolysis*, Electrochim. Acta, vol. 42, no. 12, pp. 1809-817, 1997.

(37) Wang, H. and Thonstad, J., *The Behaviour of Inert Anodes as a Function of Some Operating Parameters*, Light Metals 1989, TMS, pp. 283-290, 1989.

(38) Beck, T.R., Brooks, R.J. *Non-consumable anodea and lining for aluminium electrolytic cell*, US Patent no. 5,284,562, Feb. 8th, 1994.

(39) Windish Jr., C.F. and Stice, N.D*., Final report on the characterization of the film on inert anodes*, Prepared for the U.S. Dep. Of Energy, Contract DE-AC06-76RLO 1830, Pacific Northwest Laboratory, Richland, Washington 99352, Jan. 1991.

(40) Olsen, E., Thonstad, J, *Nickel ferrite as inert anodes in aluminium electrolysis: Part II. Material performance and long-term testing*, J. Appl. Electrochem., vol. 29, pp. 301-311, 1999.

(41) Olsen, E., *Karakterisering av Cu-dopet $NiFe_2O_4$ som inert anodematriale i aluminiumselektrolysen,* Diploma thesis, Dep. of Electrochemistry, NTH, Norway, 1991.

(42) Ødegård, R., Julsrud, S. Solheim, A. and Thovsen, K, *A Therodynamical and Experimental Study of the Electrochemically Induced Cooling of the Anode in Hall-Heroult Cells*, Metall. Trans. B, vol. 22B, pp. 831-837, Dec. 1991.

(43) DeYoung, D.H., *Solubility of oxides for inert anodes in cryolite-based melts*, Light Metals 1986, pp. 299-307, 1986.

(44) Grini-Johansen, H., *Jern som forurensningskilde i aluminiumelektrolysen*, Ph.D. thesis, Dept. of Electrochemistry, NTH, Norway, 1975.

URN:NBN:no-6347

(45) Diep, Q.B., *Structure and thermodynamics of cryolite-based melts with additions of Al_2O_3 and Fe_2O_3 Cyclic voltammetry study of Fe_2O_3 in molten cryolite*, Ph.D. thesis no.28, NTNU, Norway, 1998.

(46) Beck, T.R., *A non-consumable metal anode for production of aluminium with low-temperature fluoride melts*, Light Metals 1995, TMS, pp. 355–360, 1995.

(47) Tarcy, G.P., *Corrosion and Passivation of Inert Anodes in Cryolite-type Electrolytes*, Light Metals 1986 pp. 309-312, 1986.

(48) Chizmadzhev, Y.U. and Chirkov, Y.G., *Comprehensive treatise on electrochemistry,* chap. 5: Porous electrodes, vol. 6, edited by E. Yeager *et al.*, New York, pp. 317-391, 1983.

(49) Windisch, C.F. Jr., Strachan, D.M., Henager Jr., C.H., Greenwell, E.N. and Alcorn, T.R., *Results from a pilot cell test of inert anodes*, Pacific Northwest Laboratory, PNL-8269, UC-313, Aug, 1992.

(50) Windisch Jr., C.F., Strachan, D.M., Henager Jr., C.H., Alcorn, T.R., Taberaux, A.T., Richards, N.E., *Material Characterization of Cermet Anodes Tested in a Pilot Cell*, Light Metals 1993, pp. 445-454, 1993.

(51) Windisch, C.F. Jr., Chick, L.A., Maupin, G.D., Stice, N.D., *The effect of microstructure on the corrosion of glycin/nitrate processed cermet inert anodes: A preliminary study*, Pacific Northwest Laboratory, PNL-7733, UC-313, July, 1991.

(52) Windisch Jr., C.F. and Stice, N.D*., Characterization of the Reaction Layer or Film on PNL Inert Anodes: Progress Report for April-December 1989*, Pacific Northwest Laboratory, PNL-7326 UC-313, May 1990.

(53) Pletcher, D*., Instrumental Methods In Electrochemistry*, Southampton Electro-chemistry Group*,* University of Southampton, Ellis Horwood Series In Physical Chemistry, England, 1993.

(54) Strachan, D.M., Koski, O.H., Morgan, L.G., Westerman, R.E., Peterson, R.D., Richards, N.E. and Taberaux, A.T., *Results from a 100-hours electrolysis test of a cermet anode: Material aspects,* Light Metals 1990, edited by C.M. Bickert, TMS, pp. 395–401, 1990.

(55) Strachan, D.M., Marschman, S.C., Davis, N.C., Friley, J.R. and Schilling, C.H., *Fiscal Year 1988, Annual Report*, Pacific Northwest Laboratory, PNL-7106 UC-313, Oct., 1989.

(56) Gregg, J.S., Frederich M.S., King, H.L. and Vaccaro, A.J., *Testing of Cerium Coated Cermet Anodes in a Laboratory Cell,* Light Metals 1993, edited by S.K. Das, TMS, pp. 455-464,1993.

(57) Gregg, J.S., Frederich M.S. Vaccaro, A.J., Alcorn, T.R., Tabereaux, A.T. and Richards, N.E., *Pilot Cell Demonstration of Cerium Oxide Coated Anodes,* Light Metals 1993, edited by S.K. Das, TMS, pp. 465-473,1993.

(58) Dewing, E., Haarberg, G.M., Rolseth, S. Rønne, L. and Thonstad, J., *Solutions of CeO_2 in Cryolite Melts,* Metall. Mater. Trans. B, vol. 26B, pp. 81-86, 1995.

(59) Walker, J.K., *Cerium Oxyfluoride Coated Cermet Anodes in Hall-Heroult Cells*, Electrochem. Soc., Extended Abstract no. 397, vol. 88-1, pp. 582-583, 1988.

(60) Dewing, E.W.(Alcan), *Methods of Purifying Aluminium*, European Patent no. 835003.7, 12. July, 1985.

(61) *Fremgangsmåte ved rensning av metallsmelte bestående av aluminium forurenset med cerium eller andre sjeldne jordartmetaller, samt anvendelse av fremgangsmåten,* Patent no. 169726, Int Cl^5 C22 B21/06, Oslo Patentkontor, Norway, 1992.

URN:NBN:no-6347

3 Cermet preparation and sintering chemistry

The scope of this work is to investigate the mechanisms at the surface of the anode, and not the production of the materials. The production method described by Olsen (1), (2) with a few modifications, was therefore used for preparation of the *cer*amic-*met*al composite material (*i.e*. cermet), with a copper-nickel alloy as the metal phase in a nickel ferrite oxide matrix.

3.1 Theory of sintering

The densification of particulate ceramic compacts is theoretically referred to as *sintering* (3). Sintering is essentially removal of the pores between the starting particles accompanied by shrinkage of the component, combined with growing together and strong bonding between adjacent particles. The primary mechanisms for transport are diffusion and viscous flow. Heat is the primary source of energy, in conjunction with energy gradients due to particle-particle contact and surface tension. The driving force is reduction of surface area.

The initial stage of solid-state-sintering involves a rearrangement of particles and an initial neck formation at the contact point between each particle. The rearrangement consists of a slight movement or rotation of adjacent particles to increase the number of points of contact. Bonding occurs at the points of contact where material transport can occur and where the curvature (*i.e.* surface energy) is highest.

The second stage of sintering is referred to as *intermediate* sintering. The size of the necks between the particles grows. Porosity decreases and the centres of the original particles move closer together. This results in shrinkage equivalent to the amount of porosity decrease. The grain boundaries begin to move so that one particle (now called a *grain*) begins to grow while the adjacent grain is consumed. The direction of the grain boundary movement is determined by vacancy diffusion. This allows geometry changes that are necessary to accommodate further neck growth and removal of porosity. Intermediate sintering continues as long as pore channels are inter-connected and ends when pores become isolated. Most of the shrinkage during sintering occurs during second-stage sintering.

The third stage of sintering is referred to as *final* sintering. It involves the final removal of porosity by vacancy diffusion along grain boundaries. Therefore, the pores must remain close to the grain boundaries. Pore removal and vacancy diffusion are aided by movement of grain boundaries and grain growth. However, if grain growth is too rapid, the grain boundaries can move faster than the pores and leave them isolated inside the grain. As the grain continues to grow the pore becomes further separated from the grain boundary and has less chance of being eliminated. Therefore, grain growth must be controlled to achieve maximum removal of porosity.

Grain growth is driven by reducing the surface are, and thereby the surface energy to a minimum. Curved grain boundaries move in such a way that they gain a larger radius of curvature, that is, straighten out. This can only be achieved by growth of the grains. Smaller grains have a smaller radius of curvature and more driving energy to move, change shape, and even to be consumed by larger grains. The final distribution of grains and pores is referred to as *microstructure*.

Since the cermet contains metallic copper with a melting temperature of 1083 ^{o}C, liquid-phase sintering will occur at the sintering temperature (1350 ^{o}C). In this mode, the composition of the powder and the processing temperature are chosen so that some liquid forms, but not sufficient to wet all the solid and fill in the green-state porosity completely. In this case the liquid mainly acts to rearrange the poor green-state powder packing. A great deal of the densification is achieved at the powder rearrangement stage, but changes in grain shape are needed in order to achieve the full theoretical density.

Three factors control the rate of liquid-phase sintering (LPS): particle size, viscosity and surface tension. LPS occurs most readily when the liquid thoroughly wets the solid particles at the sintering temperature. The liquid in the narrow channels between the particles results in substantial capillary pressure, which aids densification by several mechanisms:

1. rearranges the particles to achieve better packing
2. increases the contact pressure between particles, which increases the rate of material transport by solution/precipitation
3. creep and plastic deformation
4. vapour transport
5. grain growth

Smaller particles result in higher capillary pressure and also have higher surface energy due to small radius of curvature and thus have more driving energy for densification than coarser particles.

The rate of liquid-phase sintering is also strongly affected by temperature. For most compositions a small increase in temperature results in a substantial increase in the amount of liquid present. In some cases, this can be beneficial by increasing the rate of densification. In other cases, it can be detrimental by causing excessive grain growth, which reduces the strength, or by allowing the part to slump and deform. Since a cermet is a mixture of an oxide phase and a liquid metal phase at the sintering temperature, the amount of liquid in these materials are fixed.

3.2 Chemicals

Fe_3O_4: Sydvaranger High Grade Magnetite I, 99.5 wt %, coarse grained, low silica, Sydvaranger ASA, Kirkenes, Norway.

NiO: High Purity Green Nickel Oxide, 99,98 wt %, Fisher size 4.4 µm, Lot No. Ni91-312-1-GNO, Novamet, USA.

Ni:	Ultra Pure Ni powder, type 4SP, 99.9 wt %, <10 μm, Lot No. –9/789-10, Novamet, USA.
Cu:	Dendritic Cu powder, 99,9 wt %, 1-5 μm, Lot No. NA43087/10, Novamet, USA.
Geropon SDS:	Sodium dioctyl sulfosuccinate, Anionic tenside, powderous form, Rhodia Company, USA.
Ethanol:	96 wt%, 4% water, Arcus, Norway.
n-hexane:	Merck, pa., Kebo-lab, Norway.
Ethyl Cellulose:	Sigma, powderous form, 49.4% ethoxy, E-8003, Lot 46H0066.
Ar:	AGA, >99.99%, ~200 ppm O_2

3.3 Material fabrication

Olsen (1) used Alcoa's work (4), (5) as a guide for production of anodes. Alcoa (5) found that nickel wetted the ceramic powder mix, creating a continuos metallic phase throughout the structure, socalled "wormy structure" (6). This gave good electric conductivity, but specific attack of the metallic phase by anodic dissolution of nickel led to high degree of contamination of the metal produced and anode failure. The improved cermet with copper as the metallic phase showed a lower conductivity. Copper did not wet the ceramic to the same extent as nickel did, and it produced a dispersed metallic phase in a ceramic matrix. It was therefore decided to use a metallic composition containing nickel in addition to copper to improve the wetting characteristics of the metallic phase. It has also been found (5) that agglomerate size and their number increase with increasing copper content.

The analysis of NiO-$NiFe_2O_4$-Cu cermets showed (7) that the metal phase present in the cermet was composed of approximately 85 weight % Cu and 15 weight % Ni. Hart *et al.* (7) believed that the process of nickel diffusion into the copper metal phase was controlled by a solid-state diffusion process between the excess NiO and copper metal, but according to the thermodynamics Cu is more stable than Ni. If the partial oxygen pressure in the argon atmosphere used during sintering was below a critical value, NiO may have dissociated into metal nickel and oxygen gas.

If this diffusion process achieved equilibrium during sintering, then the cermet could be prepared using a pre-alloyed Cu-Ni metal powder. The resulting cermets would not be depleted in NiO, and might produce materials that could exhibit improved corrosion properties. It was observed that the overall metal content (Cu + Ni) of the cermet samples

could be increased without bleed-outs[1] by adding 3-5 wt% Ni. A content of 5 wt% Ni made it possible to add 21 weight %Cu without bleed outs, with a higher overall content of metal phase and higher electrical conductivity as a result. Thus, 3wt % nickel was therefore added to the powder along with 17 wt% copper.

Water has been used as a suspension medium. Water, with it's high polarity may, however, give rise to oxidation reactions on the very finely grained metallic powders used. Olsen (1) decided to use a non-polar dispersant medium instead, and used hexane with 1 wt% oxidised fish oil. Iso-octane or iso-propanole can also be used instead of ethanol. Since the fish oil did not give the proper density, it was exchanged with GEROPON SDS, which is Dioctyl Sodium Sulfosuccinate and Sodium Benzoate in the present work. GEROPON SDS is a sulfosuccinate which is a very suitable anionic tenside giving excellent wetting properties in aquous solutions. Since it is not an especially good hydrophobic tenside, it has low solubility in n-hexan. It was recommended (8) to mix Geropon SDS with UFASAN CA, which is a hydrophobic tenside, giving the best properties of both of the tensides.

The tensides also give steric stabilisation, *i.e*. the chainlike organic molecule part of the tensides are absorbed on to the ceramic particles, and provides a buffer zone around each particle. One end of the chain attaches or anchors to the ceramic and has limited solubility to the solvent. The other end extends away from the particle and is soluble in the solvent. These molecules provide a mechanical barrier to agglomeration and allow particles to approach closer than would be possible without the adsorbed molecules.

The powders were prepared from commercial grade chemicals (Chapter 3.2). $NiFe_2O_4$-NiO mixtures were synthesised from specified molar ratios of NiO and Fe_3O_4. Ferrite has a lower Gibbs energy than the two individual oxides, and was easily calcined at 1000 ^oC. The reaction for forming nickel ferrite can than be described by,

$$NiO_{(s)} + \frac{1}{6}O_{2(g)} + \frac{2}{3}Fe_3O_{4(s)} \rightarrow NiFe_2O_{4(s)} \quad \Delta G^o_{1293K} = -43.238 \text{ kJ/mol} \qquad [3\text{-}1]$$

or alternatively,

$$\frac{2}{3}Fe_3O_{4(s)} + \frac{1}{6}O_{2(g)} \rightarrow Fe_2O_{3(s)} \xrightarrow{NiO} NiFe_2O_{4(s)} \quad \Delta G^o_{1293K} = -24.073 \text{ kJ/mol} \qquad [3\text{-}2]$$

Both reactions are thermodynamically favourable ($\Delta G^o_{1293K} = -19.165$ kJ/mol for the first part of equation [3-2]).

Because oxygen is needed in the process, an oxidising atmosphere must be maintained during calcination. 32.75 wt. % NiO and 67.25 wt. % Fe_3O_4 corresponds to stoichiometric $NiFe_2O_4$. A total amount of 1.0 kg of oxides was mixed with 1.0 kg ethanol, 20 grams GEROPON SDS, and milled in a plastic poly-propylene ball mill with 1.0 kg stainless steel balls for 18 hours with 75 rpm (diameter 8 cm). The steel balls were removed from the

[1] "blead-outs" means droplets of the metal alloy on the surface of the cermet after sintering.

wet mix, and the slurry was then transferred to a suitable container where it was heated in a container with hot water and continuously stirred to ensure that the solvent evaporated completely. The dry powder was then screened through a 30 and 50 mesh brass screen to obtain a free flowing powder, transferred to a sintered alumina crucible and subsequently calcined for 4 hours in an open furnace exposed to air at 1000 ^{o}C.

The powder was once again transferred to the ball mill together with 3 wt. % nickel and 17 wt. % copper. 1 kg of n-hexane and 20 grams GEROPON SDS and 30 grams of ethyl cellulose in 50 ml ethanol was added. Ethyl cellulose is very difficult to dissolve in hexane, and even ethanol, but it did, however, dissolve in 50 ml ethanol by heating the ethanol to 60^{o}C and add the ethyl cellulose very gently and keep the solution under continuous stirring at 60 ^{o}C for 30 minutes. The mixture was again milled for 18 hours, but with another set of steel balls. After milling the dispersion was wet screened and stir dried in a glass container immersed in a sealed tub of boiling water to provide a uniform dispersion of the binder in the powder. The dry mixture was then screened through a 30- and 50-mesh screen to obtain a free flowing powder.

Weyand *et al.* (5) used polyvinyl alcohol binder material and no pre compaction prior to CIP[2] to obtain dense and machinable green bodies. Olsen (1) found that a binder was unnecessary, and claimed that the ductility of the metallic powder was sufficient to produce good green bodies. The mixture was filled into special latex CIP-moulds and vibrato-compacted to achieve higher green body densities. The moulds were sealed to prevent the CIP-hydraulical liquid from entering the mix, and CIP-ed at 200 MPa (2000 bar). The green bodies with a diameter of only 1 cm, and without oxidised fish oil, cracked during CIP-ing, so the fish oil obviously acts as a binder. 3 wt% ethyl cellulose was therefore used as a binder in the present work to prevent cracking during CIP-ing.

It is important to control binder residuals and rates of binder burn-outs. Windisch and Huettig (9) used a controlled atmosphere containing 100-200 ppm oxygen. However, they reported poor heat conductivity of large green anodes, which cracked during even the most gentle burn-out cycle. Their explanation was that the outside pores closed up during sintering before the inside pores reached temperatures high enough to vaporise the binder. Binder trapped inside the anode eventually vaporised and caused pore formation and even cracking of the anode.

The sintering process used was based on the procedure described by Weyand (4), and since he used a binder it was necessary to have a binder burnout at an intermediate temperature. An inert cover gas is necessary during densification to avoid the free nickel and copper in the calcined cermet from oxidising, but reducing atmospheres like $p_{O_2} = 10^{-9}$ atm. or lower should be avoided to prevent the nickel-iron species from being reduced (4). Alcoa (5) found the optimum oxygen partial pressure to be 10^{-4} to 10^{-5} for both the calcine-sinter and the reaction-sinter compacts. The sintering was carried out in a closed tubular furnace inside a high-purity aluminium oxide tube in an argon atmosphere. The flow rate was 5 ml/min which according to Olsen (10), should give a partial oxygen pressure of approximately $6*10^{-6}$ atmospheres at room temperature. The higher nickel content

[2] CIP = Cold Isostatic Pressure

observed by Olsen (1) in cermet anodes with excess NiO should therefore not be the result of a too low oxygen pressure. However, it may be a result of a carbothermic reduction of NiO caused by the organic dispersing agent and binder left in the green body before sintering.

The following temperature cycle was used:

Temperature range	**Temperature change**
20-300°C	150°C/hour
hold 2 hours	evaporation of binder
300-1000°C	300°C/hour
1000-1350°C	175°C/hour
1350°C	Sintering for 2 hours
1350-950°C	-200°C/hour
950-20°C	Furnace off, natural cooling

Graphically, the heating and cooling curve looks like the one shown in the figure 3-1.

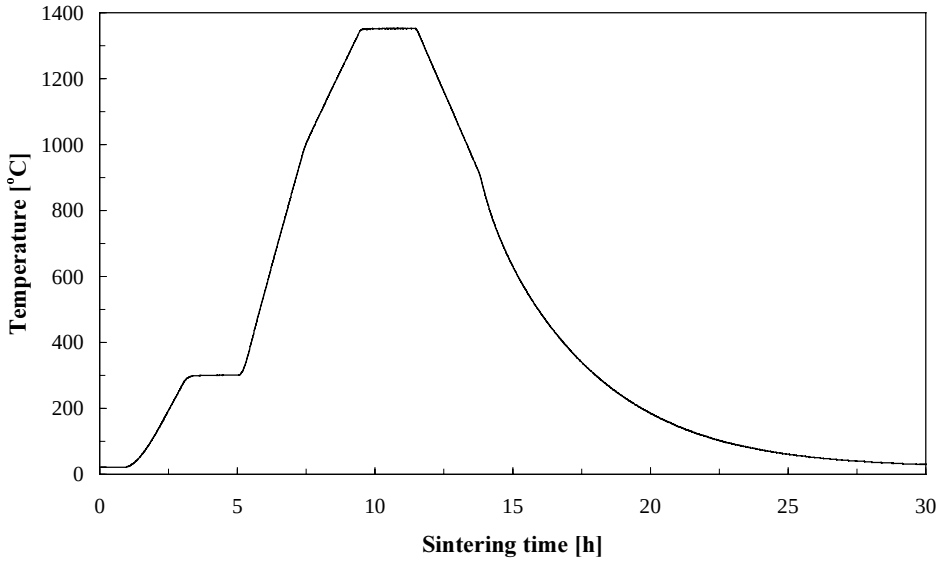

Figure 3-1: The temperature cycle used during sintering.

This procedure gave solid and dense samples with a strong (black) metallic lustre on the surface.

A solid state sintering at lower temperature has the potential benefits of energy savings and less material bleed-out giving an overall higher content of metal phase in the cermet. Lower sintering temperature has been attempted by Hart *et al.* (7) for traditional cermet anodes, but resulted in a poor microstructure and low densities.

Windisch *et al.* (11) used the Glycine-Nitrate process (3) to produce cermet anodes with a very fine-grained microstructure (grains ~ 1 μm), but these anodes obtained higher porosity and corroded severely compared to the standard anodes described by Alcoa (5) with coarser microstructure (grain size of 10-20 μm). Windisch *et al.* (11) also tried to sinter their anodes in a dry 4% N_2- 96% H_2 atmosphere at only 1130 ^oC (instead of 1350) for only 1 hour since the smaller grains were more reactive (ref. Chapter 3.1) than the traditional powders used causing more rapid sintering. 1130 ^oC is below the melting point of the metal phase, and it prevents the bleed-out of the metal phase, even when it is present at a high volume fraction, but the result was a higher electrical resistance in these anodes. They concluded that liquid phase sintering is required to achieve adequate conductivity of the metal phase. A more copper-rich phase would more likely melt and flow during sintering, which would explain the higher amount of metal bleed-out during sintering (9).

3.4 Thermodynamical considerations regarding the sintering chemistry.

While excess iron is readily accommodated in the nickel ferrite crystal lattice, only about 2 wt% of excess NiO is soluble under normal preparation conditions (12) with higher nickel concentrations precipitating in the second phase, *i.e.* NiO.

Weyand (4) has reported general expressions for the stoichiometric reactions, which take place during sintering, corresponding to the chemical used for cermet production:

$$NiO_{(s)} + Fe_2O_{3(s)} \rightarrow Ni_xFe_{3-x}O_{4(s)} + Ni_xFe_{1-x}O \quad [3\text{-}3]$$

$$NiO_{(s)} + Fe_3O_{4(s)} + Fe \rightarrow Ni_xFe_{3-x}O_{4(s)} + Ni_xFe_{1-x}O \quad [3\text{-}4]$$

$$Ni_{(s)} + NiFe_2O_{4(s)} + NiO \rightarrow Ni_xFe_{1-x} + Ni_xFe_{3-x}O_{4(s)} + Ni_xFe_{1-x}O \quad [3\text{-}5]$$

$$Cu + NiFe_2O_{4(s)} + NiO \rightarrow Cu_xNi_{1-x} + Ni_xFe_{3-x}O_{4(s)} + Ni_xFe_{1-x}O \quad [3\text{-}6]$$

There are several other chemical reactions that can take place during sintering. Some of them can be avoided, but others can not. Based on thermodynamic data collected from Barin (13) and Knacke *et al.*(14), chemical stability considerations have been made.

According to reaction [3-1] and [3-2], magnetite (Fe_3O_4) reacts with nickel oxide (NiO) and oxygen to form nickel ferrite ($NiFe_2O_4$). The Gibbs energy of formation for these reactions is negative and therefore thermodynamically possible reactions when the kinetic is fast enough. One has, however, to be aware of the fact that the reaction does not proceed below a certain oxygen pressure. If one uses the Gibbs energy of formation (ΔG^o) for reaction [3-1], it is possible to calculate the stability region for nickel ferrite by calculating when the oxygen partial pressure is low enough to make (ΔG^o) positive and thereby forcing the reaction to the left (back reaction). The stability line for nickel ferrite is given by partial pressures of oxygen higher than what equation [3-7] gives. A partial pressure of

oxygen lower than what is given by equation [3-7] indicates that $NiFe_2O_4$ converts to NiO and Fe_3O_4.

$$\ln(p_{O_2}) = -\frac{11211}{T} + 1.905 \qquad [3\text{-}7]$$

At the sintering temperature of 1350 ^oC the oxygen pressure should be higher than 0.01 atm if nickel ferrite is wanted as the only stable phase. The problem with using an oxygen atmosphere during sintering is, however, the oxidation of the metal phase in the cermet. Both nickel and copper will oxidise under such sintering conditions, and it is therefore desirable to keep the oxygen pressure as low as possible. Sintering of anodes has been successfully run at $2 \cdot 10^{-4}$ atm of oxygen (5), which is far below the calculated limit, indicating that the kinetics of the back reaction is slow.

Cermet with excess nickel oxide (NiO) has shown promising low corrosion rates during electrolysis(1), (2), (4). Thus, it is important to consider the stability of NiO during sintering. The stability region for NiO is calculated according to reaction [3-8], and the stability line for NiO at a certain temperature is expressed by the partial pressure of oxygen given by equation [3-9].

$$NiO = Ni + \frac{1}{2}O_{2(g)} \qquad [3\text{-}8]$$

$$\ln(p_{O_2}) = -\frac{26485}{T} - 3.018 \qquad [3\text{-}9]$$

According to equation [3-9] the oxygen partial pressure must be higher than $4 \cdot 10^{-9}$ to avoid NiO to be reduced to Ni during sintering at 1350 ^oC.

The reaction:

$$NiFe_2O_{4(s)} \rightarrow O_{2(g)} + \frac{1}{4}Fe_3O_{4(s)} + \frac{5}{4}Fe_{(s)} + NiO_{(s)}\,,\ \Delta G^o_{1293K} = 339.140 \text{ kJ/mol} \qquad [3\text{-}10]$$

requires an extremely low oxygen partial pressure to occur, so there is no need to worry about this reaction during sintering of nickel ferrite.

Several exchange reactions between the components of the cermet are possible thermodynamically. If metallic iron is present in the cermet, the following red-ox reactions between Fe and NiO are possible, since all the oxides of iron are more stable than NiO according to thermodynamics:

$$NiO_{(s)} + \frac{2}{3}Fe_{(s)} \rightarrow \frac{1}{3}Fe_2O_{3(s)} + Ni_{(s)} \qquad \Delta G^o_{1293K} = -38.346 \text{ kJ/mol} \qquad [3\text{-}11]$$

This reaction is reported (4) to cause volume expansion during the first part of the sintering (500-700 ^oC), and must be carefully controlled to avoid cracking. Also, the following two reactions are possible:

$$NiO_{(s)} + Fe_{(s)} \rightarrow Ni + FeO_{(s)} \qquad \Delta G^{o}_{1293K} = -55.001 \text{ kJ/mol} \qquad [3\text{-}12]$$

$$NiO_{(s)} + \frac{3}{4}Fe_{(s)} \rightarrow Ni + \frac{1}{4}Fe_3O_{4(s)} \qquad \Delta G^{o}_{1293K} = -51.685 \text{ kJ/mol} \qquad [3\text{-}13]$$

These reactions are important to have in mind when an alloy for the current connection rod is selected. Iron-containing rods have to be protected from the cermet to avoid iron oxide formation in the contact area with increased contact resistance and heat generation as a result.

Also, copper is thermodynamically more stable than Fe with a similar reaction pattern as shown for Ni in equations [3-12] and [3-13].

Metallic copper is a stable phase in contract with $NiFe_2O_4$, but oxidation to Cu(I) and Cu(II) may occur.

$$2Cu_{(s)} + \frac{1}{2}O_{2(g)} \rightarrow Cu_2O_{(s)} \qquad \Delta G^{o}_{1293K} = -75.858 \text{ kJ/mol} \qquad [3\text{-}14]$$

and,

$$Cu_{(s)} + \frac{1}{2}O_{2(s)} \rightarrow CuO_{(s)} \qquad \Delta G^{o}_{1293K} = -43.507 \text{ kJ/mol} \qquad [3\text{-}15]$$

Copper is more noble than nickel and iron, and no reaction will therefore occur between copper and NiO or $NiFe_2O_4$.

To summerise, there are several different reactions that may occur in the cermet during sintering. It is, however, not possible to give more than a qualitative discussion regarding the mechanisms without knowing anything about the kinetics of the different reactions.

3.5 Reaction mechanisms during sintering according to phase analysis

According to Olsen (2) Ni is depleted from the $NiFe_2O_4$ ceramic phase and enriched in the metal phase. This event can be explained by a too low oxygen partial pressure during sintering causing nickel oxide to decompose to nickel and oxygen. Another explanation is that $NiFe_2O_4$ is converted to NiO + Fe_3O_4 because of the low oxygen pressure during sintering.

According to Olsen's results (2), Fe seems to diffuse from the "$NiFe_2O_4$" to the "NiO" phase, forming a $Ni_xFe_{3-x}O$ phase with a "x"-value lower than 1, which one would expect for stoichiometric $NiFe_2O_4$". Olsen implies the high nickel content in the metal phase (30 percent) to be caused by a simple carbothermic reduction of the oxide phase, where the carbon sources are residues of the solvent and the dispersant. This explanation may be correct, and if one assumes 1 % fish oil in 1200 ml solvent the carbon content added corresponds to a carbothermic production of nickel metal of 50 g/kg giving approximately

32 percent nickel in the metal phase. However, this explanation does not explain the depletion of Fe in $NiFe_2O_4$ if not a carbothermic reduction of Fe(III) to Fe(II) occurs according to,

$$Fe_2O_3 + \frac{1}{2}C = 2FeO + \frac{1}{2}CO_{2(g)} \qquad \Delta G^{o}_{1293K} = -67.172 \text{ kJ/mol} \qquad [3\text{-}16]$$

Weyand *et al*. (4) did not add nickel metal to the green body before sintering, and explained the nickel content in the metal phase to originate from the exchange reaction between Cu, NiO and $NiFe_2O_4$.

$$Cu + NiFe_2O_{4(s)} + NiO \rightarrow Cu_xNi_{1-x} + Ni_yFe_{3-y}O_4 + Ni_zFe_{1-z}O \qquad [3\text{-}17]$$

This explanation seems plausible.

3.6 Analysis of the cermet anodes after sintering

The sintered samples were measured with respect to density and percent of theoretical density giving densities from 5.6 to 5.7 corresponding to 95.8 to 97.8 % of theoretical density. The density was measured using the principle of Archimedes.

SEM micrographs of anodes with 17 % excess NiO, 17% Cu and 3 wt% Ni prior to sintering showed distinct phases of metal (white) and two oxides, *i.e.* NiO-rich (light gray) and $NiFe_2O_4$-rich (dark gray). The grains were typically 10-20 μm in diameter, and the metal grains were mostly in direct contact with the $NiFe_2O_4$-rich phase (see Figure 3-2 and 3-3, which show the same materials in two different scales). Some pores with a diameter of 2-6 μm were evenly distributed in the sintered material.

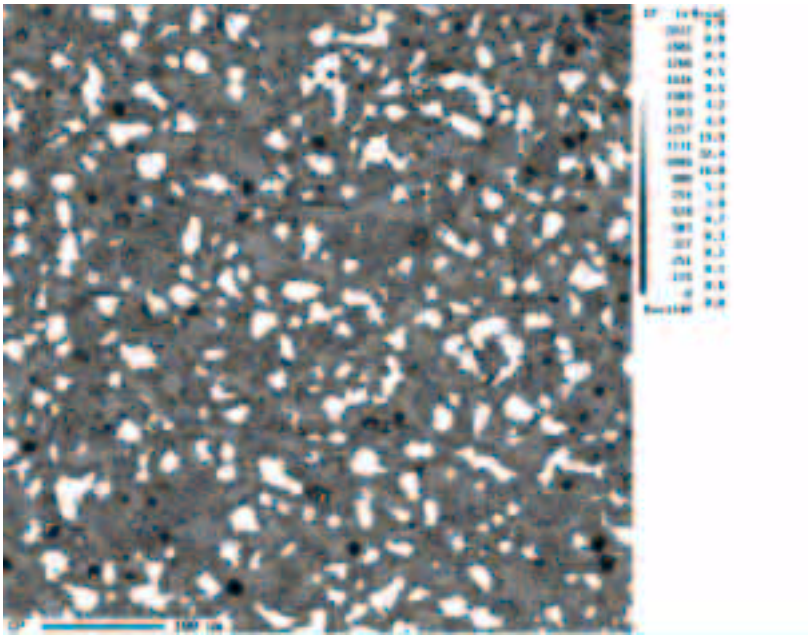

Figure 3-2: SEM-picture showing an anode with 17% excess NiO after sintering. The white grains are the metal grains, the light grey the NiO-rich phase and the dark grey a $NiFe_2O_4$-rich phase.

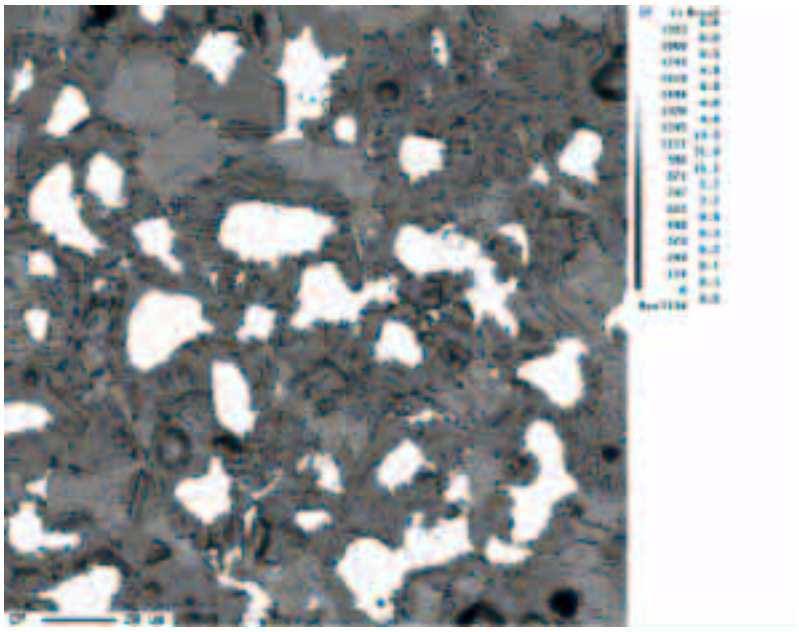

Figure 3-3: A SEM picture of a section of the centre of picture 3-2. The picture shows an anode with 17% excess NiO after sintering. The white grains are the metal grains, the light grey the NiO-rich phase and the dark grey a $NiFe_2O_4$-rich phase.

3.7 References

(1) Olsen, E, *Nickel Ferrite and Tin Oxide as Anode Materials for Aluminium Electrolysis,* doktoringeniøravhandling (Ph.D. thesis), NTH, Trondheim, ISBN 82-7119-850-5, no.100/1995.

(2) Olsen, E. and Thonstad, J., *Nickel ferrite as inert anodes in aluminium electrolysis: Part I, Material fabrication and preliminary testing*, J. Appl. Electrochem., vol. 29, pp. 293-299, 1999.

(3) Richerson, D.W., *Modern Ceramic Engineering. Properties, Processing, and Use in Design*, 2nd ed., ISDN 0-8247-8634-3, Marcel Dekker Inc., 1992.

(4) Weyand, J.D., *Manufacturing processes used for the production of inert anodes*, Light Metals1986, TMS, pp. 321-339, 1986.

(5) Weyand, J.D., DeYoung, D.H., Ray, S.P., Tarcy, G.P., and Baker, F.W., *Inert Anodes for 4Aluminium Smelting. Final Report*, Alcoa Centre, DOE/CS/40158-20, Feb., 1986.

(6) Tarcy, G.P., *Corrosion and Passivation of Cermet Inert Anodes in Cryolite-Type Electrolytes*, Light Metals 1986, TMS, pp. 309-320, 1986.

(7) Hart, P.E., Brenden, B.B., Davis, N.C., Koski, O.H. and Marchman, S.C., *Fiscal Year 1986 Annual Report,* Pacific Northwest Laboratory, PNL-6247 UC-95f, June 1987.

(8) Lanne, R.M., Sales manager, Unger Industrier ASA, Fredrikstad, Norway, Personal communication, spring 1998.

(9) Windisch Jr., C.F. and Huettig, F.R., *Fabrication of Advanced Design (Grooved) Cermet Anodes*, Pacific Northwest Laboratory, PNL 8622 UC-313, May 1993.

(10) Olsen,E. personal communication, SINTEF Materials Technology, Trondheim, Norway, Autumn 1997.

(11) Windisch Jr., C.F., Chick, L.A., Maupin, G.D. and Stice, N.D, *The Effects of Microstructure on the Corrosion of Glycine/Nitrate Processed Cermet Inert Anodes: A Preliminary Study,* Pacific Northwest Laboratory, PNL 7733 UC-313, July 1991.

(12) Elwell, D., Griffiths, B.A., and Parker, R., *Electrical conduction in nickel ferrite*, Brit. J. Appl. Phys., vol. 17, pp. 587-593, 1966.

(13) Barin, I., *Thermodynamical Data of Pure Substances*, 3rd ed., VCH Verlags-gesellschaft mb-H, D-69451, Weinheim, Germany, 1995.

(14) Knacke, O., Kubaschewski, O., Hesselmann, K., *Thermochemical Properties of Inorganic Substances*, 2nd ed., Springer-Verlag, Verlag Stahleisen, 1991.

4 Solubility of nickel oxide in cryolite-alumina melts

An absolute requirement for the material of an inert anode to be used for the production of aluminium is that it should exhibit a low solubility in cryolite-based melts. Some of the most promising materials are based on metal oxides, and their operating characteristics depend on their dissolution rates.

The source of nickel impurities in the present investigation is the dissolution of the anodes' oxide phases, which contain nickel ferrite ($NiFe_2O_4$) with excess NiO. During electrolysis, nickel is reduced into the liquid aluminium metal, and affects the physical and chemical 7properties of aluminium. More than 0.01 wt% nickel is therefore not wanted as an impurity in aluminium (1).

Literature data on the solubility of nickel oxide in cryolite are inconsistent. DeYoung (2) has investigated the solubility for NiO, Fe_2O_3 and $NiFe_2O_4$ in cryolite melts, and as a validity test for his work and to cover a wider composition range, the solubility of NiO was investigated.

4.1 Nickel as an impurity in aluminium

Some of the materials that have been investigated to be used as an inert anode are based on metal oxides and alloys, which contain nickel. The lifetime for these anodes and the content of anode impurities in the aluminium metal produced, depends on the dissolution rate of the anode components (2).

One of the most promising oxide-based anode materials is nickel ferrite ($NiFe_2O_4$), and the solubility of the anode components NiO and Fe_2O_3 will, therefore, affect the solubility of nickel ferrite. These dissolved anode components will be reduced into the aluminium metal produced, and will act as unwanted impurities.

The solid solubility of nickel (1) in solid aluminium is only 0.04 weight %. Higher contents of nickel are present as inter-granular particles in the metal. As much as 2 weight % nickel increases the strength of high-purity aluminium, but reduces the ductility. Nickel is added to aluminium-copper and aluminium-silicon alloys to improve hardness and strength at elevated temperatures and to reduce the coefficient of thermal expansion. Nickel can, however, promote pitting corrosion in dilute alloys such as 1100 [1]. The amount of nickel one can accept is limiting in alloys for use as atomic reactors, due to high neutron absorption, but in other areas it is desirable along with iron to improve corrosion resistance to high-pressure steam.

[1] 1100 = Commercially pure aluminium with 0.12 weight percent copper (1)

4.2 Chemicals

Na_3AlF_6	*cryolite*	Handpicked Greenland cryolite, Kryolittselskabet
NaF		P.a. Merck, heated under argon atmosphere at 400 ^oC for 10 hours
AlF_3		Synthetic, from Norzink, purified in the laboratory by sublimation and heated under argon atmosphere at 400 ^oC for 10 hours
LiF		P.a. Merck, > 99%
Al_2O_3	*alumina*	γ-Al_2O_3, P.a. Merck, dried at 200 ^oC
NiO		99,98%, 5 μm, from Novamet, pressed into tablets and sintered under argon atmosphere at 1100 ^oC for 20 hours
$NiAl_2O_4$		Mixed NiO and Al_2O_3 in air at 1100 ^oC for 20 hours in an alumina crucible
O_2		99.99%, AGA Gas

4.3 Experimental procedure for measuring the solubility of NiO

160 grams of electrolyte was prepared from handpicked Greenland cryolite and p.a. aluminium oxide. A tablet of sintered green NiO was positioned 2 cm above the bottom of the platinum crucible, and crushed electrolyte added. At the operating temperature, the NiO tablet was suspended in the middle of the melt.

A standard furnace as described by Xiao (3) and Diep (4) was used with oxygen atmosphere. Oxygen was used because a few preliminary experiments had been conducted at SINTEF Materials Technology with oxygen atmosphere, and a comparison between these results and the present was considered beneficial.

The small possibility that Ni(I) forms requires oxygen atmosphere to avoid the following unwanted reaction mechanism, which may influence the solubility measurements:

$$2NiO \rightarrow Ni_2O_{(dissolved)} + \frac{1}{2}O_{2(g)} \qquad [4\text{-}1]$$

if nickel oxide changes valence by producing Ni_2O. Ni_2O should, however, not be stable at 1020 ^oC. The formation of Ni(III) is according to thermodynamics (6) not possible at 1020 ^oC. According to stability diagram 2-3 one could also have used a nickel crucible and an atmosphere of oxygen or argon 4 (contains ~200 ppm O_2).

The temperature was measured with a Pt/Pt10%Rh thermocouple inside a sealed platinum tube placed 2 cm from the bottom of the platinum crucible (see Figure 4-1).

According to Sterten and Skar (7), the maximum time of experiment recommended is 8 hours if one wants to avoid a shift in the bath ratio caused by evaporation (mainly $NaAlF_4$). DeYoung, reported (2), however, that the cryolite ratio affects the solubility of nickel oxide

in cryolite very little. By reducing the flush gas in the furnace to a minimum, the evaporation loss was found to be less than 0.3 %.

Preliminary tests run at SINTEF Material Technology showed steady state solubility data of nickel concentrations in pure Greenland cryolite after 2.5 hours of stirring. Solubility tests for similar melts were, however, run for 3, 5 and 6 hours of stirring, to check this result. The following results were obtained for the three experiments: 0.181, 0.233 and 0.245 weight % nickel. Further tests indicated, however, that the difference between the results obtained for 5 and 6 hours of stirring was within the experimental uncertainty, and all the following melts were, therefore, stirred for 5 hours.

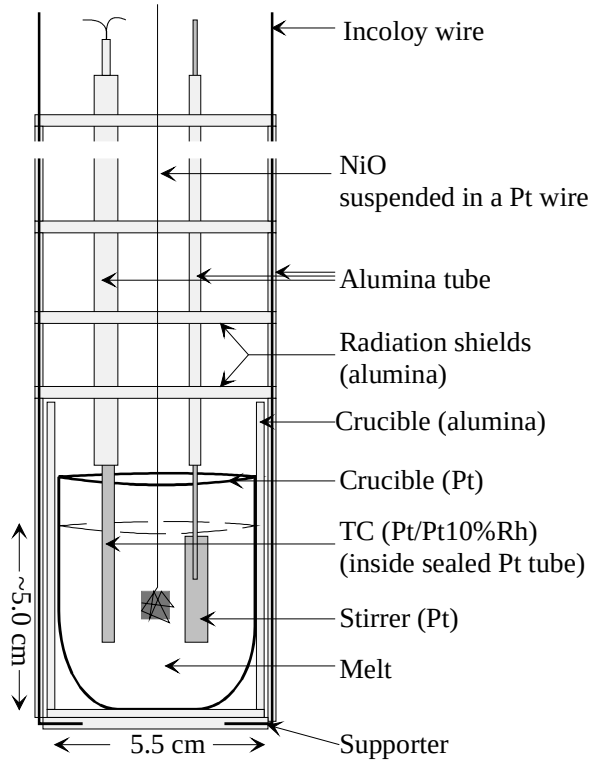

Figure 4-1: Sketch of the test equipment for the nickel solubility experiments.

To obtain an effective dissolution process, proper convection in the electrolyte is important, and a platinum stirrer was found to give adequate convection. An alumina (Alsint) stirrer was used in the alumina-saturated melts with acidic baths. Satisfactory dispersion of alumina particles in water was obtained at 65 rpm.

When the solubility limit is reached, however, a stagnant electrolyte is beneficial, since one wants any particulate nickel oxides to settle before the bath sample is collected. Thermally induced convection caused by density variations in the electrolyte was avoided by assuring constant temperature in the bath (*i.e.* maximum 2 degrees positive difference between the top and the bottom of the crucible).

The tests were carried out by preheating and melting down the electrolyte for 3 hours, stirring it for 5 hours at constant temperature, and finally letting it settle it for one hour. 3-6 grams of electrolyte were withdrawn from the solution by a silica tube that was quickly immersed 5-10 mm into the solution.

The bath samples were quenched and crushed. 1-3 grams of the crushed bath samples were dissolved in 50 ml 30 % $AlCl_3 \cdot 6H_2O$ solution, mixed with 5 ml of 30 % HCl and filled up with de-ionised water in a 100 ml polypropylene graduated flask for ICP analysis[2].

4.4 Solubility of NiO in the Na_3AlF_6-Al_2O_3-O_2 system at 1020 °C

The solubility of NiO has been found (2) to be determined by a solubility product, *i.e.* the solubility of NiO increases with decreasing alumina activity. This indicates that NiO does not dissolve as metal oxide ions like e.g. NiO_2^{2-}, because alumina then would have *increased* the solubility of those ions. A possible mechanism for such a reaction could have been:

$$NiO + \frac{1}{3}Al_2O_3 + 2NaF \rightarrow Na_2NiO_2 + \frac{2}{3}AlF_3 \qquad [4\text{-}2]$$

Increasing alumina activity then would force the reaction to the right, which would have increased the solubility of NiO as a result. The dissolved nickel species is probably a metal cation, metal fluoride ion or metal oxy-fluoride ion, so that a reduction of alumina activity will increase the solubility of NiO. As an example, the dissolution of NiO can form nickel fluoride:

$$NiO_{(s)} + \frac{2}{3}AlF_{3(l)} \rightarrow NiF_{2(l)} + \frac{1}{3}Al_2O_{3(l)} \qquad [4\text{-}3]$$

where the activity of the dissolved species is proportional to the activity of alumina to the power of minus one third.

Another complication is that at high concentrations of alumina, nickel aluminate will form as the solid phase (6):

$$NiO + Al_2O_3 \rightarrow NiAl_2O_4 \qquad [4\text{-}4]$$

This has also been observed for other metal oxides dissolved in cryolite melts, like zinc and iron oxides (8).

If nickel aluminate precipitates in the melt, the alumina concentration will decrease accordingly. This is important to take into consideration when the solubility measurements are presented as a function of weight percent alumina, which are given in Figure 4-2 below.

Belov and Gladneva (9) found a solubility of 0.20 wt% Ni(II) in cryolite at 1000 °C. Sterten and Skar (7) reported the solubility of Ni(II) in cryolite to be 0.79 wt%, while Belyaev *et al*. (10) gave the value 0.25 wt% at 1000 °C and Rolin and Bernard (11) gave 0.12 wt% at 1030 ± 15 °C. Liquidus temperatures for alumina-free cryolite measured by

[2] Ionic Plasma Coupling (5), type "Thermo Jarell Ash Atomscan 16".

Sterten and Skar (7) indicated that the cryolite used by the two latter references contained alumina because of the lower melting point reported for their *pure* cryolite, which may explain some of the discrepancy between the groups of investigations.

DeYoung (2) obtained 0.25 wt% Ni(II) in cryolite with 0.6 weight percent alumina ,which is very similar to the present results (see Figure 4-2). However, the result reported by DeYoung for 5.3 wt% alumina is 0.07 wt%, which is higher than the present results.

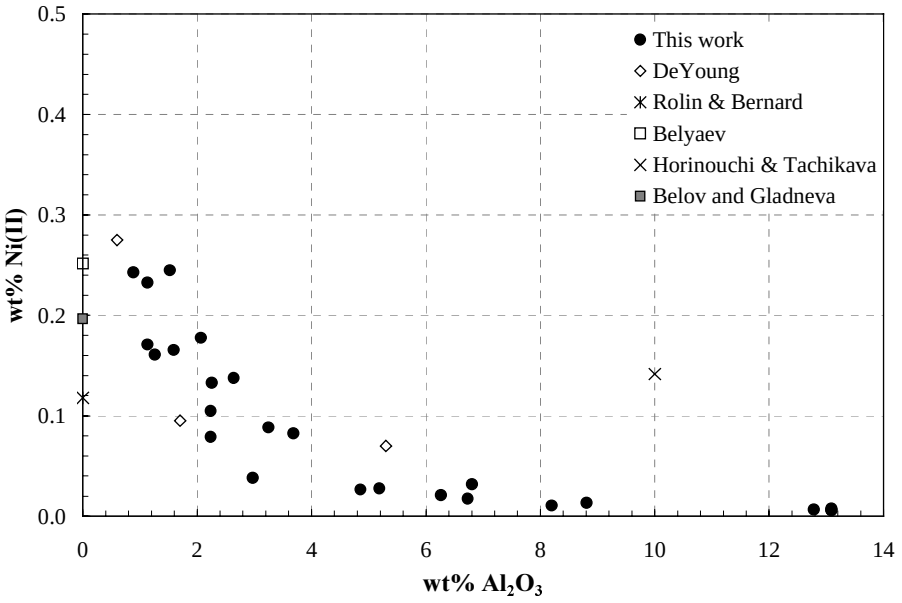

Figure 4-2: The solubility of nickel oxide, reported as wt% Ni(II), in natural cryolite as a function of wt% alumina added. The temperature is 1020 ^{o}C.

By using the average of the different results obtained in the present work for the different alumina activities, the solubility of nickel in cryolite can be expressed as follows:

$$\text{Wt\% Ni(II)} = -0.0755 + \left[\frac{0.27896}{x^{1/2}}\right], \text{ where x = wt\% } Al_2O_3 \text{ (0.9 – 13.1 wt\%)} \qquad [4\text{-}5]$$

According to Dewing and Thonstad (8) a presentation of the solubility data versus the activity of alumina in a logarithmic diagram is often more informative than a linear plot because it is possible to derive a stoichiometric relationship for the dissolution mechanism by the slope of the line, *i.e.* between alumina and Ni(II).

There was no activity data available for the ternary system under investigation, so data for the binary system cryolite-alumina were used. Several articles regarding the activity of alumina have been reported lately (8), (12), (13), (14) and (15). The activity data by Dewing and Thonstad (8) give the overall best fit for the experimental data obtained by

Holm (16) for the Na_3AlF_6-Al_2O_3 system at 1020 ^oC, and is given by the conversion equation for the molar ratio "N" for alumina:

$$N_{Al_2O_3} = \alpha \cdot a_{Al_2O_3}^{1/3} + \beta \cdot a_{Al_2O_3}^{2/3} \qquad [4\text{-}6]$$

where $\alpha = 0.0772 \pm 0.0025$ and $\beta = 0.159 \pm 0.0048$. A tabulated list of weight percent alumina *versus* alumina activity data is given in Table 4-1.

The solubility of Ni(II) can then be expressed as a function of the alumina activity, using equation [4-5],

$$\text{Wt\% Ni(II)} = 0.101 \cdot a_{Al_2O_3}^{-0.678} \qquad \text{where a = alumina activity} \qquad [4\text{-}7]$$

Table 4-1: Corresponding data for wt%, molar fraction and activity for alumina in cryolite at 1020 ^oC.

wt% Al_2O_3	**N (Al_2O_3)**	**a (Al_2O_3)**	**wt% Al_2O_3**	**N (Al_2O_3)**	**a (Al_2O_3)**
1.00	0.020	0.007	7.50	0.143	0.399
1.50	0.030	0.017	8.00	0.152	0.446
2.00	0.040	0.032	8.50	0.161	0.495
2.50	0.050	0.050	9.00	0.169	0.545
3.00	0.060	0.073	9.50	0.178	0.597
3.50	0.069	0.098	10.00	0.186	0.650
4.00	0.079	0.127	10.50	0.195	0.704
4.50	0.088	0.159	11.00	0.203	0.760
5.00	0.098	0.193	11.50	0.211	0.817
5.50	0.107	0.230	12.00	0.219	0.874
6.00	0.116	0.269	12.50	0.227	0.933
6.50	0.125	0.311	13.00	0.235	0.993
7.00	0.134	0.354	13.06	0.236	1.000

First one assumed that alumina was coming only from the amount added to the cryolite and from the natural cryolite itself (0.323%), and a logarithmic plot of these results as a function of alumina activity gave two fairly straight lines. The slope of the line for the low alumina region, *i.e.* the relative change of solubility with changing alumina activity, was close to +1/3, which indicates the following reaction mechanisms:

$$NiO + \frac{1}{3}Al_2O_3 + 2NaF \rightarrow Na_2NiO_2 + \frac{2}{3}AlF_3 \qquad [4\text{-}8]$$

For the high alumina region the slope was close to –2/3, indicating the dissolution mechanism:

$$NiAl_2O_4 + 2NaF \rightarrow Na_2NiO_2 + \frac{2}{3}Al_2O_3 + \frac{2}{3}AlF_3 \qquad [4\text{-}9]$$

Equation [4-9] indicates that the dissolution of NiO produces alumina in the melt. In addition, some of the solubility data obtained for equal melt-compositions prepared prior the experiment (*i.e.* equal amounts of alumina added to the cryolite) were very scattered, indicating that the melt compositions varied from one parallel to another.

The total amount of alumina in the melt can be expressed as the mass balance:

$$C_{alumina\ (tot.)} = C_{alumina\ added} + C_{alumina\ in\ cryolite} + C_{alumina\ impurities(furnace)} + C_{reaction\ product} \qquad [4\text{-}10]$$

The last three terms in equation [4-10] were initially considered to be negligible. However, the alumina concentrations were determined by using the LECO[3] apparatus, and these values were different from the ones only based on alumina additions. The amounts of Ni(II) in the samples are plotted as a function of the alumina concentration based on the LECO analysis in Figure 4-3.

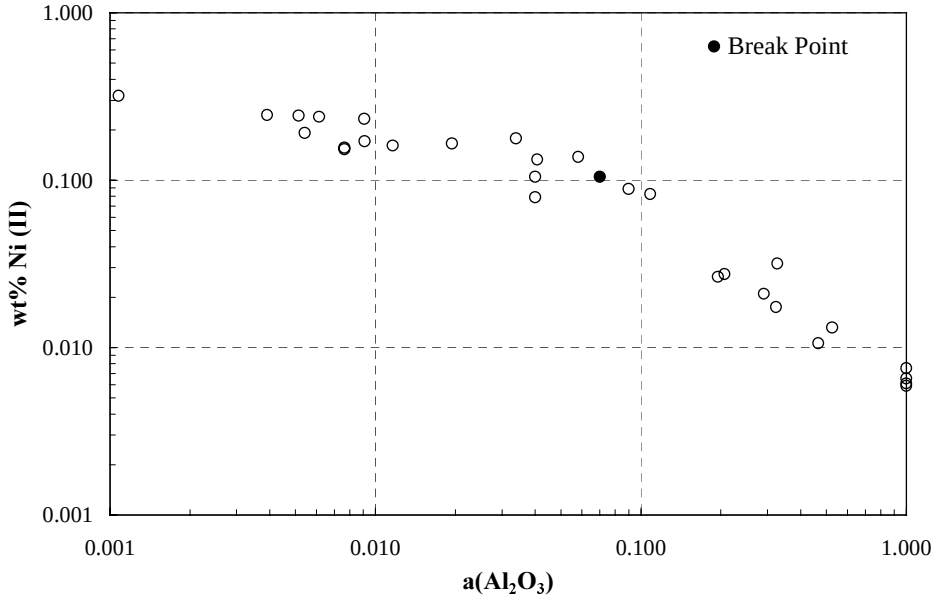

Figure 4-3: A log-log diagram of the solubility of nickel in natural cryolite as a function of alumina activity (based on LECO analysis and alumina activities from (8)). The temperature is 1020 ^oC.

[3] LECO is an apparatus used for analysing the content of oxygen in a sample by mixing a known amount of crushed sample with graphite powder in a graphite crucible. The chamber containing the crucible is then evacuated, and heated to above 2000 ^oC to assure that all the oxygen in the sample reacts with the graphite powder to form mainly CO (and small amounts of CO_2). The amount of CO is measured, indirectly giving the amount of oxygen containing species in the sample.

The results given in Figure 4-3 indicate two different slopes with a intercept (breaking point) at an alumina activity equal to 0.07 ± 0.02 (corresponding to 3.0 wt% alumina), which was calculated as shown in Chapter 4.5. The standard deviation of the intercept is based on the cross-point for the steepest and the gentlest lines given in the Figure above.

For alumina concentrations below 3.0 weight percent the solubility of Ni(II) can be expressed as,

$$\log(\text{wt\% Ni(II)}) = -0.26(\pm 0.05)\log a_{Al_2O_3} - 1.28(\pm 0.10) \quad [4\text{-}11]$$

and for alumina concentrations higher than 3.0 weight percent,

$$\log(\text{wt\% Ni(II)}) = -1.14(\pm 0.08)\log a_{Al_2O_3} - 2.21(\pm 0.04) \quad [4\text{-}12]$$

The slope for the low alumina region is close to –1/3, which indicates the following mechanism:

$$NiO + \frac{2}{3}AlF_3 \rightarrow NiF_2 + \frac{1}{3}Al_2O_3 \quad [4\text{-}13]$$

while the high alumina region the slope was–1.1, which can be described by,

$$NiAl_2O_4 + \frac{2}{3}AlF_3 \rightarrow NiF_2 + \frac{4}{3}Al_2O_3 \quad [4\text{-}14]$$

with the theoretical slope of – 4/3, which is close to the experimental value. To get –1/3 (for low cons.) and – 4/3 (for high cons.), three other conditions must be met:

1. The activity of AlF_3 is constant
2. The activity of NaF is constant (it may be involved since NiF_2 may become complexed to NiF_4^{2-})
3. The activity coefficient of NiF_2 does not vary with the alumina content.

None of those conditions is likely to be fulfilled exactly, and slopes reasonably close to these values are considered to be correct, and the final reaction mechanisms are therefore given by equations [4-13] and [4-14].

4.5 Calculation of the breakpoint for the solubility data of Ni(II) in the system Na_3AlF_6-Al_2O_3-O_2 at 1020 °C

A possible way to calculate the breakpoint, which separates the “low region” from the “high region”, is to calculate the intercept between the two slopes determined by regression analysis (18). The problem is, however, that one is not sure exactly where the breakpoint comes, so it is not possible to decide to which line the points near the breakpoint belong.

A possible way to solve this problem is to make use of the relationship between the slopes of the two lines. Suppose that at low alumina NiO is dissolving by,

$$NiO + ?? = Ni? + x \cdot Al_2O_3 \qquad [4\text{-}15]$$

The slope of the plot showing the log of solubility *versus* the log of alumina activity will then be *"–x"*. At high alumina concentration, however, $NiAl_2O_4$ is stable, and the dissolution reaction will be,

$$NiAl_2O_4 + ?? = Ni? + (x+1) \cdot Al_2O_3 \qquad [4\text{-}16]$$

and the slope will be *"– (x+1)"*. This will be true regardless of the dissolution mechanism, and the *"+1"* arises because there is one Al_2O_3 in $NiAl_2O_4$.

The problem is to find the values for the breakpoint and for *x,* which minimise the sum of squares for *all* the data. These data can only be found by trial and error. The procedure is to examine the results and then choose a plausible value for the breakpoint. Then one moves all the points to the left of the assumed breakpoint (called BP) upwards to where they would be if the slope of that line were increased by one, *i.e*. each value of "log(wt % Ni(II))" is increased by "(1 · (BP – log($a_{Al_2O_3}$)))". This procedure is illustrated in Figure 4-4.

Now all the points can be fitted by regression to a straight line, yielding a slope and a standard deviation. The procedure is repeated for several values around the predicted breakpoint value, and the "correct" value for the breakpoint is found as the value giving the regression line with the lowest sum of squares. This procedure is called the Kocks-Box Transformation (18).

Regression lines for different breakpoints (BP) and the sum of squares for each regression line (SS_E) were calculated. The result is shown in the Figure 4-5.

The minima of the sum of square curve gives $a_{Al_2O_3}$ = 0.07 (*i.e.* log *a* = -1.15) for the BP, which is the value used to calculate the Gibbs energy of formation for nickel aluminate according to equation 4-4.

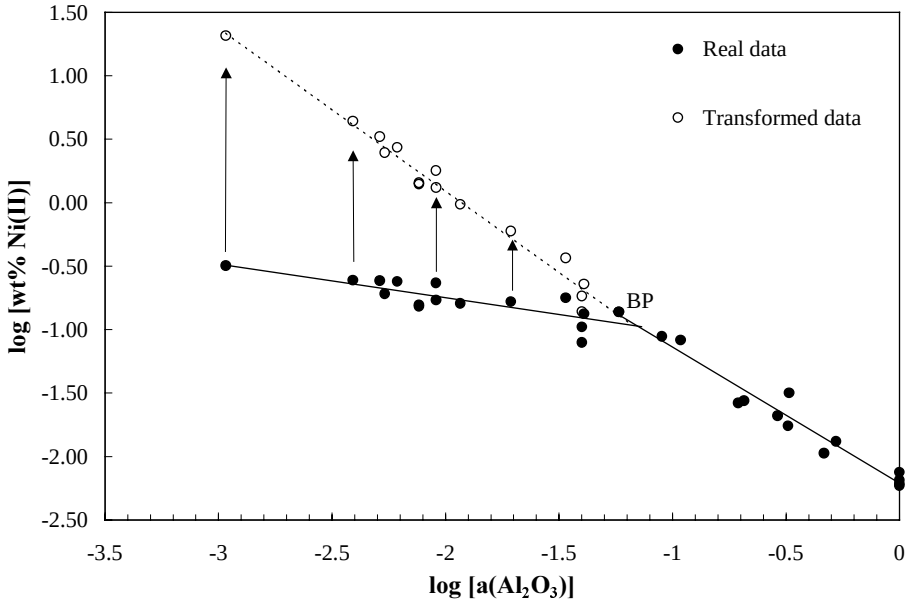

Figure 4-4: An illustration of how all the data points to the left of the breakpoint (BP) are transformed to fit one single regression line.

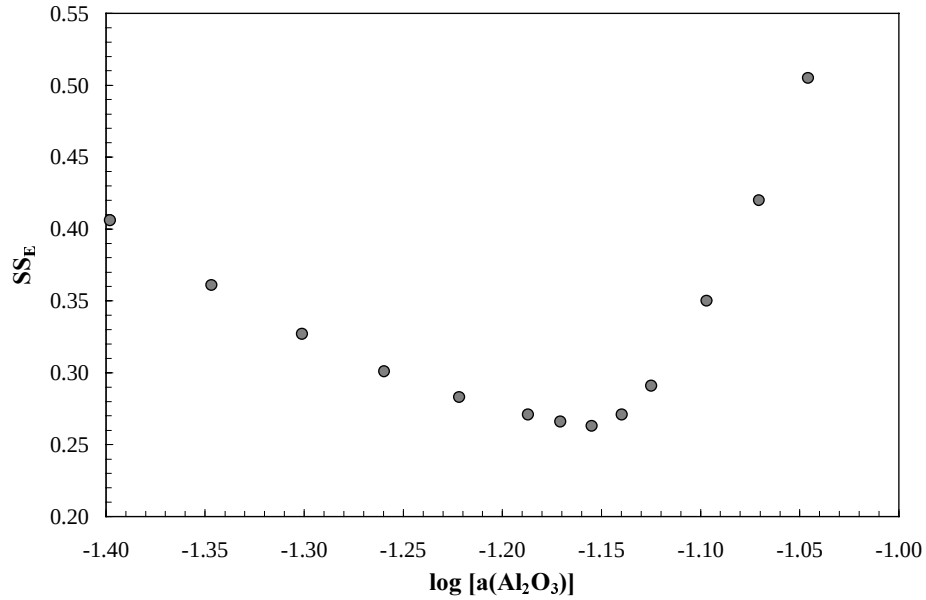

Figure 4-5: Sum of squares (SS_E) for regression lines with different alumina activities chosen as the breakpoint in the regression analysis of the solubility of Ni(II) in the system Na_3AlF_6-Al_2O_3.

4.6 Gibbs energy of formation for $NiAl_2O_4$

The phase diagram available for NiO-Al_2O_3 (17) shows the different Ni-Al-O phases occurring above 1400 ^oC, and it indicates the formation of $NiAl_2O_4$ even at infinitely low alumina concentrations. The phase diagram for $NiAl_2O_4$-Al_2O_3 (20) shows $NiAl_2O_4$ and Al_2O_3 as the only stable phase at around 1000 ^oC.

The alumina activity given at the intercept of the two slopes in Figure 4-3 can be used to calculate the Gibbs energy of formation for $NiAl_2O_4$.

The reaction considered is:

$$NiO_{(s)} + Al_2O_{3(\alpha,s)} \rightarrow NiAl_2O_{4(s)} \qquad [4\text{-}17]$$

The equation describing the Gibbs energy of formation for $NiAl_2O_4$ can be expressed as:

$$\Delta G^o_{f(NiAl_2O_4)} = -RT \cdot \ln(K) \qquad [4\text{-}18]$$

The equilibrium constant, K, is equal to "$1/a_{Al_2O_3}$", giving,

$$\Delta G^o_{f(NiAl_2O_4)} = -RT \cdot \ln\left(\frac{1}{a_{Al_2O_3}}\right) \qquad [4\text{-}19]$$

The calculated alumina activity (see Chapter 4.5 for details) at the intercept gives:

$$\Delta G^o_{f(NiAl_2O_4)} = -8.314 \cdot 1293.15 \cdot \ln\left(\frac{1}{0.07}\right) \qquad [4\text{-}20]$$

and finally,

$$\Delta G^o_{f(NiAl_2O_4)} = -28.6 \pm 2 \text{ kJ/mol} \qquad [4\text{-}21]$$

The standard deviation is based on the standard deviation of the alumina activity at the intercept, being ± 0.02, and it is based on the regression line at a = 0.07 given in Chapter 4.5.

The thermodynamic data in the literature for $NiAl_2O_4$ is very inconsistent. Fricke and Weitbrecht (19) measured CO/CO_2 ratios over Ni-NiO and Ni-$NiAl_2O_4$-Al_2O_3 mixtures. Recalculation of all their data with JANAF values (21) for the CO/CO_2 equilibrium gives a value for NiO which agrees well with values reported by Barin (6) to better than 2 kJ, so the experiments look good. For the reaction,

$$NiO + Al_2O_3 \rightarrow NiAl_2O_4 \qquad [4\text{-}22]$$

their results (19) give,

$$\Delta G^o = \Delta H^o - T\Delta S^o = -26410 + 4.560T \quad [4\text{-}23]$$

At T = 1300 K, this gives ΔG^0_{1300K} = - 20.490 kJ/mol. [4-24]

Tretjakov and Schmalzried (22) used solid state cells, and measured oxygen partial pressures of the phase mixture given by equation 4-17. From these partial pressures the Gibbs free energy of formation as well as the enthalpy and entropy of formation were calculated. The ΔG^0_{1300K} was calculated to be –16.736 kJ. They suggest that the relatively large changes of ΔH and ΔS for $NiAl_2O_4$ with temperature may be due to a high solid solubility of alumina in the spinel, or to cations going to crystallographic "non-equivalent" sites.

Levitskii and Rezhukhina (23) also used solid state cells. They used an average composition of the solid phases as constant and equal to $NiAl_{2.27}O_{4.41}$. For the reaction:

$$NiO + 1.136Al_2O_3 \rightarrow NiAl_{2.28}O_{4.41} \quad [4\text{-}25]$$

they gave:

$$\Delta G^o(\pm 0.21) = \Delta H^o - T\Delta S^o = -23.230(\pm 1.30) - 1.757(\pm 0.96)T, \ kJ/mol \quad [4\text{-}26]$$

This gives:

$$\Delta G^0_{1300K} = -25.52 \pm 0.21 \text{ kJ/mol for } NiAl_{2.28}O_{4.41} \quad [4\text{-}27]$$

Navrotsky and Kleppa (24) used solution calorimetry in a molten solvent to measure ΔH^o for $NiAl_2O_4$ directly. According to them $\Delta H^0_{970\,K} = -3 \pm 1$ kJ/mol.

Since only the value obtained by Tretjakov and Schmalzried (22) seems to fit reasonably well with the present result (eq. [4-21]), it was decided to measure the emf for the following reaction:

$$2Al_{(l)} + 3NiAl_2O_{4(s)} = 4Al_2O_{3(s,\alpha)} + 3Ni_{(s)} \quad [4\text{-}28]$$

By subtracting equation [4-29]:

$$2Al_{(l)} + 3NiO_{(s)} = Al_2O_{3(s)} + 3Ni_{(s)} \quad [4\text{-}29]$$

one gets the back reaction for [4-22].

The cell used to measure the emf was based on a galvanic cell described by Dewing (25), and it can be expressed as:

Mo	Al	LiF $AlF_{3(sat)}$	LiF $AlF_{3(sat)}$ $NiAl_2O_{4(s)}$ $Al_2O_{3\ (\alpha,\ s)}$	Ni

Figure 4-6: The electrolyte cell used to measure the Gibbs energy of formation for $NiAl_2O_4$.

A sketch of the galvanic cell is shown in Figure 4-7.

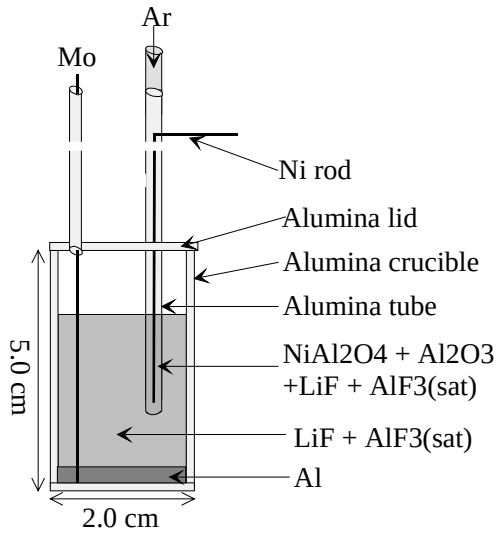

Figure 4-7: A sketch of the galvanic cell used to measure the Gibbs energy of formation for $NiAl_2O_4$.

The electrolyte used in the crucible was a liquid mixture of AlF_3 and LiF with 60 mol% AlF_3. Nickel aluminate with excess alumina was made by mixing 1 part (molar) of NiO with 2 parts of alumina to ensure excess alumina after sintering. The mixture was contained in an alumina crucible and sintered in air at 1100 ^oC for 20 hours. After cooling this mixture was crushed and mixed with electrolyte containing the same mixture of AlF_3 and LiF as in the crucible, and it was filled into a sealed alumina tube. The cell worked well, and stable emf values were obtained within 40-60 minutes at each temperature, starting at 1020 ^oC.

The electrode reactions are as follows:

Anode: $2Al + 6LiF = 6Li^+ + 2AlF_3 + 6e^-$ [4-30]

Cathode: $3NiAl_2O_4 + 2AlF_3 + 6Li^+ + 6e^- = 3Ni + 4Al_2O_3 + 6LiF$ [4-31]

The cell reaction [4-28] is the sum of [4-30] and [4-31].

As one can see from the electrode reactions, six LiF have been moved from the anode compartment to the cathode compartment and two AlF_3 from cathode to anode compartment. However, these movements cause no change in ΔG because the activities are the same on both sides. That is why one has to keep both sides saturated with AlF_3. Not only does it mean the activity of AlF_3 is the same on both sides, but it fixes the composition of the liquid so that the activities of LiF are also the same.

When using alumina-saturated electrolyte in the cell, one measures the emf for the equilibrium $Ni/NiAl_2O_4$ at alumina saturation (refers to the right hand side of the stability diagram shown in Figure 2-3, p. 24) given by:

$$3NiAl_2O_{4(s)} = 3Ni_{(s)} + \frac{3}{2}O_{2(g)} + 3Al_2O_{3(s,\alpha)} \qquad [4\text{-}32]$$

To derive the emf for equation [4-32] from [4-28], one has to subtract the emf for the Ni/NiO equilibrium, *i.e.,*

$$3Ni_{(s)} + \frac{3}{2}O_{2(g)} = 3NiO_{(s)} \qquad [4\text{-}33]$$

Since the emf was measured[4] with Mo and Ni as leads, its thermal emf , called "$Emf_{Mo\text{-}Ni}$", has to be subtracted from the measured emf for the cell to get the correct value for reaction [4-32].

$$Emf_{[4-32]} = -\left[Emf_{[4-28]} - Emf_{[4-29]} - Emf_{[4-33]} - Emf_{Mo-Ni}\right] \qquad [4\text{-}34]$$

Based on the measurements the emf for the solid electrolyte cell can be expressed as,

$$Emf_{cell} = Emf_{[4-28]} = 0.1413(\pm 0.019) - 1.190 * 10^{-3}(\pm 0.015)\cdot T \ \ [V] \quad (T = 900 - 1373K) \qquad [4\text{-}35]$$

Gibbs energy values given by Barin (6) for Al_2O_3 and from Holmes *et al.* (26) for NiO were used in the calculations of the Gibbs energy for reaction [4-29], and it can be expressed as "$Emf_{[4\text{-}29]}$" by,

$$EMF_{[4-29]} = -1.7078 - 1.311\cdot 10^{-4} * T \quad [V] \ (T = K) \qquad [4\text{-}36]$$

The emf between Mo and Ni was measured separately by short-circuiting the two rods and measuring the emf as a function of temperature in an atmosphere of argon. The "$Emf_{Mo\text{-}Ni}$" can be expressed as:

$$Emf_{Mo-Ni} = 7.524\cdot 10^{-3} - 1.748\cdot 10^{-5} * T \ \ [V] \quad (T = 673 - 1308K) \qquad [4\text{-}37]$$

[4] Measured with a Keithley 2000 multimeter

To obtain the Gibbs energy of formation for $NiAl_2O_{4(s)}$, given by [4-38],

$$NiO_{(s)} + Al_2O_{3(s,\alpha)} = NiAl_2O_{4(s,\alpha)} \quad [4\text{-}38]$$

one subtracts [4-39],

$$2Al_{(s)} + \frac{3}{2}O_{2(g)} = Al_2O_{3(s,\alpha)} \quad [4\text{-}39]$$

and adds [4-33] to the cell reaction [4-28], and multiplies the result with –1/3.

The Gibbs energy of formation is then calculated by equation [4-38] to be –27.37 kJ/mol at 1293 K, which is in excellent agreement with the value obtained from the solubility measurements (see eq. [4-21]). The same procedure was used to calculate the Gibbs energy of formation for $NiAl_2O_4$ at the other temperatures used, and the results are plotted as a function of temperature in Figure 4-8.

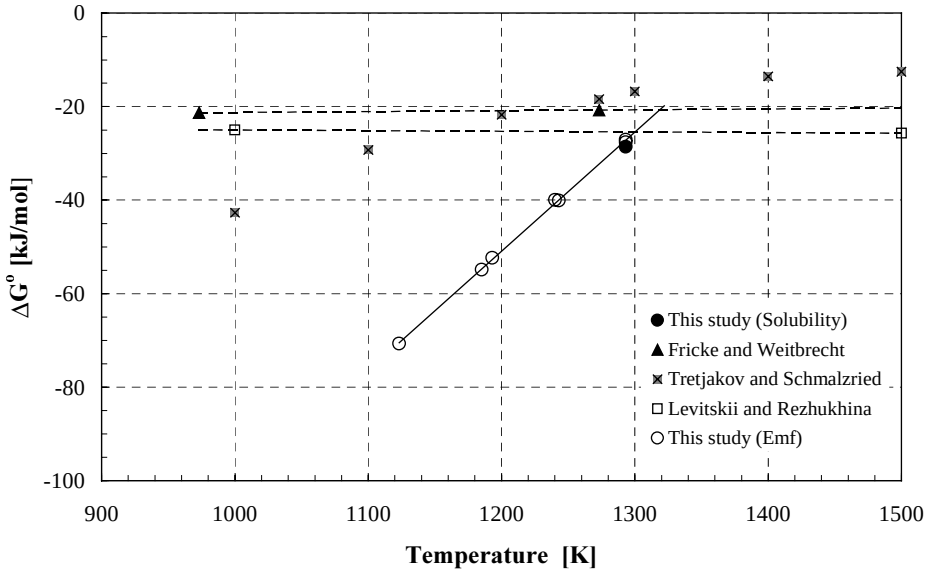

Figure 4-8: Gibbs energy of formation for $NiAl_2O_{4(s)}$ as a function of temperature for the reaction $NiO_{(s)} + Al_2O_{3(\alpha,s)} = NiAl_2O_{4(s)}$.

The Gibbs energy of formation for $NiAl_2O_4$ given for reaction [4-38] can be expressed as:

$$\Delta G_f^o = -356.774(\pm 3.546) + 0.255(\pm 0.003)\cdot T \quad kJ/mol \quad (T = 1123 - 1293K) \quad [4\text{-}40]$$

As a validation test for the emf measurements, one can calculate the entropy for the formation reaction of the metal, M, aluminate,

$$MO + Al_2O_3 = MAl_2O_4 \quad [4\text{-}41]$$

This entropy should be small in solids with perfect lattices where the only source of entropy is the atomic vibration. In reactions such as given in [4-41] there is not much change in the bonding, and hence not much change in the vibration frequencies. There can be a contribution to the entropy if the lattice is not perfect, which can happen for some spinels, but even then it is not likely to be much bigger than $-R\cdot\ln(2) \approx -6$ J/K·mol (27)[5]. This criterion was obtained for $FeAl_2O_4$ in Chapter 5.

Leviskii and Rezhukina (23) obtained an entropy of only –1.4 J/K·mol, while Fricke and Weitbrecht (19) obtained 1.8 J/K·mol. However, according to the present results given by [4-40] the entropy is –255 J/K·mol, which seems to be far too much. Contact problems occurred between the Mo rod and the aluminium pad in the crucible after a few hours of experiment, and only the first emf values recorded, *i.e.* at 1020 °C, seem to be reliable. An aluminium electrode as shown in Figure 6-18 and 6-20 in Chapter 6.7 would probably have been more reliable.

According to the results shown in Figure 4-8, the Gibbs energy of formation obtained by the solubility measurements is consistent with the present emf measurements at 1020 °C, and one might, therefore, suspect that the values reported in the literature (represented by the dotted lines in Figure 2-3, p. 24) are not correct. The revised value for the Gibbs energy of formation at 1293 K gives an alumina activity defining the stability line between NiO and $NiAl_2O_4$, which is lower than the one obtained from the thermodynamic data (29), and as a consequence the stability region for $NiAl_2O_4$ becomes larger.

From the present results, the activity coefficient of NiF_2 can be calculated. With data from Barin (6), the equilibrium constant for reaction [4-13] at 1293 K is $5.285 \times 10^{-4.}$ By choosing a reference concentration of alumina in solution to be only 0.5 weight percent, the impact on the activity of NaF and AlF_3 compared to pure cryolite can be neglected. The slope for the low alumina activities region in Figure 4-3 (*i.e.* equation [4-11]) then gives a concentration of Ni in solution of 0.332 weight percent, which correspond to a molar fraction of 0.0030 (based on NaF, AlF_3 and NiF_2 as constituents). The activity coefficient (γ) of NiF_2 is then calculated to be

$$\gamma_{NiF_{2(s)}} = 1.6 \pm 0.1 \qquad [4\text{-}42]$$

The limits of error of the activity coefficient are based on the uncertainty of the calculation of the Ni(II) content given by equation [4-11].

4.7 Analysis of crystals in cooled bath samples containing nickel

After the melt sample had been withdrawn from the solution, the furnace was turned off to cool. After cooling, the lump of bath was removed from the platinum crucible.

[5] "$-R\cdot\ln(2)$" is the ordinance contribution to the entropy, assuming ΔS^o among solids should be zero, which is a consequence of the Latimer formulae (28) if the entropy values of all the substances that occurred in a chemical reaction were additive.

The colour of the different bath samples varied with the alumina concentration. The colour of some of the samples with no additional alumina were chocolate brown, the samples with 1-1,5 wt% alumina addition were beige, the 2 wt % samples were light blue, while the 4 wt% samples were almost turquoise. The samples with more than 4 wt % alumina added gradually became less green, which is reasonable since the solubility of nickel oxide decreases with increasing solubility of alumina.

The changing colour indicates that the nature of the nickel-containing species present in the solid phase changes with the alumina concentration. Therefore, crystals in three of the solidified melts from the crucible were analysed with a wavelength dispersive analyser[6] and X-ray mapping for the elements aluminium, nickel, iron and oxygen. The samples were cryolite with 1.13, 4.3 and 5.3 wt% alumina, respectively. All the samples were saturated with nickel- containing species (*i.e*. oxide or aluminate).

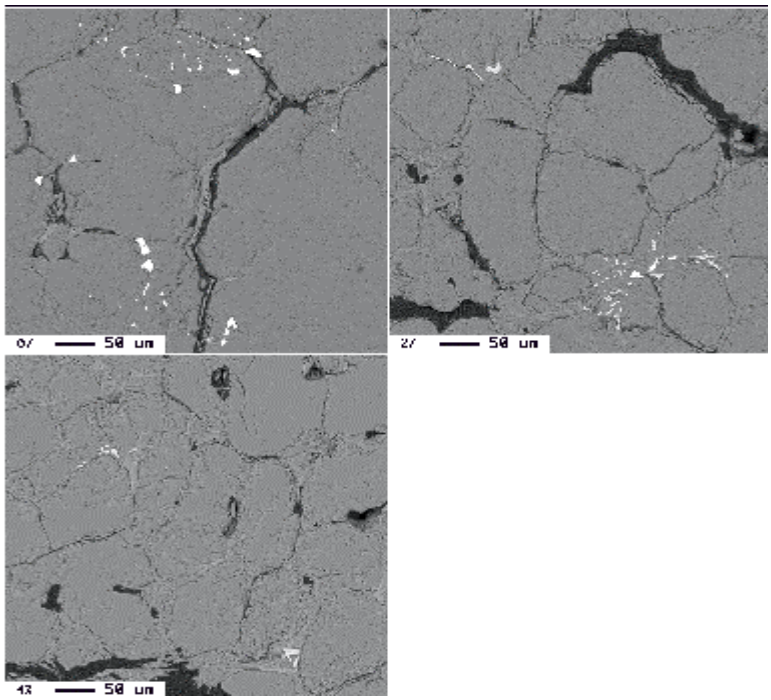

Figure 4-9: Stage scans of the three bath samples. The white spots indicate nickel-containing species.

The content of nickel-containing crystals decreased with increasing alumina content, which is expected according to the solubility measurements. For all the samples analysed, the nickel-containing crystals were typically 10-20 μm in size.

[6] Electron microscope JEOL EPMA JXA-8900R (the WDS/EDS system) designed for non-destructive x-ray microanalysis and imaging of solid materials. The analytical sensitivity ranges from a few parts per million for optimum cases, to a typical detection limit of several hundred ppm. The volume sampled is typical a few cubic microns, corresponding to a weight of a few picograms.

Analyses of 3 crystals in each sample gave the following weight percentages of the chosen oxides of nickel, iron, sodium, aluminium and silicon:

Table 4-2: Analyses of nickel-containing crystals in cryolite samples with different alumina contents calculated as oxides.

	Weight percent						
Sample	**F**	**NiO**	**Fe_2O_3**	**Na_2O**	**Al_2O_3**	**SiO_2**	**Total**
1.1 wt% alumina	0,14	33,41	46,99	0,40	3,34	2,60	86,81
4,3 wt% alumina	0,27	39,66	2,07	0,23	49,67	0,43	92,22
5,3 wt% alumina	0,39	32,22	1,86	0,34	59,51	0,33	94,49
Matrix	32,78	0,01	0,02	47,84	17,40	0,04	98,08

Be aware of the fact that fluorine and sodium "clutter up" the calculated totals given in Table 4-2. The numbers in the table are, therefore, not exact because there is a mixture of oxide and fluoride present in these samples. The concentration of Al_2O_3 in sample 1 is, nevertheless much less than in the other two samples.

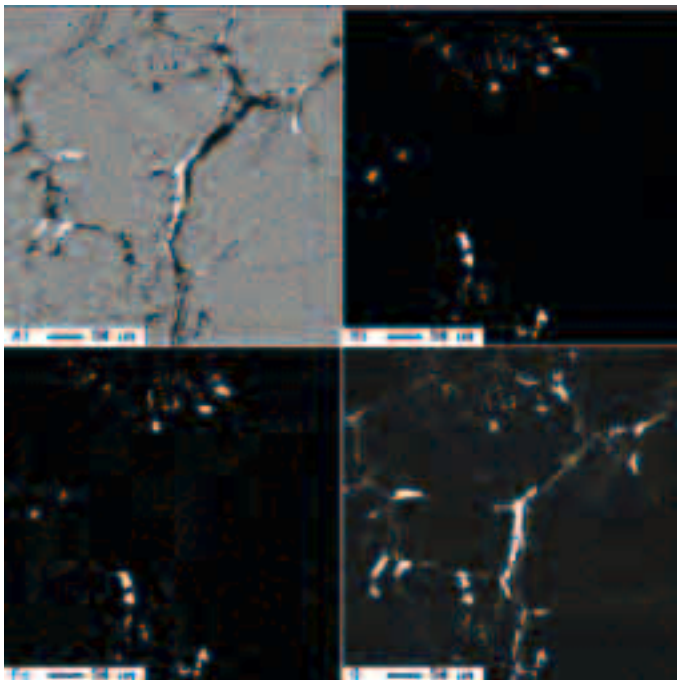

Figure 4-10:Analyses of the elements Al, Ni, Fe and O for the sample with 1.13 wt% alumina.

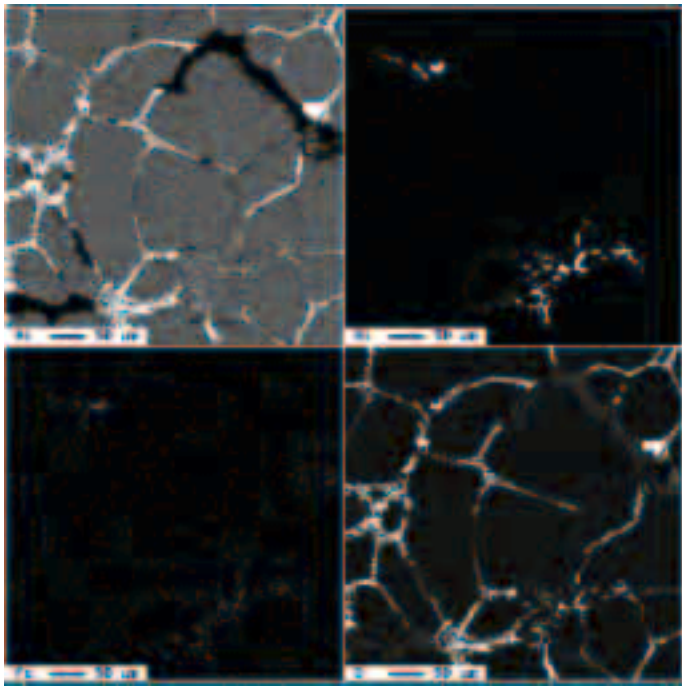

Figure 4-11: Analyses of the elements Al, Ni, Fe and O for the sample with 4.32 wt% alumina.

The results shown in Table 4-2 for crystals in Figures 4-9 to 4-11 indicate that the content of nickel in the crystals is rather constant, while the content of aluminium is increasing with increasing alumina content in the sample. The content of iron is surprisingly high for the sample with 1.13 weight % alumina (Figure 4-10), and it may indicate that this solution was contaminated with iron. Some experiments with iron-containing species were run in the furnace a few days before this experiment was conducted, and they could have contaminated the furnace lining with iron. The iron probably caused the brown colour. The furnace, described by Hovland (31), was then cleaned and the furnace tube was replaced.

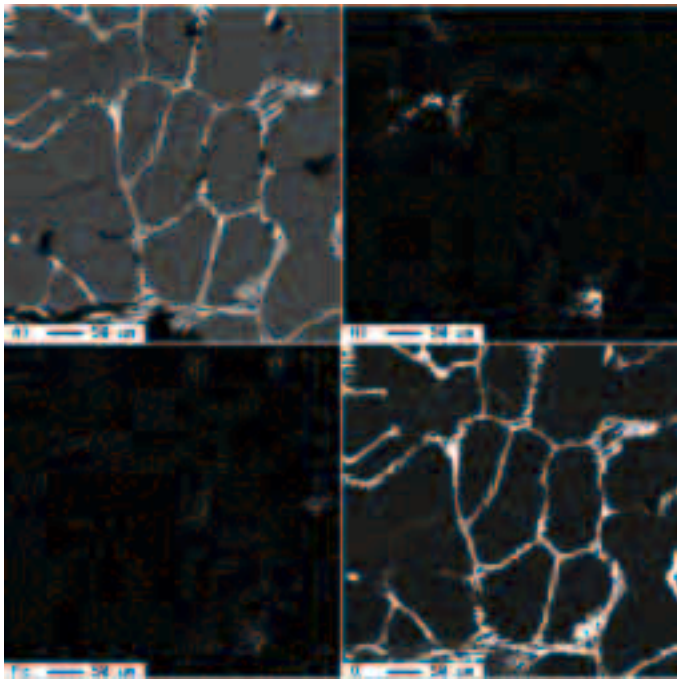

Figure 4-12: Analyses of the elements Al, Ni, Fe and O for the sample with 5.3 wt% alumina.

The X-ray mapping for 1.13 wt% alumina shown in Figure 4-10 indicates that nickel is mainly present as NiO. There are, however, some small crystals with nickel and aluminium. This phase is probably $NiAl_2O_4$. The amount of $NiAl_2O_4$ had increased relative to NiO in the sample with 4.32 wt% alumina (Figure 4-11), and in the sample with 5.3 wt% alumina (Figure 4-12) the NiO phase has disappeared completely. These results indicate that NiO is present in cryolite at low contents of alumina and the phase transition between NiO and $NiAl_2O_4$ occurs between 1.13 and 4.32 wt% alumina. This is in general agreement with the phase change between NiO and $NiAl_2O_4$ calculated to occur around 3 wt% alumina.

Most of the iron in the sample with 1.13 wt% alumina occurs together with nickel, indicating the presence of $NiFe_2O_4$ crystals. The apparent NiO/Fe_2O_3 ratio is 0.71 in these crystals.

One cooled sample with 3wt% alumina added was analysed with a mineralogical diftractometer (XRD) for the following species: burisenite (NiO), trevorite ($NiFe_2O_4$), nickel aluminate ($NiAl_2O_4$) and nickel fluoride (NiF_2). The sample with 3 wt% alumina contained nickel aluminate and probably nickel oxide. It might contain some $NiFe_2O_4$, but it was not possible to identify the phases Ni_2O_3, $Ni_2Al_{18}O_{29}$, $NiAl_{32}O_{49}$, $NiAl_{26}O_{40}$, nor NiF_2.

4.8 The effect of temperature on the solubility of NiO in the Na_3AlF_6-$Al_2O_{3(sat)}$-O_2 system

The Na_3AlF_6-Al_2O_3 (saturated) system was chosen to study the effect of temperature, being varied from 980 to 1040 ^oC. The alumina saturation in various melts was calculated by using the equation reported by Solheim *et al.* (15). The numerical results, which are presented in appendix B, show that the solubility of NiO and $NiAl_2O_4$ in the Na_3AlF_6-Al_2O_3 system increases with increasing temperature. This is similar to the results obtained for zinc oxide/aluminate (8), SnO_2 (3), (33) in cryolite-alumina melts

The partial enthalpy of dissolution of $NiAl_2O_4$ in the melt,

$$NiAl_2O_{4,solid} = NiAl_2O_{4,dissolved} \qquad [4\text{-}43]$$

can be obtained from the solubility data.

At saturation one has:

$$\Delta G^o = -RT \cdot \ln\left[\frac{"a_{NiAl_2O_{4,diss}}"}{a_{NiAl_2O_{4(s)}}}\right] \qquad [4\text{-}44]$$

where T is the temperature (K), R is the gas constant, *"* $NiAl_2O_{4,diss}$ *"* represents the dissolved nickel species and $a_{NiAl_2O_4(s)}$ is the activity of solid $NiAl_2O_4$ (equal to unity).

Since the solubility is relatively low, one can assume Henrian behaviour, where the activity of the dissociated nickel species ($NiAl_2O_{4,diss}$) can be expressed as

$$a_{NiAl_2O_4} = \gamma_{NiAl_2O_4} \cdot x_{NiAl_2O_4} \qquad [4\text{-}45]$$

where $\gamma_{NiAl_2O_4}$ is constant.

At saturation $a_{NiAl_2O_4} = \gamma_{NiAl_2O_4} \cdot x_{NiAl_2O_4} = 1$, and one gets:

$$\gamma^o_{NiAl_2O_4} = \left[\frac{1}{x^{sat}_{NiAl_2O_4}}\right] \qquad [4\text{-}46]$$

By combining equations [4-44] and [4-45] one gets,

$$-\left[\frac{\Delta G^{o}}{T}\right] = R \cdot \ln("a_{NiAl_2O_4(diss)}") = R \cdot \ln("x_{NiAl_2O_4(diss)}") + R \cdot \ln \gamma_{NiAl_2O_4} \qquad [4\text{-}47]$$

By introducing the Gibbs-Helmholtz equation:

$$\left[\frac{\partial\ (\frac{-\Delta G^{o}}{T})}{\partial\ (\frac{1}{T})}\right] = -\Delta\overline{H}^{o}_{NiAl_2O_4} \qquad [4\text{-}48]$$

one gets:

$$\left[\frac{\partial(\ln x_{NiAl_2O_4})}{\partial(\frac{1}{T})}\right] = -\left[\frac{\Delta\overline{H}^{o}_{NiAl_2O_4}}{R}\right] \qquad [4\text{-}49]$$

According to equation [4-49] $\ln(x_i^{sat})$, or ln(wt%), should vary linearly with (1/T), provided that the assumption of Henrian behaviour holds and $\Delta\overline{H}^{o}_{NiAl_2O_4}$ is constant in the temperature range used.

Figure 4-13 shows the solubility of $NiAl_2O_4$ plotted as $\ln(x_{NiAl_2O_4})$ versus 1/T. As we see, the correlation is quite good in the temperature range examined.

The least square equation for the solubility measurements is,

$$\ln(\text{wt \% Ni}) = -\ \frac{29854\ (\pm 4.851)}{T} + 18.17\ (\pm 3.79) \qquad (T = K) \qquad [4\text{-}50]$$

The partial molar enthalpy of dissolution of the oxide, $\Delta\overline{H}^{o}_{NiAl_2O_4}$, was then calculated by multiplying the slope of the line with "–R", *i.e.*,

$$\Delta\overline{H}^{o}_{NiAl_2O_4} = 248.2\ (\pm 40.3)\ \text{kJ/mol} \qquad [4\text{-}51]$$

Incidentally, it is actually the *apparent* partial molar enthalpy because the composition of the solvent is not constant, *i.e.* the saturation concentration of alumina is changing with temperature.

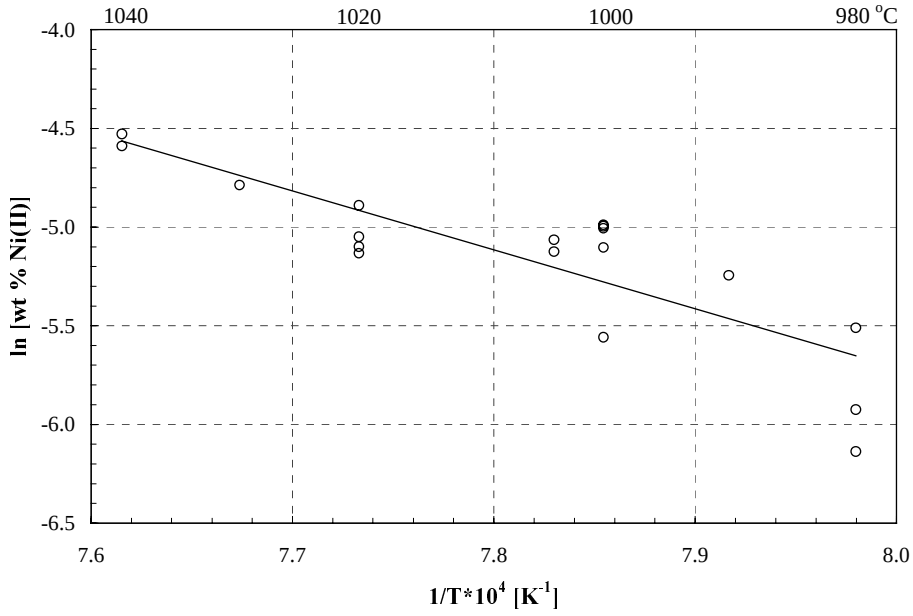

Figure 4-13: The logarithm of the saturation concentration of dissolved $NiAl_2O_4$, expressed as wt% Ni(II), as a function of the reciprocal temperature (980-1040 °C) in the Na_3AlF_6-$Al_2O_{3(sat)}$ system.

DeYoung (2) has reported the partial molar enthalpy of dissolution of NiO to be 186.6 kJ/mol, which is quite different compared to the present result. DeYoung did, however, use data for all the alumina compositions he examined. This approach is not correct according to the proposed model, which requires constant alumina activities. Furthermore, the solid phase is $NiAl_2O_4$, and not NiO, in alumina-saturated melts, so the activity of the Ni-species changes with temperature as well. DeYoung also ran the experiments for 80–100 hours, and was only bubbling air periodically through the melt for stirring. The long duration of the experiments may have caused the composition of his melts to change (7) during the experiments, even though he reported the maximum change in molar ratio (CR) to be only 0.1.

Chin (34) and Chin *et al.* (35) have reported the nickel solubility from a nickel ferrite cermet[7] to be 0.020 ± 0.003 wt% Ni(II) in alumina-saturated melts at 980 °C. Their result is ~10 times higher than the present results, and this large discrepancy is not possible to explain. Chin also reports the solubility of nickel oxide under the same conditions, but in the presence of an unpolarised aluminium pad, to be ~0.004 ± 0.002 percent. This result is more consistent with the present.

Zaikov (36) measured the solubility of nickel oxide electrodes doped with lithium oxide in alumina-saturated cryolite to be 0.003 wt % Ni(II) at 1000 °C, which is consistent with the present results.

[7] 42.9 weight percent NiO, 40.1 percent Fe_2O_3 and 17 percent copper.

Horinouchi *et al*. (37) reported the solubility of Ni(II) in cryolite with 10 percent alumina to be 0.14 wt% at 1000 ^{o}C, which is surprisingly high.

Some of the preliminary experiments in the present work were run at a high temperature, before the temperature was lowered 40 to 60 degrees and another experiment was started. When lowering the temperature of a saturated melt from an elevated to a lower temperature, small green crystals along the wall of the crucible appeared after a few hours. In one particular case, 3-4 millimetre long leaf-shaped crystals were formed. Even if they looked like green NiO crystals, XRD[8] showed that the crystals were α-alumina contaminated with nickel. Growing nickel-containing crystals in the melt by reducing the temperature may be a method to remove nickel from industrial melts in the future.

4.9 Solubility of NiO in the NaF-AlF_3-$Al_2O_{3(sat)}$-O_2 system at 1020 ^{o}C

Melts with various NaF-AlF_3 compositions were prepared by mixing natural cryolite with excess AlF_3 or NaF. The amount of alumina added prior to the experiments was based on alumina saturation limits for basic melts, as measured by Diep (4) for the system NaF-AlF_3-Al_2O_3, and for acidic melts the equation given by Solheim *et al*. (15) was used. To make sure that the melts were completely saturated, approximately 25 % excess alumina was added, and an alumina stirrer and alumina casing for the thermocouple were used for *acidic* baths (CR $\leq$ 3.0), only. α-Al_2O_3 is not stable in basic baths, and it causes the sintered alumina[9] materials to deform, crack and swell. Consequently platinum shielding around the thermocouple and a platinum stirrer had to be used in those melts.

The solubility of $NiAl_2O_4$ was determined as a function of the melt composition at 1020 ^{o}C in NaF-AlF_3-$Al_2O_{3(sat)}$ melts. The results are plotted in Figure 4-14. The numerical data are given in appendix B.

Figure 4-14 seems to indicate that there is a maximum solubility between CR = 6 and 8. However, due to the limited number of experimental points in this range, this conclusion is rather uncertain. This is in contradiction to what is reported for Fe(III) (4) and Sn(IV) (3), where a maximum was found at CR = 3, and it indicates that there are other types of complexes present in these melts.

[8] X-ray difractometry

[9] Sintered alumina is a common material to use for experiments with cryolite at high temperatures.

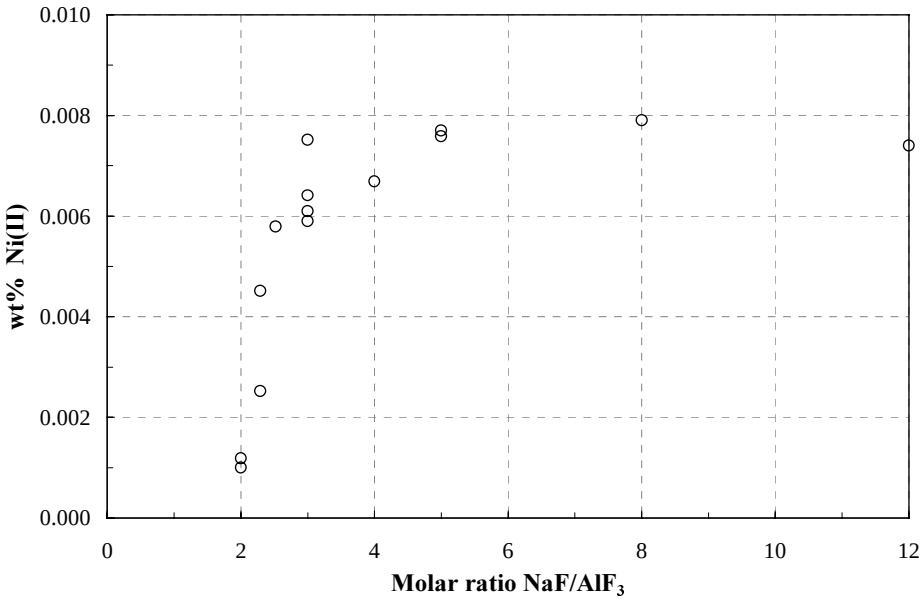

Figure 4-14: The solubility of nickel in alumina-saturated melts as a function of CR at 1020 °C and in an atmosphere of oxygen.

From the solubilities measured as a function of the alumina activity, it was concluded that NiF_2 complexes are formed in the melt. The nickel complexes may have a number of "NaF's" attached, which in general can be expressed as,

$$NiAl_2O_{4(s)} + \frac{2}{3}AlF_{3(l)} + x \cdot NaF_{(l)} = Na_xNiF_{(2+x)(l)} + \frac{4}{3}Al_2O_{3(l)} \qquad [4\text{-}52]$$

The equilibrium constant for equation [4-52], *i.e.* K_x, can be expressed as,

$$K_x = \left(\frac{a_{Na_xNiF_{(2+x)}} \cdot a_{Al_2O_3}^{4/3}}{a_{AlF_3}^{2/3} \cdot a_{NaF}^{x}} \right) \qquad [4\text{-}53]$$

By expressing equation [4-53] in a logarithmic form, one gets,

$$\log(a_{Na_xNiF_{(2+x)}}) + \frac{4}{3}\log(a_{Al_2O_3}) - \frac{2}{3}\log(a_{AlF_3}) = x \cdot \log(a_{NaF}) + \text{const.} \qquad [4\text{-}54]$$

If is assumed that the solute species have a constant activity coefficients, so that the activities can be replaced by the concentration, then one anticipates that a plot of the function,

$$\log(\text{wt\% Ni}) + \frac{4}{3}\log(a_{Al_2O_3}) - \frac{2}{3}\log(a_{AlF_3}) = x \cdot \log(a_{NaF}) + \text{const.} \qquad [4\text{-}55]$$

or an analogous function based on [4-54], which should give a straight line with a slope of "x".

In acidic melts saturated with alumina, the activity of α-alumina is 1. Since β-Al_2O_3 ($Na_2O \cdot 11Al_2O_3$) is formed in basic melts (38),(39), the following reaction has to be taken into account when calculating the alumina activity in basic melts,

$$6NaF + 34Al_2O_3 = 2AlF_3 + 3[Na_2O \cdot 11Al_2O_3] \qquad [4\text{-}56]$$

The equilibrium constant for equation [5-56] is,

$$K = \left(\frac{a_{\beta}^{3}}{a_{\alpha}^{34}}\right) \cdot \left(\frac{a_{AlF_3}^{2}}{a_{NaF}^{6}}\right) \qquad [4\text{-}57]$$

where a_α= the activity of α-Al_2O_3 and a_β= the activity of $Na_2O \cdot 11Al_2O_3$.

Rearrangement of equation [5-57] gives the activity of α-Al_2O_3 expressed as,

$$a_{\alpha} = \left(\frac{a_{AlF_3}^{2}}{K \cdot a_{NaF}^{6}}\right)^{1/34} \qquad [4\text{-}58]$$

for basic melts (CR > 3.7) where $a_\beta = 1$ (30).

The CR at which α-Al_2O_3 is converted to β-Al_2O_3 as the CR is raised is close to 3.7 (30), so at that point the equilibrium constant K simply becomes,

$$K = \left(\frac{a_{AlF_3}^{2}}{a_{NaF}^{6}}\right) \qquad [4\text{-}59]$$

Using activities reported by Sterten *et al.* for alumina-saturated melts (30), (40), at 1020 ^oC and CR = 3.7, one gets $K = 2.05*10^{-7}$, which was used in the calculations for the alpha alumina activities in basic melts.

With the use of the molar fraction of the nickel solubilities obtained in the present work, and the activity data for AlF_3 and NaF in alumina–saturated melts given by Sterten *et al.* (40), (41), the left-hand side of equation [4-55] was plotted against the logarithm of the sodium activity, as shown in Figure 4-15.

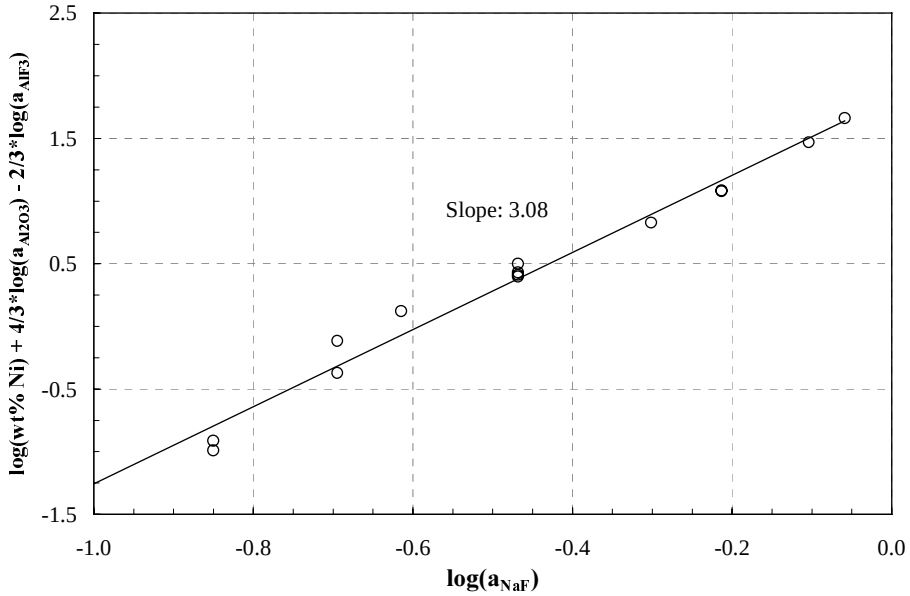

Figure 4-15: (log(wt% Ni) + 4/3*log($a_{Al_2O_3}$) – 2/3*log(a_{AlF_3})) *versus* log(a_{NaF}) in alumina-saturated cryolite melts at 1020 ^{o}C in an atmosphere of oxygen.

Within the limits of error the slope of the curve in Figure 4-15 is close to 3, which means that the most plausible reaction mechanism is,

$$NiAl_2O_4 + \frac{2}{3}AlF_3 + 3NaF \rightarrow Na_3NiF_5 + \frac{4}{3}Al_2O_3 \qquad [4\text{-}60]$$

Another method can also be applied to model the most plausible species present in the melts. By rearranging equation [4-53] one can express the relative activity of the species $Na_xNiF_{(2+x)}$ as "$a_{Na_xNiF_{(2+x)}}$" :

$$a_{Na_xNiF_{(2+x)}} = K_x \cdot \left(\frac{a_{Al_2O_3}^{4/3}}{a_{AlF_3}^{2/3} \cdot a_{NaF}^{x}} \right)^{-1} \qquad [4\text{-}61]$$

One can then model the different species by testing different "x" values in equation [4-61], changing the corresponding equilibrium constant K_x by trial and error until the best fit of the solubility measurements, expressed as "wt% Ni", is obtained. Species with "x" values from 0 to 4 were modelled, and the result is shown in Figure 4-16. The best fit was obtained for x = 3, *i.e.* Na_3NiF_5, with K_3 = 59.

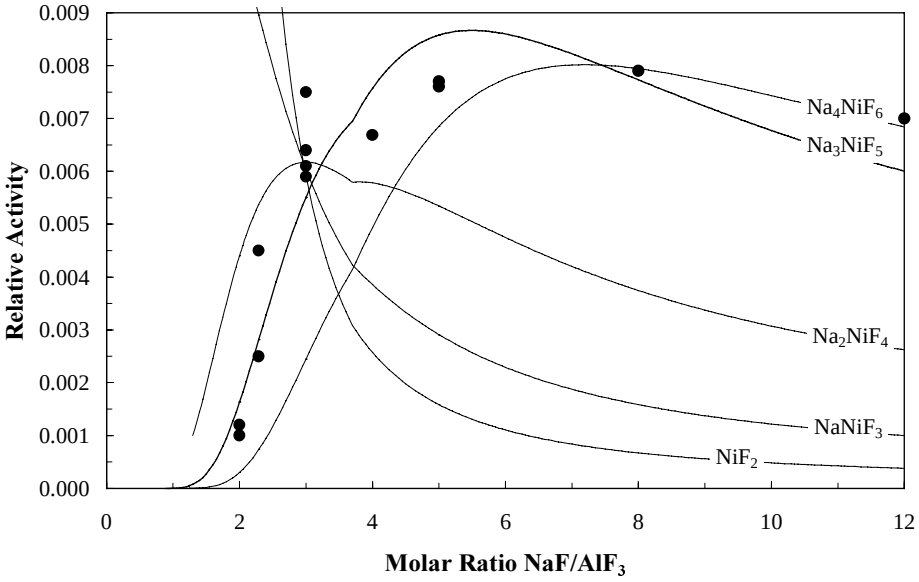

Figure 4-16: Model fitting of $Na_xNiF_{(2+x)}$ for various values of x in alumina-saturated cryolite melts as a function of the molar ratio at 1020 ^oC in an atmosphere of oxygen.

Both methods yield the same conclusion. Na_3NiF_5 seems to be the most probable nickel-containing complex formed in alumina-saturated cryolite melts.

According to Bailer *et al.* (42) there are no simple nickel halides in oxidation states 3 and 4, and it is unique amongst the first-row transition elements in forming simple halides in one oxidation state only (*i.e.* 2). NiF_2 has a tetragonal rutile structure (42), and the co-ordination compounds are exceedingly numerous.

4.10 References

(1) Hatch, J.E., *Aluminium*, *Properties and Physical Metallurgy*, American Society for Metals, 3rd ed, Metals Park, Ohio, USA,1988.

(2) DeYoung, D.H., *Solubilities of Oxides for Inert Anodes in Cryolite-Based Melts*, TMS, Light Metals 1986, pp 299-303, 1986.

(3) Xiao, H., *On the Corrosion and the Behavour of Inert Anodes in Aluminium Electrolysis,* doktoringeniøravhandling (Ph.D. thesis), no. 84, NTH, 1984.

(4) Diep, Q.B., *Structure and thermodynamics of cryolite-based melts with addition of Al_2O_3 and Fe_2O_3. Cyclic voltammetry study of Fe_2O_3 in molten cryolite,* Doktoringeniøravhandling (Ph.D. thesis) no 28, NTNU, Trondheim, Norway, 1998.

(5) Christian, G.D. and O'Reilly, J.E., *Instrumental Analysis,* chap. 11, pp 322-355, 2nd ed., Allyn and Bacon, Inc., Massachusetts, ISBN 0-205-08685-3, 1986.

(6) Barin,I., *Thermodynamical Data of Pure Substances*, 3rd ed., VCH Verlags-gesellschaft mb-H, D-69451, Weinheim, Germany, 1995.

(7) Sterten, Å. and Skar,O., *Some Binary Na_3AlF_6-M_xO_y phase diagrams*, Aluminium 64, pp1051- 1054, 1988.

(8) Dewing, E.W. and Thonstad, J., *Activities in the System Cryolite-Alumina*, Metallurgical and Materials Transactions B, Vol. 28 B, pp 1089-1093, Des. 1997.

(9) Belov, S.F and Gladneva, A.F., *Solubility of oxides in molten fluorides*, Sov. Non-Ferrous Met. Res., pp. 480-482, 1981.

(10) Grjotheim, K., Krohn, C., Malinovský, M., Matiašovský, K. and Thonstad, J., *Aluminium Electrolysis. Fundamentals of the Hall-Heroult Process*, 2nd ed., ISBN 3-87017-155-3, p. 365, 1982.

(11) Rolin, M. and Bernard, M., Bull. Soc. Chim., France pp. 1035, 1963.

(12) Solheim, A. and Sterten, Å., *Activity of alumina in the system NaF-AlF_3-Al_2O_3 at NaF/AlF_3 molar ratios ranging from 1.4 to 3*, TMS, Light Metals 1999, pp. 445-452, 1999.

(13) Solheim, A. and Sterten, Å., *Activity Data for the System NaF-AlF_3*, Ninth International Symposium on Light Metals Production, Tromsø-Trondheim, Norway, Aug. 18.–21., pp. 225-234, 1997.

(14) Solheim, A., Rolseth, S., Skybakmoen, E., Støen, L., Sterten, Å. and Støre, T., *Liquidus Temperatures for Primary Crystallization of Cryolite in Molten Salt Systems of interest for the Aluminium Electrolysis*, Met. Trans. B, *27*B, pp. 739, 1996.

(15) Solheim, A., Rolseth, S., Skybakmoen, E., Støen, L., Sterten, Å. and Støre, T., *Liquidus Temperatures and Alumina Solubility in the System Na_3AlF_6-AlF_3-LiF-CaF_2-MgF_2*, Light Metals 1995, pp. 451, 1995.

(16) Holm, J.L., *Thermodynamic Properties of Molten Cryolite and Other Fluoride Mixtures*, Thesis, Institutt for Uorganisk Kjemi, NTH, 1971.

(17) Levin, E.M. and McMurdie, H.F., *Phase Diagrams for Ceramists*, Diagram No. 2323, American Ceramic Soc. Inc., Supplement, pp. 90, 1975.

(18) Montgomery, D.C. and Peck, E.A., *Introduction to linear regression*, ISBN 0-471-05850-5, John Wiley and Sons, chap. 5.2.2, 1982.

(19) Fricke, Von R. and Weitbrecht, G., *Die Gleichgewichte CO_2/CO gegen Ni/NiO, bzw. Ni + γ-Al_2O_3/$NiAl_2O_4$ und ihre beeinflussung durch den physicalischen zustand der festen reactionsteilnehmer*, Z. Elechtrochemie, Bd. 48, no. 2, pp. 87-105, 1942.

URN:NBN:no-6347

(20) Levin, E.M. and McMurdie, H.F., *Phase Diagrams for Ceramists*, Diagram No. 4344, American Ceramic Soc. Inc., Supplement, pp. 120, 1975.

(21) JANAF, *Thermochemical Tables*, 3rd ed., National Bureau of Standards, Washington D.C., 1985.

(22) Tretjakov, Von J.D. and Schmalzried, H., *Zur Thermodynamik von Spinellphasen*, Berichte der Bunsengesellschaft, vol. 69, pp. 369-402, 1965.

(23) Levitskii,V.A. and Rezukhina, T.N., *Thermodynamic properties of cobalt and nickel aluminates from EMF data at increased temperatures*, Inorganic Materials, vol. 2, pp. 122-126, 1966.

(24) Navrotsky, A. and Kleppa, O.J., *Thermodynamics of formation of simple spinels,* J. Inorg. Nucl. Chem., vol. 30, pp. 479-498, 1968.

(25) Dewing, E.W., *Thermodynamics of the System LiF-AlF_3*, J. Electrochem. Soc., Electrochem. Sci. and Tech., vol 123, no. 9, pp. 1289-1294, Sept., 1976.

(26) Holmes, R.D., O'Neill, H.St.C. and Arculus, R.J., *Standard Gibbs energy of formation for Cu_2O, NiO, CoO and Fe_xO: High resolution electrochemical Measurements using zirconia solid electrolytes from 900-1400 K*, Geochimica et Cosmochimica Acta, Pergamon, vol. 30, pp. 2439-2452, 1986.

(27) Dewing, E.W., 648 Pimlico Place, Kingston ON K7M 5T8, Canada, personal communication, Oct. 2000.

(28) Østvold, T. and Øye, H.A., *Applied Chemical Thermodynamics, vol. 1*, Compendium, Dept. of Inorganic Chemistry, NTH, Trondheim, Sept. 1979.

(29) Knacke, O., Kubaschewski, O. and Hesselmann, K., *Thermochemical Properties of Inorganic Substances*, 2nd ed., Springer-Verlag, Verlag Stahleisen, 1991.

(30) Sterten, Å. Hamberg, K. and Mæland, I., Activities *and Phase Diagram Data of NaF-AlF_3-Al_2O_3 Mixtures Derived From Electromotive Force and Cryoscopic Measurements. Standard Thermodynamical Data of β-Al_2O_3*, Acta Chem. Scand., A36, pp. 329-344, 1982.

(31) Hovland, R., *Testing av kobber-nikkelferritt cermet som inert anode ved elektrolytisk fremstilling av aluminium*, Department of Electrochemistry, hovedoppgave (Graduation thesis), NTH, Norway, 1990.

(32) Dewing, E.W., Rolseth, S., Støen, L. and Thonstad, J., *The Solubility of ZnO and ZnAl2O4 in Cryolite Melts*, Metall Mater Trans. B., vol 28B, pp. 1099–1101, Dec. 1997.

(33) Xiao, H., Thonstad, J. and Rolseth, S., *The Solubility of SnO_2 in NaF-AlF_3-Al_2O_3 Melts,* Acta Chem. Scand., vol. 49, pp. 96–102, 1995.

(34) Chin, P.C.Y., *The Behavior of Impurity Species in Hall-Heroult Aluminium Cells*, Ph.D. thesis, Carnegie Mellon University, Pittsburgh, Pennsylvania, p. 26, Aug., 1992.

(35) Chin, P.C.Y., Sides, P.J. and Keller, R., *The Transfer of Nickel, Iron and Copper From Hall Cell Melts to Molten Aluminium,* Can. Metall. Quart., vol. 35, no. 1, pp. 61–68, 1996.

(36) Zaikov, Yuri, fax to Prof. Jomar Thonstad at Dep. of Electrochemistry, NTH, Norway, 10th Aug., 1994.

(37) Horinouchi, K., Tachikava, N. and Yamada, K., *DSA in Aluminum Reduction Cells*, Proceedings of the First International Symposium on Molten Salt Chemistry and Technology, Kyoto, Japan, April, pp. 20-22, 1983.

(38) Foster, P.A. Jr., *Phase Equilibria in the Sodium Fluoride Enriched Region of the Reciprocal System Na_6F_6-Al_2F_6-Na_6O_3-Al_2O_3*, J. Chem. Eng. Data, vol. 9, no. 2, pp. 200-203, April 1964.

(39) Holm, J.L., *Undersøkelser av endel systemer med tilknytning til aluminium-elektrolysen,* Tidsskr. Kjemi, Bergv. Met. , vol. 26, no. 10, pp. 165-171, S.T. no. 2447, Norway, 1966.

(40) Sterten, Å. and Mæland, I., *Thermodynamics of Molten Mixtures of Na_3AlF_6-Al_2O_3 and NaF-AlF_3*, Acta Chem. Scand., A39, pp. 241-257, 1985.

(41) Sterten, Å., Hamberg, K.and Mæland, I., Activities *and Phase Diagram Data of NaF-AlF_3-Al_2O_3 Mixtures Derived From Electromotive Force and Cryoscopic Measurements. Standard Thermodynamical Data of β-Al_2O_3*, Acta Chem. Scand., A36, pp. 329-344, 1982.

(42) Bailar, J.C., Emeléus, H.J., Nyholm, R. and Trotman-Dickenson, A.F., *Comprehensive Inorganic Chemistry*, Pergamon Press, Oxford, vol. 3b, ISBN 008-017275-x, 1973.

URN:NBN:no-6347

URN:NBN:no-6347

5 Solubility of iron oxides in cryolite-alumina melts

As pointed out in Chapter 4, an absolute requirement for the material of an *inert* anode to be used for the production of aluminium is that it should exhibit a low solubility in cryolite-based melts. Some of the most promising materials are based on metal oxides, and their operating characteristics depend on their dissolution rate.

When a nickel ferrite anode is used, iron dissolves from nickel ferrite ($NiFe_2O_4$) into the melt. During electrolysis, iron is reduced into the liquid aluminium metal, and it affects the physical and chemical properties of aluminium. The designation specifies the limit for iron in aluminium to be 0.20 weight percent (1).

5.1 Iron as an impurity in aluminium

Iron is the most common impurity found in aluminium products (2). It has a high solubility in molten aluminium and is therefore easily dissolved at all molten stages of production. The solubility of iron in the solid state is very low (~ 0.04 weight percent) and, therefore, most of the iron present in aluminium above this amount appears as an intermetallic second phase in combination with aluminium and often with other elements (for example silicon). Because of its limited solubility, it is used in electrical conductors in which it provides a slight increase in strength and better creep characteristics at moderately elevated temperatures. Aluminium has a natural affinity for iron and attacks and dissolves die-steel, a condition commonly referred to as soldering. Although small amounts of iron in aluminium may reduce soldering during die casting, its presence in aluminium-silicon casting alloys is generally undesirable because it forms coarse iron-rich phases that reduce ductility. An iron content of 1 weight percent or more is considered beneficial for die casting alloys to minimise die soldering.

Iron reduces the grain size in wrought products. Alloys of iron and manganese near the ternary eutectic composition, such as alloy 8006, can have useful combinations of strength and ductility at room temperature and retain strength at elevated temperatures. These properties are due to the fine grain size that is stabilised by the finely dispersed iron-rich second phase. Iron is added to the aluminium-copper-nickel group of alloys to increase strength at elevated temperatures.

Iron forms constituents like $FeAl_3$ that are cathodic to the aluminium matrix. When these are present at the surface, the protective oxide film is thin or non-existent. The local cells produced by such impurities promote pitting attack (corrosion) (2) of the surface in a conductive liquid like seawater.

The iron content (2) in aluminium alloys is restricted to a maximum of 0.8 or 1.0 weight percent in most commercial sand and permanent mould casting alloys because higher contents impair feeding ability (f. ex. viscosity) and mechanical properties – especially

ductility. In the aluminium-magnesium alloys, iron limits in the range 0.25 to 0.5 weight percent are imposed to permit attainment of specified tensile properties. A maximum of 0.2 weight percent iron is stipulated for premium-strength aluminium-silicon-magnesium or aluminium-silicon-magnesium-copper alloys to allow attainment of the required ductility and toughness. Iron combines with other elements in the alloy to form insoluble embrittling constituents that act as severe stress risers, and therefore must be kept at an absolute minimum in applications requiring high ductility. Iron contents of approximately 1 weight percent or more minimise the tendency of aluminium die casting alloys to solder to the steel die. The ternary aluminium-iron-silicon eutectic exists at approximately 0.8 weight percent iron. With 1 weight percent or more iron in the alloy, there is no significant driving force for the molten alloy to further dissolve steel dies.

5.2 Solubility of FeO

Solubility data for Fe(II) in cryolite from the literature are scarce, and the need for accurate solubility data made it necessary to investigate the solubility of Fe(II) in the NaF-AlF_3-Al_2O_3-Fe-Ar system.

Measurements of the solubility of iron ions in cryolite melts are rather complicated, since both Fe(II) and Fe(III) are present. It was believed that if one works in an atmosphere of oxygen one should be able to measure the solubility of Fe_2O_3 without Fe(II) interfering, since the activity of FeO is as low as 0.002 (calculated from (3)). If, however, one works under reducing conditions, and uses an iron crucible, the activity of Fe_2O_3 in the presence of FeO is still 0.009 (3), which is not negligible. If, on the contrary, one assumes that the Fe(III) in solution exists as complexes containing only one Fe, then the square root of this activity, *i.e*. 0.09, is the relevant number.

In a graphite crucible FeO should be reduced to Fe and CO (4),

$$FeO + C = Fe + CO_{(g)} \qquad \Delta G^{0}_{1273.15K} = -43.1\ kJ/mol \qquad [5\text{-}1]$$

so that it is not feasible to use graphite as a container for FeO solubility measurements. Although solid solution between the two spinels $FeO{\cdot}Fe_2O_3$ and $FeO{\cdot}Al_2O_3$ might be possible, none has been found reported. To determine the solubility of Fe(III) one should therefore use Pt crucible and oxygen atmosphere, adding solid Fe_2O_3 to the melt. Such results have been obtained by Diep (5).

As Dewing and Thonstad pointed out (6), only experiments where the oxygen potential is controlled should be used, and by using an iron crucible and argon as the atmosphere one stabilises Fe(II). Calculations (6) showed that at alumina saturation in pure oxygen atmosphere, 6 % of the total iron is present as Fe(II), while in an iron crucible 0.1 % of the total amount of iron in solution is present as Fe(III). Using argon atmosphere and an iron crucible is therefore the best way to stabilise FeO.

According to thermodynamics (3),(4) it should be possible to get Fe(II) in solution by adding Fe_2O_3 to an Fe crucible, achieving a reduction to FeO or $FeAl_2O_4$:

$$Fe + Fe_2O_3 = 3FeO \quad [5\text{-}2]$$

with the following reaction with alumina:

$$FeO + Al_2O_3 = FeAl_2O_4 \quad [5\text{-}3]$$

Preliminary tests at SINTEF Materials Technology (not published) to determine the Fe(II) solubility in cryolite by using Fe_2O_3 in an iron crucible were, however, no success.

Analytically, it is not easy to distinguish between Fe(II) and Fe(III). ICP will not distinguish between them, and even the classical wet chemical methods will not give exact results for the low concentration of Fe ions one expects to have in cryolite. Problems with oxidation during sampling and analysis will also affect the results. The electrochemical *chronopotentiometric* method is, however, capable to measure solubilities for different species, and this method is explained in the following.

The galvanostatic method analogous to chronoamperometry is known as chronopotentiometry (7). In this type of experiment the current imposed on the cell is instantaneously stepped from zero to some finite value, *i.e.* the overall reaction rate is fixed, and the potential of the working electrode is then monitored as a function of time.

By applying a cathodic current to the working electrode, the electrochemical reaction that occurs is simply:

$$Me^{2+} + 2\,e^- \rightarrow Me \quad [5\text{-}4]$$

provided that there are metal ions present in the melt.

The system can be described by Sand's equation (7), (8):

$$/ i\tau^{1/2} / = nFD_o^{1/2}\pi^{1/2}c_o^{\infty} \quad [5\text{-}5]$$

where n = number of electrons involved in the overall electrode reaction, F = Faraday's constant, D = diffusion coefficient of the species investigated and c_o^{∞} = the bulk concentration of the species. At the time τ, called the *transition time*, the concentration of the species investigated at the electrode surface becomes equal to zero, and the potential of the working electrode varies rapidly towards more negative values until some new electrode process occurs (8). The product " $i\tau^{1/2}$ " is independent of the applied current density and proportional to the concentration of the species c_o^{∞} being reduced, *i.e.* Fe(II). By measuring the transition time τ for different concentrations of Fe(II) added to the solution, one can plot $I\tau^{1/2}$ as a function of c_o^{∞}. The product, $/i\cdot\tau^{1/2}/$, will then increase until it levels out when the solubility limit of the dissolved species has been reached. The concentration where the transition time levels out can be used as the solubility concentration. Co-workers Jentoftsen *et al*. (9) used this procedure to investigate the solubility of iron fluoride (FeF_2) in cryolite with varying amount of alumina. Their results will be discussed later.

5.3 Chemicals

Na_3AlF_6 *cryolite*	Handpicked Greenland cryolite, Kryolittselskabet
NaF	P.a. Merck, dried under argon atmosphere at 400 ^oC for 10 hours
AlF_3	Industrial grade, from Norzink, purified in the laboratory by sublimation and dried under argon atmosphere at 400 ^oC for 10 hours
LiF	P.a. Merck, >99 %
Al_2O_3 *alumina*	γ-Al_2O_3, P.a. Merck, dried at 200 ^oC.
FeF_2	Sigma Aldrich, >95 wt% (used for the alumina saturated melt experiments)
$Fe_{0.947}O$ *wüstite*	Iron powder and hematite (Fe_2O_3) heated at 1200 ^oC in argon for 28 hours
Fe	Sigma Aldrich, powder
Fe_2O_3 *hematite*	Sigma Aldrich, 99.5 %
$FeAl_2O_4$ *hercynite*	Mixed wüstite and Al_2O_3 to 1200 ^oC for 24 hours in argon
Ar	Argon 4, AGA, 99.99 %, ~200 ppm $O_{2(g)}$
O_2	AGA, 99.99 %
YSZ	Yttria-stabilised zirconia (ZrO_2-8%Y_2O_3), Frealit-Degussit FZY, 10/6 mm tube

FeF_2 is a rather expensive material, and it was decided to use wüstite ($Fe_{0.947}O$) for the experiments with low alumina contents which were expected to have a high solubility of Fe(II). Ferrous oxide is a non-stoichiometric compound known as wüstite, $Fe_{0.947}O$. Wüstite is thermodynamically stable at temperatures above 571^oC (10). Below this temperature wüstite should disproportionate into magnetite, Fe_3O_4, and iron (eutectoid reaction), but the rate of disproportionation decreases rapidly with decreasing temperature. At room temperature wüstite is stable for an unlimited period of time. In the following $Fe_{0.947}O$ is called FeO.

$Fe_{0.947}O$ was made by mixing and dry grinding Fe powder and hematite (Fe_2O_3) in a ball mill for 28 hours. The powder was then heated in an iron crucible in argon atmosphere for 48 hours at 1200^oC. To avoid disproportionation the mixture was quenched by quickly moving the crucible to a colder part of the furnace.

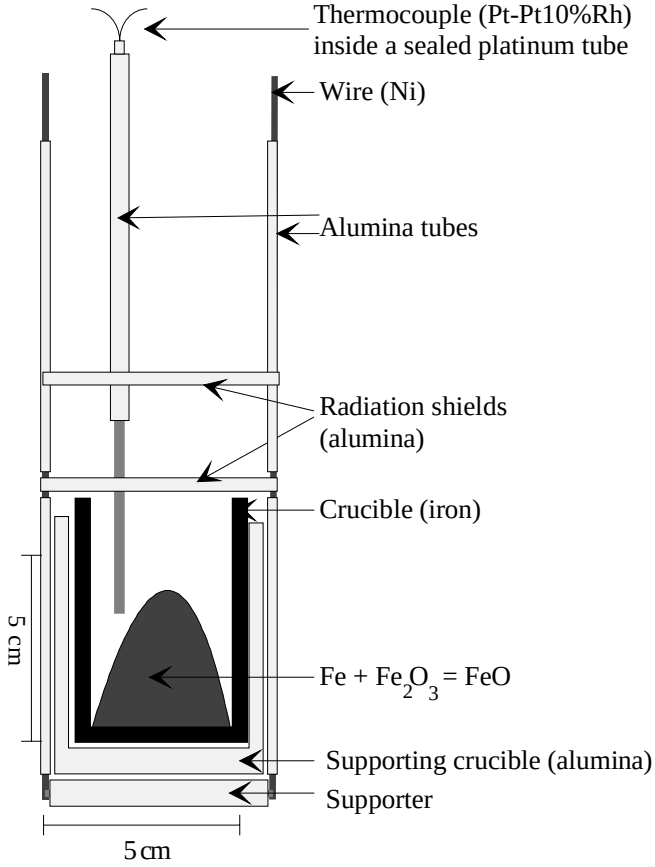

Figure 5-1: Schematics of the equipment used for preparing FeO.

The produced powder was properly ground and examined with XRD. A clear peak for FeO was found, and no peaks for Fe and Fe_2O_3.

Handpicked Greenland cryolite was used as the primary melt matrix. Synthetic cryolite melts made by NaF and sublimed AlF_3 were also used for some of the experiments with alumina-saturated melts.

5.4 Experimental procedure for measuring the solubility of FeO

All the solubility experiments with Fe(II) were run together with co-worker Trond Eirik Jentoftsen.

150 grams of electrolyte was prepared from handpicked Greenland cryolite and p.a. aluminia. A suitable amount of FeO or FeF_2 was also added to the Fe crucible before the crucible was heated.

A sealed furnace as described by Xiao (11) and Diep (5) was used with argon atmosphere. A sketch of the experimental set-up is shown in Figure 5-2. An iron crucible and argon was used to stabilise Fe(II) and to avoid the formation of Fe_2O_3 or Fe_3O_4 according to,

$$2FeO + \frac{1}{2}O_{2(g)} \rightarrow Fe_2O_3 \quad [5\text{-}6]$$

$$FeO + \frac{1}{6}O_{2(g)} \rightarrow \frac{1}{3}Fe_3O_4 \quad [5\text{-}7]$$

Figure 2-2, p. 23, illustrates where the different phases are stable as a function of the partial oxygen pressure and alumina activity.

The temperature was measured with a Pt-Pt10%Rh thermocouple inside a sealed platinum tube placed 2 cm from the bottom of the iron crucible.

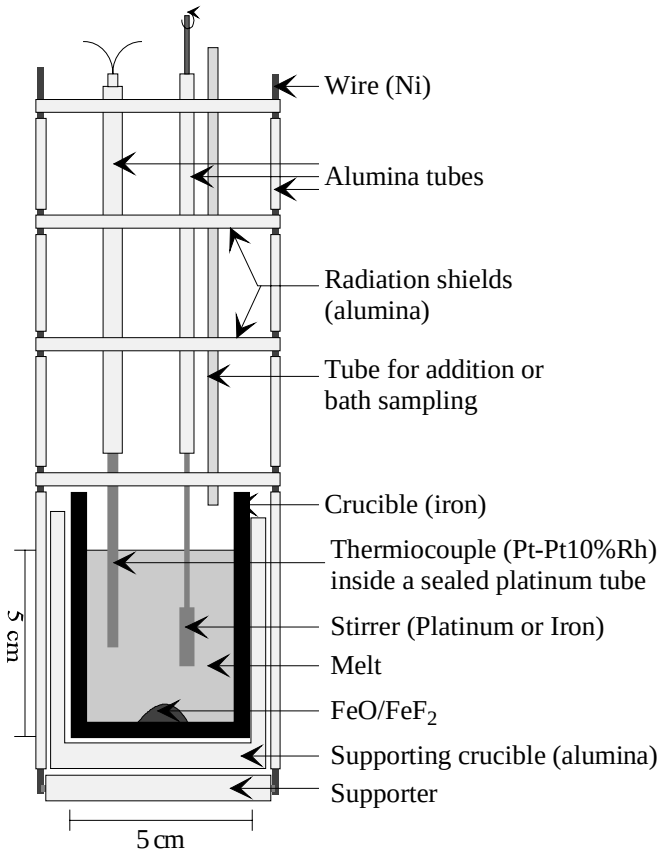

Figure 5-2: Sketch of the experimental set-up for the Fe(II) solubility measurements.

According to Sterten and Skar (12), the maximum experimental time recommended is 8 hours if you want to avoid a shift in the bath ratio caused by evaporation (mainly $NaAlF_4$). By reducing the flush gas in the furnace to a minimum (< 0.5 ml Ar/min.), the evaporation was found to be less than 0.3 %.

Preliminary tests showed steady state solubility measurements of iron concentrations in pure Greenland cryolite after 0.5 hour of stirring. To obtain an effective dissolution process, proper convection in the electrolyte is important, and a home-made iron stirrer served that purpose.

When the solubility limit is reached, however, a stagnant electrolyte is beneficial since we want all the potential particulate FeO or FeF_2 species to settle before the melt sample is collected. Thermally induced convection caused by density variations in the electrolyte was avoided by securing constant temperature in the melt (*i.e*. maximum 2 degrees decrease between the top and the bottom of the crucible).

The tests were carried out by preheating and melting down the electrolyte mixture for 3 hours, stirring it for 0.5 hours at constant temperature, and finally allowing one hour for settling. 3-6 grams of electrolyte was withdrawn from the solution by a silicon tube immersed 5-10 mm into the solution.

The melt samples were quenched and crushed. 1-3 grams of the crushed melt samples were dissolved in 30 % $AlCl_3 \cdot 6H_2O$ and mixed with 5 ml concentrated HCl and de-ionised water to get the right ionic strength for ICP analysis[1].

5.5 Solubility of FeO in the Na_3AlF_6-Al_2O_3-Fe-Ar system at 1020 ^oC

The solubility of FeO is reported (23) to increase with decreasing alumina content. This indicates that FeO or FeF_2 does not dissolve as metal oxide ions like e.g. FeO_2^{2-}, because increasing alumina then would have *increased* the solubility of those ions. A possible mechanism for such a reaction could have been:

$$3FeO + Al_2O_3 + 6NaF = 3Na_2FeO_2 + 2AlF_3 \qquad [5\text{-}8]$$

Increasing alumina activity would then force the reaction to the right, which as a result would have increased the solubility of FeO. The dissolved iron species is probably a metal cation, metal fluoride ion or metal oxifluoride ion, and hence a reduction of alumina activity will increase the solubility of FeO. As an example, dissolved FeO may form iron fluoride:

$$FeO + \frac{2}{3}AlF_3 = FeF_2 + \frac{1}{3}Al_2O_3 \qquad [5\text{-}9]$$

where the activity of the dissolved species is proportional to the activity of alumina to minus one third.

Another possibility is that the melt is in equilibrium with the solid phases iron oxide and/or iron aluminate:

[1] Ionic Plasma Coupling, type “Thermo Jarell Ash Atomscan 16”.

$$FeO + Al_2O_3 = FeAl_2O_4 \quad [5\text{-}10]$$

The formation of aluminate ha earlier been reported for zinc oxide (13), hematite (Fe_2O_3) (5) and cerium oxide (14) in cryolite melts.

If iron aluminate precipitates in the melt, the alumina concentration will decrease accordingly. This is important to take into consideration when the solubility measurements are presented as a function of alumina activity.

The solubility of Fe(II) as a function of wt% Al_2O_3 is given in Figure 5-3.

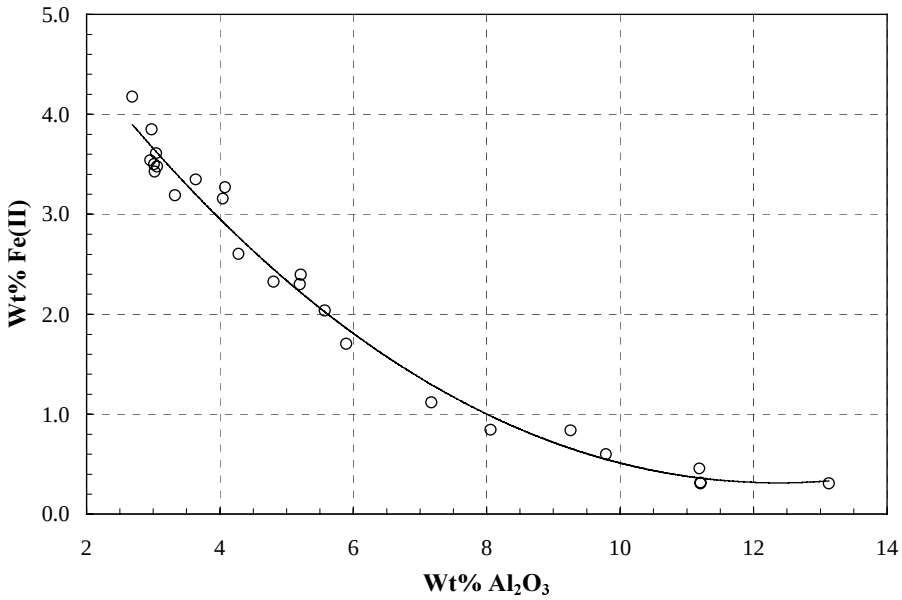

Figure 5-3: The solubility of Fe(II) in natural cryolite as a function of weight percent alumina. The temperature is 1020 ^{o}C. The alumina concentrations were measured with LECO.

By using the average of the different results obtained for the various alumina activities, the solubility of iron in cryolite can be expressed as follows:

$$\text{Wt\% Fe(II)} = -0.0004x^3 + 0.050x^2 - 1.041x + 6.342, \quad x = 2.7 - 13.0 \text{ wt \% } Al_2O_3 \quad [5\text{-}11]$$

Because of the high cost of pure FeF_2, FeO was used in the experiments with melts with low contents of alumina. As one can see from equation [5-9], that alumina is produced in this case, and that is the reason why the solubility of Fe(II) was not measured in melts with less than 2.7 weight % alumina.

According to Dewing and Thonstad (13) a presentation of the solubility data versus the activity of alumina in a logarithmic diagram is often more informative than a linear plot

because it is possible to derive a stoichiometric relationship for the dissolution mechanism by the slope of the line, *i.e.* between alumina and Fe(II).

There has been several articles regarding the activity of alumina reported lately (13), (15), (16),(17) and (18), but the activities given by Dewing and Thonstad (13) give the overall best fit for the experimental data obtained by Holm (19) for this particular system. The alumina concentrations were measured by using the LECO apparatus. The concentrations of iron in the samples are plotted as a function of the alumina concentration based on the LECO analysis in Figure 5-4.

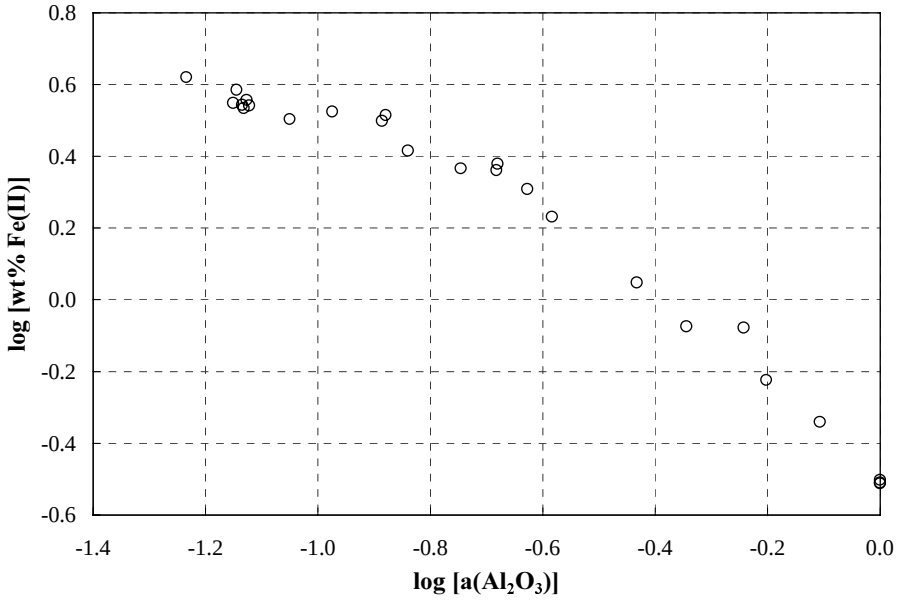

Figure 5-4: A log-log diagram of the solubility of Fe(II) in natural cryolite as a function of the alumina activity (based on LECO analysis). The temperature was 1020 ^{o}C.

The results given in Figure 5-4 give two different slopes with a breakpoint[2] (intercept) at an alumina activity (a) equal to 0.195, (*i.e*. log(a) = -0.71, which corresponds to 5.0 weight percent alumina).

A possible way to calculate the breakpoint, which separates the "low region" from the "high region", is to calculate the intercept between the two slopes found by regression (20). The problem in deciding how to draw least squares lines is that one is not sure exactly where the breakpoint is located, so it is not possible to decide which line the points near the breakpoint belong to.

A possible way to solve this problem is to make use of the relationship between the slopes of the two lines. This procedure is explained in detail in Chapter 4.5 regarding NiO solubility.

[2] See next page.

The value for the breakpoint, which minimises the sum of squares for *all* the data, was found by trial and error. The procedure was repeated for several values around the predicted breakpoint value, and the "correct" value for the breakpoint is represented by the regression line with the lowest sum of squares. Regression lines for different breakpoints (BP) and the sum of squares for each regression line (SS_E) were calculated. The result is shown in Figure 5-5.

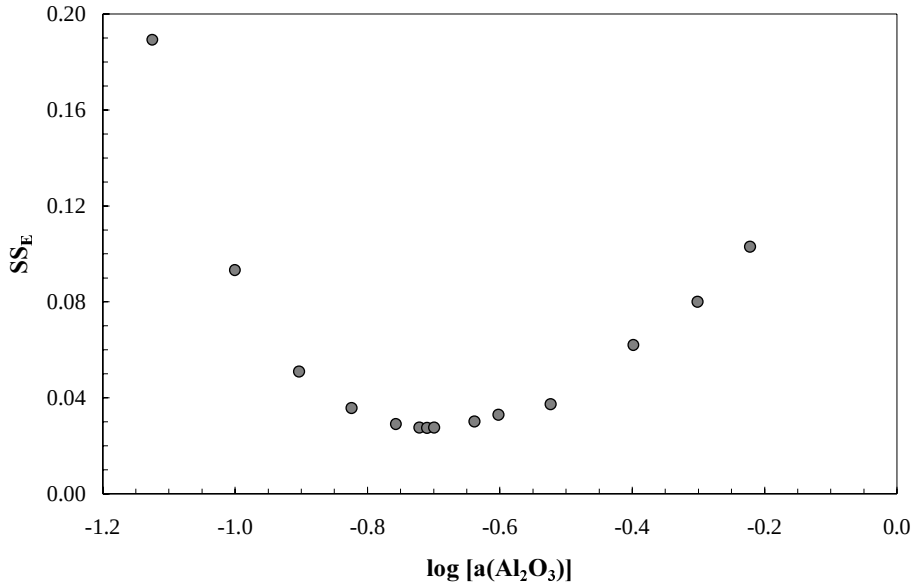

Figure 5-5: Sum of squares (SS_E) for regression lines with different alumina activities chosen as the breakpoint in the regression analysis of the solubility of iron oxide in the system Na_3AlF_6-Al_2O_3.

The minimum of the sum of squares curve gives $a_{Al_2O_3} = 0.195 \pm 0.009$ (*i.e.* log a = - 0.71), which corresponds to 5 wt% alumina. This activity was used to calculate the Gibbs energy of formation for iron aluminate.

For alumina concentrations below 5.0 weight percent the solubility of iron can be expressed as,

$$\log(\text{wt \% Fe(II)}) = -0.39\ (\pm 0{,}06) \log a + 0.11\ (\pm 0{,}06) \qquad [5\text{-}12]$$

and for alumina concentrations higher than 5.0 weight percent,

$$\log(\text{wt \% Fe(II)}) = -1.26\ (\pm 0{,}04) \log a - 0.49\ (\pm 0{,}02) \qquad [5\text{-}13]$$

where a = alumina activity.

The slope for the low alumina region is close to –1/3, which corresponds to the following mechanism:

$$FeF_2 + \frac{1}{3}Al_2O_3 = FeO + \frac{2}{3}AlF_3 \quad [5\text{-}14]$$

while the high alumina region can be described by,

$$FeF_2 + \frac{4}{3}Al_2O_3 = FeAl_2O_4 + \frac{2}{3}AlF_3 \quad [5\text{-}15]$$

with the theoretical slope of – 4/3, which is reasonably close to the one obtained, *i.e*. –1.26. These are the reaction mechanisms given by equations [5-14] and [5-15]. To get exactly –1/3 (for low cons.) and –4/3 (for high cons.), three other conditions must be met:

1. The activity of AlF_3 is constant
2. The activity of NaF is constant (it may get involved since FeF_2 may be complexed to FeF_4^{2-})
3. The activity coefficient of FeF_2 does not vary with the alumina content.

None of these conditions are likely to be fulfilled exactly, and slopes reasonably close to the theoretical values can be correct.

One of the slowly cooled samples with 8 wt% Fe(II) was examined with XRD, and the diagram indicated the presence of the $FeAl_2O_4$ phase in the melt. FeO was not detected, but since XRD only detects crystalline phased, one cannot exclude the presence of *amorphous* FeO. The presence of $FeAl_2O_4$ supports the suggested mechanism given by [5-8].

The alumina activity given at the breakpoint of the two slopes in Figure 5 can be used to determine Gibbs energy of formation for $FeAl_2O_4$.

The reaction considered is:

$$FeO_{(s)} + \alpha\text{-}Al_2O_{3(l)} = FeAl_2O_{4(s)} \quad [5\text{-}16]$$

The equation describing Gibbs energy of formation for $FeAl_2O_4$ can be expressed as:

$$\Delta G^o_{f(FeAl_2O_4)} = -RT \cdot \ln(K) \quad [5\text{-}17]$$

The equilibrium constant, K, can be expressed as $(1 / a_{Al_2O_3})$, giving,

$$\Delta G^o_{f(FeAl_2O_4)} = -RT \cdot \ln\left(\frac{1}{a_{Al_2O_3}}\right) \quad [5\text{-}18]$$

The calculated alumina activity at the breakpoint gives:

$$\Delta G^o_{f(FeAl_2O_4)} = -8{,}314 \cdot 1293{,}15 \cdot \ln\left(\frac{1}{0.195}\right) \quad [5\text{-}19]$$

and finally,

$$\Delta G^{o}_{f(FeAl_2O_4)} = -17.6 \pm 0.5 \text{ kJ/mol} \quad [5\text{-}20]$$

The standard deviation of ΔG^o has been calculated based on the standard deviation for the regression line [5-13] given for a = 0.195.

The standard Gibbs energy of formation for reaction [5-16] has been determined from electromotive force (emf) measurements of solid cells with oxygen-ion-conducting electrolytes. Rezukhina *et al*. (21) and Chan *et al.* (22) report $\Delta G^{o}_{f(FeAl_2O_4)}$ = - 23.088 kJ and - 22.548 kJ/mol, respectively at 1293 K. The corresponding average equilibrium constant is 8.35, which implies that FeO is stable at alumina activities less than 0.12 (*i.e.* log $a_{Al_2O_3}$ = - 0.92 corresponding to 0.57 wt% alumina). The discrepancy between these data and equation [5-20] will be discussed in Chapter 5.6.

Johansen *et al.* (23), (24) investigated the solubility of Fe(II) in molten cryolite in an iron crucible under argon atmosphere. The solubility of wüstite, interpolated to 1020 ^{o}C was 5.45 wt % Fe(II). Calculations where it was assumed that oxygen originated from FeO dissolved in the melt was present as alumina, gives 2.76 wt% Al_2O_3 as the correspondingly alumina concentration. Johansen *et al.*'s (23), (24) and Jentoftsen *et al.*'s (9) data are shown together with the presently obtained solubility data in Figure 5-6.

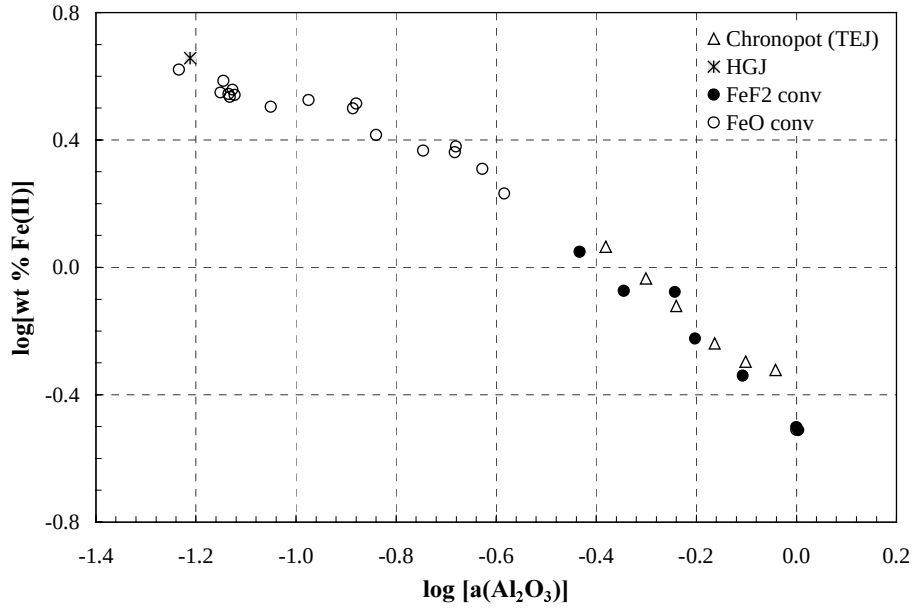

Figure 5-6: A log-log diagram of the solubility of Fe(II) in natural cryolite as a function of alumina activity (based on LECO analysis) compared with available literature data. The symbols are explained in the text below. The temperature is 1020 ^{o}C.

As we can see from Figure 5-6, the value reported by Johansen (23), (24) (called "HGJ" in Figure 5-6) is very close to the present results ("FeF2 conv" and "FeO conv" where "conv" means conventional solubility measurements). As one also can see from the Figure, Jentoftsen *et al*. (9) obtained solubility data ("Cronopot TEJ") with the chronopotentiometry method which are close to the present results, although their solubility values are slightly higher than the present results. Jentoftsen *et al*. used FeF_2 of > 95 wt% purity as additive, but since their calculations were based upon 100% FeF_2, it may explain some of the discrepancy between their results and the present. There is also a possibility that some of the FeF_2 stuck to the quartz feeding tube and/or evaporated upon addition through a quartz tube.

5.6 Gibbs energy of formation for $FeAl_2O_4$

As shown above there seems to be a rather large discrepancy between the presently derived Gibbs energy of formation of hercynite ($FeAl_2O_4$) and the values reported in the literature (21), (22), which mostly were derived from solid oxide galvanic cells. These workers assumed that the following equilibrium was valid:

$$FeO_{(s)} + \alpha Al_2O_{3(s)} = FeAl_2O_{4(s)} \qquad [5\text{-}21]$$

It has not been possible to explain the discrepancy between the present result and their results, and it was decided to check whether α-Al_2O_3 really is the stable form of alumina present in such melts or not, since thermodynamic data reported for γ-alumina seems to agree better with the present results.

The following electrochemical cell was used together with T.E. Jentoftsen:

Fe	$FeAl_2O_4$ α-Al_2O_3 Cryolite	ZrO_2 (O^{2-})	NiO	Ni

Figure 5-7: Set-up for the electrochemical cell used to determine the emf for $FeAl_2O_4$.

By adding cryolite (10 wt%) to the solid iron aluminate one stabilises α-Al_2O_3 ,(25), (26), (27). The cell voltage (emf) was measured in a cell with a Ni/NiO electrode inside an yttria-stabilised zirconia[3] (YSZ) tube immersed in a slurry of 10 wt% cryolite and $FeAl_2O_4$ + Al_2O_3 contained in an iron crucible which acted as the counter electrode. The iron crucible was connected to a rod of nickel to avoid Thomson effect between the electrodes. The experiment was run under an atmosphere of argon, and is shown in Figure 5-8.

[3] Oxygen ion conductor

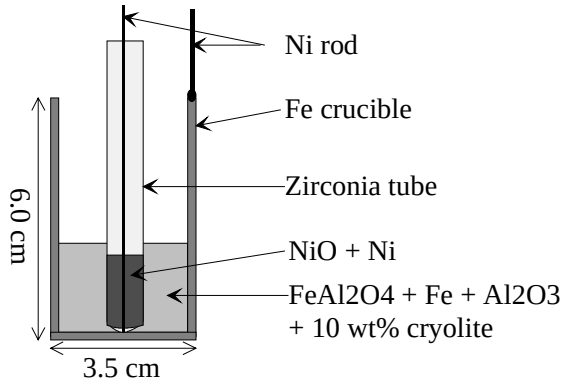

Figure 5-8: Sketch of the experimental set-up for the emf measurement for $FeAl_2O_4$.

The cell was heated very slowly (< 10 ^{o}/min) to prevent the zirconia tube from cracking, and the cell voltage (emf) was recorded for several hours after the cell temperature reached 1021 ^{o}C. The results are given in Figure 5-9.

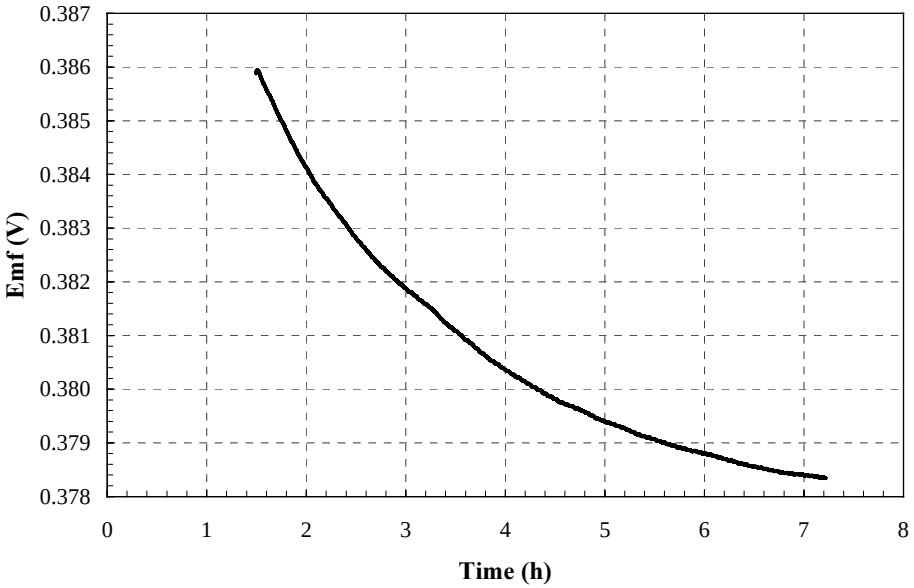

Figure 5-9: The emf for $FeAl_2O_4$ measured at 1020 ^{o}C in Ar atmosphere.

The cell measures the emf of the following reaction,

$$Fe_{(s)} + NiO_{(s)} + Al_2O_{3(s,\alpha)} = Ni_{(s)} + FeAl_2O_{4(s)} \qquad [5\text{-}22]$$

By adding the reaction for the formation of NiO, *i.e.*,

$$Ni_{(s)} + \frac{1}{2}O_{2(g)} = NiO_{(s)} \quad [5\text{-}23]$$

one gets,

$$Fe_{(s)} + \frac{1}{2}O_{2(g)} + Al_2O_{3(s,\alpha)} = FeAl_2O_{4(s)} \quad [5\text{-}24]$$

One then subtracts the reaction for the formation of wüstite (called "FeO"), *i.e.*,

$$Fe_{(s)} + \frac{1}{2}O_{2(g)} = FeO_{(s)} \quad [5\text{-}25]$$

to obtain,

$$FeO_{(s)} + Al_2O_{3(s,\alpha)} = FeAl_2O_{4(s)} \quad [5\text{-}26]$$

The Gibbs energy of formation can be calculated by the following equation,

$$\Delta G^o = -nFE^o \quad [5\text{-}27]$$

This implies that the cell voltage measured is a sum of the following formation reactions:

$$E_{cell} = E^o_{FeAl_2O_4} + E^o_{NiO} - E^o_{FeO} \quad [5\text{-}28]$$

Since a Ni/NiO reference electrode was used, the potential of the reference electrode (E^o_{NiO}) had to be added to the overall cell potential. This implies that Gibbs energy of formation for hercynite can be calculated by the following equation,

$$\Delta G^o_{FeAl_2O_4} = -nF\cdot\left[E_{cell} + E^o_{FeO} - E^o_{NiO}\right] \quad [5\text{-}29]$$

Holmes *et al*. (28) used a similar cell set up, and measured E^o_{NiO} and E^o_{FeO}, which were used for the present calculation, *i.e.,*

$$\Delta G^o_{FeO} = -275770 + 13.841\cdot T - 8.4742\cdot T\cdot\ln(T)\ [J/mol] \quad (T = 1184 - 1644) \quad [5\text{-}30]$$

$$\Delta G^o_{NiO} = -239885 + 122.350\cdot T - 4.584\cdot\ln(T)\ [J/mol] \quad (T = 900 - 1600) \quad [5\text{-}31]$$

The standard deviation of equations [5-30] and [5-31] are only 1 and 2 J/mol, respectively.

Using equation [5-29], [5-30], [5-31] and the data in Figure 5-9 for T = 1293 K one gets,

$$\Delta G^{o}_{FeAl_2O_4} = -2 \cdot 96487 \cdot [0.3755 - 0.929 + 0.643] = -17.3 \text{ kJ/mol} \quad [5\text{-}32]$$

This value is in excellent agreement with the result obtained from the present solubility measurements (see [5-20]), and it indicates that some of the values for hercynite reported in the literature (*i.e.* (21 (22) and (29)) probably are erroneous. It may seem like these authors did not have equilibrium between hercynite and $\alpha - Al_2O_3$ in their cells.

The available values reported for hercynite in the literature were recalculated to fit equation [5-24], and are plotted in Figure 5-10 together with the present results measured at 972 – 1070 °C. The present results are given in Table 5-1.

Table 5-1: The emf measurements obtained in the present work and the corresponding Gibbs energy of formation for reactions [5-24] and [5-26].

T [°C]	T [K]	Emf [mV]	ΔG^o rx. [5-24] [J/mol]	ΔG^0 rx. [5-26] [J/mol]
972	1245.15	367.2	-16006	-199080
972	1245.15	364.8	-15543	-198617
1020	1293.15	377.7	-17110	-197026
1021	1294.15	375.3	-16628	-196478
1021	1294.15	373.4	-16261	-196111
1070	1343.15	380.1	-16606	-193247

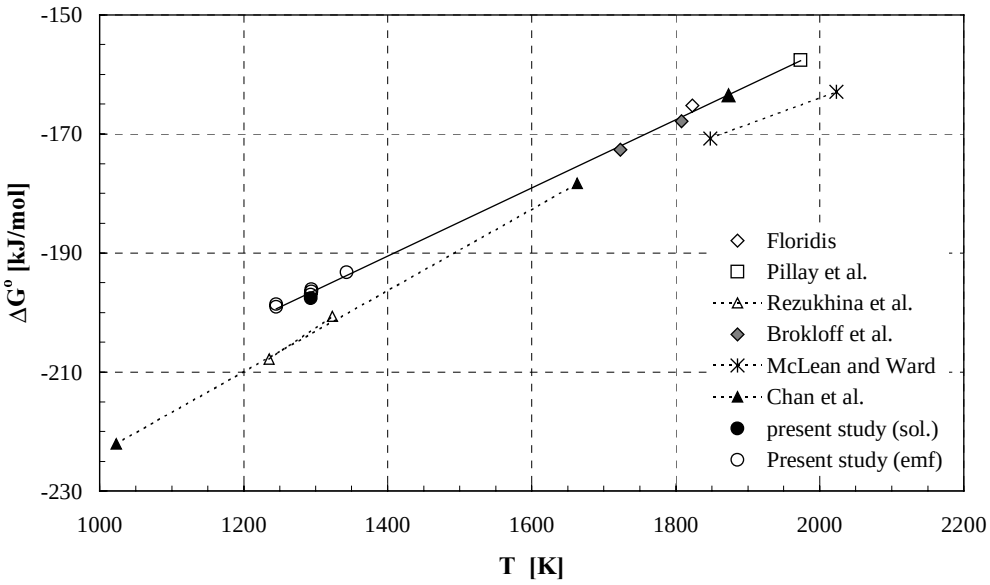

Figure 5-10: Gibbs energy of formation for hercynite *versus* temperature according to the reaction $Fe_{(s)} + 0.5O_{2(g)} + Al_2O_{3(\alpha,s)} = FeAl_2O_{4(s)}$.

As one can see from Figure 5-10, only the data of Floridis (30), Brokloff (31) and Pillay *et al.* (32) seem to fit the present data. These three papers dealt with temperatures where α-alumina is stable, while Rezukhina *et al.* (21) and Chan *et al.* (22) might have had another crystal form of alumina present in equilibrium with hercynite. It has not been possible to explain why the values reported by McLean and Ward (29) deviate from the other's above 1600 °C.

Based on the present data for ΔG^o for reaction [5-24], and those of Floridis (30), Pillay (32), Brokloff *et al.* (31) and Chan *et al.* (22) the following linear expression was derived by regression analysis of all these data,

$$\Delta G^o_{FeAl_2O_{4(s)}} = -270615(\pm 1387) + 57.222(\pm 0.856)\cdot T \left[J/mol\right], \; T = 1245 - 1973 \; K \quad [5\text{-}33]$$

Since ΔG^o can be expressed as,

$$\Delta G^o = \Delta H^o - T\Delta S^o \quad [5\text{-}34]$$

ΔS^o is given by the slope of the curve, *i.e.*,

$$\Delta S^o_{FeAl_2O_4} = 57.2 \pm 0.9 \; J/K\cdot mol \quad \text{and} \quad \Delta H^o_{FeAl_2O_4} = -270.6 \pm 1.4 \; kJ/mol \quad [5\text{-}35]$$

where T = 1245 – 1973 K

5.7 Thermodynamic calculations for $FeAl_2O_4$

Based on the data obtained from the solubility and the emf measurements, a revision was made of the data for hercynite given by Barin (3). The data used for the calculations are summarised in Table 5-2.

Table 5-2 Thermodynamic data for some elements, from Barin (3).

Element	C_p 298.15 K J/Kmol	C_p 1600 K J/Kmol	S^o 298.15 K J/Kmol	S^o 1600 K J/Kmol	H^o 1600 K J/mol
$Al_2O_3(\alpha)$	79.038	133.375	50.936	240.935	-152003
$Fe_{(s)}$	24.978	37.364	27.280	86.661	49320
Fe_2O_3	103.866	144.490	87.404	319.817	-638218
Fe_3O_4	150.730	199.302	146.147	483.821	-851472
$FeAl_2O_{4(s)}$	123.544	191.616	106.299	377.033	-1774961
$O_{2(g)}$	29.376	36.797	205.147	260.434	44266

With the use of the regression line given by [5-33], the values given at 1600 K were chosen as representative values since it is in the middle of the temperature range that the regression line is based upon. Based on the thermodynamic data from Table 5-2, ΔS^o for reaction

[5-24] is –80.780 J/Kmol. However, the present work gives –57.222 J/K·mol (equation [5-35]), which is 23.558 J/K·mol more positive than the value obtained from Barin (3).

It was assumed that the tabulated values for $Fe_{(s)}$, $O_{2(g)}$ and $Al_2O_{3(\alpha,s)}$ were correct, and by using the present results a new standard entropy for hercynite, $S^o(FeAl_2O_4)$ at 1600 K, was calculated to be 400.591 J/K·mol.

The data given by Barin (3) was checked by calculating the change in standard entropy (ΔS^o) for the following reaction,

$$Fe_3O_{4(s)} + Al_2O_{3(s,\alpha)} = FeAl_2O_{4(s)} + Fe_2O_{3(s)} \qquad [5\text{-}36]$$

which should be close to zero since there is no major structural changes involved in this reaction. Data from Barin (3) gave –3.380 and –27.906 J/K·mol at 298.15 and 1600 K, respectively. The value obtained at 298.15 K seems reasonable, but the one at 1600 K seems to be too high. If on the other hand one calculates ΔS^o using the present result for S^o, one obtains ΔS^o = –4.348 J/K·mol at 1600 K, indicating that the present results for hercynite are more precise than the data reported by Barin. A new set of data for hercynite was, therefore, recalculated based on the present results (see Table 5-3).

The standard molar heat capacity, C_p^o, can be expressed as,

$$C_p^o = a + bT + \frac{c}{T^2} \qquad [5\text{-}37]$$

To find the three unknown constants a, b and c, one can use the following boundary conditions to solve equation [5-37]:

$$C_p^o(T_1 = 298.15K) = a + bT_1 + \frac{c}{T_1^2} = 123.544\ J/(K \cdot mol) \qquad [5\text{-}38]$$

$$C_p^o(T_2 = 1500K) = a + bT_2 + \frac{c}{T_2^2} = 188.187\ \ (J/K \cdot mol) \qquad [5\text{-}39]$$

$$S^o_{T_2=1500K} - S^o_{T_1=298.15K} = \int_{T_1}^{T_2} \frac{C_p^o}{T} dT = a \ln\left(\frac{T_2}{T_1}\right) + b(T_2 - T_1) - \frac{c}{4}\left(T_2^{-4} - T_1^{-4}\right) = 294.292\ J/(K \cdot mol) \qquad [5\text{-}40]$$

The first boundary condition is taken from Barin (3), where both H° and S° are given for 298.15 K, so that the $C°_p$ could be estimated. The second boundary condition was found by assuming that the ΔC_p^o for reaction [5-36] is equal to zero at 1600 K. To fulfil this assumption, C_p^o for hercynite at 1600 K has to be 188.187 J/K·mol if the values for the

compounds $Al_2O_{3(s,\alpha)}$, $Fe_2O_{3(s)}$ and $Fe_3O_{4(s)}$ from Table 5-2 are used. The third boundary condition (eq. [5-40]) was calculated by subtracting the standard entropy at 298.15 K given in Table 5-2 from the present standard entropy of hercynite at 1600 K, *i.e.* $S^o(FeAl_2O_4)$ = 400.591 J/K·mol.

By combining the equations [5-38] – [5-40], the following new expression for the standard molar heat capacity of hercynite as a function of temperature was obtained:

$$C_p^o = a + bT + \frac{c}{T^2} = 161.512 + 0.0176097 \cdot T - \frac{3841843}{T^2} \qquad [5\text{-}41]$$

Since $S°_{298.15K}$ is known, the standard entropy, S°, can be calculated by,

$$\begin{aligned} S^o &= S^o_{298.15K} + \int_{298.15K}^{T} \frac{C_p^o}{T} dT \\ &= S^o_{298.15K} + a \ln\left(\frac{T}{298.15K}\right) + b(T - 298.15K) - \frac{c}{4}\left(T^{-4} - 298.15K^{-4}\right) \end{aligned} \qquad [5\text{-}42]$$

$H°\text{-}H°_{298.15K}$ is given by the relationship,

$$\begin{aligned} H^o - H^o_{298.15K} &= \int_{298.15K}^{T} C_p^o \, dT \\ &= a(T - 298.15K) + \frac{b}{2}\left(T^2 - 298.15K^2\right) - c\left(T^{-1} - 298.15K^{-1}\right) \end{aligned} \qquad [5\text{-}43]$$

The change in standard enthalpy, $\Delta H°_{1600K}$, for reaction [5-24] at 1600 K was then calculated to be –269120 J/mol. To obtain this value for $\Delta H°_{1600K}$ for FeO, H^o for hercynite has to be –1719165 J/mol at 1600 K if the H^o values given for $Fe_{(s)}$, $O_{2(g)}$ and $Al_2O_{3(\alpha,s)}$ in Table 5-2 are used. By subtracting the term "$H°_{1600K}–H°_{298.15K}$" given by equation [5-43], $H°_{298.15K}$ for hercynite was calculated to be –1940703 J/mol. H° for different temperatures is then easily found by adding the terms "$H°–H°_{298.15K}$" and "$H°_{298.15K}$". The standard Gibbs energy for hercynite, G°, for various temperatures is calculated from the H° and S° values. The expression "$–(G°–H°_{298.15K})/T$" is then calculated from the "$H°–H°_{298.15K}$" and "S°" values. The results of the calculations are given in Table 5-3, and the data from Barin (3) is given in Table 5-4 for comparison.

Table 5-3 Revised thermodynamic data for $FeAl_2O_4$.

T	C^o_p	S^o	$-(G^o - H^o_{298.15K})/T$	H^o	$H^o - H^o_{298.15K}$	G^o
K	←	J/Kmol	→	←	J/mol	→
298.15	123.544	106.299	106.299	-1940703	0	-1972396
300	124.108	107.331	106.567	-1940473	229	-1972673
400	144.545	155.556	121.068	-1926907	13795	-1989130
500	154.950	193.357	135.721	-1911885	28818	-2008563
600	161.406	224.565	150.137	-1896046	44657	-2030785
700	165.998	251.223	164.026	-1879664	61038	-2055521
800	169.597	274.551	177.271	-1862878	77824	-2082520
900	172.618	295.336	189.848	-1845764	94938	-2111566
1000	175.280	314.114	201.778	-1828367	112336	-2142480
1100	177.708	331.268	213.099	-1810716	129987	-2175111
1200	179.976	347.083	223.856	-1792831	147872	-2209330
1300	182.132	361.772	234.096	-1774724	165978	-2245027
1400	184.206	375.502	243.862	-1756407	184296	-2282110
1500	186.219	388.406	253.195	-1737885	202817	-2320494
1600	188.187	400.591	262.130	-1719165	221538	-2360110
1700	190.119	412.143	270.700	-1700249	240454	-2400893
1800	192.024	423.136	278.936	-1681142	259561	-2442787
1900	193.906	433.630	286.862	-1661845	278858	-2485741
2000	195.771	443.675	294.504	-1642361	298342	-2529711

Table 5-4 Thermodynamic data for $FeAl_2O_4$, from Barin (3)

T	C^o_p	S^o	$-(G^o - H^o_{298.15K})/T$	H^o	$H^o - H^o_{298.15K}$	G^o
K	←	J/Kmol	→	←	J/mol	→
298.15	123.544	106.299	106.299	-1995070	0	-2026992
300	124.025	107.064	106.301	-1995070	229	-2027189
400	141.874	145.503	111.421	-1981666	13633	-2039867
500	151.540	178.287	121.602	-1966956	28343	-2056100
600	157.986	206.517	133.457	-1951463	43836	-2075373
700	162.910	231.255	145.697	-1935409	59890	-2097287
800	167.024	253.283	157.794	-1918907	76392	-2121534
900	170.667	273.170	169.526	-1902020	93279	-2147873
1000	174.017	291.327	180.811	-1884784	110515	-2176110
1100	177.176	308.062	191.629	-1867223	128076	-2206091
1200	180.204	323.609	201.987	-1849353	145946	-2237683
1300	183.141	338.149	211.908	-1831185	164114	-2270779
1400	186.012	351.827	221.418	-1812727	182572	-2305284
1500	188.833	364.757	230.547	-1793984	201315	2341119
1600	191.616	377.033	239.322	-1774961	220338	-2378214
1700	194.371	388.732	247.769	-1755662	239637	-2416507
1800	197.103	399.920	255.777	-1736088	259211	-2455943
1900	199.817	410.649	263.777	-1716242	279057	-2496475
2000	202.480	420.967	271.380	-1696125	299174	-2538059

5.8 The effect of temperature on the solubility of FeO in the Na_3AlF_6-$Al_2O_{3(sat)}$-Fe-Ar system

The Na_3AlF_6-$Al_2O_{3(sat)}$ system was chosen to study the effect of temperature, and it was varied in the temperature range 980 – 1050 °C. The numerical results, which are presented in the appendix, show that the solubility of $FeAl_2O_4$ in the Na_3AlF_6-Al_2O_3 system increases with increasing temperature. This is similar to the results obtained (13) for zinc oxide/aluminate, SnO_2 and CeO_2 in cryolite-alumina melts.

The partial enthalpy of dissolution of Fe(II) in the melt,

$$FeAl_2O_{4\,solid} = FeAl_2O_{4\ dissociated} \qquad [5\text{-}44]$$

can be obtained from the solubility data. The procedure is shown in the Chapter 4.7, p. 77 for Ni(II).

Since the solubility is relatively low, we can assume Henrian behaviour. In that case $\ln(x_i^{sat})$, or ln(wt%), should vary linearly with (1/T), provided that the assumption of Henrian behaviour holds and $\Delta\overline{H}^0_{FeAl_2O_4}$ is constant in the temperature range studied.

Figure 5-11 shows the solubility of Fe(II) plotted as ln(wt% Fe) versus the reciprocal temperature (times 10^4). As we see, the correlation is good for the temperature range examined.

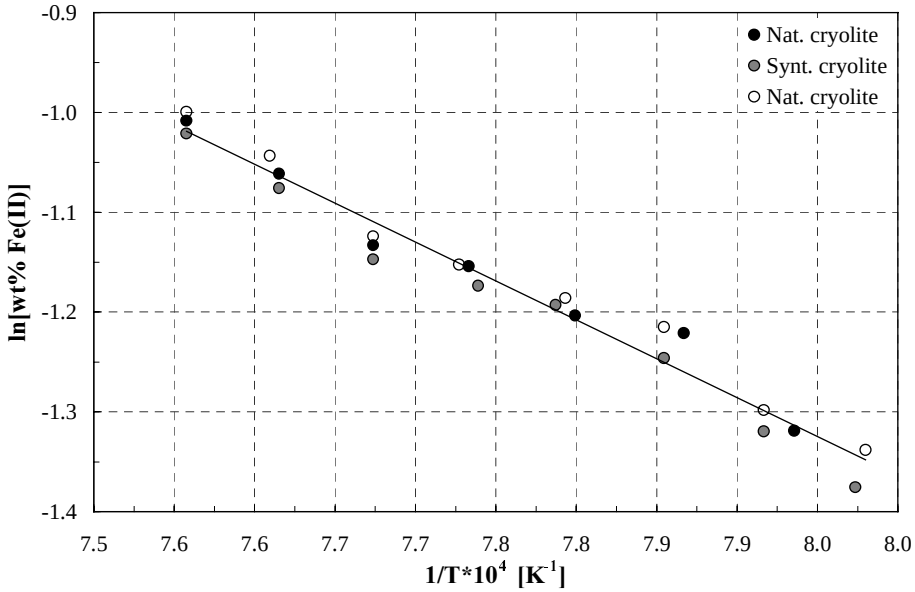

Figure 5-11: The logarithm of the saturation concentration of dissolved Fe(II) as a function of the reciprocal temperature (times 10^4) in the Na_3AlF_6-$Al_2O_{3(sat)}$ system.

The least square equation for all the solubility measurements in alumina-saturated melts is:

$$\ln(\text{wt \% Fe(II)}) = -\frac{7789\ (\pm 301)}{T} + 4.87\ (\pm 0.23) \qquad (T = K) \qquad [5\text{-}45]$$

for T' =980-1050 ^{o}C, where T = (T' +273.15) K.

The partial molar enthalpy for dissolution of the aluminate, $\Delta\overline{H}^{0}_{FeAl_2O_4}$, was then calculated from the slope of the line, *i.e*.,

$$\Delta\overline{H}^{0}_{FeAl_2O_4} = 64.8 \pm 2.5 \text{ kJ/mol}$$

DeYoung (33) has reported the partial molar enthalpy of dissolution of Fe_2O_3 to be 138 kJ/mol. Diep (5) reported the same enthalpy to be 124 ± 9 kJ/mol. No value for $FeAl_2O_4$ has been found in the literature.

5.9 Solubility of FeO and $FeAl_2O_4$ in the NaF-AlF_3-$Al_2O_{3(sat)}$ system at 1020 ^{o}C

Melts with various NaF-AlF_3 ratios were prepared by mixing natural cryolite with excess AlF_3/NaF. The amount of alumina added prior to the experiments was based on alumina saturation limits for basic baths as measured by Diep (5) for the system NaF-AlF_3-Al_2O_3, and for acidic melts the equation given by Solheim *et al*. (18) was used. To make sure that the melts were completely saturated, approximately 10 % excess alumina was added for the *acidic* baths (CR<3.0), only. α-Al_2O_3 is not stable in basic baths above CR = 3.7 (34), and it causes the sintered alumina materials to deform, crack and swell, and consequently a platinum shielding and an iron stirrer had to be used. About 5 wt% FeO was added to the NaF-AlF_3-AlF_3 mixture prior to heating. The solution was stirred for 1 hour and allowed to settle for 1 hour before a sample was withdrawn from the solution, cooled and analysed as described for the other solubility measurements.

The solubility of $FeAl_2O_4$ was determined as a function of the melt composition at 1020 ^{o}C in NaF-AlF_3-$Al_2O_{3(sat)}$ melts. The results are plotted in Figure 5-12. The numerical data are given in Appendix B.

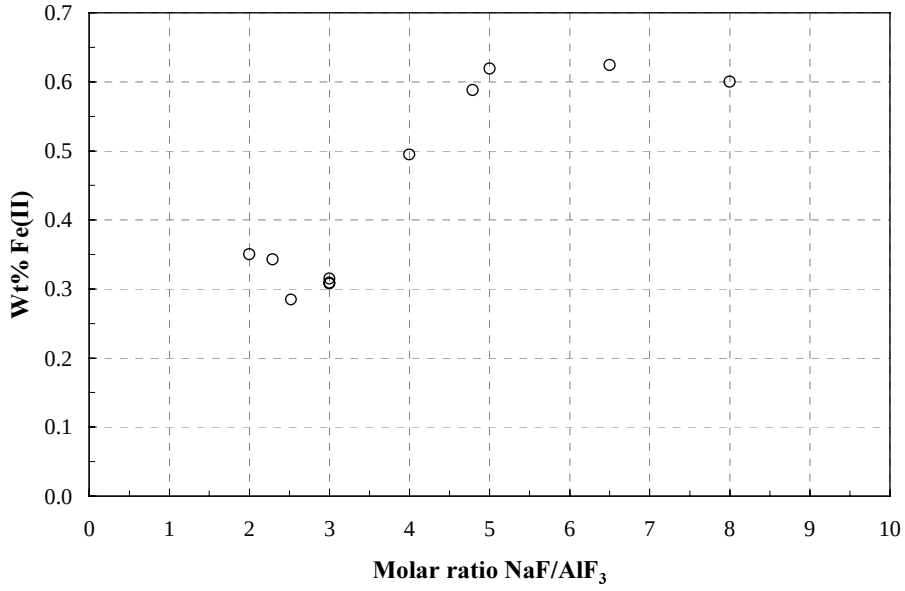

Figure 5-12: The solubility of Fe(II) in alumina-saturated melts as a function of molar ratio at 1020 ^{o}C in an atmosphere of argon.

According to the solubilities measured as a function of alumina activity, it was concluded that FeF_2-based complexes are formed in the melt. The Fe(II)-complexes may have a number of "NaF's" attached, which in general can be expressed as,

$$FeAl_2O_{4(s)} + \frac{2}{3}AlF_{3(l)} + x \cdot NaF_{(l)} = Na_xFeF_{(2+x)(l)} + \frac{4}{3}Al_2O_{3(l)} \qquad [5\text{-}46]$$

The equilibrium constant for equation [5-46], K_x, can be expressed as,

$$K_x = \left(\frac{a_{Na_xFeF_{(2+x)}} \cdot a^{4/3}_{Al_2O_3}}{a^{2/3}_{AlF_3} \cdot a^{x}_{NaF}} \right) \qquad [5\text{-}47]$$

By expressing equation [5-47] in a logarithmic form, one gets,

$$\log(a_{Na_xFeF_{(2+x)}}) + \frac{4}{3}\log(a_{Al_2O_3}) - \frac{2}{3}\log(a_{AlF_3}) = x \cdot \log(a_{NaF}) + \log(K_x) \qquad [5\text{-}48]$$

If one assumes that the solute species has a constant activity coefficient, so that its activity can be replaced by its concentration, one anticipates that a plot of the function:

$$\log(wt\%\,Fe) + \frac{4}{3}\log(a_{Al_2O_3}) - \frac{2}{3}\log(a_{AlF_3}) = x \cdot \log(a_{NaF}) + \text{const.} \qquad [5\text{-}49]$$

or an analogous function based on [5-46], will give a straight line with a slope of "x".

With the use of the present solubility data given (as "wt% Fe(II)"), and the activity data for AlF_3 and NaF in alumina–saturated melts given by Sterten *et al.* (35), (34), the left hand side of equation [5-49] was plotted as shown in Figure 5-13. The formation of β-alumina was taken into account as shown in Chapter 4.9, p. 86.

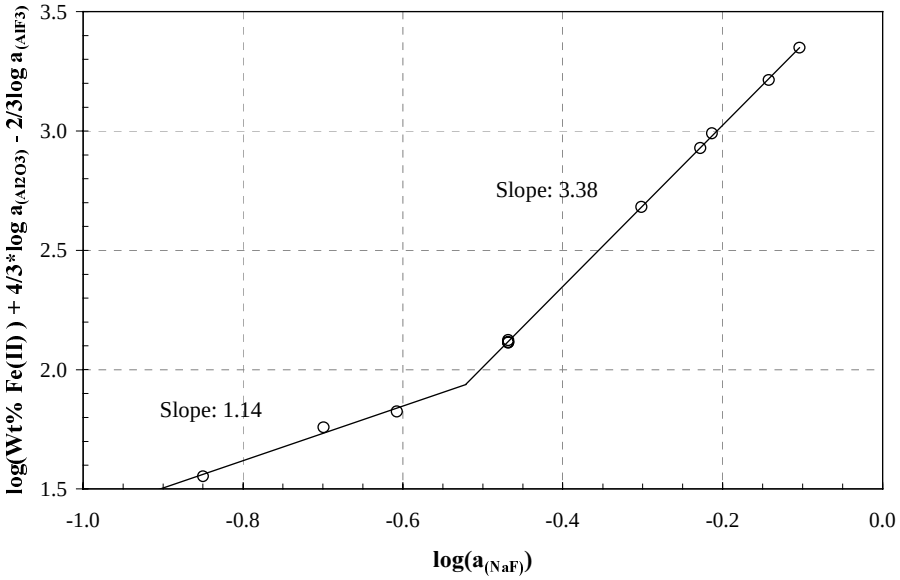

Figure 5-13: log(Wt% Fe(II)) + 4/3*log($a_{Al_2O_3}$) – 2/3*log(a_{AlF_3}) *versus* log(a_{NaF}) (eq. [5-49]) in alumina-saturated cryolite melts at 1020 °C in argon.

Within the limits of error the slope of the curve is close to 3 for the basic melts (*i.e.* for log(a_{NaF}) > -0.47), which means that the most probable reaction mechanism is:

$$FeAl_2O_4 + \frac{2}{3}AlF_3 + 3NaF \rightarrow Na_3FeF_5 + \frac{4}{3}Al_2O_3 \qquad [5\text{-}50]$$

while for the acid melts (*i.e.* for log(a_{NaF}) < -0.47) where the slope is close to 1:

$$FeAl_2O_4 + \frac{2}{3}AlF_3 + NaF \rightarrow NaFeF_3 + \frac{4}{3}Al_2O_3 \qquad [5\text{-}51]$$

seems to be the most plausible reaction mechanism.

Another method can also be applied to model the most likely species present in the melts. By rearranging equation [5-47] one can express the activity of the species "$a_{Na_xFeF_{(2+x)}}$" as:

$$a_{Na_xFeF_{(2+x)}} = K_x \cdot \left(\frac{a_{Al_2O_3}^{4/3}}{a_{AlF_3}^{2/3} \cdot a_{NaF}^{x}} \right)^{-1} \qquad [5\text{-}52]$$

One can then model the various species by testing different "x" values in equation [5-52] and change the corresponding equilibrium constant K_x by trial and error until the best fit of the solubility data, expressed as wt% Fe, is obtained. Species with "x"-values from 0 to 4 were modelled, and the result is shown in Figure 5-14. The best fit was obtained for x = 1 and 3, *i.e.* $NaFeF_3$ and Na_3FeF_5, with $K_1 = 270$ and $K_3 = 4300$, respectively. One cannot exclude Na_4FeF_6 to be present ($K_4 = 6200$), or a mixture of Na_3FeF_5 and Na_4FeF_6.

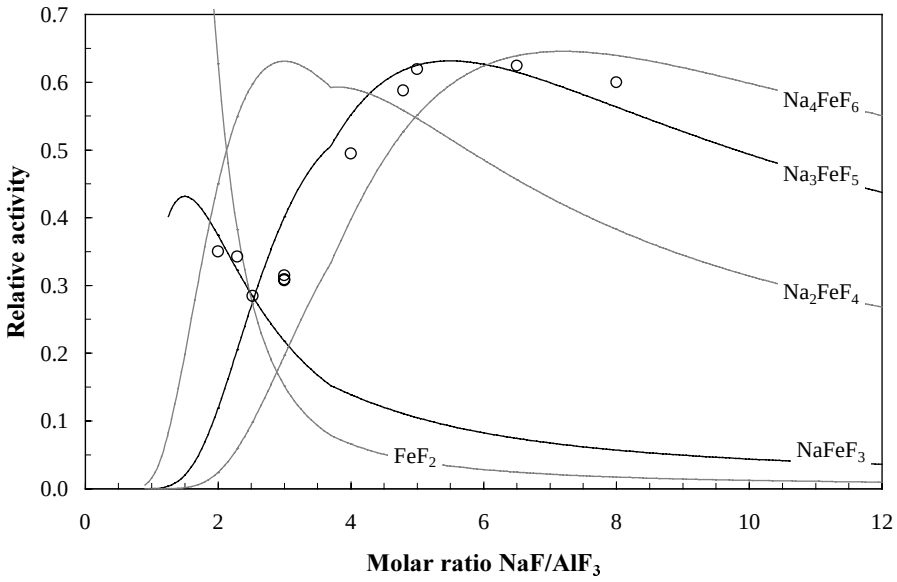

Figure 5-14: Model fitting of $Na_xFeF_{(2+x)}$ complexes in alumina-saturated cryolite melts as a function of molar ratio at 1020 ^oC in an atmosphere of argon (see text).

Both methods lead to the same conclusion. Na_3FeF_5 and Na_4FeF_6 seem to be the most plausible complexes formed in alumina-saturated basic cryolite melts, while $NaFeF_3$ seems to form in acidic melts. The conclusion seems logical since the species suggested in the basic melts having high contents of NaF, contain three or four sodium fluorides, while the one assumed to be present in the acidic melts just contains one.

5.10 Solubility of Fe_2O_3 in cryolite-alumina melts

Diep (5) measured the solubility of Fe_2O_3 in various cryolite-alumina melts, and demonstrated how important it is to control the atmosphere above the melt. As one can see from Figure 5-15, the solubility of Fe(III) in argon is higher than in oxygen, which indicates that in argon atmosphere the iron contains some Fe(II), too.

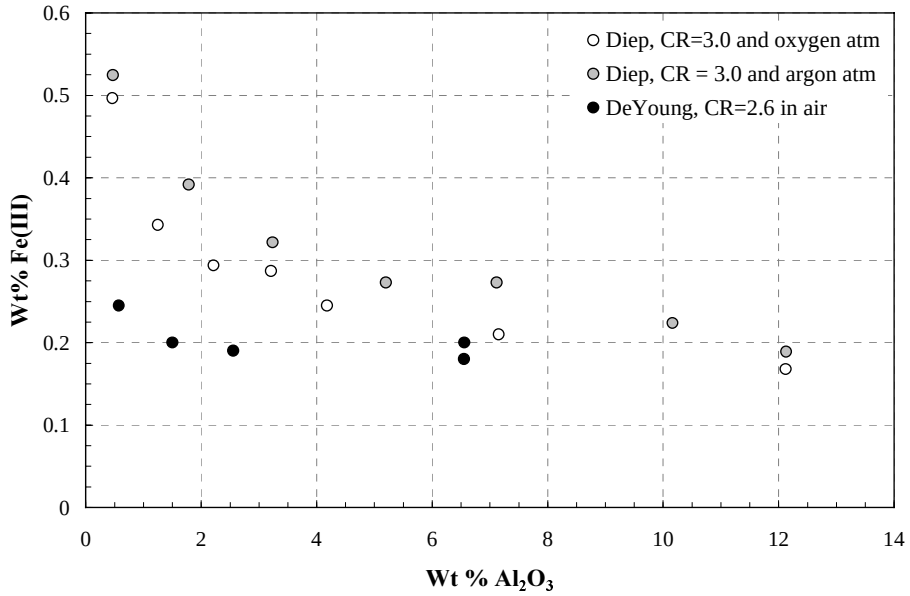

Figure 5-15: Solubility of Fe(III) in cryolite-based melts in different atmospheres as a function of the alumina concentration at 1020 ^{o}C. Data from Diep (5) and DeYoung (33).

Diep concluded that Na_3FeF_6 is the most important species in the NaF-AlF_3-Al_2O_3(sat.)-Fe_2O_3-O_2(g, 1 atm) system, besides $Na_2AlFeOF_6$, $Na_6AlFeOF_{10}$ and $Na_2AlFeO_2F_4$.

It was shown in Chapter 5.5 that FeF_2 forms in cryolite melts. If one, however, considers the reaction (36),

$$Fe_2O_{3(s)} + 2AlF_{3(s)} = 2FeF_{3(s)} + Al_2O_{3(s,\alpha)} \qquad \Delta G^{o} = 65{,}3 \text{ kJ/mol} \qquad [5\text{-}53]$$

assuming that the activity of Al_2O_3 is unity and uses $2.4*10^{-3}$ (16) as the value for the activity of AlF_3 in a NaF-AlF_3 melt with CR = 2.2 at 1250 K, one obtains,

$$\frac{a^{2}_{FeF_3}}{a_{Fe_2O_3}} = 5.76*10^{-9} \qquad [5\text{-}54]$$

Thus, Fe_2O_3 is not likely to form FeF_3 to any large extent.

Diep's (5) solubility data for Fe(III) in alumina-saturated cryolite at 1020 ^{o}C was used, but all the oxygen coming from the Fe_2O_3 was assumed present in the melt as alumina, and Diep's alumina concentrations[4] were adjusted accordingly. These solubility data for Fe(III)

[4] Diep's alumina concentrations are reported as the concentrations of alumina added to the melt prior to the experiments.

are presented as a function of alumina activity in a logarithmic diagram in Figure 5-16, which gives a line with a slope of approximately –1/6.

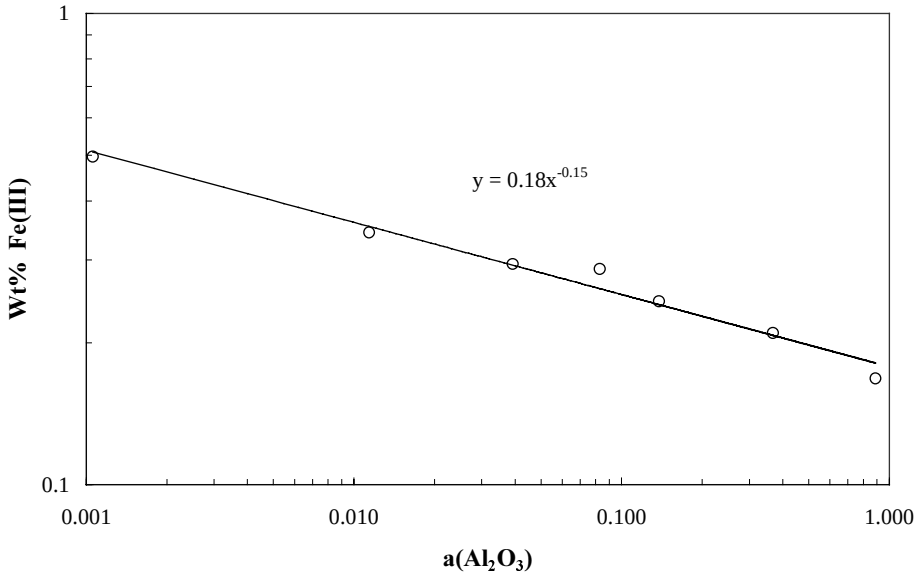

Figure 5-16: Log-log plot of the solubility of Fe(III) as a function of the alumina activity at 1020 °C in alumina-saturated cryolite in an atmosphere of oxygen. Data from Diep (5).

Diep (5) concluded that the presence of Na_3FeF_6 and some Al-Fe-O-compounds seemed to be most likely in these systems, and suggested two species, $Na_2AlFeOF_6$ and $Na_6AlFeOF_{10}$, that might explain the slope of –1/6, *i.e.* x = 2 and 6 in the following general equation:

$$\frac{1}{2}Fe_2O_{3(s)} + \frac{4}{3}AlF_3 + x \cdot NaF = Na_xAlFeOF_{(4+x)} + \frac{1}{6}Al_2O_3 \qquad [5\text{-}55]$$

However, if one assumes the formation of species without aluminium, the following general reaction mechanism might also be correct,

$$\frac{1}{2}Fe_2O_{3(s)} + \frac{1}{3}AlF_3 + x \cdot NaF = Na_xFeOF_{(1+x)} + \frac{1}{6}Al_2O_3 \qquad [5\text{-}56]$$

With the use of the equation for the equilibrium expression for [5-56], one can express the activity of $Na_xFeO_{(1+x)}$ as a proportionality function of the activities of Al_2O_3, AlF_3 and NaF, *i.e.*,

$$\frac{a_{Na_xFeO_{(1+x)}} \cdot (a_{Al_2O_3})^{1/6}}{(a_{AlF_3})^{1/3}} \alpha \ (a_{NaF})^x \qquad [5\text{-}57]$$

By expressing equation [5-57] in a logarithmic form, one gets,

$$\log(a_{Na_xFeO_{(1+x)}}) + \frac{1}{6}\log(a_{Al_2O_3}) - \frac{1}{3}\log(a_{AlF_3}) = x \cdot \log(a_{NaF}) + \text{const.} \qquad [5\text{-}58]$$

If one assumes that Henry's law is valid and the solute species has a constant activity coefficient, so that its activity can be replaced by the concentration, then one anticipates that a plot of the function,

$$\log(\text{wt\% Fe(III)}) + \frac{1}{6}\log(a_{Al_2O_3}) - \frac{1}{3}\log(a_{AlF_3}) = x \cdot \log(a_{NaF}) + \text{const.} \qquad [5\text{-}59]$$

or an analogous function based on [5-58], will be a straight line with a slope of "x".

In acidic melts saturated with alumina the activity of α-alumina is 1. Since β-Al_2O_3 ($Na_2O \cdot 11Al_2O_3$) is formed in basic melts (37), (38), this must be taken into consideration, as shown in Chapter 4.9, p. 86.

Diep's (5) alumina solubility data obtained in basic melts and alumina solubility data for basic melts reported by Solheim *et al.* (18) were used in the calculations. The activity data for NaF and AlF_3 represented by Solheim and Sterten (15), (16) are only given for CR 1.4 to 3 (acidic melts), but since Sterten *et al.* (34), (35) have earlier published activity data for alumina-saturated melts with CR= 1 to 15, Sterten *et al.*'s data were used. Equation [5-59] was then plotted as shown in Figure 5-17.

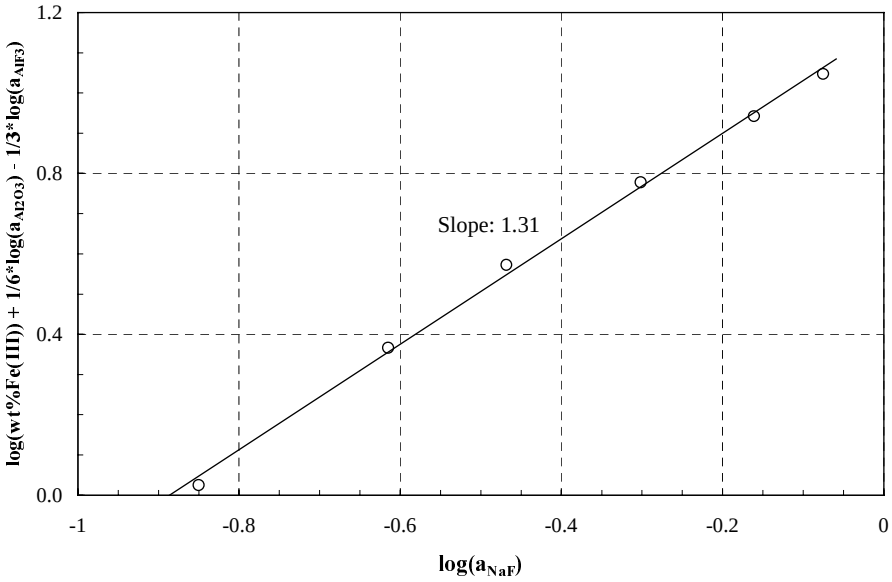

Figure 5-17: log(wt% Fe(III)) + 1/6*log $(a_{Al_2O_3})$ – 1/3*log (a_{AlF_3}) *versus* log(a_{NaF}) (eq. [5-59]) at 1020 °C in alumina-saturated cryolitic melts at 1020 °C in oxygen.

Within the accuracy the slope of the curve is close to 1, which means that the most plausible reaction mechanism is:

$$\frac{1}{2}Fe_2O_3 + \frac{1}{3}AlF_3 + NaF = NaFeOF_2 + \frac{1}{6}Al_2O_3 \qquad [5\text{-}60]$$

If one uses the same argument for the iron-oxy-aluminate, one can plot [5-55] in a similar way by setting,

$$\log(wt\%\,Fe(III)) + \frac{1}{6}\log(a_{Al_2O_3}) - \frac{4}{3}\log(a_{AlF_3}) = x \cdot \log(a_{NaF}) + const. \qquad [5\text{-}61]$$

Equation [5-61] is plotted in Figure 5-18.

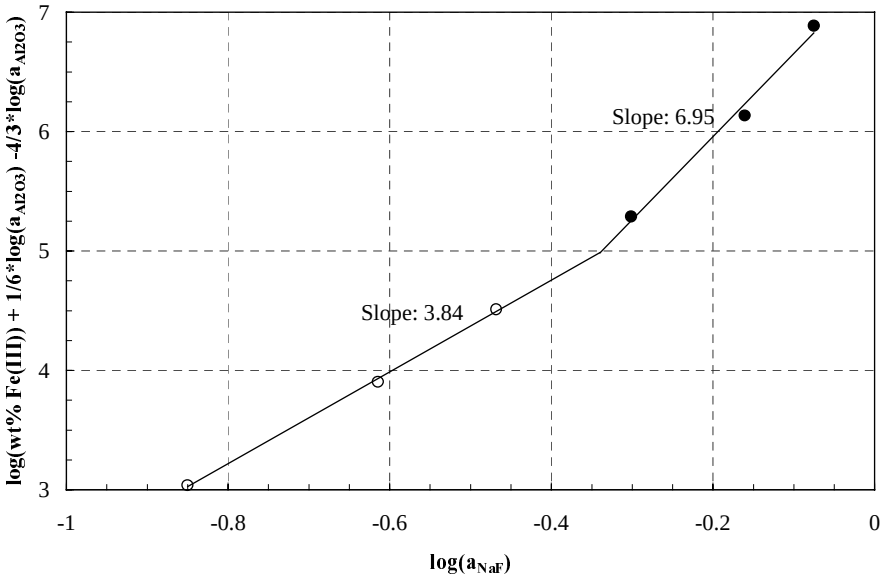

Figure 5-18: log(wt% Fe(III)) + 1/6*log $(a_{Al_2O_3})$ – 4/3*log (a_{AlF_3}) *versus* log(a_{NaF}) (Eq. [5-61]) at 1020 ^oC in alumina-saturated cryolitic melts at 1020 ^oC in oxygen.

The x value is close to 4 in acidic melts (*i.e.* log(a_{NaF}) < -0.46), which implies that $Na_4AlFeOF_8$ is a plausible species in these melts according to the following reaction mechanism,

$$\frac{1}{2}Fe_2O_3 + \frac{4}{3}AlF_3 + 4NaF = Na_4AlFeOF_8 + \frac{1}{6}Al_2O_3 \qquad [5\text{-}62]$$

while in basic melts (*i.e.* log(a_{NaF}) > -0.46) where "x" is close to 7:

$$\frac{1}{2}Fe_2O_3 + \frac{4}{3}AlF_3 + 7NaF = Na_7AlFeOF_{11} + \frac{1}{6}Al_2O_3 \qquad [5\text{-}63]$$

seems to occur.

By modelling Fe(III) species represented by equations [5-55] and [5-56] in a similar way as shown for Fe(II) by equation [5-47], one gets equations [5-64] and [5-65] respectively. These two equations are shown for different "x" values of "K_x" in the equations in Figure 5-19.

$$a_{Na_xAlFeOF_{(4+x)}} = K_x \cdot \left(\frac{a_{Al_2O_3}^{1/6}}{a_{AlF_3}^{4/3} \cdot a_{NaF}^{x}} \right)^{-1} \qquad [5\text{-}64]$$

$$a_{Na_xFeOF_{(1+x)}} = K_x \cdot \left(\frac{a_{Al_2O_3}^{1/6}}{a_{AlF_3}^{1/3} \cdot a_{NaF}^{x}} \right)^{-1} \qquad [5\text{-}65]$$

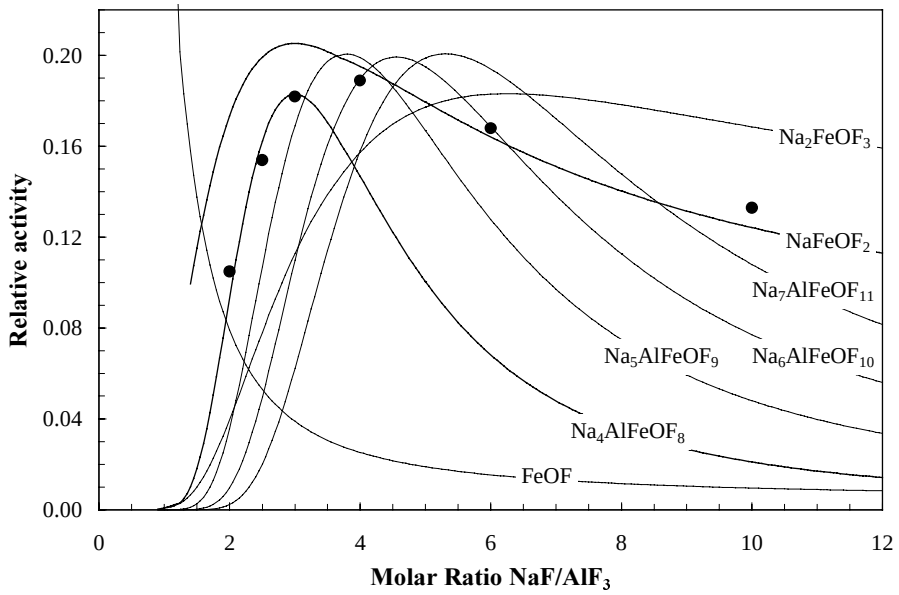

Figure 5-19: Model fitting of $Na_xFeOF_{(1+x)}$ and $Na_xAlFeOF_{(4+x)}$ in alumina-saturated cryolite melts as a function of CR at 1020 ^oC in an atmosphere of argon.

According to Figure 5-19, $NaFeOF_2$ and $Na_4AlFeOF_8$ seem to give the best fit for Diep's solubility measurements of Fe(III) expressed as weight percent Fe(III)in alumina-saturated cryolite melts. In acidic melts $Na_4AlFeOF_8$ seems to be the stable specie, while in basic melts $NaFeOF_2$ seems to be dominant.

The aluminium-containing complexes that Diep (5) suggested (Na_3FeF_6 and some $Na_2AlFeOF_6$, $Na_6AlFeOF_{10}$ and $Na_2AlFeO_2F_4$) may possibly be present in cryolite melts at low alumina concentrations, but according to the present interpretation of the solubility data the species $NaFeOF_2$ (in basic) and Na_4AlFeO_8 (in acidic) seem to be the most probable complexes in alumina-saturated cryolitic melts. One would expect the opposite to be the case, *i.e.* more sodium associated with the complex in basic melts where the activity of NaF is higher than in acidic melts. One might explain this behaviour by considering the equilibrium of these two species, *i.e.*:

$$\text{Basic}: NaFeOF_2 = NaF + FeOF \qquad [5\text{-}66]$$

$$\text{Acidic}: Na_4AlFeOF_8 = 4NaF + AlF_3 + FeOF = Na_3AlF_6 + NaF + FeOF \qquad [5\text{-}67]$$

Reaction [5-66] is more basic than [5-67].

5.11 Separation of Fe(II) and Fe(III) present in the same melt

Even if one uses an experimental arrangement that stabilises one of the two valances of iron , there will be a certain fraction of the other valence present in the same solution. If one uses pairs of Fe(II) and Fe(III) at the same activity of alumina, the amount of the other valence can be calculated. By the use of Diep's (5) solubility data obtained for Fe(III) and the present solubility data for Fe(II), the following procedure was used.

Diep's solubility data for Fe(III) given in Figure 5-15 (*i.e.* CR = 3.0 and in oxygen atmosphere) can be expressed as:

$$\text{Fe(III)} = 0.178 * a_{Al_2O_3}^{-0.153} \qquad [5\text{-}68]$$

The present solubility data for Fe(II) was calculated by the use of equations [5-12] and [5-13].

In the most general case one would expect that solutions of iron oxides in molten cryolite contain both Fe(II) and Fe(III) species and that Henry's law will apply because the concentrations are fairly low. It is convenient to take p_{O2} as the fundamental independent parameter since, once it is specified, the solid phase in equilibrium is defined and the remainig parameter, *i.e.* the activity of iron, can be calculated (6). Dewing and Thonstad (6) derived the following two equations for the solubilities of Fe(II) and Fe(III),

$$Fe + \frac{1}{2}O_2 = Fe^{2+}_{solution} + O^{2-}_{solution} \qquad [5\text{-}69]$$

$$Fe + \frac{3}{4}O_2 = Fe^{3+}_{solution} + \frac{3}{2}O^{2-}_{solution} \qquad [5\text{-}70]$$

It should be noted that these two equations are purely formal. Nothing is assumed about the chemical environment in which either the iron or the oxide ions are. Then, for a fixed composition of solvent,

$$[\text{Fe(II)}] = K_1 \cdot a_{Fe} \cdot p_{O_{2(g)}}^{1/2} \qquad [5\text{-}71]$$

and

$$[\text{Fe(III)}] = K_2 \cdot a_{Fe} \cdot p_{O_{2(g)}}^{3/4} \qquad [5\text{-}72]$$

where square brackets mean concentrations (here wt%), K_1 and K_2 constants and the pressure "p" is in bar.

For all practical purposes an experiment performed in a laboratory under normal atmospheric pressure may be regarded as being operated at one atm. Specification of a fixed solvent composition is important since AlF_3 may be involved in the dissolution reaction, and the concentration of Al_2O_3 controls the activity of O^{2-} ions. It is only if their activities are held constant that the above simple relations can be expected to hold (6).

K_1 and K_2 reflect properties exclusively of the solution and not of the solids with which it was in equilibrium when the measurements were made. This means that if one multiplies K_1 by the value of "$a_{Fe} \cdot p_{O_2}^{1/4}$" for pure FeO, then one gets the quantity of Fe(II),only, which would be in equilibrium with pure solid FeO at all alumina contents. Then, *one does not need to deal with the fact that $FeAl_2O_4$ forms at high alumina concentrations*.

The total concentration of Fe, called "Total Fe", is the experimental concentration, which is the sum of [5-71] and [5-72],

$$[\text{Total Fe}] = K_1 \cdot a_{Fe} \cdot p_{O_{2(g)}}^{1/2} + K_2 \cdot a_{Fe} \cdot p_{O_{2(g)}}^{3/4} \qquad [5\text{-}73]$$

In the measurements with Fe crucibles, $a_{Fe} = 1$, and in order to calculate the oxygen partial pressure. One has to now what is the stable solid phase (FeO or $FeAl_2O_4$) in equilibrium with with the solution at that alumina concentration. At low alumina concentrations, one has FeO at unit activity, and [5-73] can be used directly. However, if the alumina concentration is high enough to stabilise $FeAl_2O_4$, one has to calculate the alumina activity to get the partial oxygen pressure.

The formation reaction for $FeAl_2O_4$ can be expressed as:

$$Fe + \frac{1}{2}O_{2(g)} + Al_2O_3 = FeAl_2O_4 \qquad \Delta G^{o}_{1293.15K} = -196.667 \text{ kJ/mol} \qquad [5\text{-}74]$$

and the corresponding equilibrium constant $K_{FeAl2O4}$:

$$K_{FeAl2O4} = \left[\frac{a_{FeAl_2O_4}}{a_{Fe} \cdot p_{O_{2(g)}}^{1/2} \cdot a_{Al_2O_3}} \right] = 10^{-7.940} \qquad [5\text{-}75]$$

At equilibrium the activities of Fe and $FeAl_2O_4$ are unity, so $p_{O_{2(g)}}^{1/2}$ is given by:

$$p_{O_{2(g)}}^{1/2} = \left[\frac{1}{K_{FeAl2O4} \cdot a_{Al_2O_3}} \right] \qquad [5\text{-}76]$$

In the region where the alumina activity is high enough to keep the solution in equilibrium with solid $FeAl_2O_4$, the partial oxygen pressure is given by [5-76].

The partial oxygen pressure in equation [5-71] can for alumina concentrations low enough to stabilise FeO be calculated using the formation reaction for FeO:

$$FeO = Fe + \frac{1}{2}O_{2(g)} \qquad \Delta G^{o}_{1293.15K} = -180.320 \text{ kJ/mol} \qquad [5\text{-}77]$$

At equilibrium the activities of FeO and Fe (iron crucible) are unity, and the partial oxygen pressure can be expressed as:

$$p_{O_2}^{1/2} = K_{FeO} = 10^{-7.284} \qquad [5\text{-}78]$$

Since an iron crucible was used for all the solubility measurements for FeO, the Fe activity is unity, which implies that the partial oxygen pressure in [5-71] is given by equation [5-76] for the aluminate region, and:

$$[Fe(II)] = K_1 \cdot a_{Fe} \cdot p_{O_{2(g)}}^{1/2} = K_1 \cdot a_{Al_2O_3} \cdot 10^{-8.227} \qquad [5\text{-}79]$$

The expression for the FeO region follows correspondingly by combining [5-71] and [5-78]:

$$[Fe(II)] = K_1 \cdot a_{Fe} \cdot p_{O_{2(g)}}^{1/2} = K_1 \cdot K_{FeO} = K_1 \cdot 10^{-7.284} \qquad [5\text{-}80]$$

In an atmosphere of oxygen at unit activity, Fe(III) does not form aluminate (see figure 2-3), so one only has to deal with the reaction,

$$Fe_2O_3 = 2Fe + \frac{3}{2}O_{2(g)} \qquad \Delta G^{o}_{1293.15K} = 489.338 \text{ kJ/mol} \qquad [5\text{-}81]$$

with the equilibrium constant K_{Fe2O3},

$$K_{Fe2O3} = \left[\frac{a_{Fe}^{2} \cdot p_{O_{2(g)}}^{3/2}}{a_{Fe_2O_3}} \right] = 10^{-19.776} \qquad [5\text{-}82]$$

At equilibrium, the activities of Fe_2O_3 and the partial oxygen pressure are unity, and the activity of Fe is given by:

$$a_{Fe} = K_{Fe2O3}^{1/2} = 10^{-9.883} \qquad [5\text{-}83]$$

which implies that,

$$[Fe(III)] = K_2 \cdot a_{Fe} \cdot p_{O_{2(g)}}^{3/4} = K_2 \cdot 10^{-9.883} \qquad [5\text{-}84]$$

The values for K_1 and K_2 are found simultaneously by using to sets of solubility data expressed by equation [5-70] at *the same alumina activity*. The first [Fe total] corresponds to the solubility of Fe in a specific melt in an iron crucible, and the other [Fe total] is given for the solubility of Fe in the same melt composition under an atmosphere of oxygen. Equation [5-79] is given for Fe(II) in the region where $FeAl_2O_4$ is stable and [5-80] in the region where FeO is stable, while [5-84] is given for Fe(III) for all the alumina concentrations investigated.

The stability diagram for the iron phases present in a system with alumina and oxygen was constructed (see Figure 2-2 page 23), using a set of activities and thermodynamic data from (6). The activity data used are summarised in Table 5-5.

Table 5-5: Equilibrium oxygen pressures and iron activities at 1020 ^{o}C. Items 1.- 6. from (6), and 7.-8. are the present results.

#	Equilibrium	$\log(pO_2)$	$\log(a_{Fe})$	$\log(a_{Fe}*(pO_2)^{1/2})$	$\log(a_{Fe}*(pO_2)^{3/4})$
1.	Fe-$Fe_{0.947}O$	-14.567	0.000	-7.284	-10.925
2.	$Fe_{0.947}O$-Fe_3O_4	-12.887	-0.887	-7.331	-10.552
3.	Fe_3O_4-Fe_2O_3	-4.856	-6.241	-8.669	-9.883
4.	Fe_2O_3-O_2	0.000	-9.883	-9.883	-9.883
5.	Fe-$FeAl_2O_4$ ($a(Al_2O_3)$ =1)	-16.454	0.000	-8.227	-12.341
6.	$FeAl_2O_4$-Fe_3O_4 ($a(Al_2O_3)$ =1)	-7.646	-4.381	-8.204	-10.116
7.	Fe-$FeAl_2O_4$ ($a(Al_2O_3)$ =1)	-15.879	0.000	-7.940	-11.909
8.	$FeAl_2O_4$-Fe_3O_4 ($a(Al_2O_3)$ =1)	-9.232	-3.324	-7.940	-10.248

As an example of how the amounts of Fe(II) in Fe(III) can be calculated, the following treatment serves as an illustration of how it was done. At alumina saturation $FeAl_2O_4$ is the stable solid phase in an iron crucible and Fe_2O_3 is stable in oxygen atmosphere. The values of [Fe(II)] and [Fe(III)], in the calculations, given by $K_1 \cdot$"$a_{Fe} \cdot p_{O_2(g)}^{1/2}$"and $K_2 \cdot$"$a_{Fe} \cdot p_{O_{2(g)}}^{3/4}$", respectively, are given by items 4. and 5. in Table 5-5.

	Fe(II)		Fe(III)		Total Fe
1 atm O2:	1.309E-10 K_1	+	1.309E-10 K_2	=	0.178 Fe(III)
Fe crucible:	1.100E-08 K_1	+	1.154E-12 K_2	=	0.323 Fe(II)

In this particular case, the equations gave $K_1 = 1.33*10^9$, $K_2 = 2.93*10^7$, which gives 2.15% of the total iron in solution is Fe(II) in an atmosphere of oxygen and 0.50% of the total iron is Fe(III) in the iron crucible.

The same procedure was used to calculate the mixture of Fe(II) and Fe(III) in cryolite with alumina contents ranging from 1.5 wt% to alumina saturation. The results are given in Figure 5-20 in steps of 0.5 wt% alumina.

As one can see from Figure 5-20, the amount of Fe(II) in an oxygen atmosphere is considerably higher than the amount of Fe(III) in an iron crucible at any fixed solvent composition.

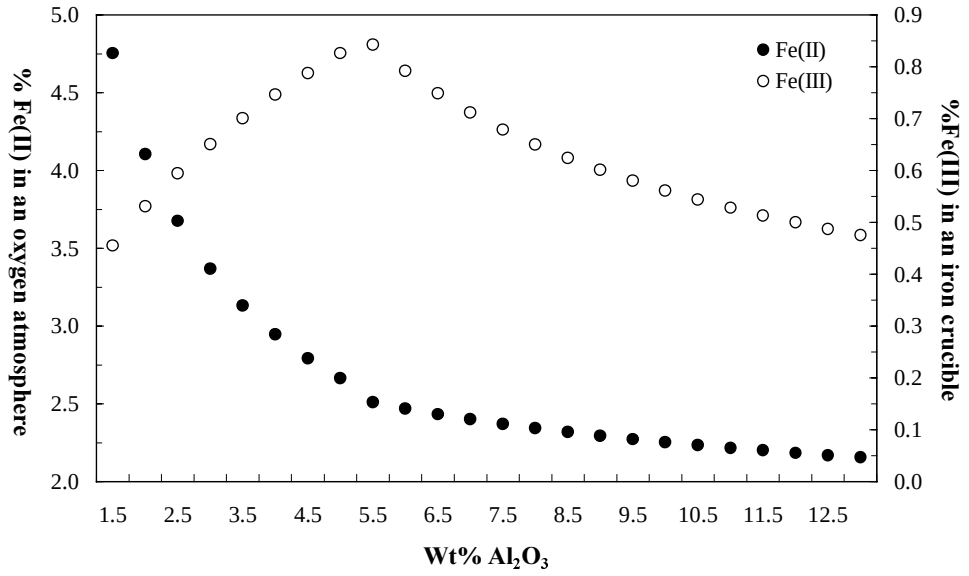

Figure 5-20: The amounts of Fe(II) in an oxygen atmosphere and of Fe(III) in an iron crucible.

Using the present results for K_1 and K_2 one can now calculate the equilibrium amounts of Fe(II) and Fe(III) at a fixed solvent composition at *all* oxygen pressures (ref. stability diagram 2-2 page 23). On a log-log plot the lines for the concentration of Fe(II) and Fe(III) are straight within the stability range of the solid phases, so the Figures are easily constructed from the data in Table 5-5. As an illustration, the procedure for how to obtain such a diagram for alumina-saturated melts at all oxygen pressures (*i.e.* along the right-hand border of diagram 2-2) will be explained.

In the $FeAl_2O_4$ range the concentration of Fe(II) is constant but the concentration of Fe(III) goes up as the oxygen pressure is raised. In the Fe_2O_3 region the Fe(III) is constant but the Fe(II) goes down as the oxygen pressure is raised. In the Fe_3O_4 region both change as shown in Figure 5-21.

The formation of Fe_3O_4 can be expressed as:

$$3Fe_{(s)} + 2O_{2(g)} = Fe_3O_{4(s)} \qquad [5\text{-}85]$$

The equilibrium constant for this reaction, $K_{[5\text{-}85]}$, is given by:

$$K_{[5-85]} = \left[\frac{1}{a_{Fe}^3 \cdot p_{O_2}^2} \right] \qquad [5\text{-}86]$$

The logarithm of [5-86] can be transformed to,

$$\log(a_{Fe}) + \frac{2}{3}\log(p_{O_2}) = -\frac{1}{3}\log(K_{[5-85]})^{-1} = C_{[5-85]} \qquad [5\text{-}87]$$

By fitting the logarithm of the concentrations of Fe(II) and Fe(III) given by reactions [5-71] and [5-72], respectively, to equation [5-87], one gets the expressions for the change of Fe(II) and Fe(III) in the Fe_3O_4–region, *i.e.*:

$$\log[Fe(II)] = C_{[5-85]} \cdot \log(K_1) - \frac{1}{6}\log(p_{O_2}) \qquad [5\text{-}88]$$

$$\log[Fe(III)] = C_{[5-85]} \cdot \log(K_2) + \frac{1}{12}\log(p_{O_2}) \qquad [5\text{-}89]$$

The same type of equations can be written for the $Fe_{0.947}O$ (called FeO'), Fe_2O_3 and $FeAl_2O_4$-regions as well. For $FeAl_2O_4$ this means that by using the formation reaction,

$$Fe_{(s)} + \frac{1}{2}O_{2(g)} + Al_2O_{3(s,\alpha)} = FeAl_2O_{4(s)} \qquad [5\text{-}90]$$

one gets the following two expressions for unit alumina activity,

$$\log[Fe(II)] = C_{[5-90]} \cdot \log(K_1) \qquad [5\text{-}91]$$

$$\log[Fe(III)] = C_{[5-90]} \cdot \log(K_2) + \frac{1}{4}\log(p_{O_2}) \qquad [5\text{-}92]$$

where $C_{[5\text{-}90]} = -\log(K_{[5\text{-}90]})$.

Figures 5-21 to 5-24 show the situation for 4 different alumina concentrations and the corresponding stable solid iron phases shown in Figure 2-2 p. 23 (*i.e.* as vertical lines).

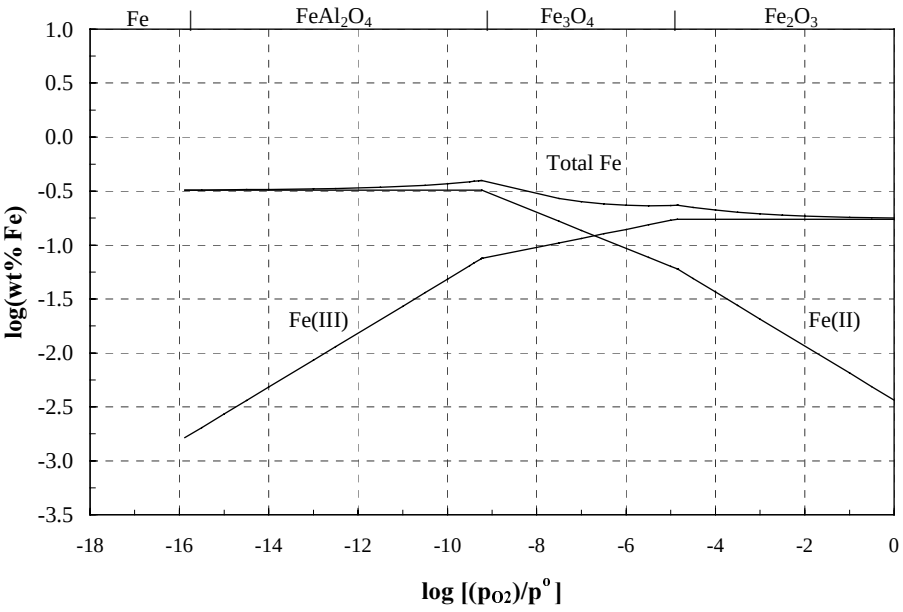

Figure 5-21: The amounts of Fe(II) and Fe(III) as a function of the partial oxygen pressure in alumina-saturated cryolite at 1020 °C.

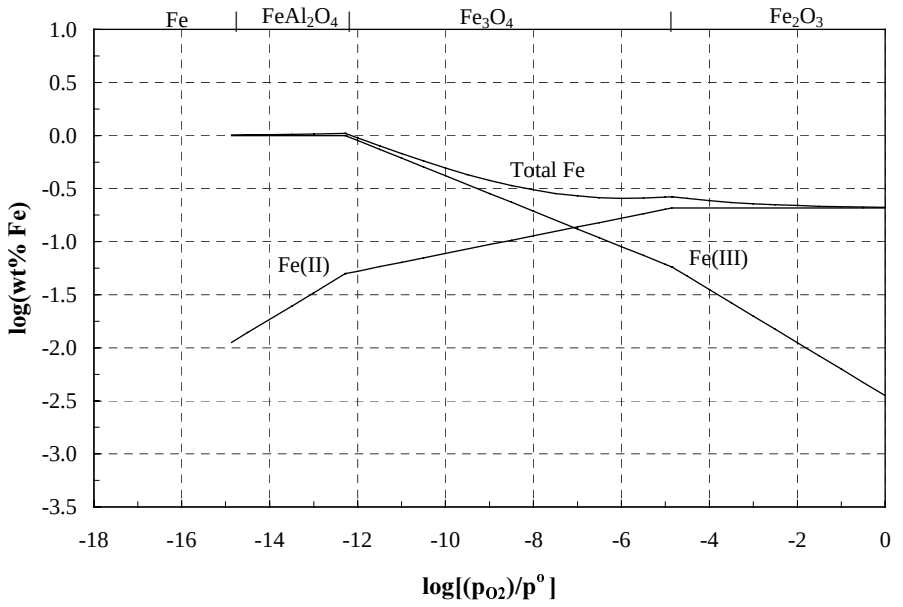

Figure 5-22: The amounts of Fe(II) and Fe(III) as a function of the partial oxygen pressure in cryolite with 6.5 wt% alumina at 1020 °C.

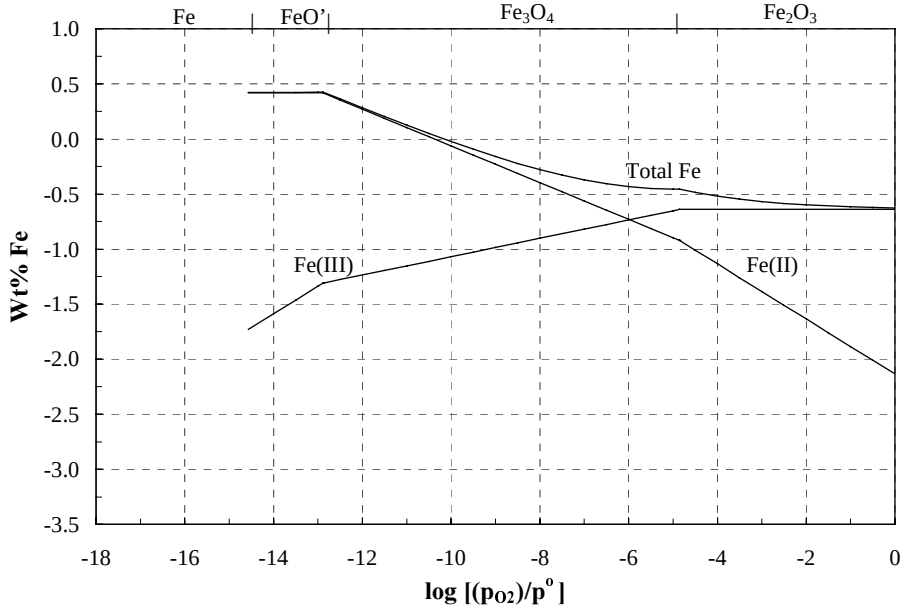

Figure 5-23: The amounts of Fe(II) and Fe(III) as a function of the partial oxygen pressure in cryolite with 4.5 wt% alumina at 1020 °C.

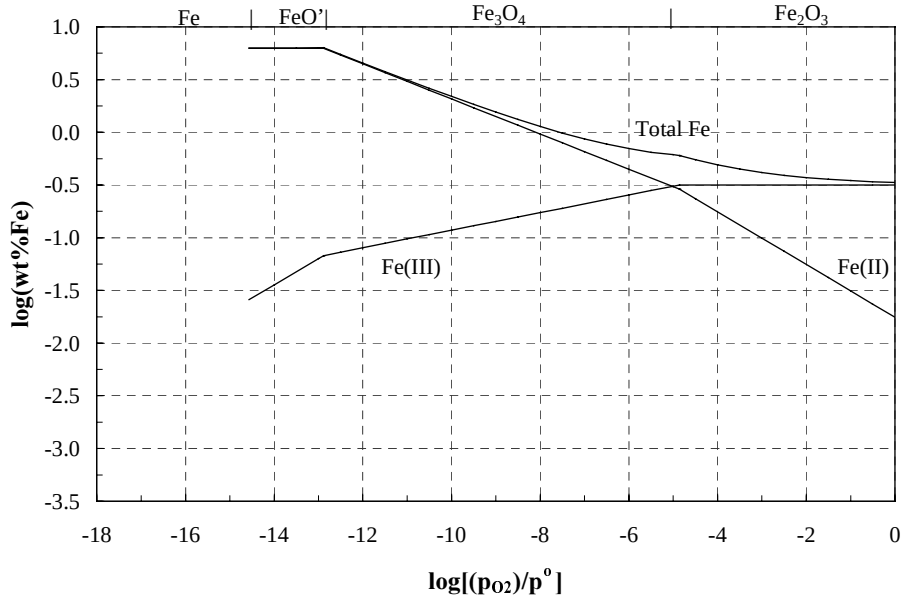

Figure 5-24: The amounts of Fe(II) and Fe(III) as a function of the partial oxygen pressure in cryolite with 1.5 wt% alumina at 1020 °C.

5.12 The reversible potential between Fe(II) and Fe(III) and its implications

The amounts of Fe(II) and Fe(III) are equal at the intercepts between the Fe(II) and Fe(III) lines in Figures 5-21 to 5-24, and it defines the reversible potential between Fe(II) and Fe(III). According to equations [5-71] and [5-72] one gets the following expression at the intercepts,

$$K_1 \cdot a_{Fe} \cdot p_{O2}^{1/2} = K_2 \cdot a_{Fe} \cdot p_{O_2}^{3/4} \qquad [5\text{-}93]$$

which can be rearranged to give,

$$p_{O2} = \left[\frac{K_1}{K_2}\right]^4 \qquad [5\text{-}94]$$

The standard potential with respect to the reversible oxygen electrode for the reaction,

$$6Fe_2O_3 = 4Fe_3O_4 + O_2 \qquad [5\text{-}95]$$

where n = 4, is given by:

$$E^o = \frac{RT}{4F} \cdot \ln\left[p_{O_2}\right] = \frac{RT}{F} \cdot \ln\left[\frac{K_1}{K_2}\right] \qquad [5\text{-}96]$$

In Figure 5-25 a log-log plot of Equation [5-96] is plotted as a function of alumina activity. The break in the curve at around –0.43V corresponds to the fact that two linear and discrete equations obtained for the solubility of Fe(II) were used in the calculations (equations [5-12] and [5-13]), and the difference in slope between those two lines was not exactly 1 as the model for the Fe(II) species present in these models predicted.

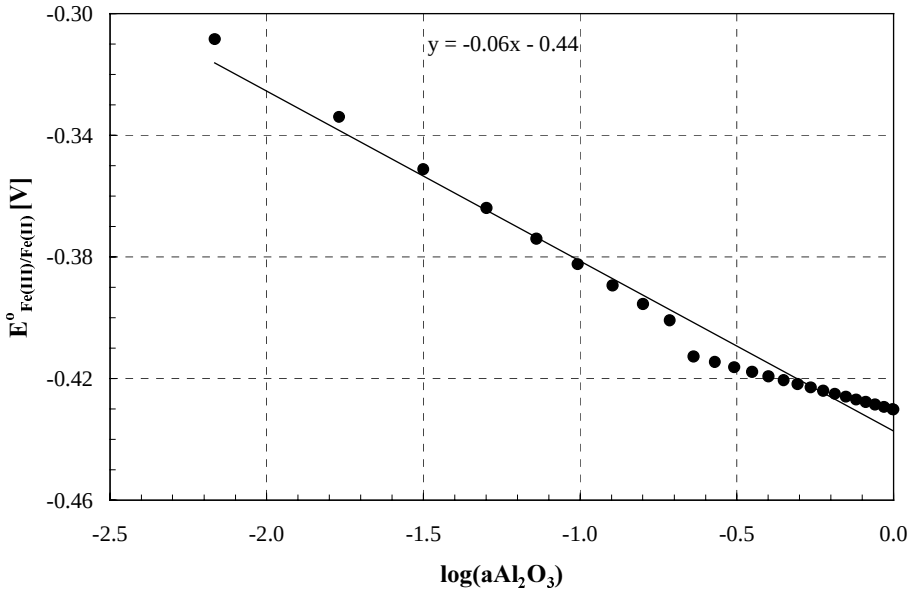

Figure 5-25: The standard potential of Fe(III)/Fe(II) with respect to a reversible oxygen electrode obtained in cryolite-alumina melts at 1020 °C.

Dewing and Thonstad (6) calculated the standard oxygen potential for Fe(III)/Fe(II) based on the assumption that both Fe(II) and Fe(III) were present in the melt as fluorides,

$$4FeF_2 + \frac{4}{3}AlF_3 + O_2 = 4FeF_3 + \frac{2}{3}Al_2O_3 \qquad [5\text{-}97]$$

with a theoretical slope for $\partial\log(p_{O2})/\partial\log(a_{Al2O3})$ being +2/3. Dewing and Thonstad (6) obtained a slope of +0.72, but since it was based on only two points they did not make any assessment of the accuracy of the results. The slope of the curve given in Figure 5-25 for the presently obtained data is, however, –0.87. The negative sign of the slope implies that one of the iron species is associated with oxide ions (O^{2-}). According to the present results a slope of -2/3 can be explained by the reaction,

$$4FeF_2 + O_2 + \frac{2}{3}Al_2O_3 = 4FeOF + \frac{4}{3}AlF_3 \qquad [5\text{-}98]$$

Taken into account the discontinuity of the curve that the slope of –0.87 was based on, the agreement between this slope and the theoretical slope of [5-98] is satisfactory.

To interpret the results for the standard potential in terms of the Hall-Heroult cell process is not easy since the process normally operates in melts with CR ~2.29 (excess AlF_3), ~5 wt% CaF_2 and 60 degrees lower temperature than for the melts the presents results were based on.

The reversible $C/CO_{2(g)}$ potential lies ~1 V below the reversible potential of $O_{2(g)}$ potential (3), but a carbon anode working at a current density of around 1 A/cm^2 has an overpotential of about 0.55 V (39), and it becomes even more positive at low alumina concentrations (40). This means that the $C/CO_{2(g)}$ during polarisation lies at –0.45 V with respect to the reversible oxygen potential. In the traditional Hall-Héroult process the anode gas, consisting of $CO_{2(g)}$ with 10 – 20 % $CO_{(g)}$, has an equilibrium oxygen potential given by:

$$CO_{(g)} + \frac{1}{2}O_{2(g)} = CO_{2(g)} \qquad \Delta G^{o}_{1233.15K} = -175.602\ \text{kJ/mol}\ (4) \qquad [5\text{-}99]$$

The partial oxygen pressure can then be calculated by inserting suitable partial pressures for $CO_{(g)}$ and $CO_{2(g)}$ into:

$$p_{O_{2(g)}} = \left[\frac{p_{CO_{2(g)}}}{p_{CO} \cdot K_{[5\text{–}99]}}\right]^2 \qquad [5\text{-}100]$$

where $K_{[5\text{-}99]}$ is the equilibrium constant for reaction [5-99].

The equilibrium oxygen potential is then given by:

$$E^{o} = \frac{RT}{2F} \cdot \ln\left[p_{O_2}\right]^2 \qquad [5\text{-}101]$$

Calculations give equilibrium oxygen potentials of –0.76 to –0.81 V at 1293.15 K. According to the results in Figure 5-25 the standard potential of Fe(III)/Fe(II) is from –0.43 to –0.31 V with respect to oxygen, indicating that the anode gas cannot be effective in oxidising Fe(II) in solution. The carbon anode itself can, however, cause some oxidation, but will be harder if the additional AlF_3 in the commercial electrolyte[5] pushes the reversible Fe(II)/Fe(III) potential in the positive direction (see [5-98]).

Based on the present calculations, it seems that the reversible Fe(III)/Fe(II) potential is too high to explain the model for loss of current efficiency proposed by Sterten and Solli (41) and Sterten (42), (43), due to iron in Hall-Héroult cells. They assumed that current is used during electrolysis to parasitic cyclic redox reactions of polyvalent impurities like iron, within the electrolyte/anode gas boundary layer:

$$Fe^{2+} + \frac{1}{2}CO_2 = Fe^{3+} + \frac{1}{2}CO + \frac{1}{2}O^{2-} \qquad [5\text{-}102]$$

where CO and CO_2 were dissolved in the melt.

The oxidation of Fe^{2+} to Fe^{3+} will, however, be a cause of concern when inert anodes are used. However, the ultimate loss of current efficiency may not be significant since the amount of iron that could be tolerated in solution would be low for other reasons like demand for low metal (Al) impurity contents and low anode corrosion rates.

[5] At 1233.15 K the equilibrium oxygen potential is –0.79 to –0.84 V.

5.13 Solubility of Fe_2O_3 in industrially interesting melts

Since solubility data were not found for Fe(III) for the particular melt composition investigated in Chapter 7, it was decided to determine it by dissolving Fe_2O_3 in a platinum crucible in an oxygen atmosphere as described by Diep (5). The results are shown in Table 5-6.

Table 5-6: Solubility of Fe(III) as a function of temperature in alumina-saturated cryolitic melts with CR = 2.29 in an oxygen atmosphere.

Temperature [^oC]	960	980	1000
Solubility of Fe(III) [wt%]	0.132	0.153	0.175

The present results seem to be slightly lower than the ones reported by DeYoung (33), but they are in general agreement with each other.

5.14 References

(1) *Technical Working Group on Inert Anode Technology*, American Society of Mechanical Engineers', CRTD - vol. 53, under contract to The U.S. Department of Energy Office of Industrial Technologies, ASME International, July, 1999.

(2) Hatch, J.E., *Aluminium*, *Properties and Physical Metallurgy*, American Society for Metals, 3 ed, Metals Park, Ohio, USA,1988.

(3) Barin, I., *Thermodynamical Data of Pure Substances*, 3rd ed., VCH Verlags-gesellschaft mb-H, D-69451, Weinheim, Germany, 1995.

(4) Knacke, O., Kubaschewski, O. and Hesselmann,K., *Thermochemical Properties of Inorganic Substances*, 2nd ed., Springer-Verlag, Verlag Stahleisen, 1991.

(5) Diep, Q.B., *Structure and thermodynamics of cryolite-based melts with addition of Al_2O_3 and Fe_2O_3. Cyclic voltammetry study of Fe_2O_3 in molten cryolite, PhD. thesis no 28, NTNU, Trondheim, Norway, 1998.*

(6) Dewing, E.W. and Thonstad, J., *Solutions of Iron Oxides in Molten Cryolite*, Metall. Mater. Trans. B, vol. 31, no. 4, pp. 609–613, Aug., 2000.

(7) Southampton Electrochemistry Group, *Instrumental Methods in Electrochemistry*, University of Southampton, Ellis Horwood Series in Physical Chemistry, pp 73-74, 1993.

(8) Delahay, P., *New Instrumental Methods in Electrochemistry. Theory, Instrumentation and Applications to Analytical and Physical Chemistry*, Interscience Publishers, Inc., Catalogue No. 54-7991, New York, p. 20, 1954.

(9) Jentoftsen, T.E., Dewing.E.W., Haarberg, G.M. and Thonstad,J., *The Solubility of FeO and $FeAl_2O_4$ in Cryolite Based Melts*, to be published at the Twelfth International Symposium on Molten Salts, J. Electrochemical Soc., Oct., pp. 473–484, 1999.

(10) Ullmann's Encyclopaedia of Industrial Chemistry, VCH Verlagsgesellschaft mbH, Weinheim, Germany, vol 14A, 5th ed., p. 463, 1989.

(11) Xiao, H., *On the Corrosion and the Behavour of Inert Anodes in Aluminium Electrolysis,* doktoringeniøravhandling NTH, no. 8, Norway, 4, 1984.

(12) Sterten, Å. and Skar, O., *Some Binary Na_3AlF_6-M_xO_y phase diagram*, Aluminium 64, pp. 1051- 1054, 1988.

(13) Dewing, E.W. and Thonstad, J., *Activities in the System Cryolite-Alumina*, Metall. Mater. Trans. B, Vol. 28 B, pp 1089-1093, Dec. 1997.

(14) Dewing, E.W. and Thonstad, J., *Communication: Solution of CeO_2 in Cryolite Melts*, Metall. Mater. Trans. B, vol. 28B, p. 1257, dec. 1997.

(15) Solheim, A. and Sterten, Å., *Activity of alumina in system NaF-AlF_3-Al_2O_3 at NaF/AlF_3 molar ratios ranging from 1.4 to 3*, Light Metals1999, pp. 445 – 452, 1999.

(16) Solheim, A. and Sterten, Å., *Activity Data for the System NaF-AlF_3*, Ninth International Symposium on Light Metals Production, pp. 225, Tromsø-Trondheim, Norway, Aug. 18.–21., 1997.

(17) Solheim, A., Rolseth, S., Skybakmoen, E., Støen, L., Sterten, Å. and Støre, T., *Liquidus Temperatures for Primary Crystallization of Cryolite in Molten Salt Systems of interest for the Aluminium Electrolysis*, Met. Trans. B, *27*B, pp. 739-742, 1996.

(18) Solheim, A., Rolseth, S., Skybakmoen, E., Støen, L., Sterten, Å. and Støre, T., *Liquidus Temperatures and Alumina Solubility in the System Na_3AlF_6-AlF_3-LiF-CaF_2-MgF_2*, Light Metals 1995, pp. 451–460, 1995.

(19) Holm, J.L., *Thermodynamic Properties of Molten Cryolite and Other Fluoride Mixtures*, Thesis, Institutt for Uorganisk Kjemi, NTH, Norway, 1971.

(20) Montgomery, D.C. and Peck, E.A., *Introduction to linear regression*, ISBN 0-471-05850-5, John Wiley and Sons, Chapt. 5.2.2, 1982.

(21) Rezukhina, T.N., Levitskii, V.A. and Ozhegov, P., *Thermodynamic Properties of Iron Aluminate*, Russ. J. Phys. Chem., 1963, vol. 37, pp. 358-359, 1963.

(22) Chan, J.C., Alcock, C.B. and Jacob, K.T., *Electrochemical measurements of the oxygen potential of the system iron-alumina-hercynite in the temperature range 750 to 1600 ^oC,* Can. Met. Quart., vol. 12, no. 4, pp. 439–443, 1973.

(23) Johansen, H.G., *Jern som forurensningselement i aluminiumelektrolysen*, Dr.ing. (Ph.D.) thesis, NTH, Norway, 1975.

(24) Johansen, H.G., Sterten, Å. and Thonstad, J., *The Phase Diagram of the Systems Na_3AlF_6-$Fe_{0.947}O$ and Na_3AlF_6-FeF_2 and Related Activities of FeF_2 from Emf Measurements,* Acta Chem. Scand., vol. 43, pp. 417-420, 1989.

URN:NBN:no-6347

(25) Kachnovskaya, I.S., Osovik, V.I. and Kukhotkina, T.K., *Phase Transformation and Alumina Dissolution in Cryolite*, Sov. J. Non Ferrous Met., vol. 12, no. 44, pp. 44-46, 1971.

(26) Zhou, R-S. and Snyder, R.L., *Structures and Transformation Mechanisms of the η,γ and θ Transition Aluminas,* Acta Cryst., vol. B47, pp. 617-630, 1991.

(27) Wefers, K. and Misra, K., *Oxides and Hydroxides of Aluminium*, Alcoa Technical Paper No. 19, Revised, Alcoa Laboratories, 1987.

(28) Holmes, R.D., O'Neill, C.O. and Arculus, R.J., *Standard Gibbs free energy of formation for Cu_2O, NiO, CoO and Fe_xO: High resolution electrochemical measurements using zirconia solid electrolytes from 900-1400 K*, Geochim. Cosmochim. Acta, vol. 30, pp. 2439-2452, 1986.

(29) McLean, A. and Ward, R.G., *Thermodynamics of hercynite formation*, J. of The Iron and Steel Intstitute, pp.8-11, Jan. 1966.

(30) Floridis, T.P., *Activity of Oxygen in Liquid Iron Alloys*, D.Sc. thesis, Massachusettes Institute of Technology, 1957, sited by Pillay *et al.* (32).

(31) Brokloff, J.E., Ph.D. thesis, University of Michigan, 1964, sited by McLean and Ward.

(32) Pillay, T.C.M., D'Entremont, J. and Chipman, J., *Stability of Hercynite at High Temperatures,* J. Am Cer. Soc., vol. 43, no. 11, pp. 583-585, Nov. 1960.

(33) DeYoung, D.H., *Solubilities of Oxides for Inert Anodes in Cryolite-Based Melts*, Light Metals 1986, pp 299-303, 1986.

(34) Sterten, Å. Hamberg, K. and Mæland, I., Activities *and Phase Diagram Data of NaF-AlF_3-Al_2O_3 Mixtures Derived From Electromotive Force and Cryoscopic Measurements. Standard Thermodynamical Data of β-Al_2O_3*, Acta Chem. Scand., A36, pp. 329-344, 1982.

(35) Sterten, Å. and Mæland, I., *Thermodynamics of Molten Mixtures of Na_3AlF_6-Al_2O_3 and NaF-AlF_3*, Acta Chem. Scand., A39, pp. 241-257, 1985.

(36) Ray, S.P., *Inert Anodes for Hall Cells,* Light Metals 1986, pp. 287-298, 1986.

(37) Foster, P.A. Jr., *Phase Equilibria in the Sodium Fluoride Enriched Region of the Reciprocal System Na_6F_6-Al2F6-Na6O3-Al2O3*, J. Chem. Eng. Data, vol. 9, no. 2, pp. 200-203, April 1964.

(38) Holm, J.L., *Undersøkelser av endel systemer med tilknytning til aluminium-elektrolysen,* Tidsskrift for Kjemi, Bergvesen og Metallurgi, vol. 26, no. 10, pp. 165-171, S.T. no. 2447, Norway, 1966.

(39) Dewing, E.W., *The Chemistry of the Alumina Reduction Cell*, Can. Met. Quart., vol. 30, no. 3, pp. 153–161, 1991.

(40) Thonstad, J., *The Electrode reaction on the C, CO_2 Electrode in Cryolite-Alumina Melts–Part I. Sready State Measurements,* Electrochim. Acta, vol 15, pp. 1569-1580, 1970.

(41) Sterten, Å. and Solli, P.A., *Cathodic Process and Cyclic Redox Reactions in Aluminium Reduction Cells*, J. Electrochem. Soc., vol. 25, pp. 809 - 816, 1995.

(42) Sterten, Å., *The Cathode Process and Back Reaction in Aluminium Reduction Cells*, Acta Chem. Scand., vol. 44, pp. 873-878, 1990.

(43) Sterten, Å., *Redox Reactions and Current Loss in Aluminium Reduction Cells*, Light Metals 1991, TMS, pp. 445 - 451, 1991.

URN:NBN:no-6347

URN:NBN:no-6347

6 Solubility of copper oxides in cryolite-alumina melts

Copper is the main metallic constituent in the nickel ferrite cermet investigated in the present work. Since the copper-rich alloy carries most of the current, it is of crucial importance that the metal phase remains stable during electrolysis. Copper may oxidise to Cu(I) and Cu(II), and the solubility limits for these two oxides in various melts is important to investigate to find the optimum melt composition where the solubility of copper ions are at the lowest.

During electrolysis, dissolved copper compounds are reduced into the liquid aluminium metal, affecting the physical and chemical properties of aluminium.

6.1 Copper as an impurity in aluminium

Copper (1) is one of the 5 elements together with zinc, magnesium, manganese and silicon, which form the basis for the principal commercial aluminium alloys. The most common aluminium alloys containing copper are the age-hardening alloys Al-Cu, Al-Cu-Mg and Al-Zn-Mg-Cu and the casting alloy Al-Si-Cu.

At 550 ^{o}C, the liquid solubility of copper in aluminium is 33.15 weight %, while the solid solubility is 5.67 weight %. Aluminium-copper alloys containing 2 to 10 % copper, generally with other additions, form important families of alloys. Both cast and wrought aluminium-copper alloys respond to solution heat treatment and subsequent ageing with an increase in strength and hardness and a decrease in elongation. The strengthening is maximum between 4 and 6 % copper, depending upon the influence of other constituents present.

The wrought form of casting aluminium alloys contain copper and minor additions of other elements like manganese, titanium, vanadium and zirconium which raise the re-crystallisation temperature of aluminium and its alloys. An alloy of this nature retains its properties well at elevated temperature, can readily be fabricated, and has good casting and welding characteristics. The stability is often reflected in the small reduction of strength with time at an elevated temperature.

All known metallic additions to aluminium reduce its electrical conductivity. Copper is one of the elements which increases the resistance the least, *i.e*. 0.344 $\mu\Omega\cdot$cm per weigh % added. As a comparison, iron increases the resistance with 2.56 $\mu\Omega\cdot$cm per weight %, and nickel 0.81 $\mu\Omega\cdot$cm.

Copper reduces the corrosion resistance of aluminium to a greater extent than any other alloying element. The influence of copper is highly dependent upon its amount, form, and distribution throughout the microstructure. In solid solution, copper shifts the corrosion potential of aluminium in the cathodic direction, the value depending on the amount

present. The corrosion potential is independent of the heat treating temperature if all the copper is in solid solution at the heat treating temperature.

6.2 Thermodynamical treatment of the stability of the copper valences

According to thermodynamics, a copper crucible under an argon atmosphere should stabilise Cu(I), while an oxygen atmosphere should stabilise Cu(II) in a platinum crucible. The use of platinum crucible may cause reduced Cu (from redox reactions between copper ions and impurities like Fe(II) in the melt) to alloy with the crucible. According to the binary Cu-Pt phase diagram (2), Cu is completely soluble in solid platinum at 1020 ^{o}C, but based on equation [6-3] the Cu activity will be low if the partial oxygen pressure is kept high.

Cu_2O can be decomposed to copper metal according to the equation,

$$Cu_2O = 2Cu + \frac{1}{2}O_{2(g)} \qquad [6\text{-}1]$$

where $\Delta G_f{}^{o}$ = 74.445 kJ/mol at 1020 ^{o}C (3). This gives a partial oxygen pressure of $9.67*10^{-7}$ atmosphere, which is far below the content of oxygen in the argon 4 (*i.e*. 99.99% Ar). This implies that argon 4 can be used safely without any reduction of Cu(I) to copper metal, which was used in the present investigation.

A system where CuO is dissolved in cryolite contained in a platinum crucible will probably cause a reduction of some of the Cu(II) to Cu(I) under an argon atmosphere. According to thermodynamics, the reaction,

$$CuO = Cu_2O + \frac{1}{4}O_{2(g)} \qquad [6\text{-}2]$$

has ΔG^{o} = 46.77 kJ/mol at 1020 ^{o}C (3), giving a partial oxygen pressure of 0.18 atmosphere. This implies that CuO will be reduced to Cu_2O if the partial pressure of oxygen is lower than 0.18 atmospheres. Therefore, an oxygen atmosphere should be used to stabilise Cu(II).

Sterten *et al.* measured the solubility of Cu(I) and Cu(II) in cryolite-alumina melts (4), (5), (6) and (7) using argon 4. Argon 4 contains around 200 ppm oxygen, which means that Cu_2O is the stable phase. Since Sterten *et al.* used an argon atmosphere for measuring the solubility of both CuO and Cu_2O, mainly the solubility of Cu(I) was measured in both systems. If the two data sets are compared according to *copper* solubility, they seem to describe the same system (see Figure 6-15).

CuO can be decomposed to copper metal according to the equation,

$$CuO = Cu + \frac{1}{2}O_{2(g)} \qquad [6\text{-}3]$$

where ΔG^o = 41.865 kJ/mol at 1020 ^oC. This gives a partial oxygen pressure of $4.15*10^{-4}$ atmosphere, which is only slightly above the content of oxygen in argon 4 used by Sterten *et al.* (4), (5), (6) and (7).

Thermodynamic data (8), (9), (10) and phase diagrams (11), (12) for the systems Cu_2O-Al_2O_3 and CuO-Al_2O_3 show the formation of copper aluminates in the solid state at high alumina concentrations.

Based on data from Jacob and Alcock (8) stability diagrams for the copper phases present as a function of alumina, oxygen and temperature were constructed. Figure 2-4 shows the diagram at 1020 ^oC. Only CuO and $CuAl_2O_4$ are stable under an oxygen atmosphere at 1020 ^oC. If on the other hand air is used, the phase diagram predicts that one is operating at a partial pressure of oxygen very close to several phase boundaries. There is a risk of getting a mixture of both Cu_2O and $CuAlO_2$ in the solutions depending on the alumina activity. If the temperature is changed from 1020 ^oC to 1025 ^oC, the dotted line in Figure 2-4 is coincident with the CuO/Cu_2O line, and it goes through the triple-point where CuO, $CuAl_2O_4$ and $CuAlO_2$ coexist at 1000 ^oC. The window showing the stability region for CuO increases at the expense of Cu_2O and $CuAl_2O_4$ with decreasing temperature.

Cyclic voltammograms (6) of CuO in cryolite melts contained in a copper crucible gave only one peak in the anodic direction, and there were some uncertainties whether this peak corresponded to the oxidation of Cu to Cu(I) or to Cu(II). The peak current as a function of sweep rate showed a linear behaviour, which indicates the dissolution reaction to be diffusion controlled.

6.3 Chemicals

Na_3AlF_6	*cryolite*	Handpicked Greenland cryolite was crushed and used as primary melt matrix.
NaF		P.a. Merck, heated under argon atmosphere at 400 ^oC for 10 hours.
AlF_3		Synthetic AlF_3 from Norzink, purified in the laboratory by sublimation and heated under an atmosphere of argon at 400 ^oC for 10 hours.
Al_2O_3	*alumina*	γ-Al_2O_3, P.a. Merck, dried at 200 ^oC.
LiF		P.a. Merck, > 99%
Cu_2O	*cuprite*	Johnson Matthey GmbH, 99,5 % Cu_2O, < 60 mesh, LOT: H22E19.
CuO		P.a. Merck, > 99 % CuO, powder.
Ar		Argon 4, AGA Gas, 99.99 % Ar, ~200 ppm $O_{2(g)}$
O_2		AGA Gas, 99.99 % $O_{2(g)}$

6.4 Experimental procedure for measuring the solubility of copper oxides

160 g of melt was prepared from the correct mixture of cryolite and alumina. Sufficient copper oxide was mixed with the melt to ensure excess copper oxide in the melt after saturation was reached. Cu(I) was stabilised by adding Cu_2O powder to the mixture of cryolite and AlF_3 contained in a copper crucible under an atmosphere of argon, while Cu(II) was stabilised by adding CuO to the melt contained in a platinum crucible under an atmosphere of oxygen. The test equipment shown in Figure 6-1 was lowered into a corrundum tube, in a resistance-heated furnace, and sealed. Approximately 4 ml/min of gas was flushed through the sealed corrundum tube during the experiment.

The temperature was measured continuously with a Pt/Pt10%Rh thermocouple inside a sealed platinum tube placed 2 cm from the bottom of the crucible. Constant temperature in the melt was obtained, with a maximum of 2 degrees temperature difference between the (hotter) top and the bottom of the crucible. Thermally induced convection was then avoided.

After the mixture had melted, proper convection was achieved in the melt by using a platinum stirrer for two hours, and then letting the melt settle for one hour before 5-8 grams of melt was withdrawn from the melt by a silica tube immersed 2-5 mm into the solution.

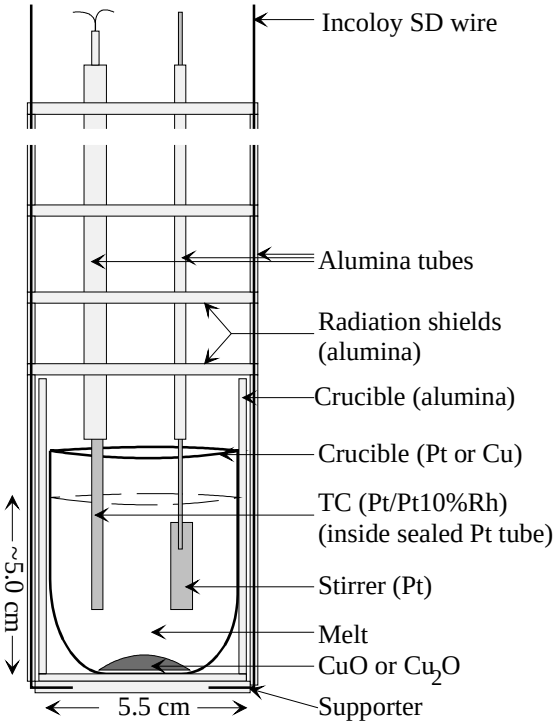

Figure 6-1: Sketch of the test equipment used for the copper oxide solubility experiments.

The melt samples taken from the various melts were analysed in the same way as described for nickel in Chapter 4.3 p. 62.

6.5 Solubility of Cu_2O

Cu(I) was stabilised by using a copper crucible and argon atmosphere.

6.5.1 Solubility of Cu_2O as a function of alumina concentration at 1020 °C

The solubility of Cu_2O, called "wt% Cu(I)", was measured as a function of the alumina concentrations in natural cryolite at 1020 °C. The results are presented in Figure 6-2.

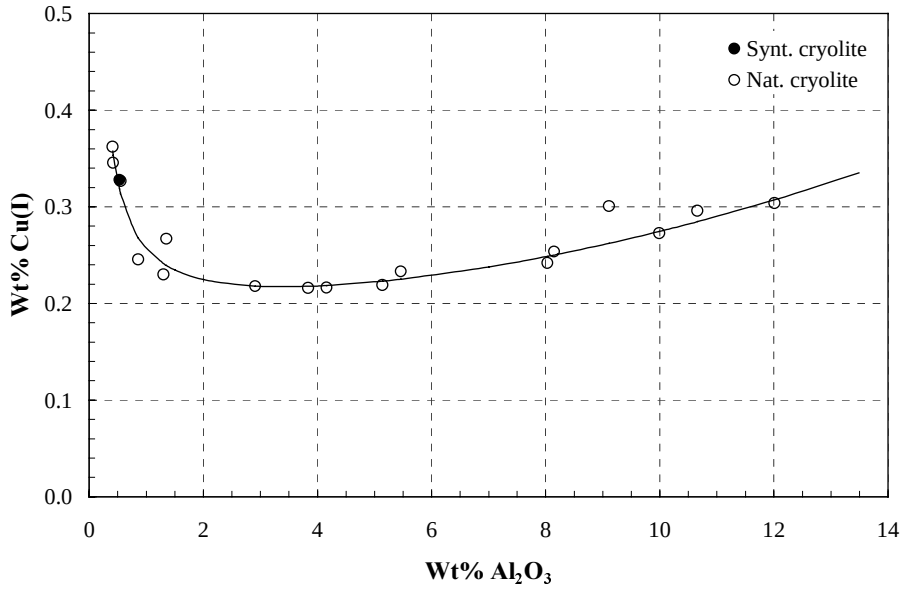

Figure 6-2: Solubility of Cu(I) as a function of the alumina concentration in natural cryolite at 1020 °C in an atmosphere of argon. The alumina concentration was determined with the LECO apparatus (data in Appendix B).

The samples taken from various melts had different colours depending on the amount of alumina in the melts. Some of the samples are shown in Figure B-1 in Appendix B. The colour of the samples depended on the alumina concentrations in the melt, and the colour change indicates different compounds formed in low and high alumina melts. The colour changed from brown *via* orange to yellow with increasing alumina content.

According to Figure 6-2, the solubility of Cu_2O depends strongly on the alumina concentration, *i.e.* the Cu_2O solubility decreases with increasing alumina concentration down to around 2 wt%, where it starts to increase slowly again.

The solubility of Cu(I) can be expressed as:

$$\text{wt\%Cu(I)} = 0.1835 + 0.0014 \cdot x + 0.0007 \cdot x^2 + \frac{0.071}{x} \quad , x = \text{wt\%}\,Al_2O_3 \ (\textit{i.e}\ 0.41\text{–}13.06) \qquad [6\text{-}4]$$

The interpretation of the present results is presented in Chapter 6.9.

6.5.2 Solubility of Cu_2O as a function of temperature

The solubility of Cu_2O was measured as a function of temperature in cryolite without alumina addition. These results are shown in the Arrhenius plot in Figure 6-3.

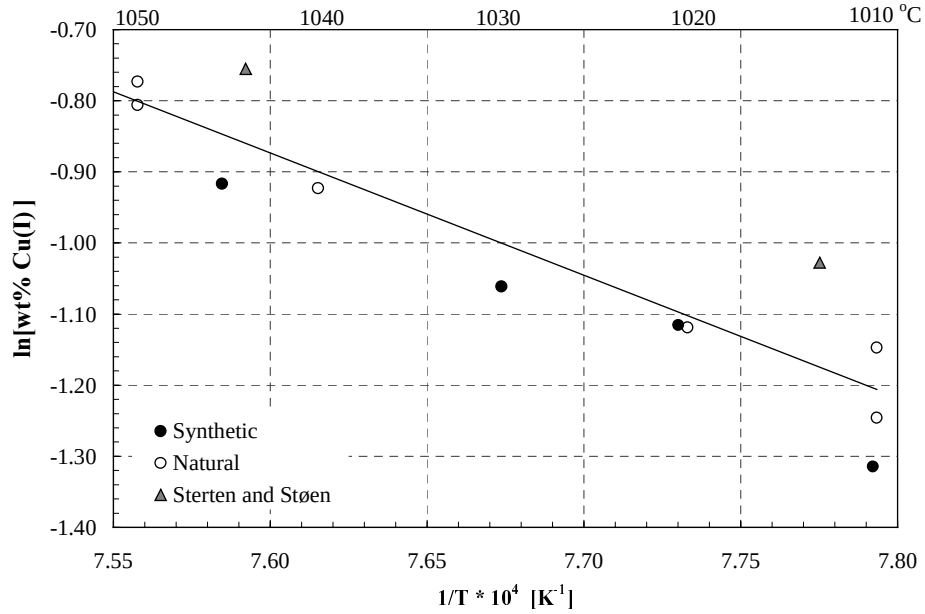

Figure 6-3: Arrhenius plot of the solubility of Cu(I) in cryolite as a function of temperature. The best-fit line is calculated for the solubility data in natural cryolite. ▲ from Sterten and Støen (5).

As one can see from Figure 6-3, it may seem like the solubility of Cu(I) oxide is lower in synthetic cryolite made of pure NaF and sublimated AlF_3. This result is unexpected since natural cryolite contains traces of alumina, which would decrease its solubility of Cu(I) oxide. These values were, however, obtained in the very first experiments where the amount of Cu_2O added to the melt was around half the amount of Cu_2O added in the experiments with natural cryolite. The melts with synthetic cryolite might not have been properly saturated with Cu(I) because some of the dissolved Cu(I)-containing species evaporated making the addition of Cu_2O prior to the experiment insufficient to achieve saturation, or the reason might be that less Cu_2O in solution requires longer time than the actual stirring time used (2 hours) to reach saturation.

The regression line in Figure 6-3 can be expressed as:

$$\ln(\text{wt\%Cu(I)}) = -\frac{17201\ (\pm 1630)}{T} + 12.2\ (\pm 1.3) \qquad [6\text{-}5]$$

By multiplying the slope of the line with "–R", one gets the partial molar enthalpy of dissolution (see Chapter 4.8, p. 81) for Cu_2O, *i.e.,*

$$\overline{\Delta H}^{o}_{Cu_2O} = 143.0\ \ (\pm 13.6)\ \text{kJ/mol} \qquad [6\text{-}6]$$

In section 6.9 it is shown that alumina is produced in these melts by the dissolution of Cu_2O. The alumina activity is therefore not independent of temperature, so the value, that is calculated for the partial molar enthalpy is only apparent.

The solubility of Cu(I) was also measured as a function of temperature in alumina-saturated melts. These results are shown in Figure 6-4.

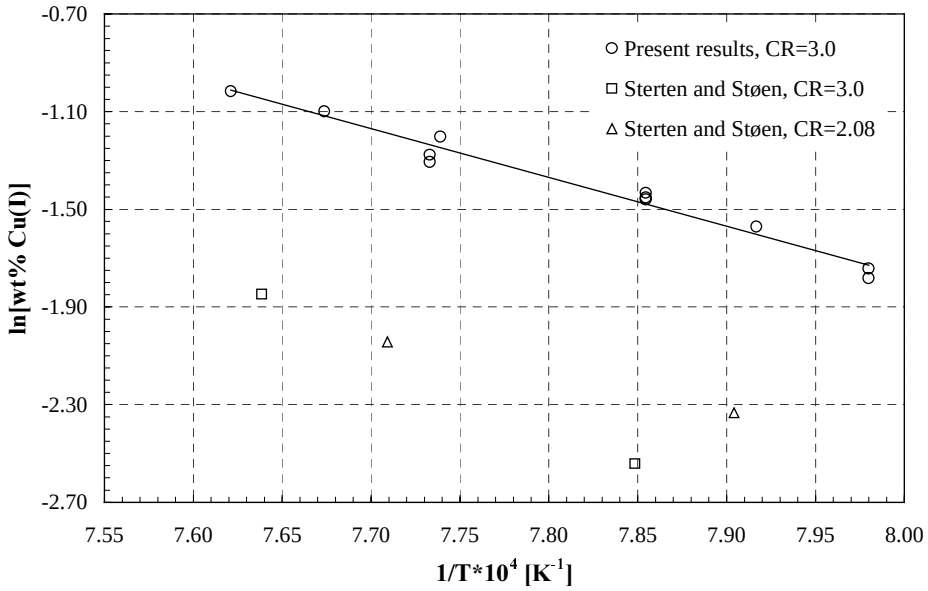

Figure 6-4: Arrhenius plot of the solubility of Cu(I) in alumina-saturated cryolite as a function of the reciprocal temperature. Present results and data from Sterten and Støen (5).

The present results fit a straight line in an Arrhenius plot, and the solubility increases with increasing temperature. The results obtained by Sterten and Støen (5) are surprisingly low.

The regression line in Figure 6-4 can be expressed as:

$$\ln(\text{wt\%Cu}) = -\frac{19987\ (\pm 1112)}{T} + 14.2\ (\pm 0.9) \qquad [6\text{-}7]$$

By multiplying the slope of the line with "–R", one gets the partial molar enthalpy of dissolution for $CuAlO_2$, *i.e.,*

$$\overline{\Delta H}^{o}_{CuAlO_2} = 166.2\ (\pm 9.2)\ \text{kJ/mol} \qquad [6\text{-}8]$$

This value is much lower than the values calculated for Ni(II) (*i.e.* 248.2), but higher than the one for Fe(II) (*i.e*. 64.8).

6.5.3 Solubility of Cu_2O as a function of molar ratio at 1020 ^oC

The solubility of Cu_2O was measured in a similar way as described above as a function of the molar ratio (CR) at 1020 ^oC, and the results are shown in Figure 6-5.

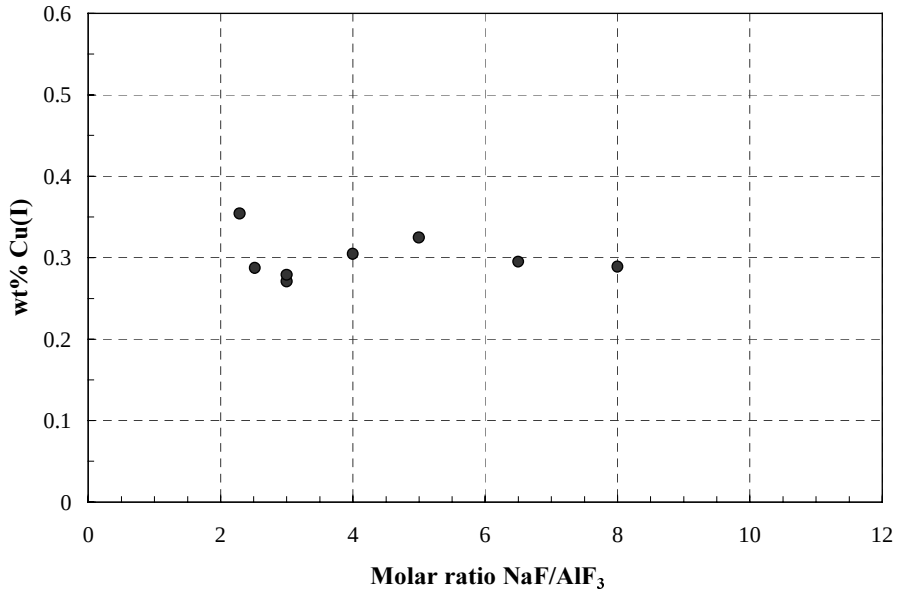

Figure 6-5: Solubility of Cu(I) as a function of molar ratio in alumina-saturated melts at 1020 ^oC in a copper crucible and with an atmosphere of argon.

According to Figure 6-5, the cryolite ratio does not seem to influence the solubility much at constant temperature, even though there is an upward trend for acidic melts.

Not many solubility data has been found in the literature, but this phenomenon is supported by solubility data reported by Sterten and Støen (5) for various temperatures and molar ratios, as shown in Figure 6-6. Sterten and Støen added Cu_2O to an cryolite-alumina melt

contained in an copper crucible using argon atmosphere, and determined the saturation concentration at various temperatures with atomic absorption.

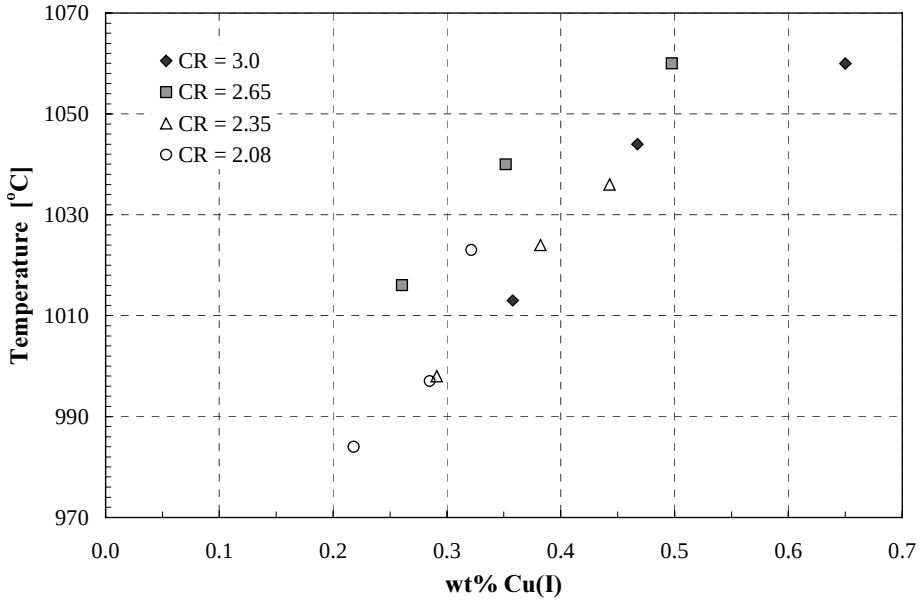

Figure 6-6: Solubility of Cu(I) in cryolite melts with different molar ratios (CR) as a function of temperature, data from Sterten and Støen (5).

According to data reported by Sterten and Støen (5), by Sterten and Skar (4) and by Skar (13), the molar ratio does not seems to influence the solubility so much at alumina-saturation.

6.5.4 Thermodynamical treatment of the binary phase diagram Na_3AlF_6-Cu_2O

In a phase diagram for a binary mixture of two components, A and B with no solid solution, solid B can be in equilibrium with a liquid melt with composition x_A at a temperature T. It can be shown (14) that:

$$\Delta\bar{S}_A = -R \cdot \ln(x_A) = \Delta H_f \cdot \left(\frac{1}{T} - \frac{1}{T_f}\right) \qquad [6\text{-}9]$$

where $\Delta\bar{S}_A$ is the entropy of fusion A, of ΔH_f is the enthalpy of melting of A, R is the ideal gas constant and T_f is the melting temperature of the mixture.

Equation [6-9] can be rearranged to,

$$\ln(x_A) = \ln(1 - x_B) = \frac{\Delta H_f}{R} \cdot \left(\frac{1}{T_f} - \frac{1}{T} \right) = \frac{\Delta H_f}{R} \cdot \left(\frac{T - T_f}{T_f \cdot T} \right) \quad [6\text{-}10]$$

When x_A approaches 1 and T approaches T_f, equation [6-10] in ideal solutions becomes (14):

$$\Delta T = \left(\frac{R \cdot T_f^2}{\Delta H_f} \right) \cdot x_B \quad [6\text{-}11]$$

If "n_B" mol B is added to "n_A" mol A, which dissolves into "c" mol new particles in the melt, the expression for freezing point depression becomes,

$$\Delta T = \left(\frac{R \cdot T_f^2}{\Delta H_f} \right) \cdot \left(\frac{c \cdot n_B}{n_A + c \cdot n_B} \right) \quad [6\text{-}12]$$

By plotting the temperature depression ΔT versus x_B given by equation [6-12] for the number of particles c = 1, 2, 3, 4, 5 *etc.*, one can compare the experimentally achieved depression values with the lines given by equation [6-12] for different values for c. The line that gives the best fit for the experimental values corresponds to the number of particles, *i.e.* the c value, formed when B is dissolved in A.

If species A is cryolite and species B is Cu_2O, T_f for cryolite = 1011 ^oC (1284.15 K) and H_f for cryolite = 114 kJ/mol (15), one can calculate lines for ideal freezing point depression. These lines are shown in Figure 6-8, together with the present experimental freezing point depression data and the ones obtained by Skar (13) and (4) and by Sterten and Støen (5).

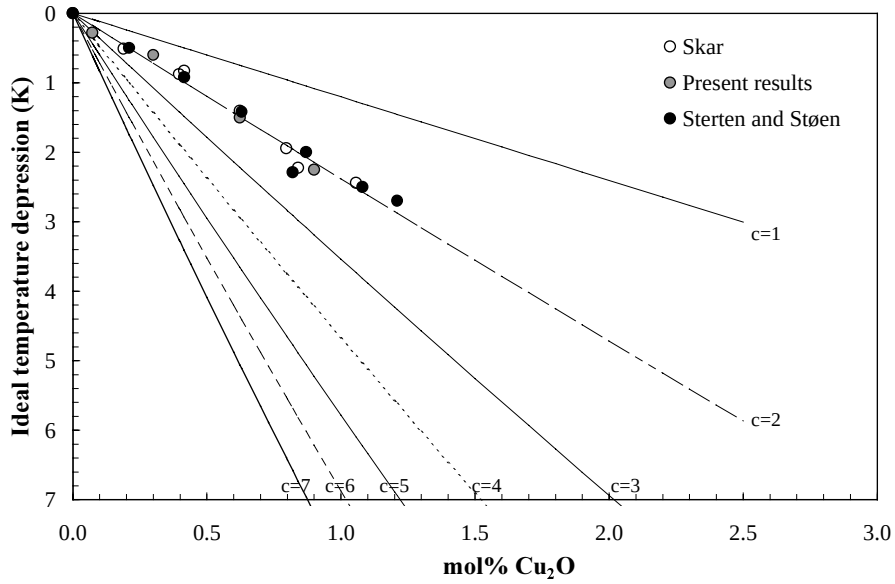

Figure 6-7: Freezing point depression for Cu_2O in cryolite. Present results and raw data from Skar (13) and Sterten and Støen (5).

As one can see from Figure 6-7, the experimental points suggest the formation of two new species. Sterten and Støen (5) and Sterten and Skar (4) assumed the formation of *three* new species from Cu_2O according to,

$$Cu_2O + 2AlF_3 = Al_2OF_6^{2-} + 2Cu^+ \qquad [6\text{-}13]$$

They used another value for H_f, *i.e.* 106.745 kJ/mol (4), which partly explains why they opted the slope three instead of two, even though it would make very little difference to the slope. If one assumes that $Al_2OF_6^{2-}$ is already present in the melt before Cu_2O additions, only two *new* species are formed according to [6-13].

X-ray analysis of melt samples from Sterten and Støen's experiments (5) indicated Cu_2O to be the only stable solid copper phase in this system, also when CuO was added to the melt, but metallic Cu particles were also found in the crucible after the experiment. The copper particles may have been caused by redox-reactions between copper ions and impurities like iron (Fe(II)) from the cryolite used.

One might consider consumption of Cu_2O according to the reaction:

$$3Cu_2O_{(s)} + 2AlF_{3(s)} = Al_2O_{3(s,\alpha)} + 3CuF_{2(s)} + 3Cu_{(s)}, \quad \Delta G^o_{1273K} = 234.9 \text{ kJ/mol} \qquad [6\text{-}14]$$

but since the standard Gibbs energy for reaction [6-14] is positive, this reaction is unlikely.

The solubility of Cu_2O was measured in synthetic cryolite made from NaF and AlF_3. The freezing point depressions of the various melts were measured by reducing the temperature by 0.5 degree per minute, and by measuring the temperature in the melt every 5 seconds while the melt was stirred continuously. The heat transport in liquids is much faster than in the solid phase. This implies that cooling curves give more accurate liquidus temperatures than heating curves do. The cryolite corner of the phase diagram for the binary system Na_3AlF_6-Cu_2O was established. The phase diagram is shown in Figure 6-8 and is based on the solubility data, the liquidus temperature of cryolite (16), (17), *i.e.* 1011 °C, and a theoretical slope for the liquidus line corresponding to the formation of two new species in the melt as expressed by equation [6-12]. The experimental liquidus data shown in Figure 6-7 is omitted in Figure 6-8 to clearly separate the liquidus line from the solidus line.

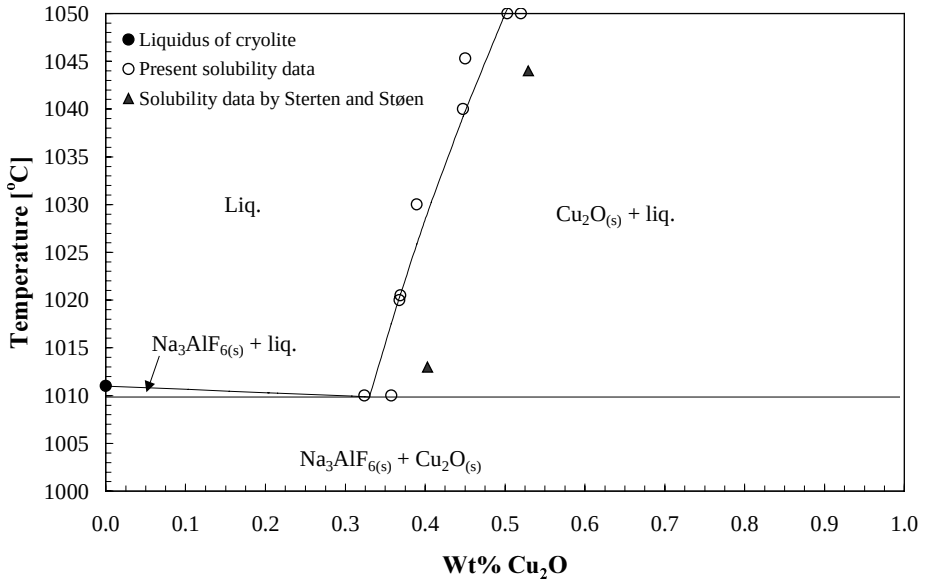

Figure 6-8: The cryolite corner of the phase diagram Na_3AlF_6-Cu_2O. Present results and data from Sterten and Støen (5).

The theoretical liquidus line for cryolite with Cu_2O in Figure 6-8 can be expressed as:

$$T_{liq} = 1011 - 3.892 \cdot (wt\%\,Cu_2O) \qquad \text{for wt\% } Cu_2O < 0.32 \qquad [6\text{-}15]$$

The solidus line for Cu_2O in Figure 6-8 can be expressed as T_{sol}:

$$T_{sol} = 1116.9 + 96.576 \cdot \ln(wt\%\,Cu_2O) \qquad \text{for wt\% } Cu_2O > 0.32 \qquad [6\text{-}16]$$

The eutectic point was presently found to be at 1009.8 °C ± 0.1 °C and 0.33 ± 0.02 wt% Cu_2O. Sterten and Skar (4) and Skar (13), however, determined the eutectic point to be at

1008.1 ± 1.5 °C and 0.73 ± 0.07 wt% Cu_2O based on cryoscopic measurements, only. The deviation might be explained by the fact that they used natural cryolite instead of synthetic cryolite. The natural cryolite used contained 0.2-0.4 wt% alumina, which decreases the liquidus of cryolite (16), (17) by 1.5 - 2 degrees. With such a low total freezing point depression, the eutectic point can be difficult to determine. They used 1011 °C as the liquidus temperature for alumina-free cryolite. 1011 °C is, however, too high to be achieved for *natural* cryolite (16), (17), and it may indicate why they got a lower eutectic temperature than the present result. Sterten and Støen (5) reported a similar phase diagram where the eutectic point was around 1008.5 °C and at about 0.4 wt% Cu_2O, which is more in agreement with the present results with respect to the eutectic concentration. A lower eutectic temperature can be explained if Cu_2O forms more than two species, but even the assumption of 3 new species formed lowers the theoretical eutectic point only to (0.328, 1009.3). The following sub-Chapters will show that one will have a certain quantity of Cu(II) present in these solutions, which might influence the freezing point depression.

No other phase diagrams for this system have been found in the literature.

6.6 Solubility of CuO

Cu(II) was stabilised by using oxygen atmosphere and a platinum crucible. The experiments were run in the same way as described for Cu_2O using a cell set-up as shown in Figure 6-1.

6.6.1 Solubility of CuO as a function of the alumina concentration at 1020 °C

The samples taken from the various melts had different colours depending on the content of alumina in the melts. Some of the samples are shown in Figure B-2 in Appendix B. As one can see, the colour changed from dark brown for the cryolite melts to yellow for the alumina-saturated melts.

The solubility of CuO, called "wt% CuO" was measured in natural cryolite as a function of alumina concentration at 1020 °C, and the results are shown in Figure 6-9.

The solubility of CuO can be expressed as wt% Cu(II):

$$\text{wt\%Cu(II)} = 0.4232 - 0.0391 \cdot x + 0.0028 \cdot x^2 + \frac{0.5322}{x} \quad , x = \text{wt\%}Al_2O_3 \text{ (}i.e.\text{ 1.03–13.06)} \qquad [6\text{-}17]$$

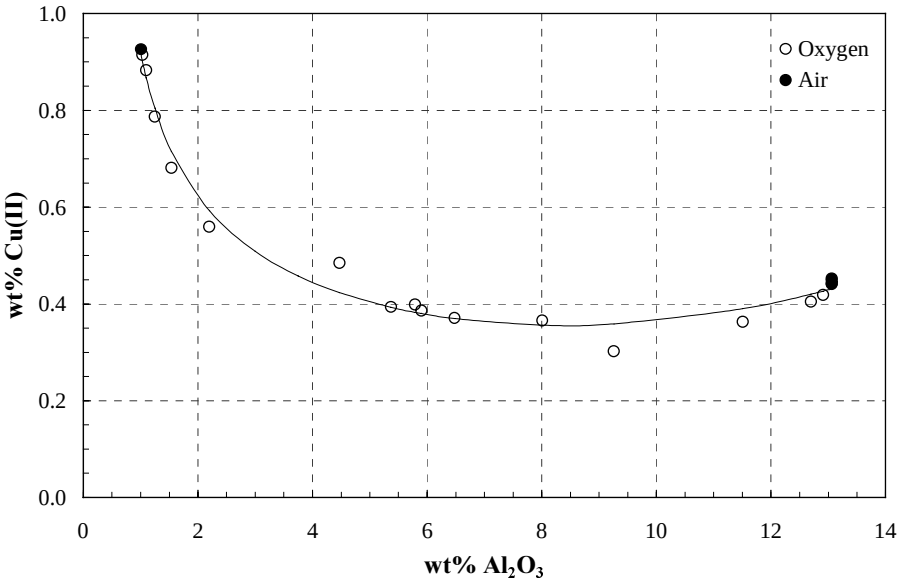

Figure 6-9: Solubility of Cu(II) as a function of alumina concentration in natural cryolite at 1020 ^{o}C in an atmosphere of oxygen. The alumina concentrations were measured with the LECO apparatus. Data in Appendix B.

As one can see from Figure 6-9, the solubility of Cu(II) strongly depends on the alumina concentration. The downward trend in the low-alumina region indicats the formation of a Cu(II) fluoride, but the upward trend in the high region implies the formation of an oxy-compound. The interpretation of the results is treated in Chapter 6.10.

6.6.2 Solubility of CuO as a function of temperature

The solubility of CuO was measured in natural cryolite as a function of temperature, and the results are shown in the Arrhenius plot in Figure 6-10.

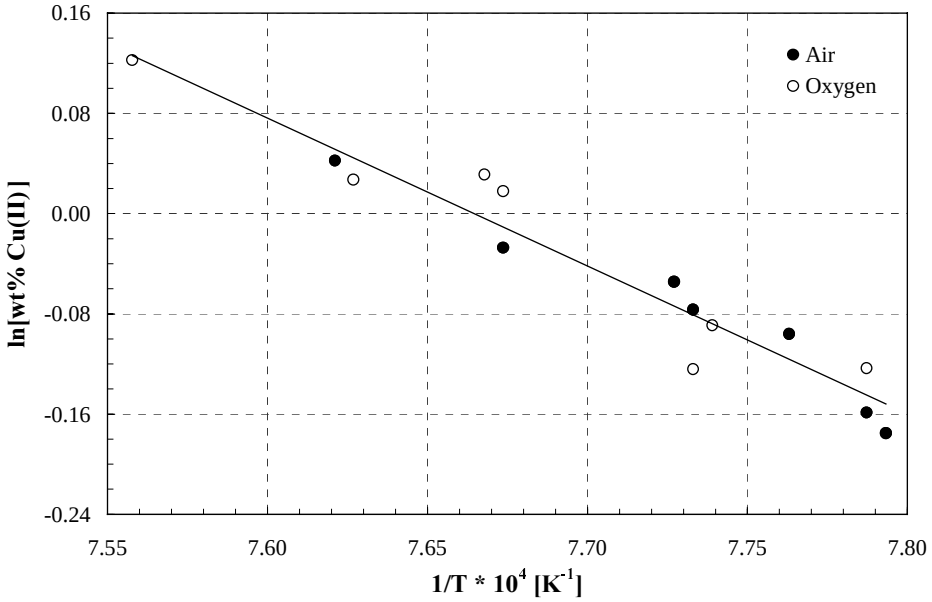

Figure 6-10: Arrhenius plot of the solubility of Cu(II) in cryolite as a function of the reciprocal temperature in an atmosphere of air and oxygen, respectively.

The regression line for all the data given in Figure 6-10 can be expressed as:

$$\ln(\text{wt\%Cu(II)}) = -\frac{11806\ (\pm 911)}{T} + 9.1\ (\pm 0.7) \qquad [6\text{-}18]$$

By multiplying the slope of the line with "–R", one gets the partial molar enthalpy of dissolution for CuO, *i.e.*,

$$\overline{\Delta H}^{o}_{CuO} = 98.2\ \ (\pm 7.6)\ \text{kJ/mol} \qquad [6\text{-}19]$$

In section 6.10 it is shown that alumina being produced in these melts by the dissolution of CuO. The alumina activity is therefore not independent of temperature, so the value that is calculated for the partial molar enthalpy is only apparent.

The solubility of Cu(II) oxide was measured in alumina-saturated cryolite as a function of temperature, and the results are shown in the Arrhenius plot in Figure 6-11.

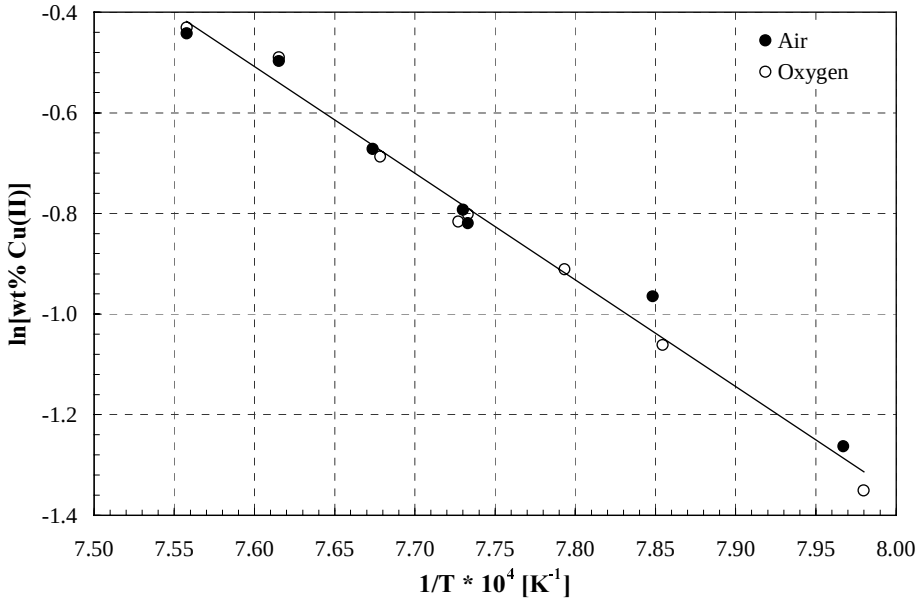

Figure 6-11: Arrhenius plot of the solubility of Cu(II) in alumina-saturated cryolite as a function of the reciprocal temperature in an atmosphere of air and oxygen, respectively.

The regression line in Figure 6-11 can be expressed as:

$$\ln(\text{wt\%Cu(II)}) = -\frac{21206\ (\pm 690)}{T} + 15.6\ (\pm 0.5) \qquad [6\text{-}20]$$

The value is lower than the value calculated for Ni(II) (*i.e.* 248.2), but higher than the value for Fe(II) (*i.e.* 64.8).

In alumina-saturated melts in oxygen atmosphere $CuAl_2O_4$ is the stable solid phase (see Figure 2-4). By multiplying the slope of the line in Figure 6-11 with "–R", one gets the partial molar enthalpy of dissolution for $CuAl_2O_4$, *i.e.*,

$$\overline{\Delta H}^{o}_{CuAl_2O_4} = 176.3\ \ (\pm 5.7)\ \text{kJ/mol} \qquad [6\text{-}21]$$

Sterten (7) has reported the solubility of CuO in cryolite and in alumina-saturated cryolite as a function of the temperature. The melts were, however, contained in a platinum crucible under an *argon* atmosphere. Sterten (7) probably did not consider the atmosphere above the melt when measuring the solubility of CuO, but according to thermodynamics one needs a certain oxygen pressure to stabilise Cu(II).

The solubility of CuO obtained by Belyalev (18) for 1000 ^{o}C (1.13 wt% CuO), and by Rolin and Bernard (19) (1.17 wt% CuO) for 1030 ± 15 ^{o}C in cryolite were reported by

Grjotheim *et al*. (15). These two solubility concentrations deviate by a factor of almost 3 compared to the one presently obtained, but the experimental conditions (atmosphere, cryolite impurities and type of crucible) may have been different. Rolin and Bernard used a platinum crucible in an open furnace. One may therefore assume the atmosphere to be air. They used a visual method to determine the solubility, *i.e.*, by adding small Tablets of CuO, one by one, and visually observe when the Tablet did not dissolve any longer. Belyalev also reported a solubility concentration of 0.68 wt% CuO in cryolite with 5 wt% alumina at 1000 ^{o}C.

Sterten and Støen (5), (7) probably measured the solubility of Cu(I) oxide in both cases. If one plots their results for Cu_2O and CuO and plot them as wt% Cu, one gets very similar solubilities as shown in Figure 6-12.

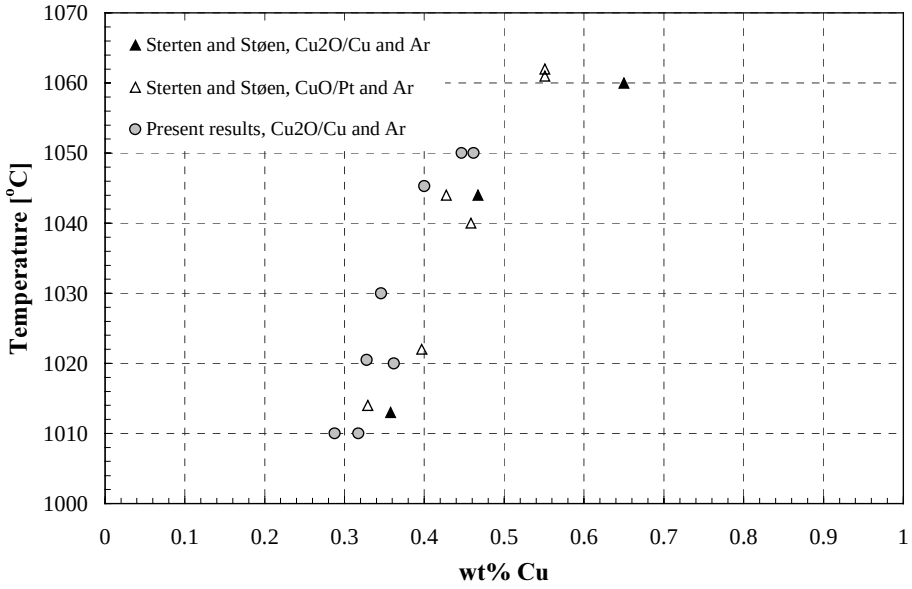

Figure 6-12: Solubilities of Cu_2O and CuO measured in alumina-free cryolite under an atmosphere of argon shown as a function of temperature, present and Sterten and Støen's data (5),(7).

6.6.3 Solubility of CuO as a function of molar ratio at 1020 ^{o}C

The solubility of CuO was measured as a function of molar ratio in alumina-saturated melts at 1020 ^{o}C in an atmosphere of oxygen. The results are plotted in Figure 6-14.

According to Figure 6-14, the cryolite ratio has little influence on the solubility of CuO at constant temperature, even though there is an upward trend for acidic melts.

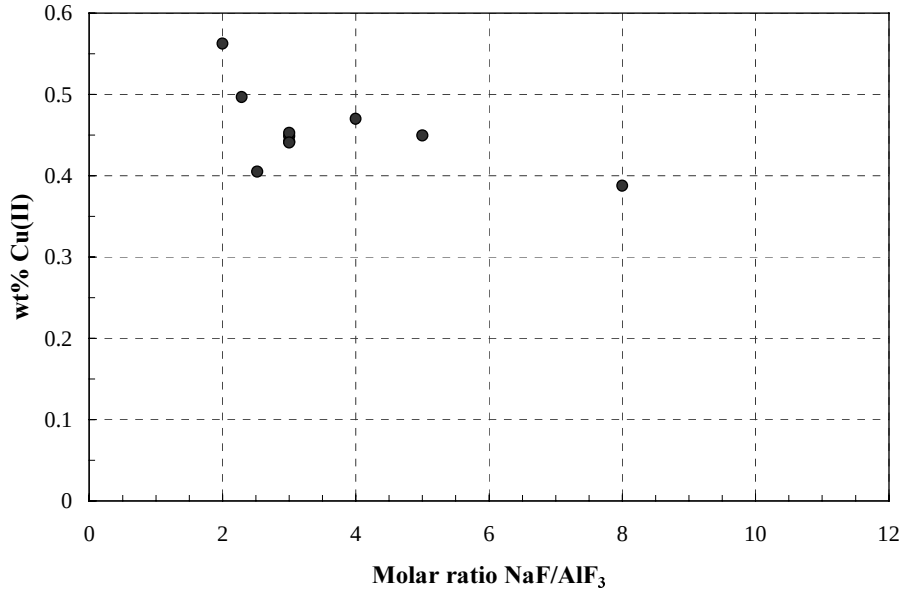

Figure 6-13: Solubility of Cu(II) as a function of molar ratio in alumina-saturated melts at 1020 ^{o}C in an atmosphere of oxygen.

6.6.4 Thermodynamic treatment of the binary phase diagram Na_3AlF_6-CuO

The freezing point depressions of CuO additions in pure cryolite were measured, and the cryolite corner of the phase diagram for the binary system Na_3AlF_6-CuO was established. The phase diagram is shown in Figure 6-17, based on the present solubility data, the liquidus point for cryolite (16), (17) and the theoretical slope for the formation of two[1] species from CuO using equation [6-12].

As one can see from Figure 6-14, Cu(II) seems to describe the cryolite corner of a simple eutectic phase diagram where the eutectic point is given at 1004.7 ^{o}C and 1.02 wt% CuO.

The theoretical liquidus line for cryolite with CuO in Figure 6-15 using equation [6-12], assuming two new species formed, can be expressed as

$$T_{liq} = 1011 - 6.201 \cdot (\text{wt\% CuO}) \qquad \text{for wt\% CuO} < 1.02 \qquad [6\text{-}22]$$

The solidus line for CuO in Figure 6-15 can be expressed as T_{sol}:

$$T_{sol} = 5.666 \cdot (\text{wt\% CuO})^2 + 97.359 \cdot (\text{wt\% CuO}) + 900 \qquad \text{for wt\% CuO} > 1.02 \qquad [6\text{-}23]$$

[1] Assuming that CuO simply dissolves as "Cu^{2+}_{sol}" and "O^{2-}_{sol}" species. See Chapter 6.10 and equation [6-81] for further details.

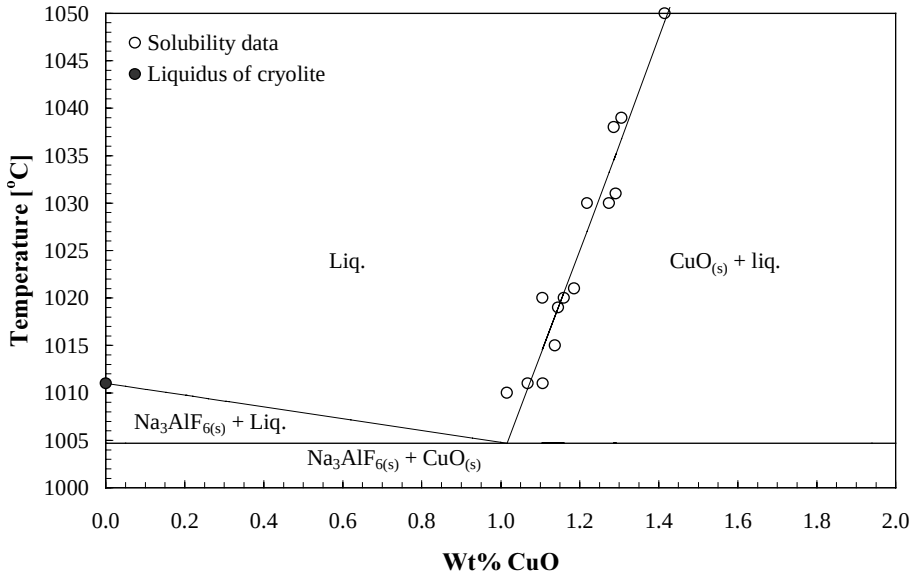

Figure 6-14: The cryolite corner of the phase diagram Na_3AlF_6-CuO.

Sterten (7) reported a similar phase diagram, but these data were obtained under an atmosphere of argon and with an eutectic temperature of 1008, *i.e*. close to the same eutectic temperature he reported for Cu_2O (5). No other phase diagram for this system has been found in the literature.

6.7 Gibbs energies of formation for $CuAlO_2$ and $CuAl_2O_4$

It was shown in Chapters 4 and 5 that by plotting the solubilities of Ni(II) and Fe(II) as a function of alumina activity (20) in a logarithmic diagram, one gets a negative bend in the curves when the stable solid phase changes from an oxide to an aluminate.

According to Figures 6-15 and 6-16 showing the solubility of Cu(I) and Cu(II), there is no downward bend in the curves when $CuAlO_2$ and $CuAl_2O_4$ are formed, and if one introduces the literature values for the alumina activity corresponding to the formation of the aluminates from Jacob and Alcock (8), the bend does not correspond to the region where one would expect the mechanisms to change from oxide to aluminate since there is simply no negative bend. The solubility data may seem to indicate that the thermodynamic data for Cu(I) and Cu(II) aluminates in the literature are wrong. It was therefore decided to measure Gibbs energy of formation by using emf cells for Cu(I) and Cu(II) as shown in Figures 6-17 and 6-19, respectively. These cells were based on a similar cell design described by Dewing (21).

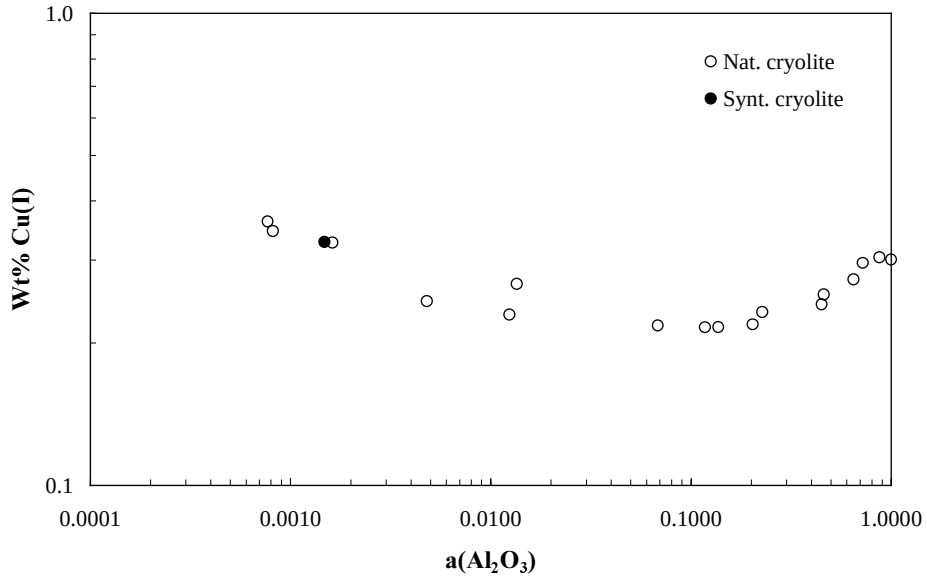

Figure 6-15: A log-log diagram of the solubility of Cu(I) as a function of the alumina activity at 1020 ^{o}C.

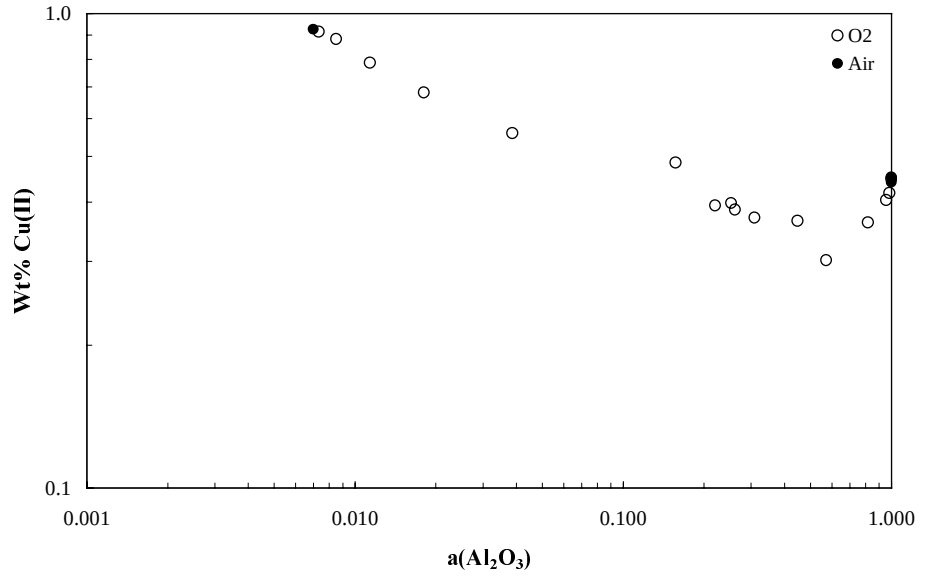

Figure 6-16: A log-log diagram of the solubility of Cu(II) as a function of the alumina activity at 1020 ^{o}C.

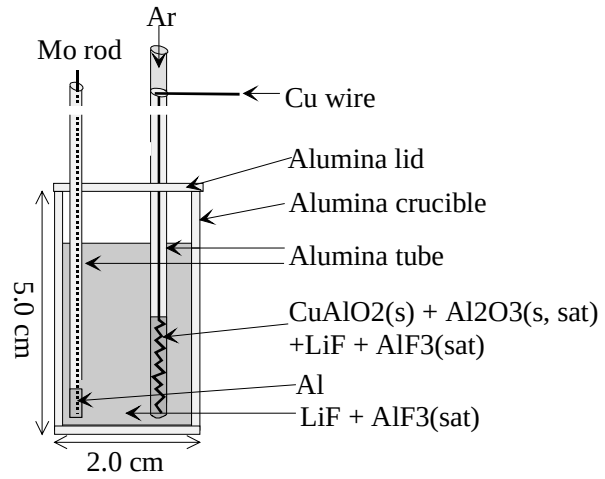

Figure 6-17: Cell set-up to measure emf for $CuAlO_2$ at 1025 – 1300 K in argon.

$CuAlO_2$ was produced by mixing Cu_2O with excess Cu and alumina, and heating the mixture for 48 hours in an argon atmosphere in an alumina crucible. The material inside the aluminate containing electrode was saturated with alumina, giving unit activity for all the species involved. The Li-based melt has an eutectic temperature around 710 ^{o}C, and was liquid at all the temperatures where the emf was measured.

The electrode reactions for the emf cell shown in Figure 6-17 can be expressed as:

$$\text{Anode}: \quad Al + 3LiF = 3Li^{+} + AlF_3 + 3e^{-} \qquad [6\text{-}24]$$

$$\text{Cathode}: AlF_3 + 3CuAlO_2 + 3Li^{+} + 3e^{-} = 3LiF + 2Al_2O_3 + 3Cu \qquad [6\text{-}25]$$

The cell reaction then becomes:

$$Al_{(l)} + 3CuAlO_{2(s)} = 2Al_2O_{3(s,\alpha)} + 3Cu_{(s)} \qquad \Delta G^{o}_{1293.15\,K} = -491.67\ \text{kJ/mol} \qquad [6\text{-}26]$$

According to the electrode reactions, Li^{+} ions are transported through the solid alumina membrane. However, the transfer of the three Li^{+} ions does not cause any change of Gibbs energy because the composition of the liquid is the same on the two sides, *i.e.* saturated with AlF_3. The transport through the membrane is not diffusion, but electrolytic migration. The transport number of Li^{+} is essentially one in this melt (21), so that it is the Li^{+} ions that carry the current through the cell.

Subtracting the formation of alumina from [6-26], *i.e.*,

$$Al_{(l)} + \frac{3}{4}O_{2(g)} = \frac{1}{2}Al_2O_{3(s,\alpha)} \qquad \Delta G^{o}_{1293.15\,K} = -631.52\ \text{kJ/mol} \qquad [6\text{-}27]$$

and by multiplying the result by 1/3, one gets:

$$CuAlO_{2(s)} = Cu_{(s)} + \frac{1}{4}O_{2(g)} + \frac{1}{2}Al_2O_{3(s,\alpha)} \quad \Delta G^{o}_{1293.15K} = 46.62 \text{ kJ/mol} \qquad [6\text{-}28]$$

Steady state values for the emf for the cell shown in Figure 6-17 were obtained after approximately 40 minutes at constant temperature. The emf values were measured[2] at various temperatures from 1000 to 1300 K (data in Appendix B), and according to the regression analysis of the raw data it can be expressed as:

$$Emf_{cell} = -1.564\,(\pm 0.095) * 10^{-4} \cdot T + 1.890\,(\pm 0.011) \quad [T = K] \qquad [6\text{-}29]$$

Since a copper wire and a molybdenum rod were used in the cell, the Thomson voltage between the two materials has to be subtracted from the emf for the cell reaction, called "$Emf_{Mo\text{-}Cu}$". The copper wire was twisted around the end of the molybdenum rod and squeezed into a sintered alumina tube, and in a closed furnace with argon atmosphere the emf between these two materials was measured as a function of temperature:

$$Emf_{Mo-Cu} = 6.8693 * 10^{-12} T^3 - 1.3114 * 10^{-8} T^2 - 4.3876 * 10^{-6} T + 2.1249 * 10^{-4}$$

where T = 300-1300 K. [6-30]

Gibbs energy of formation can be calculated by,

$$\Delta G = -nFE \qquad [6\text{-}31]$$

for reactions [6-26] to [6-28], and the values are given in Table 6-1 at 1020 ^{o}C. Gibbs energy of formation for $CuAlO_2$ was calculated for all the temperatures for which emf values were obtained, and the results are visualised in Figure 6-18.

[2] Measured with a Keitley 2000 multimeter

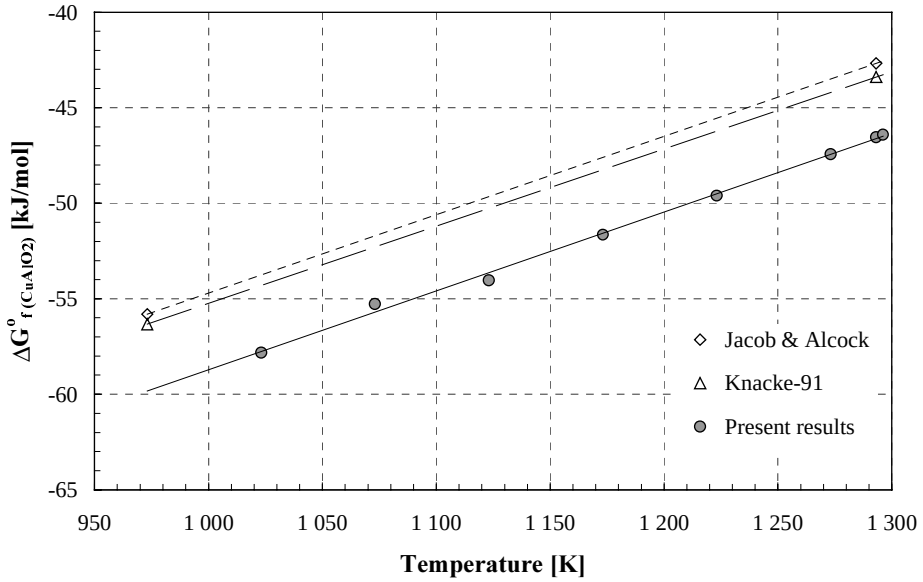

Figure 6-18 Gibbs energy of formation for $CuAlO_2$ given as a function of temperature for the reaction: $0.5Al_2O_3 + Cu + 0.25O_2 = CuAlO_2$. The alumina activity is unity.

The presently obtained values for the Gibbs energy of formation for $Cu_2Al_2O_4$ are substantially more negative than the data found in the literature (3), (8). Even though the data from Jacob and Alcock (8) and Knacke *et al.* (3) are almost identical, it should be noted that Knacke *et al*. in their compilation used the values of Kubaschewski and Alcock (22), so these two data sets are coming more or less from the same source.

Table 6-1: Tabulated values for the standard Gibbs energy used to calculate ΔG^o for $CuAlO_2$ at 1020 ^oC. Data for Al_2O_3 from Knacke *et al.* (3).

#	**Reaction:**	ΔG^o **[J/mol]**
1	$Al + 3CuAlO_2 = 2Al_2O_3 + 3Cu$	-491669
2	$Al + 3/4O_2 = 1/2Al_2O_3$	-631520
3	$CuAlO_2 = 1/2Al_2O_3 + Cu + 1/4O_2$	46617

Gibbs energy of formation of $CuAlO_2$ according to the back reaction of [6-28] can be expressed with the regression line:

$$\Delta G^o_{CuAlO_2} = 0.04129(\pm 0.00181)\cdot T - 100.024(\pm 2.151)\ \left[kJ/mol\right]\ (T = 1023 - 1293K) \qquad [6\text{-}32]$$

In Chapter 2, the stability diagram for solid copper phases was designed by using data from Jacob and Alcock (8) and the present results. The emf data were measured at unit activity. Since one wants to find the intercept between the equilibrium lines Cu-Cu_2O and Cu-

$CuAlO_2$, one simply has to express the two equations [*2*-41] and [*2*-43] (p. 26) as a function of the partial oxygen pressure as described in Chapter 2.1.4. and find the pressure which corresponds to the same alumina activity in the two equations. This procedure gives log(alumina activity) = -0.727, which is the value to be used in Chapter 6.8 to separate Cu(I) and Cu(II) and to construct Figure 2-4.

A similar cell as described for $CuAlO_2$ was made to measure the Gibbs energy of formation for $CuAl_2O_4$ (as shown in Figure 6-19).

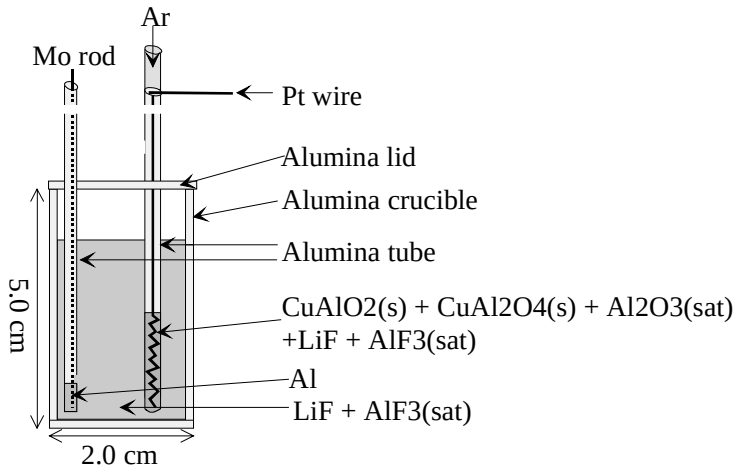

Figure 6-19: Cell set-up to measure emf for $CuAl_2O_4$ at 1025 to 1300 K in argon.

The content inside the aluminate electrode is saturated with alumina, giving unit activity for all the species involved. $CuAl_2O_4$ was produced by mixing CuO with excess alumina and keep it in an alumina crucible at 1000°C for 48 hours.

The electrode reactions for the emf cell shown in Figure 6-19 can be expressed as:

$$\text{Anode}: \quad Al + 3LiF = 3Li^+ + AlF_3 + 3e^- \qquad [6\text{-}33]$$

$$\text{Cathode}: AlF_3 + 3CuAl_2O_4 + 3Li^+ + 3e^- = 3LiF + 2Al_2O_3 + 3CuAlO_2 \qquad [6\text{-}34]$$

The cell reaction then becomes:

$$Al_{(l)} + 3CuAl_2O_{4(s)} = 3CuAlO_{2(s)} + 2Al_2O_{3(s,\alpha)} \qquad [6\text{-}35]$$

Subtracting the formation of alumina, *i.e.*,

$$Al_{(l)} + \frac{3}{4}O_{2(g)} = \frac{1}{2}Al_2O_{3(s,\alpha)} \qquad \Delta G^{o}_{1293.15\,K} = -631.520 \ \text{kJ/mol} \qquad [6\text{-}36]$$

and multiplying the result by 1/3, one gets:

$$CuAl_2O_{4(s)} = CuAlO_{2(s)} + \frac{1}{4}O_{2(g)} + \frac{1}{2}Al_2O_{3(s,\alpha)} \quad [6\text{-}37]$$

The emf values measured for the cell, Emf_{cell}, are tabulated in Appendix B. By regression analysis of the raw data it was given by:

$$Emf_{cell} = -6.768(\pm 0.095) * 10^{-4} \cdot T + 2.942(\pm 0.011) \quad [6\text{-}38]$$

Since a platinum wire and a molybdenum rod were used in the cell, the Thomson voltage between the two materials has to be subtracted from the Emf for the cell reaction. The emf between these two materials, $Emf_{Mo\text{-}Pt}$, was measured as a function of temperature as described for "$Emf_{Mo\text{-}Cu}$":

$$Emf_{Mo-Pt} = 3.8342 * 10^{-12} T^3 - 1.9648 * 10^{-8} T^2 - 5.9464 * 10^{-6} T + 3.4417 * 10^{-3}$$

where T = 300-1300 K [6-39]

By subtracting [6-37] from [6-40], one gets [6-41],

$$Cu_{(s)} + \frac{1}{4}O_{2(g)} + \frac{1}{2}Al_2O_{3(s,\alpha)} = CuAlO_{2(s)} \qquad \Delta G^o_{1293.15\,K} = -46.617\,kJ/mol \quad [6\text{-}40]$$

$$Cu_{(s)} + \frac{1}{2}O_{2(g)} + Al_2O_{3(s,\alpha)} = CuAl_2O_{4(s)} \qquad \Delta G^o_{1293.15K} = -56.892\ kJ/mol \quad [6\text{-}41]$$

The Gibbs energy of formation for $CuAl_2O_4$ was calculated in a similar way as shown for $CuAlO_2$, and data for 1020 ^oC are given in Table 6-2. The result is visualised in Figure 6-20.

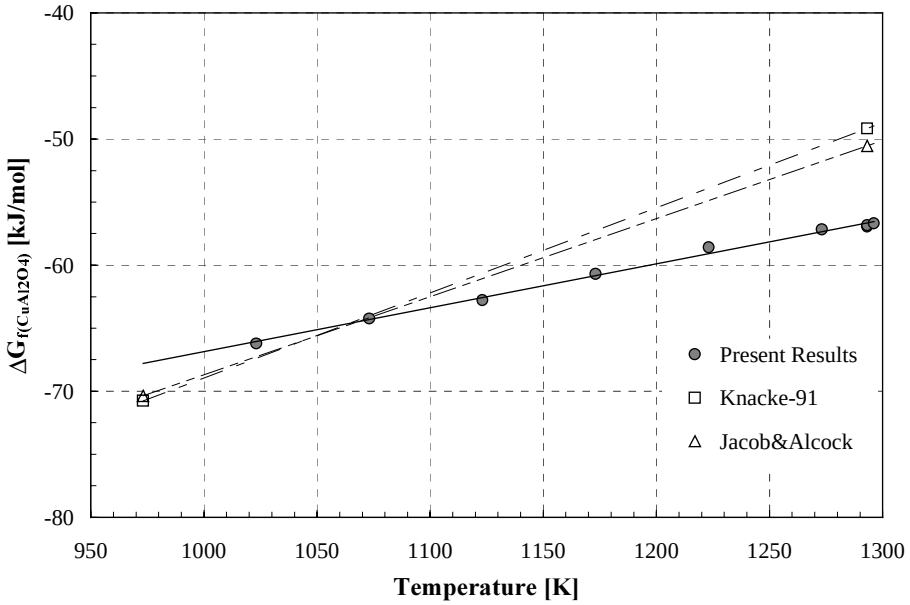

Figure 6-20: Gibbs energy of formation for $CuAl_2O_4$ given as a function of temperature by the reaction: $Cu_{(s)} + 0.5O_{2(g)} + Al_2O_{3(s,\alpha)} = CuAl_2O_{4(s)}$. The alumina activity is unity.

Even though the data from Jacob and Alcock (8) and Knacke *et al.* (3) are almost identical, it should be noted that Knacke *et al*. used the average values by Jacob and Alcock (8) and by National Bureau of Standards (23), so these two data sets are more or less the same, as pointed out above.

Based on regression analysis and the best-fit line of the data presented in Figure 6-20, Gibbs energy of formation of $CuAl_2O_4$ according to [6-41] can be expressed as:

$$\Delta G^{o}_{CuAl_2O_4} = 0.03478\ (\pm 0.0009)\cdot T - 101.643\ (\pm 1.108)\ [kJ/mol]\quad (T = 1023 - 1293\,K) \qquad [6\text{-}42]$$

Table 6-2: Tabulated values for standard Gibbs energy used to calculate ΔG^o of formation for $CuAl_2O_4$ at 1020 ^oC. Data for reaction 2 from Knacke *et al.* (3).

#	**Reaction:**	**ΔG^o [J/mol]**
1	$Al + 3CuAl_2O_4 = 3CuAlO_2 + 2Al_2O_3$	-600693
2	$Al + 3/4O_2 = 1/2Al_2O_3$	-631520
3	$CuAl_2O_4 = CuAlO_2 + 1/4O_2 + 1/2Al_2O_3$	10275
4	$CuAlO_2 = Cu + 1/2Al_2O_3 + 1/4O_2$	46617
5	$CuAl_2O_4 = Cu + 1/2O_2 + Al_2O_3$	56892

The new values for Gibbs energies of formation for $CuAlO_2$ and $CuAl_2O_4$ were used to revise the stability diagram for copper as a function of the alumina activity, as shown in

Figure 2-4, p. 27, and they are used to separate the content of Cu(I) from Cu(II) in the same solution, and *vice versa* in Chapter 6.8. The intercept between the lines given for the equilibria CuO-$CuAl_2O_4$ and $CuAl_2O_4$-$CuAlO_2$ in Figure 2-4 was found to be given at log(alumina activity) = -0.597 (*i.e.* alumina activity = 0.25). The activity data used are summarised in Table 6-3.

Table 6-3: Equilibrium oxygen pressures and copper activities at 1020 °C. Data for reactions marked with "*" are calculated from Jacob and Alcock's data (8).

	#	Equilibrium	log $p(O_2)$	log a(Cu)	log $[aCu*p(O_2)^{1/4}]$	log $[aCu*p(O_2)^{1/2}]$
*	1	Cu-Cu_2O	-6.067	0.000	-1.517	-3.033
*	2	Cu_2O-CuO	-0.728	-1.335	-1.517	-1.699
*	3	CuO-$O_{2(g)}$	0.000	-1.699	-1.699	-1.699
	4	Cu-$CuAlO_2$ (aAl_2O_3 =1)	-7.521	0.000	-1.880	-3.760
	5	$CuAlO_2$-$CuAl_2O_4$ (aAl_2O_3 = 1)	-1.660	-1.468	-1.883	-2.298
	6	O_2-$CuAl_2O_4$ (aAl_2O_3 = 1)	0.000	-2.298	-2.298	-2.298
*	7	Cu-$CuAlO_2$ (aAl_2O_3 =1)	-6.897	0.000	-1.724	-3.448
*	8	$CuAlO_2$-$CuAl_2O_4$ (aAl_2O_3 = 1)	-1.269	-1.407	-1.724	-2.042
*	9	O_2-$CuAl_2O_4$ (aAl_2O_3 = 1)	0.000	-2.042	-2.042	-2.042

As explained in Chapter 4.6, p. 76, one can use the entropy for the formation reaction for the aluminates as a validation test for the emf measurements. The entropy for these reactions should be small, *i.e*. around 6 J/K·mol. Based on the present result, the entropy for the reaction,

$$Cu_2O + Al_2O_3 = 2CuAlO_2 \qquad [6\text{-}43]$$

was calculated to be –11 J/K·mol, which is acceptable. However, the entropy for the reaction,

$$CuO + Al_2O_3 = CuAl_2O_4 \qquad [6\text{-}44]$$

was calculated to be ~ 48 J/K·mol, which seems to be too high. No explanation can be given for this apparently high value, and additional work is needed to really understand the mechanisms involved.

6.8 Separation of Cu(I) and Cu(II) present in the same melt

It seems likely that a certain quantity of Cu(I) is coexisting in a solution of Cu(II) species, and *vice versa*. To make a proper analysis of the dissolution mechanisms for the two Cu valence states occurring in the melt, one needs to separate the two oxidation-states from each other.

The same method as described by Dewing and Thonstad (24) to split Fe(II) and Fe(III) (see Chapter 5) was used to split Cu(I) and Cu(II). In the most general case one may expect that solutions of copper oxides in molten cryolite will contain both Cu(I) and Cu(II) species and that Henry's law will apply because the concentrations are fairly low. It is convenient to

take p_{O_2} as the fundamental independent parameter since, once it is specified, the solid phase in equilibrium is defined and the remaining parameter, *i.e.* the activity of copper, can be calculated. The dissolution reactions for Cu_2O and CuO can then be given as,

$$Cu + \frac{1}{4}O_{2(g)} = Cu^{+}_{solution} + \frac{1}{2}O^{2-}_{solution} \quad [6\text{-}45]$$

and,

$$Cu + \frac{1}{2}O_{2(g)} = Cu^{2+}_{solution} + O^{2-}_{solution} \quad [6\text{-}46]$$

It should be noted that these two equations are purely formal. Nothing is assumed about the chemical environment in which either the copper or the oxide ions are. Then, for a fixed composition of solvent the "pure" solubility of Cu(I) and Cu(II) can be expressed as,

$$[Cu(I)] = K_3 \cdot a_{Cu} \cdot p_{O_2}^{1/4} \quad [6\text{-}47]$$

and,

$$[Cu(II)] = K_4 \cdot a_{Cu} \cdot p_{O_2}^{1/2} \quad [6\text{-}48]$$

where square brackets mean concentrations, K_3 and K_4 are constants and "p" is partial pressure in bar.

K_3 and K_4 reflect properties exclusively of the solution and not of the solids with which it was in equilibrium when the measurements were made. This means that if one multiplies K_3 by the value of "$a_{Cu} \cdot p_{O_2}^{1/4}$" for pure Cu_2O, then one gets the quantity of Cu(I) only, *i.e.* [Cu(I)], which would be in equilibrium with pure solid Cu_2O at all alumina contents. Then, *one does not need to deal with the fact that at high alumina concentrations $CuAlO_2$ actually forms*.

The total Cu concentrations in these two systems, which are the concentrations that have been measured experimentally, are given by the sum of [6-47] and [6-48]:

$$[\text{Total Cu}] = K_3 \cdot a_{Cu} \cdot p_{O_2}^{1/4} + K_4 \cdot a_{Cu} \cdot p_{O_2}^{1/2} \quad [6\text{-}49]$$

In the measurements with Cu crucibles, a_{Cu} is unity, and in order to calculate the oxygen partial pressure, one has to know what is the stable solid phase (*i.e.* Cu_2O or $CuAlO_2$) in equilibrium with the solution at a given alumina concentration. At low alumina concentrations, Cu_2O is at unit activity, and [6-47] can be used directly. However, if the alumina concentration is high enough to stabilise $CuAlO_2$, one has to calculate the alumina activity to derive the partial oxygen pressure.

The formation reactions for $CuAlO_2$ can be expressed as:

$$Cu + \frac{1}{4}O_{2(g)} + \frac{1}{2}Al_2O_3 = CuAlO_2 \qquad \Delta G^{o}_{1293.15K} = -46.617\ kJ/mol \quad [6\text{-}50]$$

with a standard Gibbs energy ΔG^o, presently obtained, and the corresponding equilibrium constant K_{CuAlO2}:

$$K_{CuAlO_2} = \left[\frac{a_{CuAlO_2}}{a_{Cu} \cdot p_{O_2}^{1/4}}\right] = 10^{1.880} \quad [6\text{-}51]$$

At equilibrium, the activities of Cu (copper crucible) and $CuAlO_2$ are unity, and the partial oxygen pressure is given by:

$$p_{O_{2(g)}}^{1/4} = \left[\frac{1}{K_{AlCuO_2} \cdot a_{Al_2O_3}^{1/2}}\right] = \left[\frac{1}{10^{1.880} \cdot a_{Al_2O_3}^{1/2}}\right] \quad [6\text{-}52]$$

In the region where the alumina activity is high enough to keep the solution in equilibrium with solid $CuAlO_2$, the partial oxygen pressure is given by [6-52]:

In the region where Cu_2O is stable, the partial oxygen pressure in equation [6-47] can be calculated using the reaction of formation of Cu_2O:

$$\frac{1}{2}Cu_2O = Cu + \frac{1}{4}O_{2(g)} \qquad \Delta G^{o}_{1293.15K} = 37.547\,kJ/mol \quad [6\text{-}53]$$

At equilibrium the activities of Cu_2O and Cu (copper crucible) are unity, and the partial oxygen pressure can be expressed as:

$$p_{O_2}^{1/4} = K_{Cu_2O} = 10^{-1.517} \quad [6\text{-}54]$$

The activity of Cu_2O is unity in the range of alumina concentrations low enough to stabilise Cu_2O, implying that the partial oxygen pressure is given by [6-54] in this region.

Since a copper crucible was used for all the solubility measurements for Cu_2O, the Cu activity is unity, which implies that the partial oxygen pressure in [6-46] is given by equation [6-52] for the aluminate region, and:

$$[Cu(I)] = K_3 \cdot \left[\frac{1}{10^{1.880} \cdot a_{Al_2O_3}^{1/2}}\right] \quad [6\text{-}55]$$

The expression for the Cu_2O region follows similarly by combining [6-47] and [6-54]:

$$[Cu(I)] = K_3 \cdot 10^{-1.517} \qquad [6\text{-}56]$$

One can also carry out an analogous process for the solution with the same alumina content at unit oxygen pressure, which leads to the expression for the "pure" Cu(II) solubility, *i.e.* [Cu(II)], in the hole alumina range given by [6-48][3]. In the region where $CuAl_2O_4$ is stable:

$$[Cu(II)] = K_4 \cdot a_{Cu} \cdot p_{O_2}^{1/2} = K_4 \cdot \left[\frac{1}{K_{CuAl_2O_4} \cdot a_{Al_2O_3}} \right] = K_4 \cdot \left[\frac{10^{-2.298}}{a_{Al_2O_3}} \right] \qquad [6\text{-}57]$$

The expression for the CuO region follows in a similar way as shown for Cu_2O, and is given by:

$$[Cu(II)] = K_4 \cdot a_{Cu} \cdot p_{O_2}^{1/2} = K_4 \cdot K_{CuO} = K_4 \cdot 10^{-1.699} \qquad [6\text{-}58]$$

The values for K_3 and K_4 are found by solving simultaneously two sets of solubility data expressed by equation [6-49] at the same alumina activity. The first [Cu total] corresponds to the solubility of Cu in a specific melt in a Cu crucible, and the other [Cu total] is given for the solubility of Cu in the same melt composition under an atmosphere of $O_{2(g)}$. These calculations were made in a spread-sheet for 1.5 to 13 wt% alumina. Best-fit lines for the Cu-solubility data and the presently obtained Gibbs energies of formation were used.

The "pure" solubilities of Cu(I) and Cu(II) were then calculated using equations [6-47] and [6-48], respectively, using [6-55] to [6-58]. The amounts of Cu(I) *in oxygen* and Cu(II) *in copper*, are given in Figure 6-21 as wt%. The numbers are tabulated in Table B15 in Appendix B.

[3] K_{CuO} and $K_{CuAl_2O_4}$ are the equilibrium constants for the formation reactions of CuO (*i.e.* [6-3], p. 140) and $CuAl_2O_4$ (*i.e.* [6-41], p. 163), respectively.

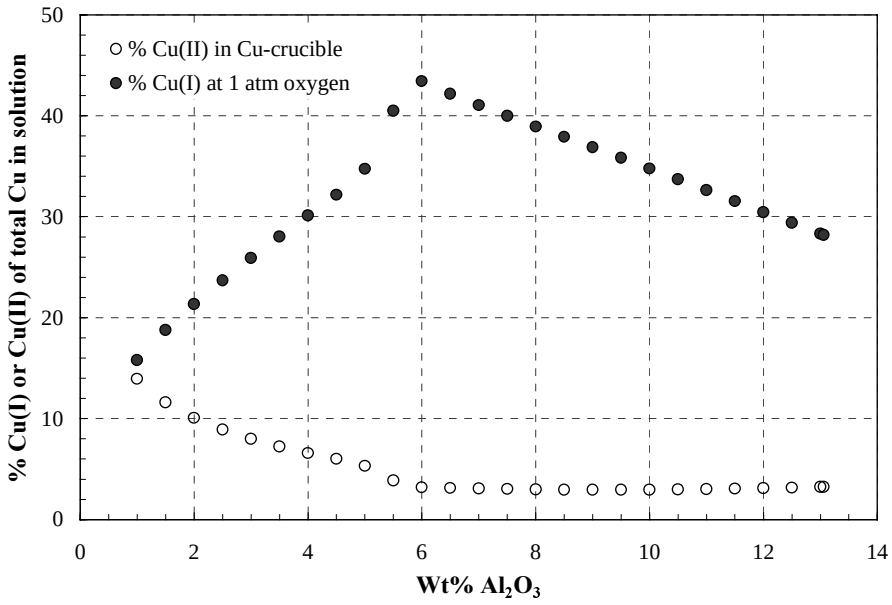

Figure 6-21: % Cu(I) or Cu(II) of total Cu in solution as a function of the alumina content in cryolite at 1020 ^{o}C.

Using the present results for K_3 and K_4 one can now calculate the equilibrium quantities of "pure" Cu(I) and Cu(II) for a fixed solvent composition at *all* oxygen pressures (*i.e.* vertical lines in the stability diagram 2-4). On a log-log plot the lines for the concentrations of Cu(I) and Cu(II) are straight within the stability ranges of the different solid phases, and can be derived from the data in Table B-8 in Appendix B. As an illustration, the procedure to obtain such a diagram for alumina-saturated melts at all oxygen pressures (*i.e.* along the right-hand border of Figure 2-4 p. 27) is explained below for the $CuAl_2O_4$ region.

The formation of $CuAl_2O_4$ can be expressed according to reaction [6-40]. For a fixed alumina activity, the logarithms of the concentrations of Cu(I) and Cu(II) can then be expressed by equations [6-47] and [6-48], respectively, by using the logarithm of the copper aluminate activity derived from [6-41]. By using the same method as described for iron in Chapter 5.11, p. 128, one gets the following expressions at unit alumina activity,

$$\log[\mathrm{Cu(I)}] = C_1 - \frac{1}{4}\cdot\log(p_{O_2}) \qquad [6\text{-}59]$$

and,

$$\log[\mathrm{Cu(II)}] = C_2 \qquad [6\text{-}60]$$

where C_1 and C_2 are constants.

Equations [6-59] and [6-60] imply that in the $CuAl_2O_4$ range the concentration of Cu(II) is constant at a fixed alumina activity, but the concentration of Cu(I) goes down as the

pressure of oxygen is raised. In the $CuAlO_2$ region the concentration of Cu(I) is constant while Cu(II) increases with increasing oxygen pressure (see Figure 6-25).

Four different alumina concentrations based on the stability diagram for Cu (Figure 2-4 p.27) were chosen to give an illustration of how the copper concentrations vary with the partial pressure of oxygen at constant alumina activity, and the results are represented in Figures 6-22 to 6-25.

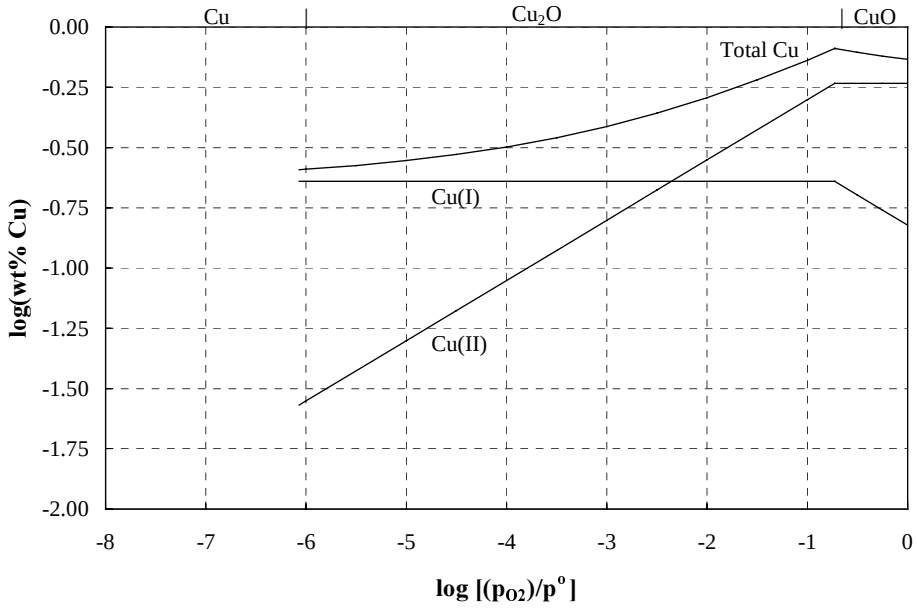

Figure 6-22: The amounts amount of Cu(I) and Cu(II) as a function of the partial oxygen pressure in cryolite with 1.5 wt% Al_2O_3. T = 1020 °C.

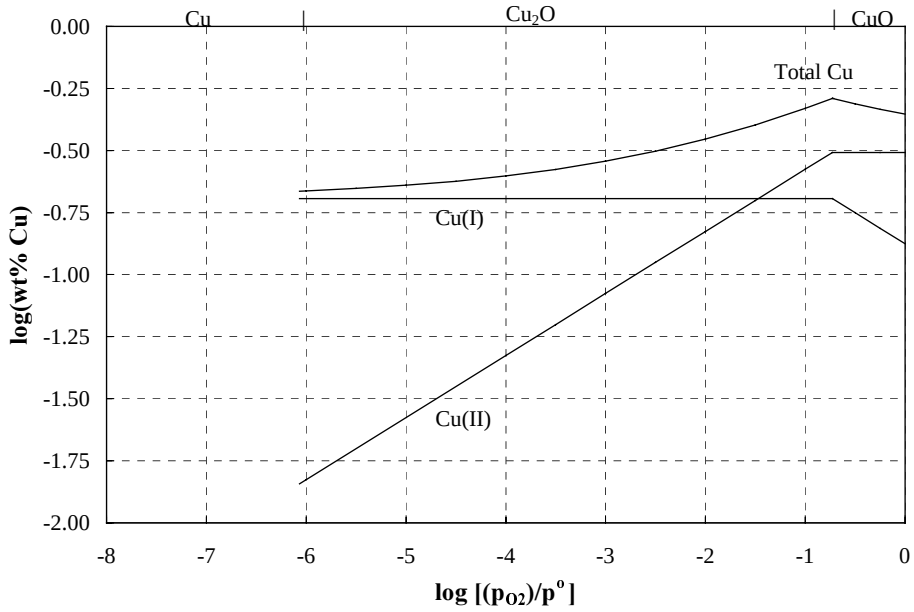

Figure 6-23: The amounts of Cu(I) and Cu(II) as a function of the partial oxygen pressure in cryolite with 4.5 wt% alumina. T = 1020 °C.

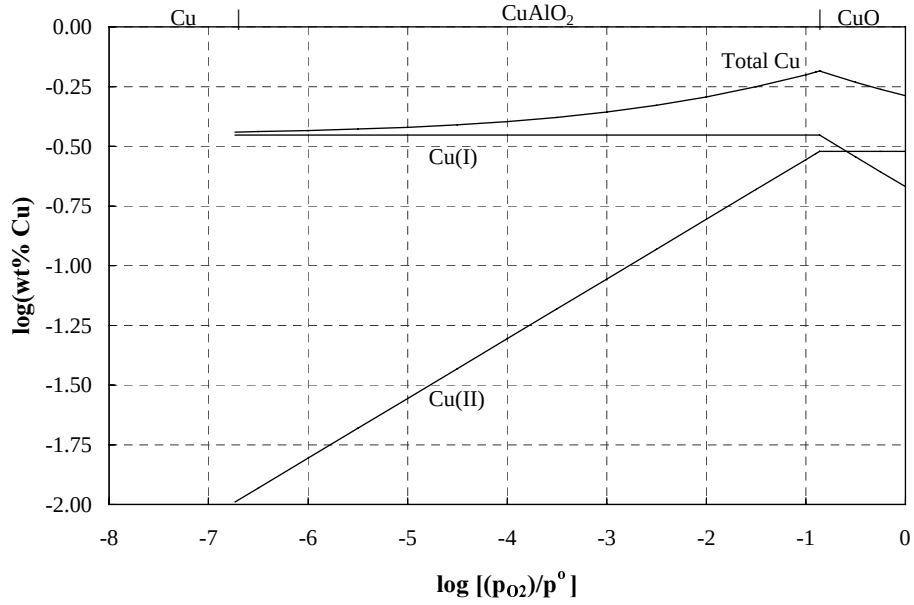

Figure 6-24: The amounts of Cu(I) and Cu(II) as a function of the partial oxygen pressure in cryolite with 7.5 wt% alumina. T = 1020 °C.

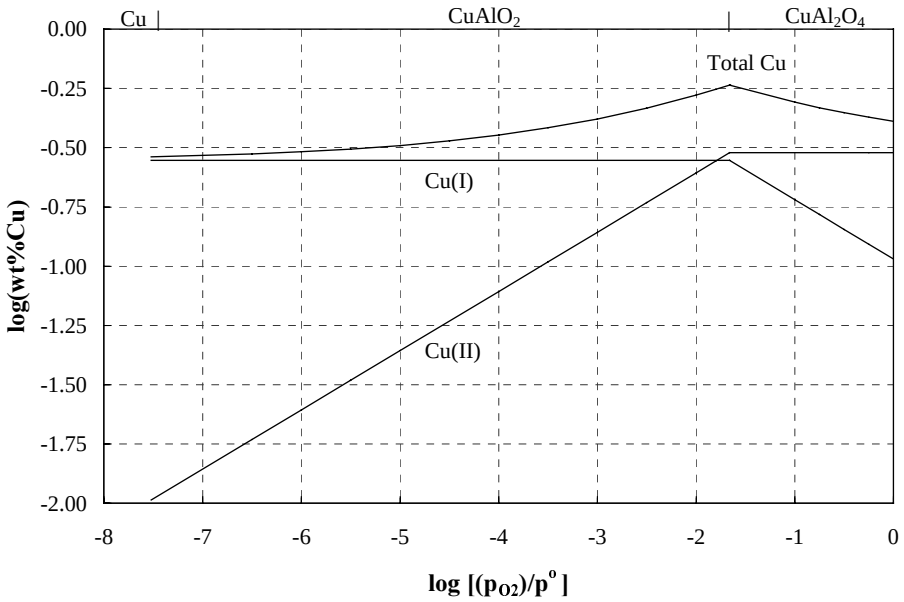

Figure 6-25: The amounts of Cu(I) and Cu(II) as a function of the partial oxygen pressure in cryolite at alumina saturation. T = 1020 °C.

6.9 Cu(I) species in molten cryolite-alumina melts

Figures 6-15 and 6-16 suggest that there are at least four Cu species involved, *i.e.* two Cu(I) and two Cu(II) species at low and high alumina activities, respectively. Each of the species has two parameters to assign (the power for the alumina activity, and the equilibrium constant K_i) which makes 8 parameters. In addition one has 2 estimated parameters for the equilibrium constants for the 2 solid aluminates ($CuAlO_2$ and $CuAl_2O_4$). In other words, there is no way one can sort out everything unambiguously.

The slope for the low alumina region in Figure 6-15 is reasonably close to –1/6 (indicating the formation of CuF according to equation [6-61]), before the Cu concentration starts to rise again indicating the formation of an oxy-compound. However, since it was shown that there is a mixture of both Cu(I) and Cu(II) in these melts, and the relative amounts of these two oxidation states vary with the alumina content, one cannot use these data directly to find a dissolution mechanism.

$$\frac{1}{2}Cu_2O + \frac{1}{3}AlF_3 = CuF + \frac{1}{6}Al_2O_3 \qquad [6\text{-}61]$$

In Chapter 6.8 Cu(I) and Cu(II) were separated from each other, and called the "pure solubility". On the basis of the "pure" solubility data calculated by equations [6-47] and [6-48], respectively, it is possible to predict which species form in the cryolite-alumina melts. The "pure" solubility data for Cu(I) is shown in Figure 6-26 for alumina concentrations from 1.5 to 13.06 wt% in steps of 0.5 wt%.

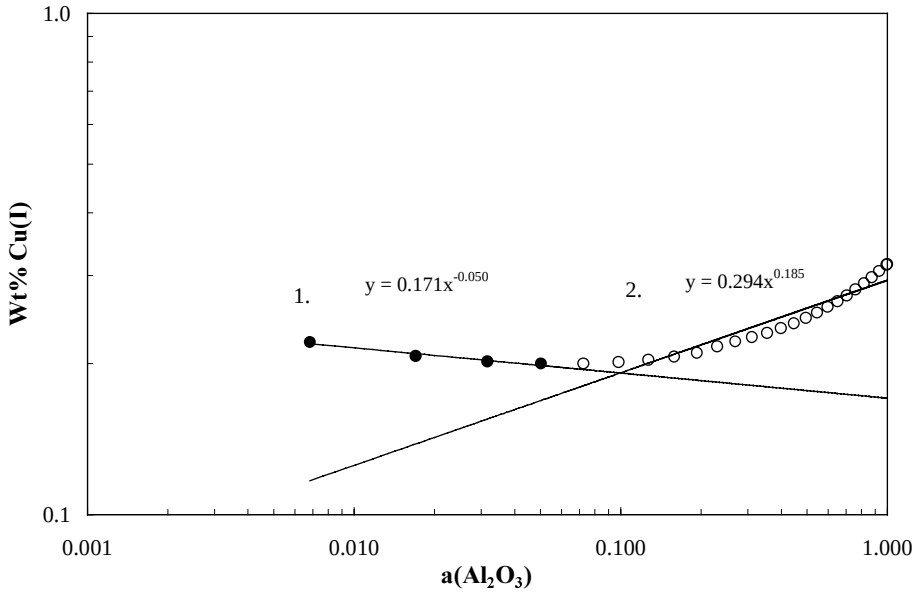

Figure 6-26: "Pure" solubility of Cu(I) as a function of alumina activity at 1020 ^{o}C.

From Figure 6-26 it looks like there is a coexistence of at least two Cu(I) species. The slope of the low-alumina region is close to –1/20, which cannot be explained by a dissolution process that involves Cu_2O. The lowest slope that is conceivable is –1/6, which corresponds to the dissolution process [6-61].

For simplification it is assumed that the species are present in the solution as neutral entities. The method was based on the supposition that whatever species one has, each contains only one Cu, and one cannot have a species containing only half an oxygen. The slope of zero, implying a Cu_2O-species in solution, is, therefore, ruled out.

The slope for the high-alumina region is close to +1/6. In this region it has been shown in previous sections that copper aluminate ($CuAlO_2$) is the stable solid phase. The dissolution process that can be explained by the slope of +1/6 is:

$$CuAlO_2 + \frac{1}{6}Al_2O_3 + 4NaF = \frac{1}{2}Na_8Cu_2O_5 + \frac{4}{3}AlF_3 \qquad [6\text{-}62]$$

The slope for the low alumina region in Figure 6-26 should be steeper, since the oxy-species present at the same time will reduce the negative slope. One might expect the same to be the case for the high-alumina region[4], using the same argument for the presence of a Cu fluoride. The following dissolution process can explain a slope of +1/3,

[4] The slope should be more positive.

$$CuAlO_2 + \frac{1}{3}Al_2O_3 + 5NaF = Na_5CuO_3 + \frac{5}{3}AlF_3 \qquad [6\text{-}63]$$

Two models can now be made for the two suggested systems CuF-$Na_8Cu_2O_8$ and CuF-Na_5CuO_3, respectively. The first assumption is that the two reactions [6-61] and [6-62] given in each system are independent of each other, and that both equilibria are satisfied simultaneously. One also has to assume that the activities of all components except alumina are constant. Since Cu_2O and $CuAlO_2$ are solid, they will have unit activity, while varying alumina activity affects the NaF and AlF_3 activities. This is, however, a second order effect, which is neglected to make the models easier to solve. By assuming that Henry's law applies to these systems, the activities for the solute species are replaced by concentrations, giving the following equations based on the dissolution mechanisms [6-61] to [6-63], respectively.

$$[CuF] = K_5 \cdot a_{Al_2O_3}^{-1/6} \qquad [6\text{-}64]$$

$$[Na_8Cu_2O_5] = K_6 \cdot a_{Al_2O_3}^{1/6} \qquad \text{(Model 1)} \qquad [6\text{-}65]$$

$$[Na_5CuO_3] = K_7 \cdot a_{Al_2O_3}^{1/3} \qquad \text{(Model 2)} \qquad [6\text{-}66]$$

Brackets mean that the solubilities of the copper species are given as "mol per 100 g solution". This concentration unit was chosen in preference of, for example, weight percent, because it simplifies the models since it does not change between each iteration. The constants K_5, K_6 and K_7 are not true equilibrium constants since they do not contain the activity terms for NaF and AlF_3, and hence they are only proportionality constants. The models require the two reactions to be independent of each other and that both equilibria are satisfied simultaneously.

The total copper concentration, [Cu(I)], for the two systems is then given by:

$$[Cu(I)] = [CuF] + [Na_8Cu_2O_8] \qquad [6\text{-}67]$$

and,

$$[Cu(I)] = [CuF] + [Na_5CuO_3] \qquad [6\text{-}68]$$

The ratio between the two oxy-species and CuF in the two proposed systems, CuF -$Na_8Cu_2O_5$ and CuF - Na_5CuO_3, are then found by dividing equation [6-65] by [6-64],

$$\frac{[Na_8Cu_2O_5]}{[CuF]} = \frac{K_6}{K_5} \cdot a_{Al_2O_3}^{1/3} \qquad [6\text{-}69]$$

and by dividing equation [6-66] by [6-64],

$$\frac{[Na_5CuO_3]}{[CuF]} = \frac{K_7}{K_5} \cdot a_{Al_2O_3}^{1/2} \qquad [6\text{-}70]$$

The total concentration of Cu(I) can be expressed by the sum of [6-64] and [6-65],

$$[Cu(I)] = K_5 \cdot a_{Al_2O_3}^{-1/6} + K_6 \cdot a_{Al_2O_3}^{1/6} \qquad [6\text{-}71]$$

and by the sum of [6-64] and [6-66],

$$[Cu(I)] = K_5 \cdot a_{Al_2O_3}^{-1/6} + K_7 \cdot a_{Al_2O_3}^{1/3} \qquad [6\text{-}72]$$

By multiplying equations [6-71] and [6-72] with $a_{Al_2O_3}^{1/6}$, one gets,

$$[Cu(I)] \cdot a_{Al_2O_3}^{1/6} = K_5 + K_6 \cdot a_{Al_2O_3}^{1/3} \qquad \text{(Model 1)} \qquad [6\text{-}73]$$

$$[Cu(I)] \cdot a_{Al_2O_3}^{1/6} = K_5 + K_7 \cdot a_{Al_2O_3}^{1/2} \qquad \text{(Model 2)} \qquad [6\text{-}74]$$

which should give two straight lines with K_5 as the intercept and K_6 and K_7, as the slopes of each curve if [6-73] is plotted as a function of $a_{Al_2O_3}^{1/3}$ and [6-74] as a function of $a_{Al_2O_3}^{1/2}$, respectively.

An iteration approach has to be performed to determine the K values, which can be used in equations [6-64] to [6-66] to express the contents of each species in the melt, separately. Since the oxy-species contain oxygen, their oxygen contents have to be subtracted from the measured alumina concentrations to get the true alumina concentration in the melt. The LECO apparatus does not distinguish between the sources of oxygen in the samples, so the alumina concentrations measured by LECO actually contain also the oxygen contribution from the cuprous oxy-comples.

The iteration procedure used is explained for $Na_8Cu_2O_5$, but is similar for Na_5CuO_3. As a first approximation one ignores the oxygen content in the oxy-compound, and plots $[Cu(I)] \cdot a_{Al_2O_3}^{1/6}$ *versus* $a_{Al_2O_3}^{1/3}$ using equation [6-73]. Regression analysis of the plot gives the first approximation of K_5 and K_6. Equation [6-69] can then be used for all the alumina concentrations to express the ratio between CuF and $Na_8Cu_2O_5$ in the melt at the same time. Since $Na_8Cu_2O_5$ contains 2.5 oxygen atoms per Cu atom, 2.5 times the Cu(I) concentration is subtracted from the original oxygen content in alumina to get a first approximation of the real alumina concentration in the melt. $[Cu(I)] \cdot a_{Al_2O_3}^{1/6}$ is once again plotted *versus* $a_{Al_2O_3}^{1/3}$ with the revised alumina activities, giving new approximations of K_5 and K_6. This iteration procedure is repeated until the K-values do not change from one iteration to the other, and the fit for the regression line, expressed as R^2, is as close to 1 as

possible. If the final plot of $[Cu(I)]\cdot a_{Al_2O_3}^{1/6}$ is fairly straight, it is taken as an adequate interpretation of the results. The models assume constant activity of all compounds except alumina and constant activity coefficients of the copper species. Neither of these conditions can be expected to be exactly correct, and for that reason one cannot expect more than "fairly" straight lines.

The same iteration procedure was applied to the two possible mechanisms in the CuF-Na_5CuO_3 system. $[Cu(I)]\cdot a_{Al_2O_3}^{1/6}$ was plotted by using equation [6-74], which gives values for K_5 and K_7. The only difference from the first iteration method is that since Na_5CuO_3 contains 3 oxygen atoms per copper ion, 3 times the Cu(I) concentration is subtracted from the original oxygen content in alumina.

The final plot of $[Cu(I)]\cdot a_{Al_2O_3}^{1/6}$ *versus* $a_{Al_2O_3}^{1/3}$ for the system CuF-$Na_8Cu_2O_5$ is given in Figure 6-27, and a similar plot of $[Cu(I)]\cdot a_{Al_2O_3}^{1/6}$ *versus* $a_{Al_2O_3}^{1/2}$ for the system CuF-Na_5CuO_3 is given in Figure 6-28.

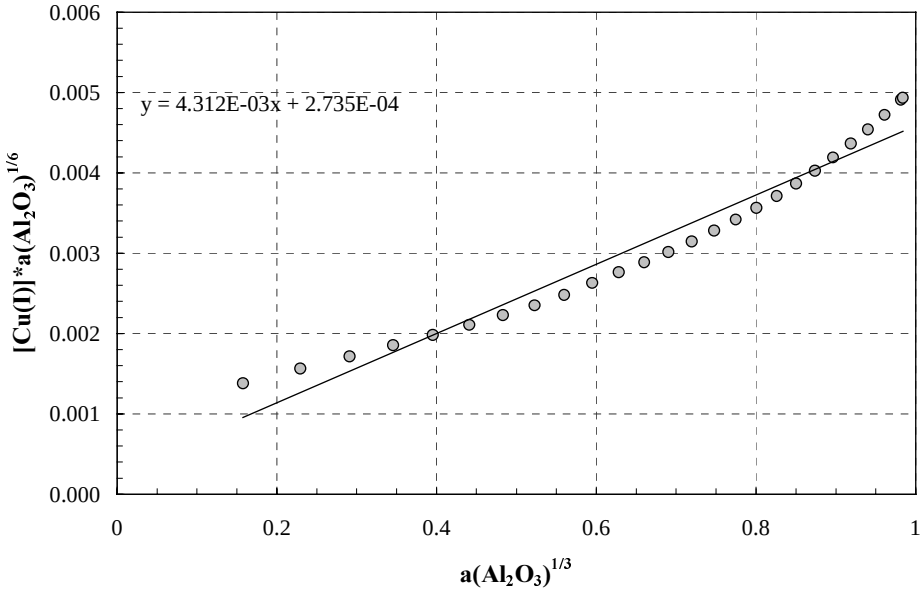

Figure 6-27: Plot of $[Cu(I)]\cdot a_{Al_2O_3}^{1/6}$ *versus* $a_{Al_2O_3}^{1/3}$ for the system CuF-$Na_8Cu_2O_5$ (Model 1). R^2 is 0.956 and the standard error for the regression line is 0.0045.

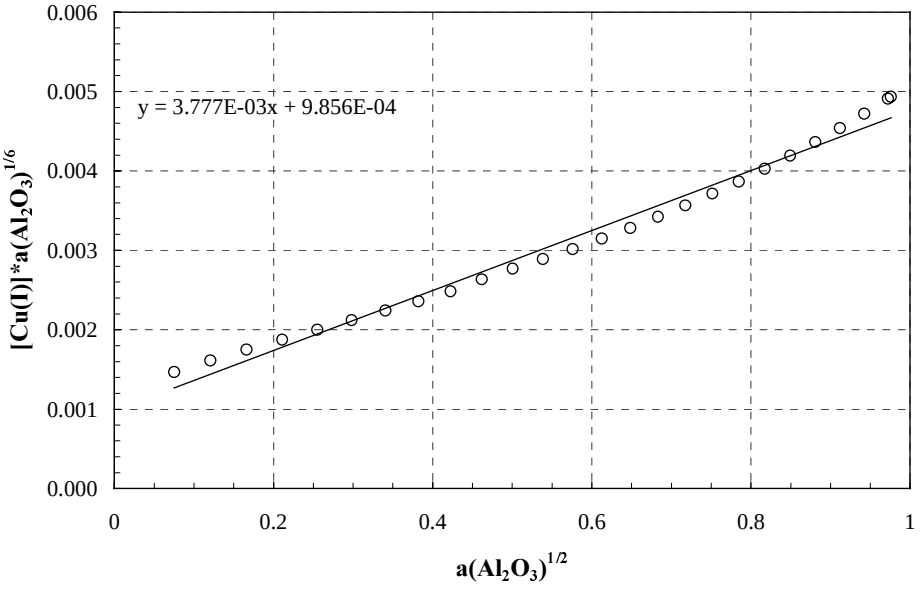

Figure 6-28: Plot of $[Cu(I)] \cdot a_{Al_2O_3}^{1/6}$ *versus* $a_{Al_2O_3}^{1/2}$ for the system CuF-Na_5CuO_3 (Model 2). R^2 is 0.984 and the standard error for the regression line is 0.0041.

The regression lines shown in Figures 6-27 and 6-28 are given by equations [6-75] and [6-76], respectively,

$$\left[Cu(I)\right] \cdot a_{Al_2O_3}^{1/6} = 43.12 * 10^{-4} + 2.735 * 10^{-4} \cdot a_{Al_2O_3}^{1/3} \qquad [6\text{-}75]$$

$$\left[Cu(I)\right] \cdot a_{Al_2O_3}^{1/6} = 37.77 * 10^{-4} + 9.856 * 10^{-4} \cdot a_{Al_2O_3}^{1/2} \qquad [6\text{-}76]$$

The K values obtained from the iterations can be used to express the solubilities of the different Cu(I) species as a function of alumina activity using equations [6-64] to [6-66]. The results are given in Figure 6-29 for the system CuF-$Na_8Cu_2O_5$ and in Figure 6-30 for the system CuF-Na_5CuO_3.

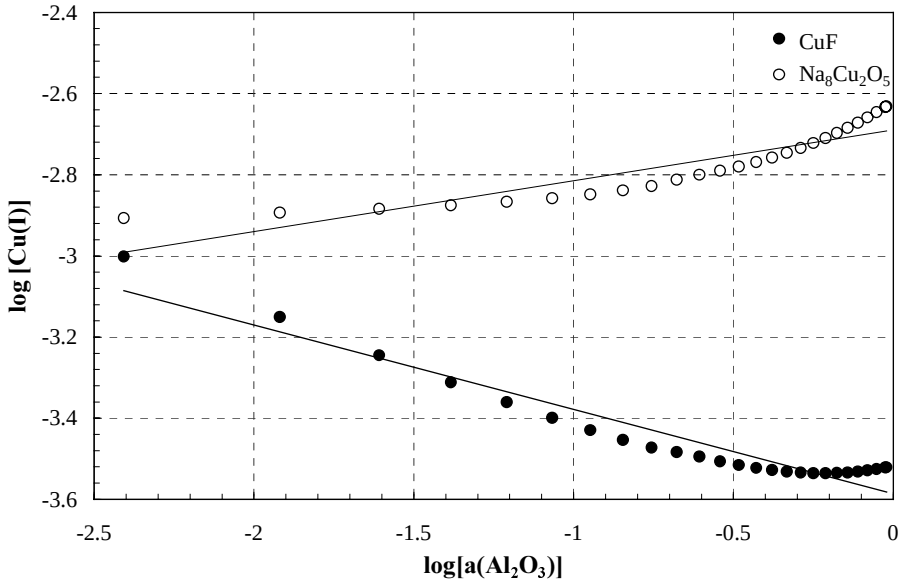

Figure 6-29: Log-log plot of the concentration of CuF and $Na_8Cu_2O_5$ in cryolite, expressed as [Cu(I)], *versus* alumina activity (model 1).

The concentrations of CuF and $Na_8Cu_2O_5$ shown in Figure 6-29 are given by equations [6-77] and [6-78], respectively,

$$\log([CuF]) = -0.208 \cdot \log(a_{Al_2O_3}) - 3.586 \qquad [6\text{-}77]$$

$$\log([Na_8Cu_2O_5]) = 0.125 \cdot \log(a_{Al_2O_3}) - 2.689 \qquad [6\text{-}78]$$

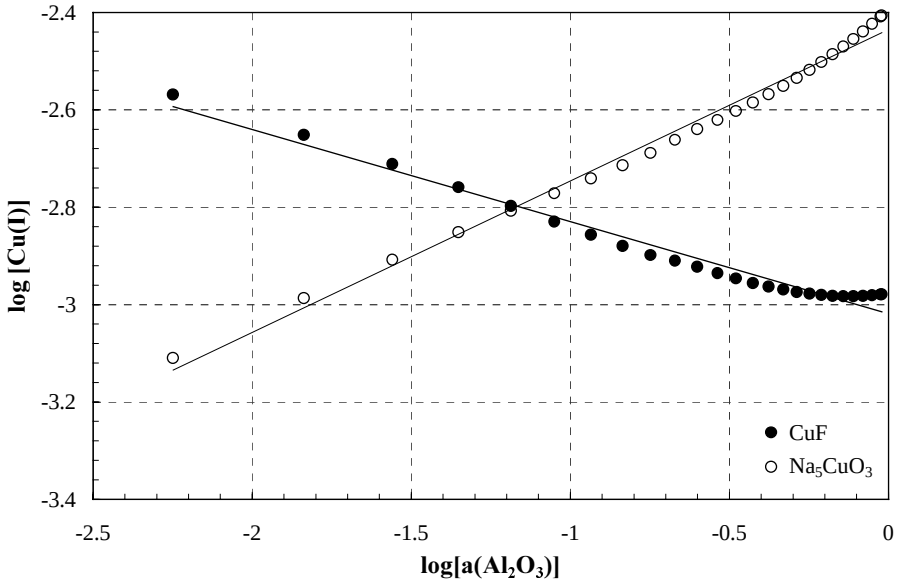

Figure 6-30: Log-log plot of the concentrations of CuF and Na_5CuO_3 in cryolite, expressed as [Cu(I)], *versus* the alumina activity (model 2).

The concentrations of CuF and Na_5CuO_3 shown in Figure 6-30 are given by equations [6-79] and [6-80], respectively,

$$\log([CuF]) = -0.189 \cdot \log(a_{Al_2O_3}) - 3.019 \qquad [6\text{-}79]$$

$$\log([Na_5CuO_3]) = 0.311 \cdot \log(a_{Al_2O_3}) - 2.435 \qquad [6\text{-}80]$$

Na_5CuO_3 gives an overall better fit of the solubility data than $Na_8Cu_2O_5$ does. In addition, the slopes obtained from the iterations for the system CuF-Na_5CuO_3 correspond better with the proposed dissolution processes for CuF-Na_5CuO_3. Na_5CuO_3 is, therefore, the most plausible species in coexistence with CuF in cryolite melts at 1020°C. However, it cannot be excluded that these two species are parts of larger complexes where additional NaF and AlF_3 groups are associated. According to Bailar *et al.* (25), Cu(I) has most commonly a co-ordination number of 4, *i.e.* tetrahedral, while 2 and 3 are much more uncommon. It should be noted that Na_5CuO_3 is a species found on a purely mathematical basis, and it has not been found reported in the literature.

6.10 Cu(II) species in molten cryolite-alumina melts

The "pure" solubility data for Cu(II) was found the same way as shown for Cu(I), and the results are shown in Figure 6-31.

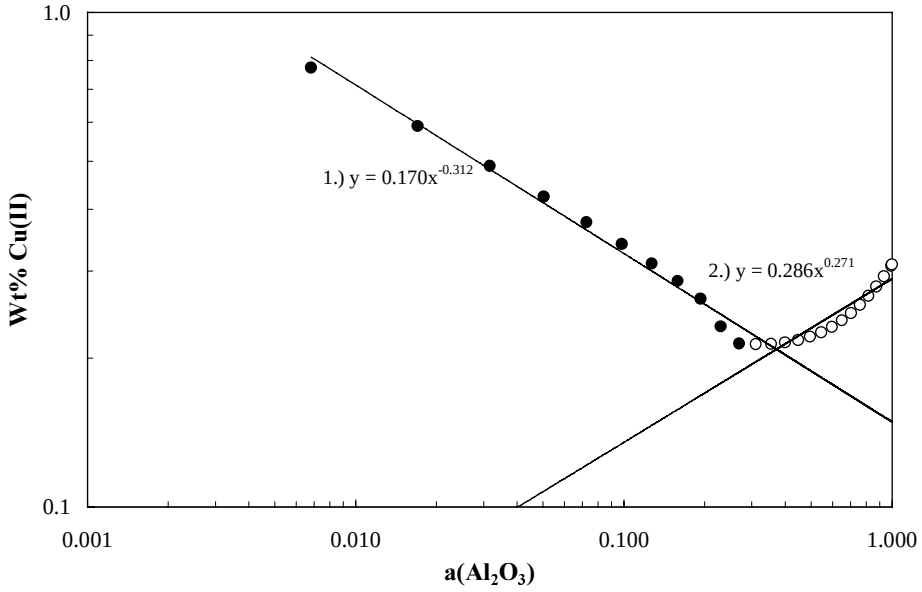

Figure 6-31: "Pure" solubility of Cu(II) as a function of alumina activity at 1020 ^{o}C.

As one can see from Figure 6-31, it looks like Cu(II) forms at least two different species in the cryolite-alumina system. In the low alumina region the slope of the solubility data is close to –1/3, which can be explained with the following dissolution process:

$$CuO + \frac{2}{3}AlF_3 = CuF_2 + \frac{1}{3}Al_2O_3 \qquad [6\text{-}81]$$

In the region where copper aluminate is stable the overall fit for these data give a slope close to +1/3. A slope of +1/3 can be explained by the dissolution mechanism,

$$CuAl_2O_4 + \frac{1}{3}Al_2O_3 + 8NaF = Na_8CuO_5 + \frac{8}{3}AlF_3 \qquad [6\text{-}82]$$

In addition the following reaction mechanisms were considered and evaluated with the same type of regression analysis as described for Cu(I),

$$CuAl_2O_4 + \frac{n}{3}Al_2O_3 + (6+2n)NaF = Na_{(6+2n)}CuO_{(4+n)} + \frac{(6+2n)}{3}AlF_3 \qquad [6\text{-}83]$$

where n = 2, 3, 4 and 5.

The concentration of CuF_2 in solution can according to equation [6-81] be described by,

$$[\text{Cu(II)}] = K_8 \cdot a_{Al_2O_3}^{-1/3} \qquad [6\text{-}84]$$

and if one uses $Na_{16}CuO_9$ as an illustration of one of the oxy-complexes formed according to [6-83], its concentration can be described as,

$$[\text{Cu(II)}] = K_9 \cdot a_{Al_2O_3}^{5/3} \qquad [6\text{-}85]$$

For this particular model, the sum of [6-84] and [6-85] gives the total Cu(II) concentration in solution, *i.e.*,

$$[\text{Cu(II)}] = K_8 \cdot a_{Al_2O_3}^{-1/3} + K_9 \cdot a_{Al_2O_3}^{5/3} \qquad [6\text{-}86]$$

By multiplying equation [6-86] with $a_{Al_2O_3}^{1/3}$, one gets,

$$[\text{Cu(II)}] \cdot a_{Al_2O_3}^{1/3} = K_8 + K_9 \cdot a_{Al_2O_3}^{2} \qquad [6\text{-}87]$$

Similar equations for all the suggested dissolution mechanisms for the oxy-complexes were combined with the one for CuF_2, and the iteration method described for Cu(I) was used to find the K-values, and the final slopes for the different dissolution processes. The results are summarised in Table 6-4. The theoretical slope of CuF_2 is –0.333.

Table 6-4: Solubility constants for expressing the solubility of Cu(II) by CuF_2 and various oxy-complexes as a function of alumina activity in cryolite at 1020 °C. K_A represents the intercept with the y-axis, and the K_B values the slope of the lines for the oxy-complex.

Complex	K_A*10^3	K_B*10^3	R^2	Slope CuF_2	Slope complex	Theoretical slope complex
Na_8CuO_5	1.673	2.449	0.762	-0.200	0.284	0.333
$Na_{10}CuO_6$	1.942	2.426	0.834	-0.206	0.619	0.667
$Na_{12}CuO_7$	2.079	2.523	0.893	-0.209	0.959	1.000
$Na_{14}CuO_8$	2.166	2.660	0.933	-0.210	1.300	1.333
$Na_{16}CuO_9$	2.230	2.822	0.959	-0.263	1.641	1.667

"Slope CuF_2" and "Slope complex" refer to the stoichiometric relationships between the dissolved copper species and the alumina in the proposed dissolution mechanisms.

According to Table 6-4, the coexistence of CuF_2 and $Na_{16}CuO_9$ give the overall best fit for the solubility data for Cu(II), since the slopes for CuF_2 and $Na_{16}CuO_9$ are closest to the theoretical slopes for these mechanisms and R^2 for this complex is closest to one.

The K values and the separate concentrations obtained for the system CuF_2-$Na_{16}CuO_9$ are given in Figures 6-32 and 6-33, respectively.

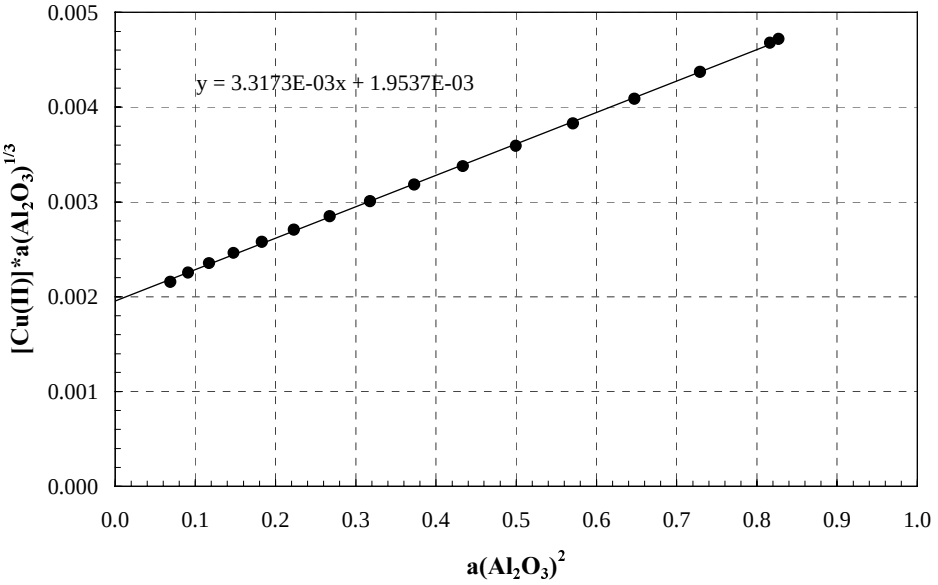

Figure 6-32: Plot of $[Cu(II)] \cdot a_{Al_2O_3}^{1/6}$ *versus* $a_{Al_2O_3}^{2}$ for the system CuF_2-$Na_{16}CuO_9$.

The regression line in Figure 6-32 can be expressed as,

$$[Cu(II)] \cdot a_{Al_2O_3}^{1/3} = 3.32 * 10^{-3} + 1.95 * 10^{-3} \cdot a_{Al_2O_3}^{2} \qquad [6\text{-}88]$$

The complex $Na_{16}CuO_9$ gives the best fit for the solubility data in coexistence with CuF_2, but complexes with lower contents of $Na_{2x}O_x$ cannot be ruled out. Neither can it be excluded that these species are parts of larger complexes where additional NaF and AlF_3 groups are associated, even though it seems unlikely because of the size.

The concentrations of CuF_2 and $Na_{16}CuO_9$, shown in Figure 6-33 are given by equations [6-89] and [6-90], respectively,

$$\log([CuF_2]) = -0.263 \cdot a_{Al_2O_3} - 2.531 \qquad [6\text{-}89]$$

$$\log([Na_{16}CuO_9]) = 1.641 \cdot a_{Al_2O_3} - 2.565 \qquad [6\text{-}90]$$

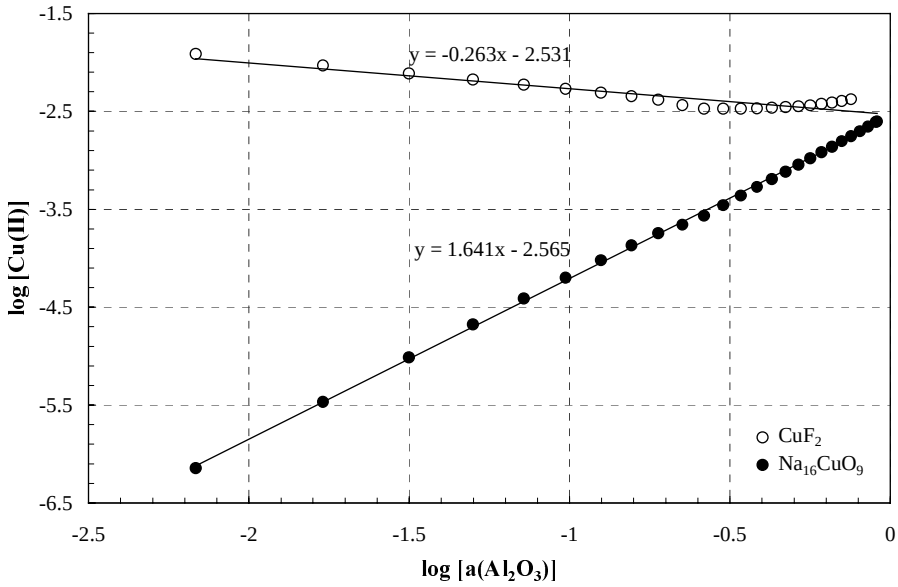

Figure 6-33: Plot of the concentration of CuF_2 and $Na_{16}CuO_9$ in cryolite, expressed as [Cu(II)], *versus* alumina activity on a logarithmic scale.

The bending of the upper curve observed in Figure 6-33 for the highest alumina activities might indicate that the LECO apparatus gives erroneous values for high alumina concentrations. An even more plausible explanation is caused by the fact that the pure solubility data were calculated by using pairs of solubility data with the same unadjusted alumina activities. As a result these alumina activities are a little too high. These alumina activities were not adjusted for the oxygen content present in the oxy-complexes, which means that the error in the alumina activities used are increasing with increasing alumina activity. Since the oxy-complexes that seem to form, are different for Cu(I) and Cu(II), and thereby contain different amounts of oxygen, the error is increasing at a different rate in these two systems, and it is highest in the Cu(II) system since the proposed Cu(II) oxy-complex contains more oxygen than the Cu(I)-complex. According to Bailar *et al.* (25) Cu(II) has most commonly the co-ordination number 6, then 4 and 5. Na_2CuF_4 is for example a common species. The existence of $Na_{16}CuO_9$ is hard to explain physically, but according to Melnik *et al.* (26), (27) there exist numerous Cu(II) compounds. Melnik *et al.* (27) review data for more than 230 trimeric and ogliomeric Cu(II) co-ordination compounds, including 73 trimeric, 5 tetrameric, 5 pentameric, 12 hexameric, 4 octameric, 2 nonameric and even 1 dodecameric derivatives. There are also several examples of distortion isomerism.

6.11 Solubility of CuO in industrially interesting melts

Because of the high melting temperature of cryolite and the fact that cryolite freezes out on the side-wall as insulation and that side-wall protection are wanted from an industrial point of view, cryolite melts with excess AlF_3 are normally used in industrial cells. To keep the

solubility of alumina at an acceptable level, melts with molar ratio 2.2–2.4. The ratio 2.29 is a common melt composition. It was therefore decided to measure the solubility of CuO in a melt with molar ratio 2.29 and alumina saturation and with 5 wt% alumina. The results of 6 experiments are shown in Figure 6-34.

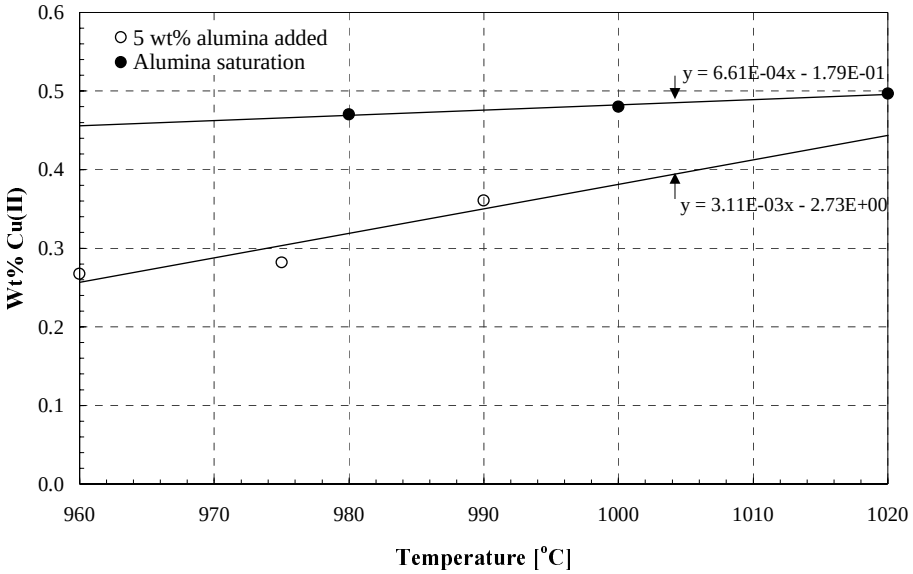

Figure 6-34: Plot of the concentration of CuO shown as "wt% Cu(II)" in a melt with molar ratio 2.29 and in an oxygen atmosphere.

As one can see from Figure 6-34, the alumina-saturated melt has a higher copper solubility than the melt with 5 wt% alumina. This trend is the same as shown at molar ratio 3.0, indicating the formation of an oxy-compound. The saturation concentration is ~10 % higher at molar ratio 2.29 than at molar ratio 3.0 at 1020 ^{o}C.

Dalsbotten (28) measured the solubility of Cu(II) as already described at different CR. His results are presented in figure 6-35.

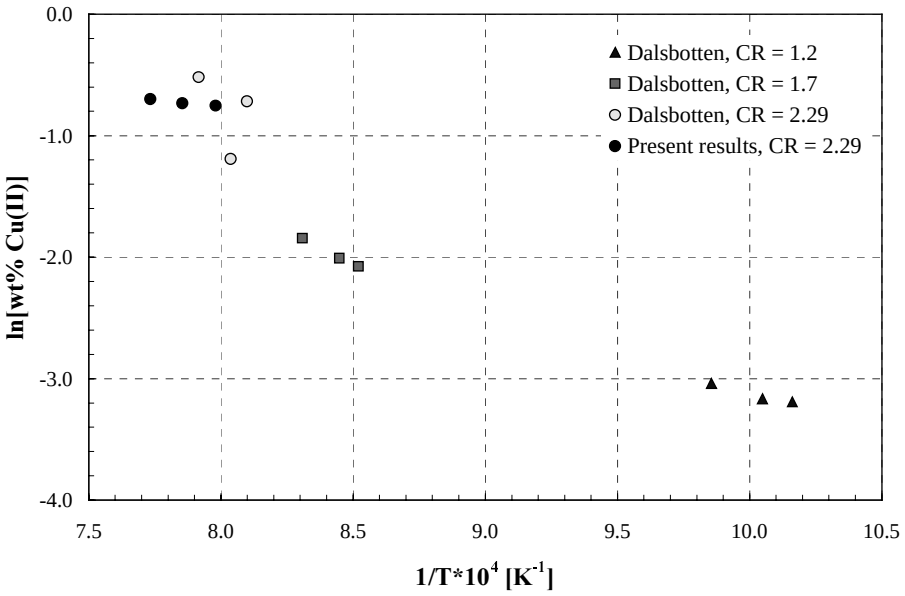

Figure 6-35: Plot of the concentration of CuO shown as "wt% Cu(II)" in a alumina-saturated melts at different molar ratios in an oxygen atmosphere.

According to figure 6-35 the saturation concentration of Cu(II) is dependent on both temperature and melt composition. Interpolation of data from one temperature to another should, therefore, be made with caution. Even at CR = 1.2 the saturation concentration of copper is relatively high to be interesting for copper as a material used as inert anode in cryolite, and should be used with caution in such melts.

Low ratio bath with an operating temperature of only 750 ^{o}C has been suggested (29), (30) and (31), and the phase diagram is shown in Appendix B10 for this temperature. As one can see, the stability region for CuO has increased tremendously. CuO is found to have a higher solubility in cryolite-based melts than Cu_2O, which is in disfavour for using low-melting baths when copper is used.

6.12 Concluding remarks

The mechanisms proposed at low alumina concentrations seem to be satisfactory, but there is still some uncertainty, both experimental and theoretical, about what is going on at the high alumina side. More work is needed to find out what is happening with the copper aluminates.

6.13 References

(1) *Aluminium*, *Properties and Physical Metallurgy*, American Society for Metals, edited by Hatch, J.E., 3rd ed., SAN 204-7586, Metals Park, Ohio, USA, 1988.

(2) Metals Handbook, *Metallography Structure and Phase Diagrams*¸ Am. Soc. for Metals, Metals Park, Ohio, p. 96, 1973.

(3) Knacke, O., Kubaschewski, O. and Hesselmann, K., *Thermochemical Properties of Inorganic Substances*, 2nd ed., Springer-Verlag, Verlag Stahleisen, 1991.

(4) Sterten, Å. and Skar, O., *Some Binary Na_3AlF_6-M_xO_y phase diagram*, Aluminium 64, pp.1051- 1054, 1988.

(5) Sterten, Å. and Støen, L., *Expomat –E3.6 Badkjemi – Statusrapport 1993 E3.6.01. tungtløselige oksider*, Report STF34 F93249, SINTEF Metallurgy, 1993.

(6) Sterten, Å., *E3.6 Badkjemi Statusrapport 1995,* SINTEF note, 1995.

(7) Sterten Å., *P3.8 Badkjemi – Statusrapport 1996*, SINTEF note, 1996.

(8) Jacob, K.T. and Alcock, C.B., *Thermodynamics of $CuAlO_2$ and $CuAl_2O_4$ and Phase Equilibria in the System Cu_2O-CuO-Al_2O_3,* J. Am. Cer. Soc., vol. 58, no 5-6, pp. 192-195, May-June, 1975.

(9) Kubaschewski, O., *The thermodynamic properties of double oxides (A review)*, High Temp.- High Pressures, vol. 4, pp. 1-12, 1972.

(10) Wagman, D.D., Evans, W.H., Parker, V.B., Schumm, R.H., Halow, I., Bailey, S.M., Churney, K.L and Nuttall, R.L., *The NBS Tables for inorganic and C_1 and C_2 organic substances in SI units*, J. Phys. Chem. Ref. Data, vol. 11, Suppl. 2, pp. 2-154 to 2-155, 1982.

(11) Levin, E.M. and McMurdie, H.F., *Phase Diagrams for Ceramists*, J. Am. Cer. Soc, Figs. 2085- 2094, pp. 11-13, Supplement, 1969.

(12) Mishra, S.K., Chaklader, C.D., *The System Copper Oxide-Alumina*, J. Am. Cer. Soc., Discussions and Notes, vol. 46, p. 509, 1963.

(13) Skar, O., *Liquiduskurver i kryolittsmelter ved tilsatser av oksyder*, Graduation thesis, Dept. of Electrochemistry, NTH, Trondheim, Noway, 1981.

(14) Førland, T., *in* Sundheim, B.S., *Fused Salts*, Chapt. 2, McGraw-Hill, Inc., New York, USA, 1964.

(15) Grjotheim, K., Krohn, C., Malinovsky, M., Matiasovsky, K. and Thonstad, J., in *Aluminum Electrolysis Fundamentals of the Hall-Heroult Process*, 2nd ed., Aluminium-Verlag, Dusseldorf, ISBN 3-87017-155-3, 1982.

(16) Solheim, A., Rolseth, S., Skybakmoen, E., Støen, L., Sterten, Å. and Støre, T., *Liquidus Temperatures for Primary Crystallization of Cryolite in Molten Salt Systems of interest for the Aluminium Electrolysis*, Met. Trans. B, *27*B, pp. 739, 1996.

(17) Solheim, A., Rolseth, S., Skybakmoen, E., Støen, L., Sterten, Å. and Støre, T., *Liquidus Temperatures and Alumina Solubility in the System Na_3AlF_6-AlF_3-LiF-CaF_2-MgF_2*, Light Metals 1995, pp. 451, 1995.

(18) Belyaev, A.I., Rapoport, M.B. and Firsanowa, L.A., *Metallurgie des Aluminiums*, Veb Verlag Technik Berlin, vol. 1, p. 74, 1956.

(19) Rolin, M. and Bernard, C., *Solubilité des oxydes dans la cryolithe fondue*, Bull. Soc. Chim. France, no 187, pp. 1035-1038, 1963.

(20) Dewing, E.W. And Thonstad, J., *Activities in the System Cryolite-Alumina*, Metall. Mater. Trans. B, vol 28 B, pp. 1089-1093, 1997.

(21) Dewing, E.W., *Thermodynamics of the System LiF-AlF_3,* J. Electrochem. Soc., Electrochemical Sci. and Tech., pp. 1289-1294, Sept. 1976.

(22) Kubaschewski, O. and Alcock, C.B., *Metallurgical Thermochemistry*, Pergamon Press, 5th ed., 1979.

(23) National Bureau of Standards, Table*s of Chemical Thermodynamical Properties*, J. Phys. Chem., Ref. Data, vol. 11, Suppl. no. 2, 1982.

(24) Dewing, E.W. and Thonstad, J., *Solutions of iron Oxides in Molten Cryolite*, Metall. Mater. Trans. B, vol. 31, no. 4, pp. 609–613, Aug. 2000.

(25) Bailar Jr., J.C., Emeleus, H.J., Nyholm, R. and Trotman-Dickenson, A.F., *Comprehensive Inorganic Chemistry*, Pergamon Press, Oxford, vol 3B, ISBN 008-017275-x, 1973.

(26) Melnik, M, Kabesova, M., Macaskova, L. and Holloway, C.E*., Copper(II) coordination compounds: Classification and analysis of crystallographic and structural data II. Mononuclear-, hexa-, hepta- and octacoordinate compounds*, J. Coord. Chem., vol. 45, no. 1-4, pp. 31–145, 1998.

(27) Melnik, M, Kabesova, M., Macaskova, L. and Holloway, C.E*., Copper(II) coordination compounds: Classification and analysis of crystallographic and structural data IV. Trimeric and ogliomeric compounds*, J. Coord. Chem., vol. 48, no. 3, pp. 271–374, 1999.

(28) Dalsbotten, S. B*., Solubility of Copper and Nickel Oxides in Cryolite-Based Electrolytes*, Diploma Thesis, Dept. Materials Tech. and Electrochem., NTNU, Dec. 2000.

(29) Beck, T.R., *Production of Aluminium With Low Temperature Fluoride Melts*, Light Metals 1994, pp. 417-423, 1994.

(30) Lu, H., Fang, K., Hong, Y., and Gao, B., *A new electrolytic aluminium production process*, ALUMINIUM, vol. 75, no. 12, pp. 1113-1118, 1999.

(31) Beck, T.D., *A Non-Consumable Anode for Production of Aluminium With Low-Temperature Fluoride Melts*, Light Metals 1995, pp. 355-360, 1995.

URN:NBN:no-6347

URN:NBN:no-6347

7 Cell design and mass transport considerations

The scope of the work was to investigate the transport mechanisms for anode components and the kinetics involved between the anode and the cathode. To carry out such a test, one needs a cell with good convection and low or no gradients present in the bulk of the electrolyte. A first approach to this problem is therefore to find a proper cell design.

7.1 Cell design considerations

7.1.1 A laboratory cell with horizontal electrodes

A cell with horizontal electrodes is the only orientation used by the smelters today to produce aluminium. Olsen *et al.* (1), (2) investigated the behaviour of many different cermet anodes on a laboratory scale. A sketch of Olsen's horizontal laboratory cell (2) is shown in Figure 7-1 below.

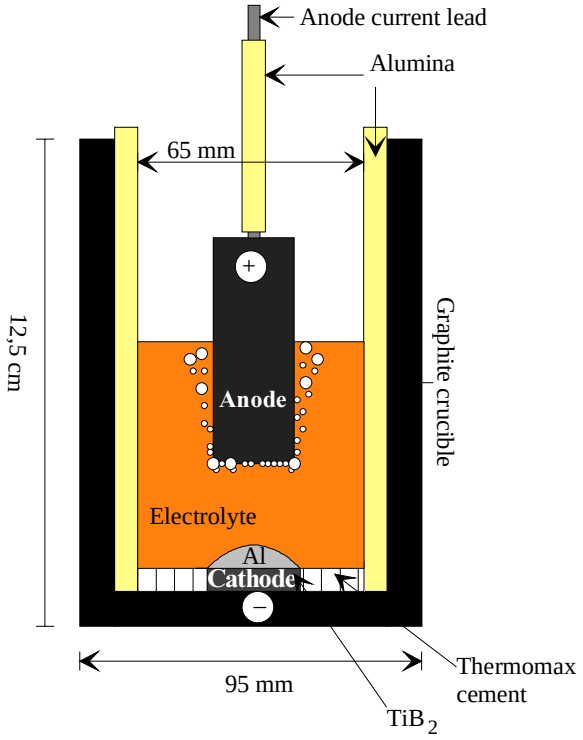

Figure 7-1: Small electrolysis cell with a horizontal inert anode, redrawn from (2).

The problem with such a cell is that you have little control of the current distribution at the anode. Olsen (2) estimated that approximately 40% of the current was passing through the horizontal part of the anode (*i.e.* bottom). However, the current distribution is very dependent on the cell geometry, anode and cathode size, conductivity of the electrolyte, the shape of the metal pad, the conductivity of the anode material *etc.*

An autopsy of a used cell similar to the one given in Figure 7-1 showed aluminium with a hemispherical shape at the TiB_2 cathode. Figure 7-2 shows how one believes the alumina pad to grow at the TiB_2 cathode as the electrolysis proceeds.

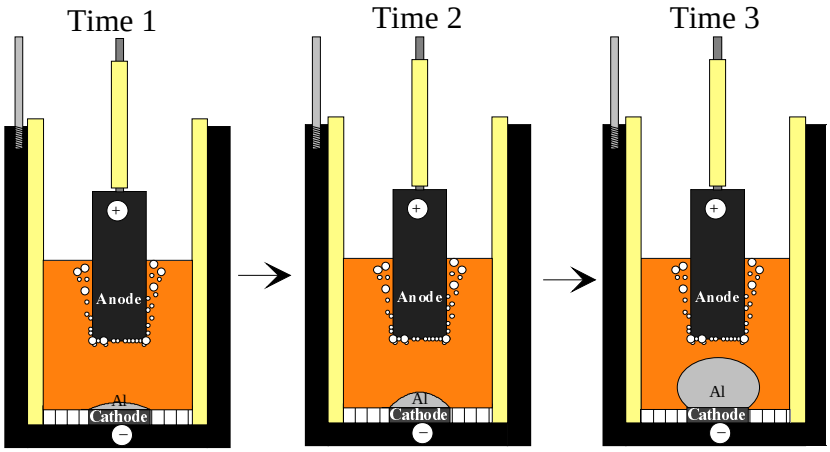

Figure 7-2: Development of a metal pad in an electrolysis cell with a horizontal inert anode. Time 1 < Time 2 < Time 3.

If order to investigate how the inert anode components behave in a cell during electrolysis, one needs to control the mass transport. It is very difficult to keep stable conditions in a cell like the one shown in Figure 7-1 because of the growing metal pad. Not only does the surface area of the ball (sphere) change during the experiment, the distance between the anode and cathode and the mass transport conditions change as well (3). It is also very difficult to keep the shape of the ball constant when frequently withdrawing aluminium samples from the cell. Even the current distribution at the anode will probably change during the experiment. This effect can be minimised by increasing the interpolar distance, *i.e.* the distance between the anode and the cathode. Increased interpolar distance will on the other hand give unrealistic electrolysis conditions since the idea of inert anodes is to decrease the interpolar distance to a minimum to save energy.

It is possible to reduce the height of the aluminium sphere by increasing the size of the cathode. There will, however, be a chance for the formation of a stagnant layer near the cathode (3). Mass transfer coefficients for Fe, Si and Ti at the electrolyte-metal interface found in industrial prebake cells (4) were 10 times higher than the ones reported by Olsen for this laboratory cell (1), indicating low convection near the cathode in the laboratory cell. The corrosion of the anode may also be very dependent of the cell design used (5).

Attempts were made to insulate the vertical sides of the anode with a layer of various insulating materials. It was, however, not easy to find a material which,

- could withstand cryolite melts and oxygen at 1000 ^{o}C
- had low electrical conductivity
- had low content of impurities
- had approximately the same coefficient of thermal expansion as the cermet anode
- was not too expensive

$NiAl_2O_4$ and $NiFe_2O_4$ were considered because of their low electrical conductivity, but it is not possible to avoid chemical dissolution of these materials, which would make it impossible to trace where nickel (and iron) came from (*i.e.* from the cermet $NiFe_2O_4$-containing anode or from the insulating material). The conductivity of these insulating materials is, however, sufficient for current leakage if the thickness of the insulating layer is low. The limitation of the size of the cermet, which was possible to use together with the different prefabricated crucible dimensions available, would, therefore, have given anodes with only a very thin cermet core if current leakage should have been avoided.

A sintered alumina tube was also considered as insulation. Olsen (2) reported, however, that the alumina dissolved near the corner of the anode (see Figure 7-3), and it was, therefore, considered unsuitable for this application.

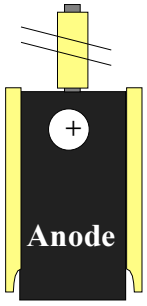

Figure 7-3: A worn horizontal inert anode with vertical alumina insulation.

Boron nitride (BN) can be used in experiments with a CO_2-producing *carbon* anode. A tube of BN was, therefore, mechanically shaped to fit as a shield around the anode, and tested. In the initial experiments the BN cracked after 4 hours electrolysis at CR = 2.3 and 960 ^{o}C, and the experiment was terminated. The furnace was then turned off and the anode was allowed to cool in a position approximately 5 cm above the melt level. There was no sign of disintegration of the BN sleeve, but it cracked during electrolysis. BN was also found to oxidise at 1020^{o}C in oxygen atmosphere (the surface turned black and it had blistering pits). A sketch of a cell with BN-insulated anode is shown in Figure 7- 4.

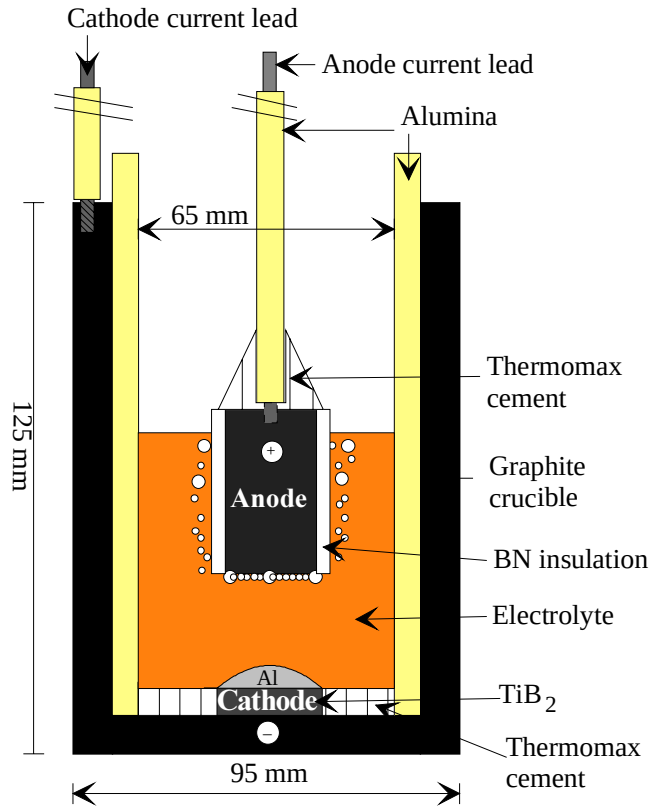

Figure 7-4: Small electrolysis cell with a horizontal inert anode with BN insulation.

Another problem in a cell with horizontal electrodes is the melt circulation (6). An inert anode produces very small gas bubbles compared to conventional carbon anodes (7), causing little gas-induced convection in the bulk of the cell. The circulation near the cathode will be reduced further if the interpolar distance is increased, and it may produce a stagnant layer (3). A sketch of an autopsied cell fed with 50 % of the theoretical alumina consumption, which was found sufficient (2) to maintain alumina saturation, is shown in Figure 7-5.

Holes were drilled into the anodes to make connection to an inconel rod using copper-based conductive cement. Between the inconel and the anode substrate, baked into the copper cement, were a 0.25 mm platinum foil wrapped around the tip of the rod to prevent galvanic oxidation of the rod. The conductive cement was cured stepwise for 2 hours in air at 90, 190 and 290 ^{o}C, respectively, to ensure proper electrical conductivity.

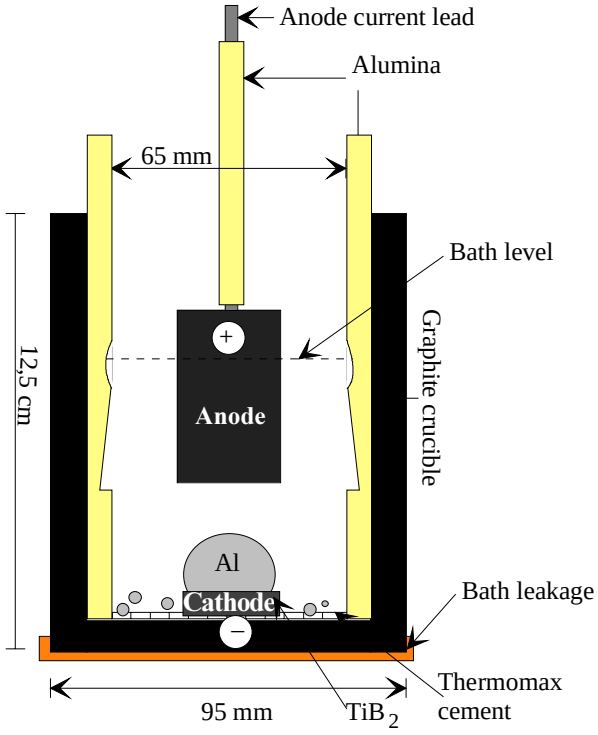

Figure 7-5: A sketch of an autopsied cell fed with 50 % of the theoretical alumina consumption. The reduction in the thickness of the alumina insulation is exaggerated.

The reduction in the thickness of the alumina insulation shown in Figure 7-5 is exaggerated. The profile showing the wear was, nevertheless, evident, and it indicates a depletion of alumina in the melt in the vicinity of the anode, and poor convection in the cell (6). There is probably a stagnant layer near the bottom of the cell, which influences the mass transport near the cathode metal.

The thermomax cement at the bottom of the cell (see Figure 7-5) contains mainly alumina, and it was totally dissolved in the melt at the end of the experiment. This dissolution allowed melt to penetrate into and even through the graphite crucible, leading to melt leakage as a result. The penetration of sodium in carbon is generally considered to be much higher than for aluminium in carbon (8). A reduction of cryolite ratio (CR) is, therefore, expected in such cells.

Mechanical stirring will probably improve the melt circulation and alumina dissolution, but there will be a risk for droplets from the growing aluminium pad to reach the anode where aluminium can react with the anode.

As already mentioned, oxygen bubbles generated at inert anodes in cryolite melts are known to be small (7). The small bubbles may give poor gas induced circulation in the bulk electrolyte around the anode and, therefore, alumina depletion near the anode, which in most cases will cause a higher solubility of anode constituents near the anode surface.

Proper upward gas-induced flow is reported (9) to agitate the melt and improve the dissolution of alumina. These dissolved anode constituents may precipitate farther away from the anode where the alumina concentration is higher and the solubilities are lower (6), (10). A cell configuration where the gas lift effect is used to mix the melt will be beneficial, and this would probably work more efficiently for vertical electrodes.

7.1.2 A laboratory cell with vertical electrodes

All the drawbacks mentioned for a traditional cell with horizontal electrodes led to the consideration of a cell with vertical electrodes. A sketch of the cell, which was used, is given in Figure 7-6.

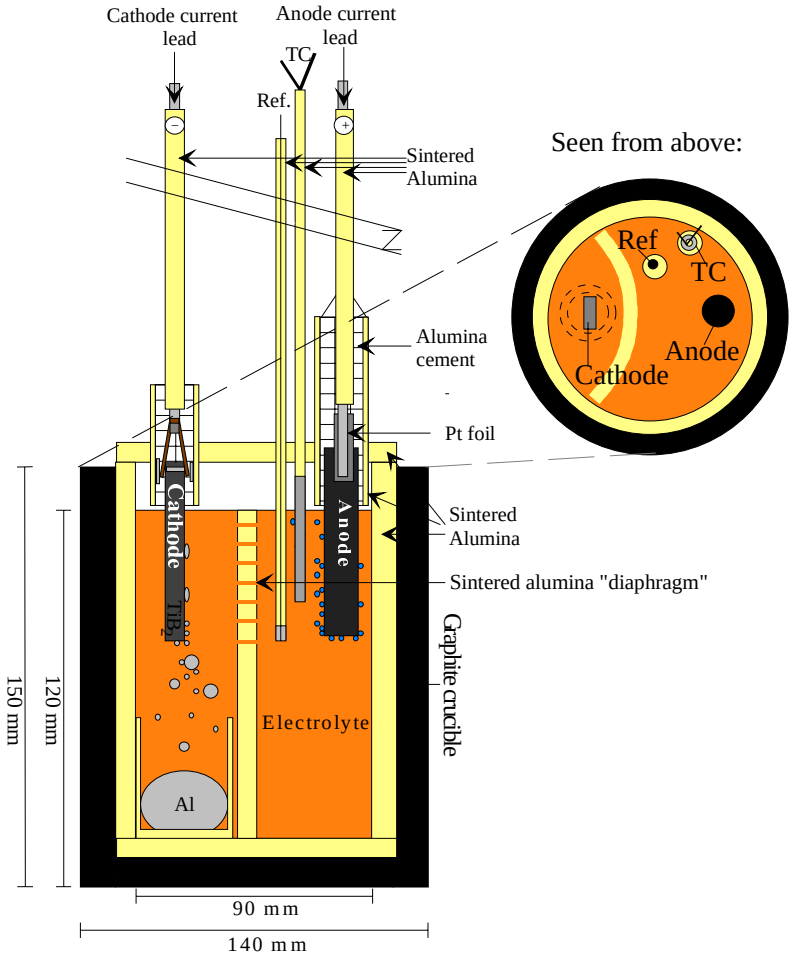

Figure 7-6: A sketch of a laboratory cell with vertical electrodes.

The alumina “diaphragm” between the anode and the cathode compartments is a sintered alumina wall with 1 mm wide and 2 cm long openings 1 cm apart to ensure current flow without too much mixing of the electrolyte and loss of current efficiency. The

"diaphragm" reduces the back reaction between aluminium droplets and the oxygen evolved at the anode.

Windisch *et al.* (11) suggested that the temperature gradients due to current gradients in the anode should be considered when a new cell is designed. To achieve uniform current distribution on a vertical electrode can be a problem when the electrode material has low conductivity and all the current is entering the anode through a current lead at one end of the electrode. The result may be that most of the current is passing through the upper part of the electrode. An internal rod of high conductivity material, for example copper, may be the solution to this particular problem. The present anodes had an inconel rod inside a platinum foil drilled 15 mm into the anode and attached with a copper-based cement.

The aluminium produced was collected in an alumina cup, which was placed underneath the TiB_2 cathode (see Figure 7-6).

A cylindrical TiB_2 tube serving as cathode, with an anode in the centre of the cell, would have given a uniform current distribution at the anode. A tube-shaped TiB_2 cathode would have been expensive to buy and difficult to fabricate. One can also obtain good electrical current distribution at the anode by placing several cathodes around the anode. However, in this case a system with one anode and one cathode was the only set-up possible because of the size limitation of the crucible.

7.2 Model for dissolution and reduction of anode constituents

The anode materials are not completely insoluble in cryolite melts, as shown in Chapters 2, 4, 5 and 6, and the validation test is often to find a way to describe the dissolution kinetics of the anode constituents. If one considers dissolution of an oxide, it can be described as the so-called Keller-Evans Model (5),

$$M_xO_{y(anode)} \rightarrow M_xO_{y(dissolved)} \qquad [7\text{-}1]$$

According to this model, the rate of dissolution depends (12) on the mass transport conditions, on the mass transfer coefficient of the anode, k_a, the concentration gradient (the difference between the saturation limit for the oxide, c_{sat}, and the concentration in the electrolyte, c_{bulk}) and the anode surface area, A_a (12):

$$\text{Dissolution rate} = k_a A_a (c_{sat} - c_{bulk}) \qquad [7\text{-}2]$$

An essentially uniform concentration, c_{bulk}, is assumed since the convective mass transport within the interface electrolyte caused by oxygen evolution is very fast.

Removal of the dissolved anode constituents by cathodic reduction (and by evaporation) maintains a concentration gradient and a continuous dissolution. There are two possible ways in which these impurities can be removed at the cathode. An electrochemical reduction of anode constituents, M^{n+}, can occur at the melt-cathode interface according to:

$$M^{n+} + n \cdot e^{-} \rightarrow M_{\text{in Al}} \qquad [7\text{-}3]$$

or by a chemical reaction with aluminium

$$3M_xO_{y\,(\text{dissolved})} + 2y\,Al \rightarrow 3x\,M_{\text{in Al}} + y\,Al_2O_3 \qquad [7\text{-}4]$$

The reduction at the cathode can be expressed in a similar way as the dissolution rate at the anode, but since the reaction at the cathode is considered to be fast, the concentration gradient $c_{bulk} - c_{surface}$ is reduced to c_{bulk}.

$$\text{Reduction rate} = k_c A_c c_{bulk} \qquad [7\text{-}5]$$

At steady state conditions, the dissolution rate at the anode and the corresponding reduction rate at the cathode are equal, provided that there exists no other "sinks" for the oxide impurities. This assumption is an approximation since red-ox reactions and precipitation of solid particles containing anode constituents may occur in the melt or on the side-walls and evaporation of volatile species containing impurities from the anode can occur to a certain extent. The Keller-Evans model can be expressed as,

$$k_a A_a \cdot (c_{sat} - c_{bulk}) = k_c A_c c_{bulk} \qquad [7\text{-}6]$$

Rearrangement of the equation gives an expression for c_{bulk}:

$$c_{bulk} = \left[\frac{k_a \cdot A_a}{k_a A_a + k_c A_c}\right] \cdot c_{sat} \qquad [7\text{-}7]$$

By introducing this expression for c_{bulk} in equation 7-6, one can express the dissolution rate at the anode as (12):

$$k_a A_a \cdot (c_{sat} - c_{bulk}) = k_a A_a \cdot \left[1 - \frac{k_a A_a}{k_a A_a + k_c A_c}\right] \cdot c_{sat} \qquad [7\text{-}8]$$

The mass transfer coefficient at the gas-evolving anode is expected to be much higher than that at the cathode, giving an overall larger influence on the critical dissolution rate expressed by equation [7-8]. According to equation [7-8], a small cathode area favours anode stability.

Híveš *et al*. (3) used a similar cell set-up as shown in Figure 7-1. They investigated how a change of the cathode area influenced the mass transfer coefficients at the cathode, k_c. The mass transfer coefficients were almost identical for the anode constituents Ni, Fe and Cu, measured in the same type of experimental set-up as the present, but the mass transfer coefficient increased one order of magnitude when reducing the initial cathode area from 20 to 6 cm^2. The anode area was ~35 cm^2 in all the experiments. Their conclusion was that

the fluid dynamic conditions in the inter-electrode gap strongly affect the contamination of the produced aluminium (5).

7.3 Mass transfer at the anode

Gas evolution at an electrode generally leads to a high mass transfer coefficient. At a current density of 1 A/cm^2 and 960 ^{o}C, oxygen is evolved at a non-consumable anode at a rate of 0.24 cm^3 per cm^{2}s anode area (12).

The bulk concentration of anode constituents increases according to:

$$\frac{\partial c_{bulk}}{\partial t} = \left[\frac{k_a A_a}{V}\right] \cdot (c_{sat} - c_{bulk}) \qquad [7\text{-}9]$$

where V is the melt volume. The dissolution of oxides from the anode into the melt is usually assumed to be mass transfer controlled (5), (12), and by assuming no initial contamination of the anode constituents in the electrolyte, the concentrations may be described (2), (13) by the mass transfer equation,

$$k_a A_a \cdot (c_{sat} - c(t)) - k_c A_c \cdot c(t) = V \cdot \frac{\partial c_{bulk}}{\partial t} \qquad [7\text{-}10]$$

where c(t) is the bulk concentration as a function of the time t.

Rearrangement of this equation gives a first order differential equation,

$$\frac{k_a A_a \cdot c_{sat}}{V} - \frac{k_a A_a}{V} \cdot c(t) - \frac{k_c A_c}{V} \cdot c(t) = \frac{\partial c_{bulk}}{\partial t} \qquad [7\text{-}11]$$

with the distinct solution (2), (14),

$$c(t) = \frac{k_a A_a c_{sat}}{k_c A_c + k_a A_a} \cdot \left(1 - e^{\frac{-(k_c A_c + k_a A_a)\cdot t}{V}}\right) \qquad [7\text{-}12]$$

Further details regarding the mathematical solution can be found in Greenberg (15).

The equation can be simplified by introducing the constant “B”,

$$B = \frac{k_a A_a c_{sat}}{k_a A_a + k_c A_c} \qquad [7\text{-}13]$$

By assuming $k_a >> k_c$ and $A_a \cong A_c$, “B” can be set equal to “c_{sat}”.

The equation can be further simplified by introducing the time constant "τ",

$$\tau = \frac{V}{k_c A_c + k_a A_a} \qquad [7\text{-}14]$$

The final equation expressing the time dependent concentration of dissolving species under mass transport control with zero initial concentration of this species (2) is then given by,

$$c(t) = B \cdot \left(1 - e^{-\frac{t}{\tau}}\right) \approx c_{sat} \cdot \left(1 - e^{-\frac{t}{\tau}}\right) \qquad [7\text{-}15]$$

It is, however, necessary to incorporate the initial concentration of the contaminant, c_o, to make this equation valid for the electrochemical cell containing natural cryolite. Furthermore, since the final steady state concentration of the electrolyte is dependent on the mass transport of the impurities from the bulk to the bath/metal interface, it is not strictly correct to use the saturation concentration, c_{sat}, as the steady state concentration. It can, however, be substituted with "c_∞" denoting the steady state concentration, giving the overall expression,

$$\left(\frac{c(t) - c_o}{c_\infty - c_o}\right) = \left(1 - e^{-\frac{t}{\tau}}\right) \qquad [7\text{-}16]$$

which transforms into,

$$c(t) = c_\infty - (c_\infty - c_o) \cdot e^{-\frac{t}{\tau}} \qquad [7\text{-}17]$$

However, as time proceeds the time-dependent part of equation [7-12] becomes negligible, and the steady state contamination of the melt, c(∞), can be expressed by,

$$c(\infty) = \frac{k_a A_a c_{sat}}{k_c A_c + k_a A_a} \qquad [7\text{-}18]$$

As already mentioned, for a mass controlled process the rate of dissolution of oxides at a gas evolving anode will be much more rapid than the alloying of the species into the cathodically deposited metal. One may therefore assume that the value of c(∞) should be close to c_{sat} for the anode constituents. However, according to the results presented in Figure 7-8, c(∞) was lower than c_{sat} for Fe and Cu.

7.4 Partial reduction and incomplete alloying at the anode

Reduced components frequently tend to re-enter the electrolyte, either as a metallic phase or, after partial reduction, as lower-valent species (12). These species can then be re-oxidised at the anode, or by gaseous anode products. This phenomenon has been observed as an imbalance of impurities contained in the electrolyte and in the deposited cathode metal. Based on a diffusion-limited flux for the impurities between the anode and the cathode metal calculated by Keller *et al*. (12), a higher impurity content would be expected in the aluminium than in the melt.

It has been postulated (12) that impurities are reduced at the cathode at their diffusion-limited current, but that only a fraction, " f ", alloys with the cathode metal in the process. This effect is qualitatively the same as if a portion of the impurities is partially reduced to a lower-valent state that re-enters the electrolyte bulk. Given the high mass transport rates in the electrolyte bulk, it can be assumed that the impurities get re-oxidised rather quickly. The re-appearance and re-dissolution of anode constituents by this mechanism helps to keep their concentration in the electrolyte high, thereby reducing the rate of dissolution from the anode (12).

The critical dissolution rate can therefor be modified by taking the fraction, f, which alloys with the metal, into account, and equation [7-8] can be expressed as:

$$\text{Critical dissolution rate} = k_a A_a \cdot \left[\frac{k_a A_a}{k_a A_a + f \cdot k_c A_c} \right] \cdot c_{sat} \qquad [7\text{-}19]$$

Equation [7-19] is well suited for tests, in cells with proper convection and melt circulation. The oxygen evolution at the inert anodes is, however much calmer and with smaller bubbles than what one gets with carbon anodes. A stagnant layer and concentration gradients in the cell can, therefore, be a problem when using inert anodes. It may cause higher dissolution rates in the diffusion layer surrounding the anode, which may get depleted with respect to alumina. Further out in the melt where the alumina concentration is higher, the saturation limits for the anode constituents are reached very quickly, and may even result in precipitation of the species in the bulk electrolyte, as already mentioned.

According to Shkuryakov *et al.* (16) concentrations of the impurities CuO and NiO decreases more rapidly than what can be attributed to purely diffusion control of the reduction process at the surface of the aluminium. Not only do dissolved impurities diffuse to the electrolyte-aluminium interface, but also a transport of partly reduced impurities and solid metallic crystals of the impurities, reduced in the bulk of the melt by the dissolved aluminium, diffuse from the bulk to the interface. Due to higher specific masses of the impurities in comparison to the electrolyte, these impurity "particles" can precipitate on the surface of the aluminium. Impurities may also accumulate on the surface of the solid phases, *i.e*. lining materials, in alumina sludge on the bottom of the cell, side and bottom crust *etc*. Shkuryakov *et al.* (16) did not find any indication of the formation of measurable amounts of volatile condensates of the melt containing these impurities.

7.5 Chemicals

NaF	Merck A/S, p.a., >99%
AlF_3	Alufluor, Helsingborg, Sweden, >97%
Al_2O_3	γ-Al_2O_3, water-free, Kebo Lab., >99.5 %, dried at 200 ^oC
CaF_2	Merck A/S, p.a.
Aremco Coat 543	Copper rich binder, Lot no. 10006768, Aremco Products, Inc., New York, USA
Graphi Coat 623-L	Binder for 623-P, Lot. no. 30005407, Aremco Products, Inc.
Graphi Coat 623-P	TiB_2 Powder, Lot. no. 100967, Aremco Products, Inc.
Alumina Cement	Alumina-rich binder, Lot. no. AC-94, Zircar Products, Inc., New York, USA

7.6 Experimental

The vertical cell set-up shown in Figure 7-6 was used. The cell was made of a graphite crucible with lining of a sintered alumina tube and a bottom consisting a sintered alumina disk. To prevent the graphite crucible from oxidising, or at least to reduce the oxidition, a mixture of TiB_2 powder (623-P) and an organic binder (623-L) was painted on the outside of the crucible. This mixture was also painted at the alumina cement protecting the connection between the TiB_2 cathode and the electrical lead from oxidising (see Figure 7-6). An alumina-based binder was painted on the alumina cement on top of the anode to prevent oxidation of the connection between the anode and the electrical lead. Argon purging from underneath and above the cell was also applied during the experiments.

The melt was an alumina-saturated mixture of cryolite-based melt with molar ratio 2.29 and 5 wt% CaF_2. CaF_2 is a natural impurity in alumina used to feed aluminium producing cells, and normally a steady state concentrations at around 5 weight percent is found in industrial cells. Strachan *et al.* (17) did not find any correlation between the CaF_2 content and the cermet anode performance, but it was used since it will be present in a future electrolysis cell, and it has some influence on the properties of molten cryolite-based melts (18).

Anodes containing stoichiometric $NiFe_2O_4$ and 17wt% Cu prior to sintering (see Chapter 3) were pre-electrolysed for 90 minutes in a separate cell and slowly cooled in an argon atmosphere. Pre-electrolysis was necessary (2) to remove small metal droplets formed on the anode surface during sintering (see Chapter 3). The feed was a mixture of 20 wt % pre-melted and crushed cryolite-based melt with molar ratio 2.0 and 80 wt % alumina. This mixture was used to maintain a constant molar ratio in the electrolyte throughout the test by co-workers Skybakmoen and Gulbrandsen (20). A vibrator was connected to the feeding tank above the cell to ensure that the feed entered the melt and to prevent it from sticking to

the walls inside the feeding tube. 4 grams of the mixture was fed automatically every 24 minutes.

The first experiment was run with addition of melt without alumina because of all the alumina present as insulating walls in the cell. However, the "diaphragm" between the anode and the cathode (see Figure 7-6) deteriorated and lost its strength after approximately 24 hours, so alumina addition in the anode compartment was found to be necessary. In the next two experiments alumina in quantities corresponding to a current efficiency of 70 % was added together with the crushed melt, (*i.e.* 20% melt and 80% alumina*)*. Ten grams of this mixture was fed to the cell every hour to keep the melt level and the melt composition constant.

A galvanostatic current supply was used to give a current density of 1 A/cm^2. Since the electrodes were close to the outer walls of the cell, it was assumed that the current was mainly passing through the half of the anode surface that was facing the cathode. The electrodes were polarised and immersed 4 cm into the melt before the electrolysis was started. After the experiments were terminated, the electrodes were raised above the surface of the melt, and cooled together with the cell.

The electrolysis tests were run for 48 hours at 960 ^{o}C. The temperature was measured with a Pt-Pt10%Rh thermocouple inside a sealed platinum tube, and an aluminium reference electrode was used to monitor the cathode potential.

7.7 Results

In the first experiment a stable reference voltage of 3.2 - 3.5 volts and a cell voltage of 5.2 ± 0.2 volts at 960 ±3 ^{o}C was obtained. However, formation of a solid coarse deposit on the cathode (see Figure 7-7) made it impossible to take metal samples. The cell voltage did not change during electrolysis, despite the growth at the cathode. A visual inspection of the layer, indicated that the deposit contained a mixture of metallic aluminium and frozen melt, probably cryolite. The black area shown at the bottom of the cathode in Figure 7-7 contains impurities from the dissolved anode constituents. The solid layer did not dissolve when the temperature was elevated to 1000 ^{o}C. Also the side of the cathode that was turning away from the anode was covered.

X-ray diffraction analysis of crushed cathode deposit (see Figure 7-7) detected the following phases: cryolite (Na_3AlF_6) chiolite ($Na_5Al_3F_{14}$), Ni and some Al_2O_3. Some broad bands representing Fe/AlFe/AlNi were also detected. These phases were probably alloys of Al and the anode constituents. Some of the crushed cathode deposit was mixed with concentrated HCl, and gas evolution (H_2) indicated the presence of metallic Al, Ni and/or Fe. A chemical analysis with ICP for the elements Ni, Fe and Cu showed 2.10 wt% Fe, 1.03 wt% Cu and 3.33 wt% Ni.

In a patent Frizzle *et al*. (19) also reported the formation of such a cathodic deposit in acidic melts operated at around 800 ^{o}C. They reported the deposit on the cathode to be cryolite, or cryolite and sub-oxides of aluminium together with alumina. In addition a thin deposit was reported to form around balls consisting of metallic aluminium that had been

separated from the cathode, preventing the aluminium in these balls from agglomerating into a continuos phase of molten aluminium. Instead, these balls, which contained metallic aluminium that had been coated with deposits, remained suspended within the electrolyte. The balls that diffuse back into the melt back-react (dissolve), causing poor current efficiency (19). The deposit on the small balls was believed to be electrolyte and/or alumina. The lumpy, black deposit formed at the bottom of the cathode is reported (19) to deposit at modest current densities with a composition similar to the melt composition. The black colour may come from the formation of a sub-oxide of aluminium (19), which is a black semiconductor.

Figure 7-7: Growth on a TiB_2 cathode after 48 hours of electrolysis. The cathode shown was suspended 90^o counter-clockwise in the electrolysis cell.

The main cause of the deposit on the cathode and on the balls containing metallic aluminium was believed (19) to be insufficient dissolution of alumina in the electrolyte, particularly at locations adjacent to the cathode. The grey cryolite deposit can be formed at high current densities (~1–2 A/cm^2) (19), a low concentration of AlF_3 and coarse alumina feed. Initial deposits may be formed by metal sulphides formed from aluminium sulphate or other sulphurous compounds (19).

To avoid unwanted solid cathode deposit, one needs good wetting between the TiB_2 and the aluminium produced (19). After the experiments were conducted, it was found that soaking the TiB_2 cathodes with aluminium before use may ensure good wetting and more effective removal of aluminium droplets from the cathode during electrolysis. Known expedients (19) for increasing dissolution of alumina in the electrolyte can reduce or eliminate formation of the deposits by, for example, increasing the melt temperature, but it has the drawback of causing the anodes to deteriorate too rapidly.

An increase of the amounts of alumina to super-saturation gives dispersed alumina particles in the molten electrolyte, which is beneficial (19), but it might cause muck formation in the cell and an increase in energy consumption. A reduction of current density (*i.e.* < 0.3 A/cm^2) also makes it possible to avoid the deposits (19) by enlarging the cathode area and increasing the number of electrodes in the cell. Addition of 0.004 to 0.2 wt % of nickel, iron, copper, cobalt and molybdenum fluorides/oxides/carbonates may also prevent the deposit formation (19). As a result the formation of deposits on the cathode surface are prevented, or if such deposits tend to form initially, they are eliminated or reduced. Similarly, the formation of a deposit around the balls containing metallic aluminium is prevented or eliminated, and the net result is that the TiB_2 cathode surface is wetted with a layer of metallic aluminium.

Melt samples were withdrawn from the cell with a cold graphite rod that was dipped into the melt in the anode compartment at intervals throughout the experiments. The melt samples were crushed and analysed with ICP as described in Chapter 4. The analytical data of the melt samples is shown in Figure 7-8.

The condensate from the vapour phase over the anode was analysed with ICP after two of the experiments were terminated and cooled to room temperature. It contained approximately 120 ppm Fe, 13 ppm Cu and 9 ppm Ni. The ratio of the content of impurities in the condensate relative to the concentration in the melt at steady state are ~1.0 for Fe, 0.26 for Cu and 0.27 for Ni. The amount of impurities leaving the cell by evaporation is proportional to the amount of evaporation, which should be kept low. This implies that proper hooding should be used and the superheat[1] should be kept as low as possible during operation.

The high iron concentration during the first hours of electrolysis was probably caused by iron impurities present in the electrolyte prior to electrolysis, as confirmed by observations by Olsen *et al.* (1), (2) and by Skybakmoen and Gulbrandsen (20). One should note that the highest iron concentrations are only one third compared to that reported by Olsen *et al.* (1), (2) who used natural Greenland cryolite, which contains more iron impurities than the presently used electrolyte. The apparent dip in the iron concentrations after 1–3 hours may be explained by the fact that the initial impurity content of iron masks the behaviour of the iron dissolved from the anode. Stagnant layers in the bottom part of the cell may have slowed down the transfer of these species before the cell had reached stable operating conditions (2).

[1] The superheat $\Delta T = T_{operation} - T_{liquidus}$

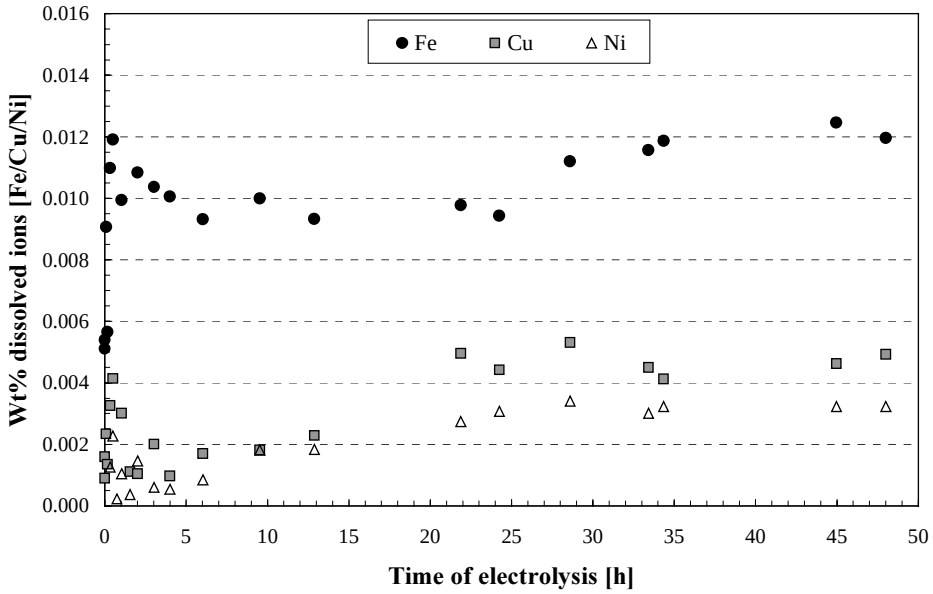

Figure 7-8: Analysis of Fe, Ni and Cu in the melt during aluminium electrolysis with a cermet anode. Temperature ~960 ^{o}C and CR = 2.29, at $Al_2O_{3(sat)}$ and 5 wt% CaF_2.

The initial high concentrations of Cu are somewhat unexpected, but it probably indicates that 90 minutes of pre-electrolysis was insufficient to dissolve all the copper droplets formed on the anode surface during sintering. The copper-rich metal phase will be subject to anodic dissolution, but since the metallic copper phase does not form a continuous network in the anode, the electrochemical process should slow down rapidly when the exposed Cu in the outer region of the anode is dissolved. The ceramic matrix being in electrochemically stable state will undergo only chemical dissolution. The process should thereafter be controlled by chemical dissolution of the oxide phase with only a limited number of Cu particles being exposed to the electrolyte when the interface recedes as the ceramic phase dissolves (2). One should note that the melt used composition initially contains around 40 ppm of Cu impurities (20).

The overall behaviour of the anode constituents was similar to that observed by Olsen *et al.* (1), (2) for $NiFe_2O_4$ anodes without excess NiO, even though they used a cell with horizontal electrodes. Their 50 hours experiments were conducted with a higher melt volume and with a higher cathode area and anode area / cathode area ratio than those described in Chapter 7.1. The cell set-up and geometry seem to be very important parameters to consider for obtaining proper convection, alumina distribution and temperature control in the cell.

The solubility of Fe_2O_3 in such a melt was measured (see Chapter 5) to be 1300 ppm at 960 ^{o}C, which is more than 10 times higher than the (more or less) steady state value obtained for iron in the electrolysis experiments (see Figure 7-8). The solubility of FeO was not measured at CR = 2.29 and 960 ^{o}C, but ~3440 ppm Fe(II) was obtained at CR = 2.29 and

1020 ^{o}C (see Chapter 5). and ~2600 ppm Fe(II) at CR = 3.0 and 980 ^{o}C. The solubility of Ni(II) in such a melt without CaF_2 was measured to be ~9 ppm at 960 ^{o}C.

The concentration of Ni in the electrolysis cell reached ~32 ppm, which is supported by results obtained by Skybakmoen and Gulbrandsen (20). This value is well above the solubility value obtained for Ni. It is rather unlikely that the presence of 5 wt% CaF_2 will increase the solubility of Ni, so values for Ni above saturation may indicate that very small Ni- containing solid particles were spalling off (disintegrating from) the anode during electrolysis. These small particles may also be formed as a result of redox reactions in the melt or by precipitation of NiO or $NiAl_2O_4$ if there existed a concentration gradient with respect to Ni between the anode surface and the bulk electrolyte.

The solubility of Cu(II) was measured to be 4600 ppm (see Chapter 6) in a similar melt, which is much higher than the 50 ppm obtained in the electrolysis experiments. The solubility of Cu(I) was not measured at 960 ^{o}C, but 2750 ppm was obtained at 1020 ^{o}C. As previously described, very little copper is in direct contact with the melt during electrolysis, so one would, therefore, expect concentrations below saturation of Cu in the melt. However, a Cu-containing metal anode should be used with caution in such melts because of the high Cu(II) solubility.

Equation [7-17] can be used to determine the mass transfer coefficients, k_i, in the system by curve fitting this equation by iteration to fit the measured values for the melt sample with the least deviation. This procedure was used for the experimental results presented in Figure 7-8, and the results are given in Figure 7-9. The data used for equation [7-17] in Figure 7-9 are given in table 7-1. Since it was not possible to take any metal samples in the present experiments, the values for k_a and k_c in table 7-1 was taken from Olsen and Thonstad (1) for this system.

Table 7-1: Values used in equation [7-17] for Fe, Cu and Ni, respectively in Figure 7-9. k_a and k_c are from Olsen and Thonstad (1).

Volume [m^3]	7.63E-04	τ_{Fe}	1.91E-01
k_a (Fe) [m/s]	8.68E-04	τ_{Cu}	7.55E-02
k_a (Cu) [m/s]	2.20E-03	τ_{Ni}	1.52E+00
k_a (Ni) [m/s]	1.08E-04	$C_{sat, Fe}$ [wt%]	0.0120
k_c (Fe) [m/s]	2.99E-06	$C_{sat, Cu}$ [wt%]	0.0050
k_c (Cu) [m/s]	2.86E-06	$C_{sat, Ni}$ [wt%]	0.0032
k_c (Ni) [m/s]	1.59E-06	$C_{o, Fe}$ [wt%]	0.0053
A_a [cm^2]	4.59	$C_{o, Cu}$ [wt%]	0.0012
A_c [cm^2]	5	$C_{o, Ni}$ [wt%]	0.0001

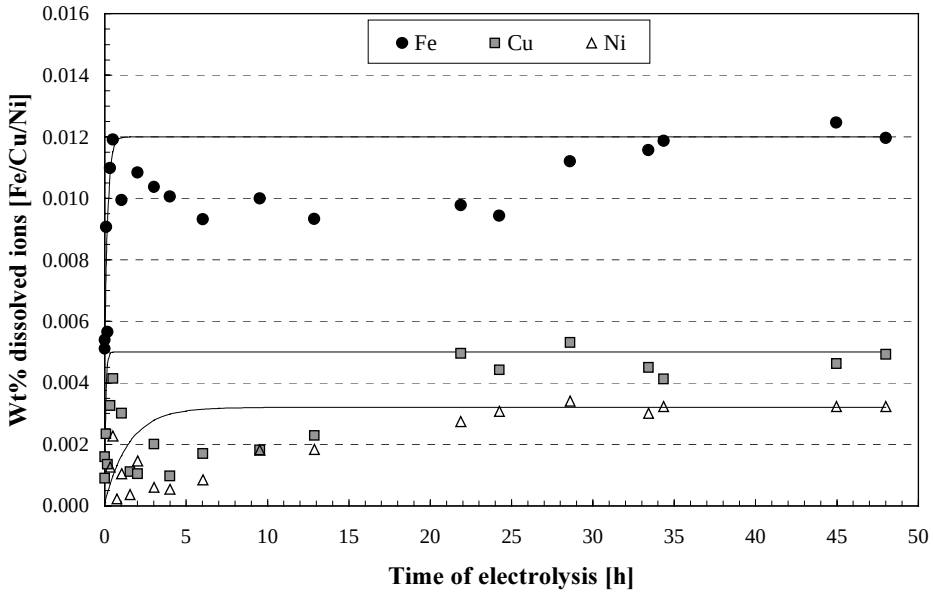

Figure 7-9: Best fit of equation [7-17] for the melt analysis of Fe, Ni and Cu during aluminium electrolysis of a cermet anode. Temperature ~960 ^{o}C and CR = 2.29 at alumina saturation and 5 wt% CaF_2.

Olsen and Thonstad (1) used only the results from the first 100 minutes to adjust the parameters for the mass transfer coefficient for the anode k_a, the initial concentration, c_o and the steady state concentrations, $c(\infty)$. The modelling shown in Figure 7-9 seems to fit reasonably well with the experimental data only for the first hour of electrolysis. It looks like the model only is valid for this initial period, since the melt concentrations reached steady state values for Fe and Cu which were much lower than the saturation concentrations.

The relative amounts of anode constituents reduced to metal did not reflect the composition of the anode material. Olsen and Thonstad (1) and Ray (21) found that substantially more iron and copper than nickel are reduced to metal compared to what can be explained by uniform dissolution of the anode material. Cu may be dissolved anodically in the first period of electrolysis, and since the model used is based on the assumption of a simple chemical dissolution mechanism, this concept is therefore of doubtful significance for Cu (1).

How the impurities in the melt evaporate may affect the total amount of species entering the metal, but also deposition of for example nickel-containing compounds on the alumina liner in the cell may occur. Visual p*ost-mortem* examination of a cell where some of the graphite crucible had been completely burned away, had a light sky-blue colour on the outside of the alumina liner, which is the colour of $NiAl_2O_4$. The liner was, however, not analysed any further. According to the stability diagram shown in Figure 2-3, p. 24, $NiAl_2O_4$ may form under the conditions described, but it is unlikely that $FeAl_2O_4$ forms at

such high oxygen pressure as it is on an oxygen-evolving anode (see Figure 2-2, p. 23). Olsen reported (22), however, to have found traces of $FeAl_2O_4$ by XRD on one of his anodes used under similar conditions. Except for the outer ~50 μm of the surface, the metal depleted zone of the anode seems to be at least as dense as the interior of the anode. No sign of pores where found in the region where the metal phase had disappeared, which is supported by findings by Olsen and Thonstad (1). This might indicate that some kind of displacement reaction occurs at the surface of the anode producing a dense layer, which protects the interior of the anode.

The aluminium metal produced in the cell was removed after the cell was cooled, since it was not possible to withdraw metal samples during electrolysis because of the formation of a solid deposit on the cathode (similar to the solid deposit shown in Figure 7-7, but *much* less). How the change in cathode area changed the mass transport at the cathode is difficult to predict, but since deposit was found only ~15 % of the bottom of the cathode, one would expects this effect to be negligible. The aluminium metal contained 0.22 wt% Fe, 0.05 wt% Cu and 0.05 wt% Ni.

In one experiment, the anode was raised until only ~1 cm of the anode dipped into the melt after the initial 50 hours, and electrolysis was conducted with ~5 A/cm^2 for an additional 5 hours without any addition of alumina nor crushed melt. Samples from the melt from the anolyte and catholyte were then taken just before the current was turned off, which gave the following results. In the anode "compartment" the analyses showed 161 ppm Fe, 32 ppm Cu and 29 ppm Ni, while the cathode compartment contained 570 ppm Fe, 743 ppm Cu and 1047 ppm Ni. The anode looked like the tip of a worn pencil after the experiment. It was cut into two equal parts, from the tip and upward, and analysed with. Visual inspection of the anode revealed a copper-rich zone ~2-5 mm into the anode, which was confirmed by SEM analysis (see Fig. 7-13).

The high concentrations of Cu and Ni in the melt (*i.e.* catholyte) indicated that the metal phase was dissolving rapidly into the melt. This might be caused by increased temperature in the anode due to the high current and the corresponding ohmic heat produced in the anode, and the temperature measured only 2 cm from the anode showed a temperature rise of 10 degrees during the last 30 minutes of electrolysis. Results from an earlier experiment with BN-insulated horizontally oriented anodes with high ohmic resistance in the contact between the anode lead and the anode supports this assumption. In that experiment there was no Pt-foil around the anode lead, which resulted in corrosion of the lead in contact with the anode. The anodic reference voltage and the temperature rose rapidly after 4 hours before the experiment was terminated. Visual inspection of this anode after the experiment indicated the presence of a copper-rich metal phase at the surface of the anode when the BN insulation was removed. It looked as if the metal phase had melted and flowed out of the anode.

Chin (23), (24) investigated the transfer of Ni, Fe and Cu from their oxides dissolved in alumina-saturated cryolite into aluminium that was added after the melts were saturated with Ni, Fe and Cu. The transfer of the impurities into the metal was incomplete in the

"*non*-electrolytic experiments"[2] without agitation, and only 55% of total Ni, 63% of total Fe and 15% of total Cu were alloyed into the aluminium. A major part of the Ni and the Fe not found in the aluminium remained in the bulk of the melt, but essentially all of the Cu that remained in the melt was found in a 1-2 mm thick "skim layer" around the Al metal. Chin concluded that the overall tra1nsfer to the metal appeared to have been limited by formation of reduced species in the "skim layer" that were not incorporated into the liquid metal because of large interfacial tensions between the impurities and the liquid metal and/or the presence of an alumina barrier that decreased the wetting of the reduced species.

According to Windisch *et al.* (11),(25) broken pieces of cermet anodes fell into the melt during a pilot test of such anodes, and some of the pieces that broke off were not removed form the melt. However, no evidence of a steady increase in the metal impurity content was found, even though the level increased rather steadily throughout the tests. It was believed that the pieces of the anodes, which have a higher density than both the melt and the metal, were submerged into the muck on the bottom of the cell, and did not significantly affect the metal purity. Little change was observed regarding the impurity concentrations in the melt throughout the test, despite increased levels in the metal. The melt concentrations were around 0.002 wt% Cu, 0.025 wt% Fe and 0.0065 wt% Ni.

Visual inspections of the present electrolytes when samples were withdrawn from the cell showed a transparent melt. However, if aluminium is pored into liquid un-polarised cryolite melts, the melt becomes non-transparent (opaque), which may be attributed to Al dissolving into the melt. The transparent melt observed when oxygen-evolving anodes are used may imply that the melt is oxidising even close to the aluminium cathode. One might expect the solubility of oxygen to be high in these melts since they are transparent, indicating no aluminium dissolution, but Numata and Bockris (26) measured the solubility with a radiotracer method to be only $3.0*10^{-6}$ mol/l·atm at 957 ^{o}C, CR = 2.3 and 5.33 wt% alumina. For comparison the solubility of CO_2 is 1000 times higher under similar conditions (26).

7.8 Post test analysis of cermet anodes

Some of the anodes were post tested after electrolysis with SEM and element mapping[3]. The middle cross section of the vertically oriented anode used in the experiment represented in Figures 7-8 and 7-9 were analysed with SEM, as shown in Figure 7-10.

[2] only liquid melt with aluminium addition, *i.e.* no electrolysis.
[3] Electron Microscope JEOL EPMA JXA-8900R (see footnote 6 Chapter 4.5 p. 77).

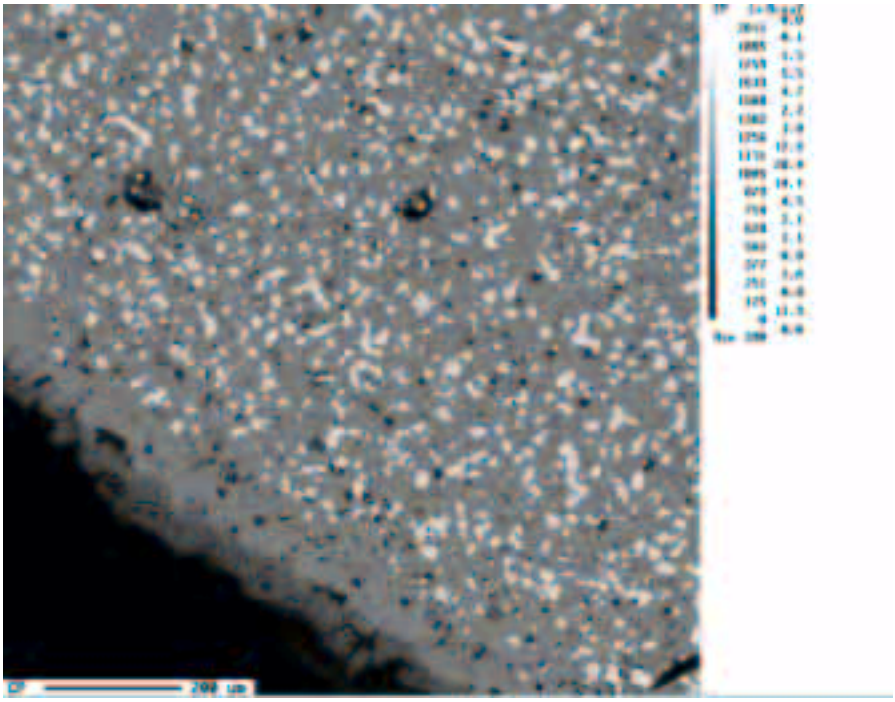

Figure 7-10: SEM picture of the middle cross section of a cermet anode after 50 hours of electrolysis (temperature ~960 ^{o}C and CR = 2.29 with alumina saturation and 5 wt% CaF_2).

Figure 7-11: Picture showing the interior of a cermet anode (with 17% excess NiO, 17% Cu and 3 % Ni prior to sintering) cut into two pieces after 22 hours of electrolysis in alumina saturated melt with CR =2.29, T = 960 ^{o}C and 1 A/cm^2. The numbered squares in the sketch of the anode illustrate which part of the anode that was analysed by element mapping Figure 7-12 shows the mapping labelled number 1.

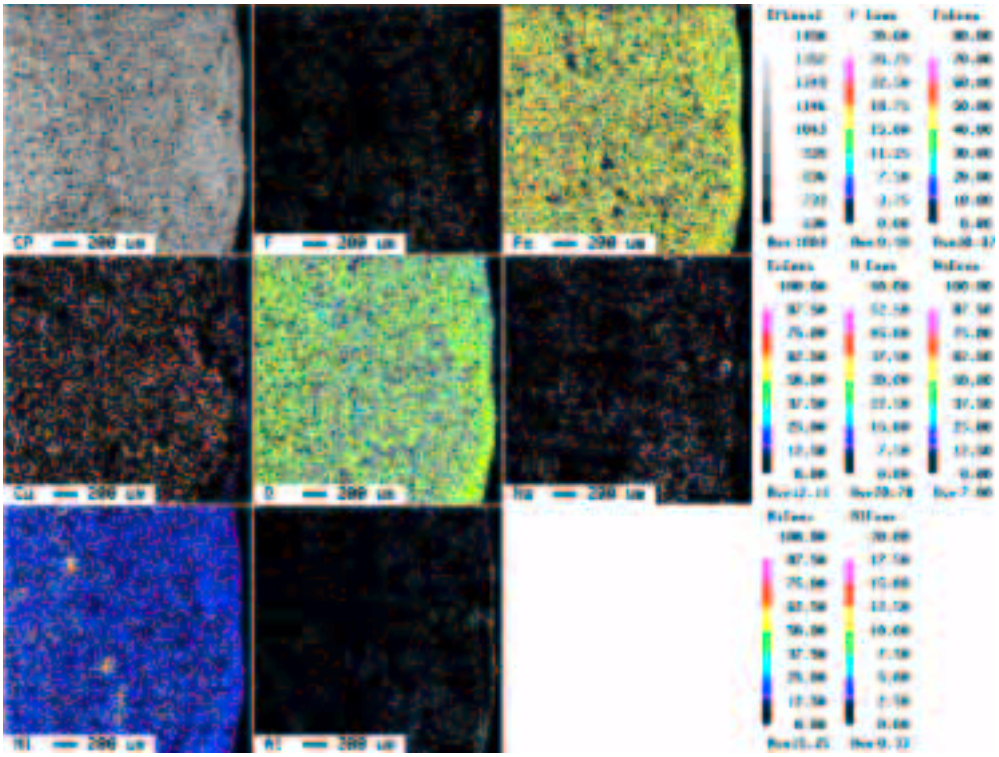

Figure 7-12: Mapping of the middle section of the anode from the surface (right side) to the interior of the anode (left). The picture shows 2 mm of the anode (label no.1 in Figure 7-11).

As one can see from Figure 7-10, in the outer 100 - 150 µm of the anode the metal phase (white spots) is completely removed from the anode. The thickness of the depleted zone of the circular cross section examined was varying from 100 µm on the side of the anode which had been facing the cathode to 1-2 µm at ~90^{o} angle from the zone where maximum thickness was measured. The backside of the anode facing the crucible wall looked unaffected of the electrolysis. It seemed likely that the thickness of the depleted zone was directly related to the total amount of charge passing through the anode.

The bottom end of the anode shown in Figure 7-11 was dipped 2-3 mm into the electrolyte. The small piece cracked off the lower right corner of the anode when it was cut with a diamond saw. As one can visually see from the figure, the anode was enriched with copper 2-5 mm from the surface of the anode. Mapping analysis requires a polished surface. The mapping analysis of the polished anode sample (*i.e.* the other half of the anode showed in figure 7.11) did not show the enrichment of copper in the outer 10 mm of the anode (see sketch in Figure 7-11). It seems like some of the metal phase had been removed during the polishing of the sample. Figure 7-12 shows the mapping pictures of Fe, Ni, Cu, O, F, Na and Al present in the outer 2 mm of the anode. It appears that some melt has penetrated ~1 mm into the anode. Aluminium is enriched at the cermet's surface layer, which also has been reported by Olsen and Thonstad (1). This might imply formation of $NiAl_2O_4$ at the surface, which is not beneficial in large amounts because of it's low electrical conductivity.

Olsen and Thonstad (1) analysed with XRMA the oxide phases in a cermet used under similar conditions as the present. Their analysis showed that the oxide phases were stable with regard to composition during electrolysis, as the relative amounts of Ni and Fe did not change from the interior (>2 cm from the surface) to the outer surface. The metallic phase was, however, systematically depleted with respect to Ni in the alloy, going from the interior to the surface of the anode.

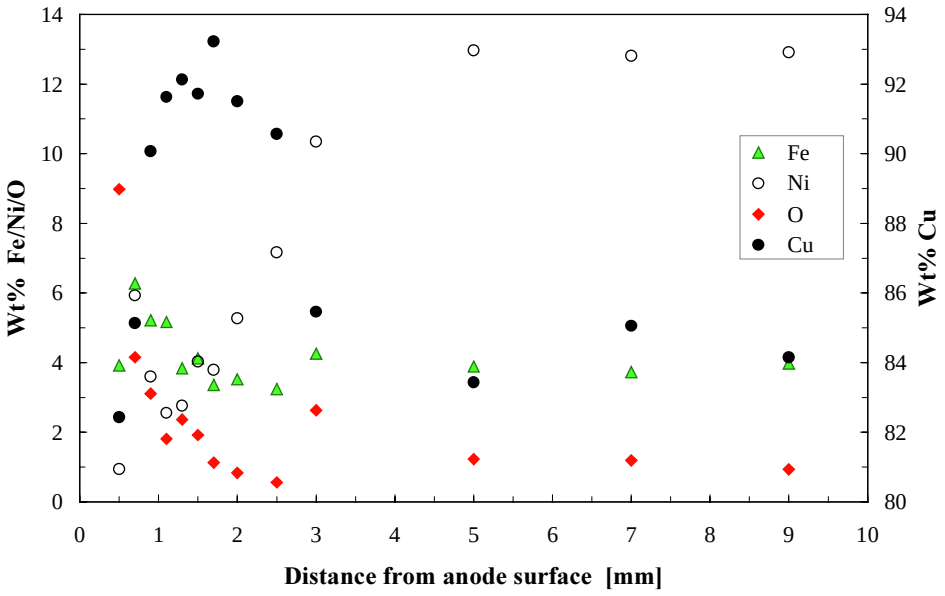

Figure 7-13: Wt % Fe, Ni, Cu and O in the metal phase as a function of the distance from the lower surface of a stoichiometric $NiFe_2O_4$ cermet with 17% Cu after 50 hours of electrolysis.

SEM-analysis of the metal phase in the anode shown in Figure 7-10 was investigated as a function of distance from the anode's lower surface. The results are shown in Figure 7-13.

Figure 7-13 shows that Cu is totally absent in the metal phase in the outer 0.5 mm of the anode, but rises to a maximum about 1.5 mm into the anode before it levels off at around 4 mm into the anode. The concentration of Ni rises from zero to 13 % at around 4 mm into the anode. The concentration of Fe is reasonably constant throughout the anode at around 4 %. The metal grains in the outer 0.5-2 mm of the anode have been slightly oxidised. However, the standard deviation of the analysis is around 1 percent, so the content of oxygen in the metal phase is more or less zero at 1.5-2.0 mm into the anode. These results are in agreement with the observation shown in Figure 7-11. It looks like there is a diffusion of copper in the anode towards the surface of the anode. It might be explained by the presence of a copper "front" moving towards the exterior of the anode, and not a selective oxidation of Ni from the metal phase as indicated by Tarcy (27) for a nickel-rich

metal phase[4]. This conclusion is supported by oxidation tests conducted by Kofstad and Haugsrud (28), (29) (see Chapter 2.2, p. 29).

The results presented in Chapter 6 show that the saturation concentration of Cu(I) and Cu(II) in the electrolyte is much higher than the concentrations measured in the electrolysis tests. The deviation between the steady state concentration and the saturation concentration produces a gradient that may make the copper diffuse in the anode. The diffusion mechanisms in the cermet are not known, but it might take place by lattice or grain diffusion. Cu diffusion in Cu-Ni alloys is reported (29) to be 2-3 orders of magnitude higher than for diffusion of Ni in the same alloy. Since the vapour pressure of Cu is only $7.2 \cdot 10^{-10}$ atm at 1000 ^{o}C (28), it is unlikely that Cu vapour transport causes the diffusion of Cu towards the exterior of the anode.

The locally higher concentration of Ni in two metal grains 0.7-1.0 mm into the anode may be explained by the fact that electrolyte is present in this region (see Figure 7-12), and since the solubility of Cu oxides are higher than for NiO, which forms on the surface of the metal grains, one might expect selective oxidation of Cu here. If CuF or CuF_2 is formed in this region, these phases would be liquid at 960 ^{o}C, and would easily be transported away from the anode by the gas-induced convection caused by electrolysis in the transport pores. The cracks in the outer region shown in Figure 7-10 clearly indicate that transport pores are present. However, if the metal grains that were analysed in the outer surface were very small, the electron beam used during the element mapping might have penetrated the metal grains and entered into the Ni rich oxide phases surrounding the metals grains. This might also explain the locally high Ni concentrations in the two grains analysed near the outer surface (see figure 7-13).

7.9 Validation of the Keller-Evans model

The dissolution mechanisms described in Chapter 7-3 was first suggested by Keller and Evans (5), and one therefore calls it the “Keller-Evans model”. However, this model has not been generally accepted (1), (2).

Olsen and Thonstad (1) measured the concentrations of anode constituents from cermet anodes made of the oxide phase $NiFe_2O_4$ with 0, 17 and 23 weight percent excess NiO and in total 20 wt % metal phase containing approximately 15 weight percent Ni and 85 weight percent Cu. The horizontally oriented anodes were used in an electrolyte with molar ratio 2.2, 5 weight percent CaF_2 and alumina saturation at 960 ^{o}C. Olsen and Thonstad (1), (2) achieved melt concentrations of Fe and Cu at steady state, which were considerably below the saturation concentrations. Their conclusions were based on solubility data reported by DeYoung (30), which are higher than the presently obtained data for Ni(II) and Fe(III) in this melt composition. Still, the steady state values obtained by Olsen and Thonstad (1), (2) were lower than the present solubility data.

[4] A nickel-rich metal phase is continuous in the $NiFe_2O_4$ matrix, compared to the copper-rich metal phase which are finely dispersed in the oxide matrix (see white grains in Figure 7-10).

If the concentrations are lower than the saturation limits, it implies that the rate of dissolution of species from the anode is of the same order as the mass transfer rate of species into the cathode metal (1). On the other hand, if super-saturated concentrations are found, it may indicate that a concentration gradient is present near the anode. If there is an alumina-depleted zone (*i.e.* unsaturated), near the anode, anode constituents dissolve until the *local* saturation limit is reached. Further away from the anode, the dissolved anode constituents precipitate as solid particulate, probably oxides, because here the alumina concentration is higher. There might even be red-ox reactions between the anode constituents and dispersed aluminium, forming metallic Cu, Ni and Fe. If Fe(II) is present in the melt, it can react with Cu ions, which are more noble, forming Cu metal and Fe(III).

These particles may be so small that they remain suspended in the electrolyte. This mechanism is supported by observation of Olsen and Thonstad in their cells (1), where autopsies of the cooled cells revealed a greyish layer of electrolyte above the cathode "*where gas-induced circulation had been ineffective*". Chin (23), (24) reported a 1-2 mm thick "skim-layer" metal enriched with copper metal found in post-tests of the melt just above the aluminium. Chin also analysed the skim-layer with SEM and XRD, but did not detect any impurity-containing metal crystals. He concluded that Cu as well as the Ni and Cu species existed in very fine and well-dispersed form. Olsen and Thonstad (1) also reported the Ni concentration to be lower for the material not containing excess NiO, which might indicate that NiO particles/grains break loose from the anode and cause super-saturation of Ni in the melt. This explanation has earlier been published by Windish *et al.* (11) for $NiFe_2O_4$ cermets, and for SnO_2 anodes by Wang and Thonstad (10).

According to Híveš *et al*. (3), the concentrations of Ni, Fe and Cu in the melt of a cell set-up similar to the one shown in Figure 7-1, did not depend on the size of the cathode, even when the mass transfer coefficients electrolyte-metal were 10 times higher for the small cathode-area (6 cm^2) experiments than for the large cathode area (20 cm^2) experiments. The concentrations of Ni and Fe in the melt reached steady state after less than one hour, and the mass transfer coefficients anode-electrolyte (~10^{-5} m/s) were 1 to 2 orders of magnitude higher than the ones obtained for the electrolyte-metal interface (10^{-7} m/s). The metal contamination data (3) showed, however, that the concentrations in the produced metal in the cells with a small cathode contained much more impurities than the ones with a big cathode. The reason was probably that during the large cathode area experiments the height of the produced metal was only doubled, and there were no significant changes in the planar shape of the metal surface, and hence there were no significant changes in the distance between anode and cathode (like "Time 1" shows in Figure 7-2). During the small cathode area experiments the volume of the produced metal increased 5 times from the initial value (like Figure 7-2 illustrates). Because of the electrolyte-metal interfacial tension, the planar surface at the beginning of the experiment gradually changed to a hemispherical shape, which could enhance the circulation of the electrolyte near the phase boundary metal-electrolyte. It seems likely that the hydrodynamic conditions in the electrode gap play an important role for the metal contamination.

To test the model represented by equation [7-18], one need reliable values for the saturation concentrations of the melts used in the experiments. Many articles refer to the work done by Alcoa (30), (31). The present results, regarding the solubility of Ni(II) (see

Chapter 4), and Diep's (32) solubility data for Fe(III) in alumina-*saturated* melts are, however, ~50 % lower than Alcoa's solubility data (30), (31) given for Ni(II) and ~30% lower for Fe(III). The concentrations of iron and copper from $NiFe_2O_4$ cermet anodes reached steady state values, which were lower than the saturation concentrations for the pure oxides, while the Ni concentration was several times higher. Other mechanisms than what the "Keller-Evans" model predicts seem to be at play, and the dissolution of the anode does not seem to be controlled by the saturation concentrations of the anode constituents in the melt. Based on the present results, a combination of controlled dissolution of the anode and small amounts of anode spalling seem to be important factors describing the anode dissolution after an initial operation period of only a few hours.

7.10 Concluding remarks

Based on the limited amount of data it is not possible to predict any new model that explains the dissolution mechanisms for the cermet material investigated. The steady state nickel concentration obtained after 50 hours of electrolysis was higher than the saturation concentration, indicating that grains/particles/flakes of the anode spall off or disintegrate. Whether this is a general behaviour of inert anode materials or not is impossible to say, and more testing of several different materials is, therefore, necessary.

Since the dissolution model seems to be more complex than the simple Keller-Evans mass-transport model predicts, one has to investigate the anode reactions and kinetics more thoroughly. Electrochemical measurements like cyclic voltammetry and impedance measurements might give new information about the behaviour of these anode materials.

7.11 References

(1) Olsen E. and Thonstad, J., *The behaviour of nickel ferrite cermet materials as inert anodes*, Light Metals 1996, TMS, pp. 249-257, 1996.

(2) Olsen, E., *Nickel ferrite and tin oxide as anode materials for aluminium electrolysis*, Ph.D. thesis, no. 100, ISBN 82-7119-850-5, NTH, Trondheim, Norway, 1995.

(3) Híveš, J., Olsen, E. and Thonstad, J., *Mass transport controlled dissolution of $NiFe_2O_4$ cermet anodes*, Ninth Int. Symp. of Light Metals Prod., ed. J. Thonstad, NTNU, Trondheim, Norway, Aug. 18.-21., 1997.

(4) Jentoftsen, T.E., *A laboratory and industrial investigation of impurities in the electrolyte used in the Hall-Héroult process,* Ph.D. thesis, to be published, NTNU, Trondheim, 2001.

(5) Evans, J.W. and Keller, R., *Factors affecting the life of inert anodes for aluminium electrolysis*, Extended Abstracts, Fall Meeting of The Electrochemical Society, San Diego, USA, pp. 966-967, 1986.

(6) Bratland, D., Brun, M., Grjotheim, K. and Thonstad, J., *A study of the effect of cell geometry, bath convection, and the boundary equilibrium on the operation of laboratory cells*, Light Metals 1979, TMS, pp. 397-409, 1979.

(7) Peterson, R.D., Richards, N.E., Taberaux, A.T., Koski, O.H., Morgan, L.G. and Strachan, D.M., *Results of 100 hours electrolysis test of a Cermet Anode: Operational Results and Industry Perspective*, Light Metals 1990, pp. 385-393, 1990.

(8) Sørlie, M. and Øye, H.A., *Cathodes in Aluminium Electrolysis*, 2nd ed., Aluminiuim-Verlag GmbH, ISBN 3-87017-230-4, 1994.

(9) Dawless, R.K., LaCamera, A.F., Troup, R.L., Ray, S.P. and Hosler, R.B., *Molten Salt Circulation Design for an Electrolytic Cell*, US Patent no. 5.938.914, Aug. 1999.

(10) Wang, H. and Thonstad, J., *The behaviour of inert anodes as a function of some operating parameters*, Light Metals 1989, pp. 283-290, 1989.

(11) Windisch, C.F. Jr., Strachan, D.M., Henager Jr., C.H., Greenwell, E.N. and Alcorn, T.R., *Results from a pilot cell test of inert anodes*, Pacific Northwest Laboratory, PNL-8269, UC-313, DE-AC06-76RLO 1830, Battelle Memorial Institute, Aug., 1992

(12) Keller, R., Rolseth, S. and Thonstad, J., *Mass transport considerations for the development of oxygen-evolving anodes in the aluminium electrolysis*, Electrochimica Acta, vol. 42, no 12, pp. 1809-1817, 1997.

(13) Thonstad, J. and Olsen, E., *Development and Experience with Non-Consumable Anodes in Aluminium Electrowinning*, Molten Salts Forum, Vols. 5-6, pp. 297-302, 1998.

(14) Kreyszig, E., *Advanced Engineering Mathematics*, chap. 1.8, 6th ed., John Wiley & Sons Inc., ISBN 0-471-62787-9, 1988.

(15) Greenberg, M.D., *Foundations of Applied Mathematics*, 1st ed., Prentice-Hall Inc., ISBN 0-13-329623-7, 1978.

(16) Shkuryakov, N.P., Dalinenko, E.N., Lebedev, O.A. and Vinokurov, V.B., *Kinetics of reduction of metal oxide impurities in electrolysis of cryolite-alumina melts*, J. Appl. Chem. USSR, Vol. 63, no. 6, pp. 1243-1249, June, 1990.

(17) Strachan, D.M., Marschman, S.C., Davis, N.C., Friley, J.R. and Schilling, C.H., *Fiscal Year 1988, Annual Report*, Pacific Northwest Laboratory, PNL-7106 UC-313, Oct., 1989.

(18) Grjotheim, K., Krohn, C., Malinovský, M., Matiašovský, K. and Thonstad, J., *Aluminium Electrolysis. Fundamentals of the Hall-Héroult Process,* 2nd ed., Aluminium-Verlag, Düsseldorf, ISBN 3-87017-155-3, 1982.

(19) Frizzle, P.B., Brown, C.W., Juric, D.D. and Brooks, R.J., *Cathalytic Dissolution of Aluminium Oxide During Electrolytic Reduction of Alumina*, Patent No. WO9941431, 1999.

(20) Skybakmoen, E. and Gulbrandsen, H., private conversations, SINTEF Materials Technology, Electrolysis Group, Trondheim, Norway, spring 2000.

(21) Ray, S., *Inert Anodes for Hall Cells*, Light Metals 1986, TMS, pp. 287-298, 1986.

(22) Olsen, E., *Karakterisering av Cu-dopet $NiFe_2O_4$ som inert anodemateriale i aluminiumselektrolysen,* Diploma Thesis, Dept. of Electrochemistry, 1991.

URN:NBN:no-6347

(23) Chin, P.C.Y., *The Behaviour of Impurity Species in Hall-Heroult Aluminium Cells*, Ph.D. thesis, Carnegie Mellon University, Pittsburgh, 1992.

(24) Chin, P.C.Y., Sides, P.J. and Keller, R., *The Transfer of Nickel, Iron and Copper from Hall Cell Melts to Molten Aluminum*, Can. Metall. Quart., vol. 35, no.1, pp. 61-68, 1996.

(25) Alcorn, T.R., Taberaeaux, A.T., Richards, N.E., Windisch, C.F., Strachan, D.M., Gregg, J.S., and Frederick, J.S, *Operational Results of Pilot Cell Test with Cermet "Inert" Anodes*, Light Metals 1993, pp. 433-443, 1993.

(26) Numata, H. and Bockris, J O'M., *Interactions of Gases in Molten Salts: Carbon Dioxide and Oxygen in Cryolite Alumina Melts*, Metall. Trans. B., vol. 15, pp. 39-46, 1984.

(27) Tarcy, G.P., *Corrosion and Passivation of Cermet Inert Anodes in Cryolite-type Electrolytes*, TMS, Light Metals 1986, pp. 309–320, 1986.

(28) Haugsrud, R. and Kofstad, P., *On the High-Temperature Oxidation of Cu-Rich Cu-Ni Alloys*, Oxidation of Metals, vol. 50, Nos. 3-4, pp. 189-213, 1998.

(29) Haugsrud, R., *On the High Temperature Oxidation of Copper-Nickel Based Alloys*, Ph.D. thesis, University of Oslo, Norway, 1999.

(30) DeYoung, D.H., *Solubility of oxides for Inert Anodes in Cryolite-Based Melts*, Light Metals 1986, pp. 299-307, 1986.

(31) Weyand, J.D., DeYoung, D.H., Ray, S.B., Tarcy, G.P. and Baker, F.W., *Inert Anodes for Aluminium Smelting. Final Report*, Alcoa Centre, DOE/CS/40158-20, Feb., 1986.

(32) Diep, Q.B., *Structure and thermodynamics of cryolite-based melts with addition of Al_2O_3 and Fe_2O_3. Cyclic voltametry study of Fe_2O_3 in molten cryolite*, Ph.D. thesis no. 28, NTNU, Trondheim, Norway, 1998.

8 Electrical conductivity of cermet materials

A stable and high electrical conductivity of the cermet anode material is of crucial importance in order to achieve low power consumption, thermal balance and even current distribution in an electrolysis cell where such anodes are used. The conductivity has to be 100 % electronic, and not ionic, in order to maintain a stable composition of the anode material and good electrical conductivity over time (1). The ceramic part of the composite is known to have very low conductivity, *i.e.* about 0.8 S/cm for $NiFe_2O_4$ and even lower for NiO, compared to a traditional anode made of carbon, which achieves nearly 200 S/cm (2). This is one of the reasons why the poorly conducting ceramic phases are mixed with a metal phase to increase the electrical conductivity.

The electrical conductivity also affects the temperature distribution in the anode, and low electrical conductivity leads to temperature gradients in the anode.

If the connection between a vertical anode and the current lead is placed at one end of the anode, the current distribution will be affected by the electrical conductivity of the anode material used. Solheim (3) estimated the current distribution (CD) by assuming primary CD only and no edge effect. On an anode with a conductivity of 50 S/cm immersed vertically 30 mm into the electrolyte with a cathode 30 mm apart, the current density of the upper 5-10 mm was 3-4 % higher than the average current density. However, when the conductivity of the anode was only 5 S/cm, the CD was about 35 % higher in the upper region and correspondingly lower at the bottom of the anode.

The cermet material has to achieve electrical conductivity that is competitive with carbon and it has to be stable over time if the cermet shall have a sustainable future. Olsen *et al.* (4), (5) measured the conductivity of three different cermet compositions, but obtained some unexplained and odd results, especially for the stoichiometric $NiFe_2O_4$ anode material. That is the reason why the conductivity of these materials was measured.

8.1 General electrical properties

The electrical conductivity of a material is somewhat analogous to its thermal conductivity. The magnitude of conduction is a function of the amount of energy present in the material, *i.e*. the size of the electric field, the number of carriers and the amount of dissipation (6). When one considers the effect of variables such as composition, structure, and temperature on the electrical conductivity, one is concerned with the concentration of charge carriers and their mobility.

The carriers in metals are electrons. Because of the metallic bond, these electrons are relatively free to move through the lattice, resulting in a high electrical conductivity. Alloying of a pure metal distorts the uniformity of its structure and reduces the electrical conductivity. An increase in temperature also disrupts the structure due to lattice vibrations and results in a decrease in electrical conductivity.

Ceramic materials show a wide range of electrical conductivity behaviour (7). Like metals, some transitions metal oxides such as CrO_2 and TiO conduct by electrons. This is caused by an overlap of electron orbitals such that unfilled d or f bands are present. Under the influence of an electric field, these electrons are relatively free to move and carry charge through the material. In other ceramic materials such as oxides and halides, ions can be carriers and provide ionic conduction. The degree of conductivity is largely dependent on the energy barrier that must be overcome for the ion to move from one lattice position to the next. The ionic conductivity is low at low temperature, but it increases with increasing temperature when the temperature is high enough to overcome the barrier to lattice diffusion. The presence of lattice defects such as vacancies and interstitials in the structure aids conduction, and controlled additions of impurities can be made to increase the electrical conductivity.

Other metal oxides, such as NiO, Cu_2O and Fe_2O_3, have an energy gap between the filled and empty electron bands such that conduction will occur only when external energy is supplied to bridge the energy gap. These materials are known as semiconductors (6). An increase in temperature can provide energy. For instance, NiO and Fe_2O_3 are insulators at room temperature, with conductivities of less than 10^{-16} S/cm. In the range 250 to 1000 K the conductivity increases nearly linearly to values in the range 10^{-4} to 10^{-2} S/cm. Semi-conducting properties can be achieved in many ceramics by doping or by forming lattice vacancies through non-stoichiometry.

Semiconductor spinel materials such as Fe_3O_4 diluted in controlled solid solutions with non-conducting materials such as $MgAl_2O_4$, show thermistor behaviour. Semi-conducting properties can also be achieved or controlled by mixing a conducting or semi-conducting material with a non-conducting material, often without significantly affecting other properties (6).

8.2 The spinel structure

A number of oxides of the general formula AB_2O_4, such as nickel aluminate spinel, $NiAl_2O_4$, have a cubic structure which can be viewed as a combination of the rock salt and zinc blende structures (6). The oxygen ions are in face-centred cubic close packing. As shown in the Figure below, for an elementary cell of this structure there are 4 O atoms, 4 octahedral interstices and 8 tetrahedral interstices. This makes a total of 12 interstices to be filled by 3 cations, one divalent and two trivalent. In each elementary cell 2 octahedral and 1 tetrahedral sites are filled. 8 of these elementary cells are arranged so as to form a unit cell containing 32 oxygen ions, 16 octahedral cations and 8 tetrahedral cations as illustrated in Figure 8-1.

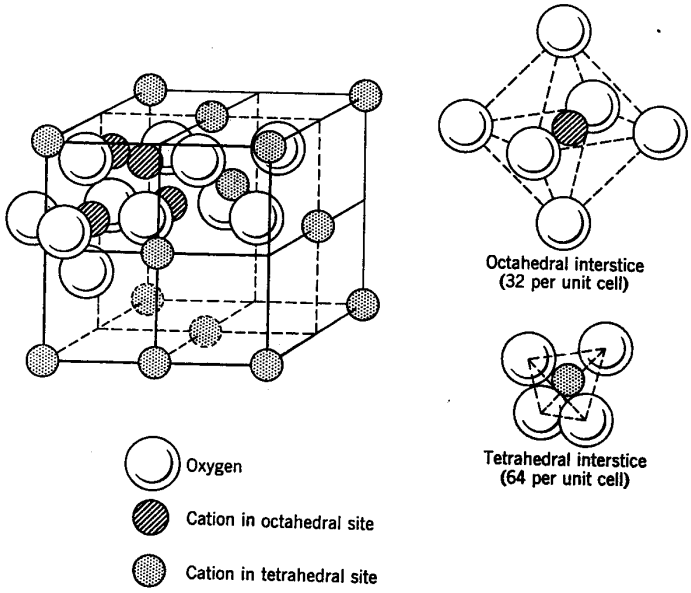

Figure 8-1: Spinel structure, from (6).

There are two types of spinels. In the *normal* spinel the A^{2+} ions sit on tetrahedral sites and the B^{3+} ions are on the octahedral sites. This is the structure observed for $FeAl_2O_4$ and $NiAl_2O_4$, and several ferrites ($ZnFe_2O_4$ and $CdFe_2O_4$) and aluminates ($MgAl_2O_4$, $CoAl_2O_4$ $MnAl_2O_4$ and $ZnAl_2O_4$). In the *inverse* spinels, the A^{2+} ions and half the B^{3+} ions are on octahedral sites, whereas the other half of the B^{3+} are on tetrahedral sites, $B(AB)O_4$. This is the more common structure, and it is observed for $FeNiFeO_4$, Fe_3O_4, $FeMgFeO_4$, $FeTiFeO_4$, $ZnSnZnO_4$, and many other ferrites of importance for their magnetic properties (6).

8.3 Conductivity of cermets with different amounts of metal phase

The conductivity of pure $NiFe_2O_4$ is poor, and it is reported (8), (9) to be only 0.8 S/cm at 1000 ^oC. Alcoa (8) experimented with different amounts of metal phase in the cermet, and measured its influence on electrical conductivity. Increasing the copper concentration increased the conductivity, particularly above 10 weight percent (see Figure 8-2 to 8-3). Alcoa also showed that the cermets have semi-conducting behaviour, which means that the conductivity increases with temperature. The effect of increasing temperature was steep above 500 ^oC. The temperature affects electrical conductivity relatively more than the content of copper metal does. The positive effect of increasing copper concentration is, however, increasing with increasing temperature.

Copper powder, which was not screened before mixing and sintering, gave higher conductivity than obtained with screened copper powder. Comparison of the results presented in Figure 8-2 and 8-3 show this effect.

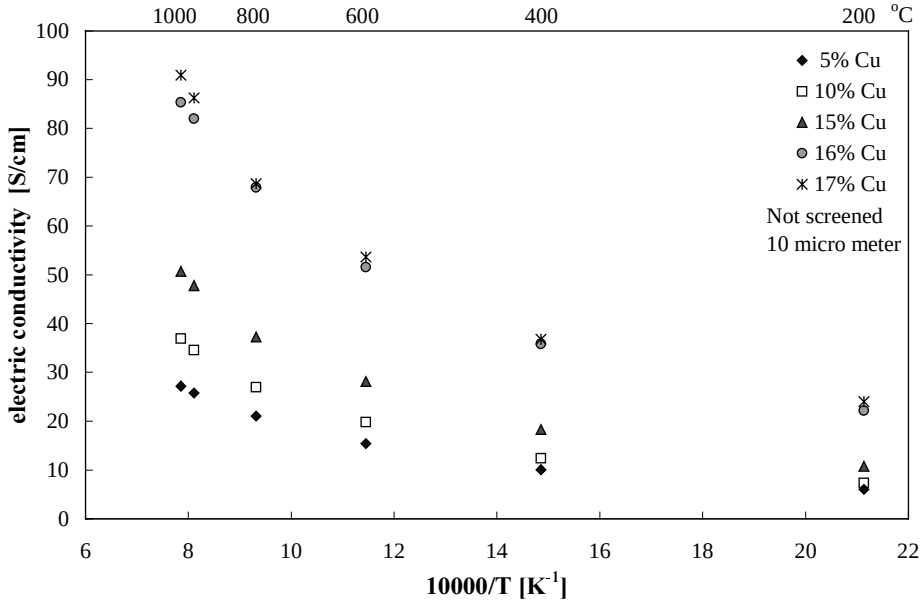

Figure 8-2: Conductivity of stoichiometric nickel ferrite mixed with different amounts of copper as a function of the inverse temperature. The copper powder used for these anodes was not screened. Data from (8).

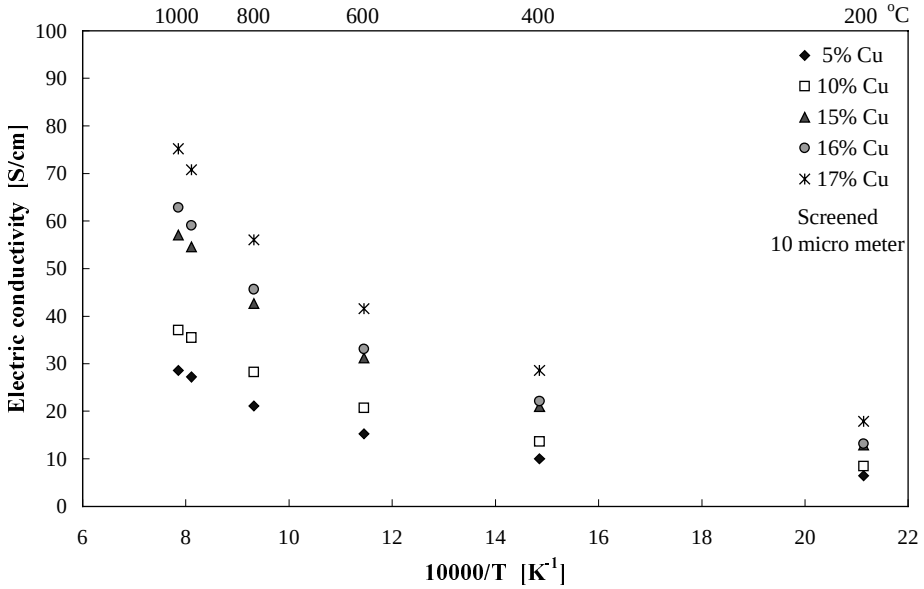

Figure 8-3: Conductivity of stoichiometric nickel ferrite mixed with different amounts of copper as a function of the inverse temperature. The copper powder used for these anodes was screened. Data from (8).

10 µm particle sized metallic copper gave (8) 50-60 % higher conductivity than 1 µm did.

8.4 How to measure the electrical conductivity

Several available methods were considered to measure the conductivity of cermets as a function of temperature. Most often, the electrical conductivity is measured by the two-points method, the four-points method and by the Van der Pauw's method (10), (11), (12), (13).

Olsen *et al.* (4), (5) used the four-points method, but as already mentioned his home-made equipment gave odd results for the stoichiometric cermet where the conductivity suddenly increased from almost zero to 200 S/cm. Above 1000 ^{0}C Olsen's conductivity data dropped unexpectedly for all his materials. Since the main issue for the present investigation was to find out how the conductivity changed as a function of temperature, and roughly how much it changed, it was decided that the two-points method to be used at plane parallel samples was appropriate.

The two-points method implies that two points at a defined distance apart from each other and with constant and equal areas are in contact with an external circuit which applies a constant current through these two points. By measuring the potential drop over the sample defined between these two points when a current is passed, one can calculate the corresponding conductivity of the sample. The samples were ground plane parallel with a thickness of 0.5 $\pm$ 0.001 cm and with a diameter of 1.0 cm.

The electrical resistance R was calculated using Ohm's law:

$$R = \frac{E}{I} \qquad [8\text{-}1]$$

where I is the applied current and E is the measured voltage. The conductivity κ was calculated using the formula:

$$\kappa = \frac{\ell}{A \cdot R} \qquad [8\text{-}2]$$

where ℓ is the gauge length of the specimen and A is the cross-sectional area of the specimen. Inserting Ohm's law, one gets:

$$\kappa = \frac{\ell \cdot I}{A \cdot E} \qquad [S/cm] \qquad [8\text{-}3]$$

8.5 Apparatus used to measure conductivity

A sketch of the experimental set-up used to measure the electrical conductivity is shown in Figure 8-4 together with a sketch of the electrical circuit of the cell.

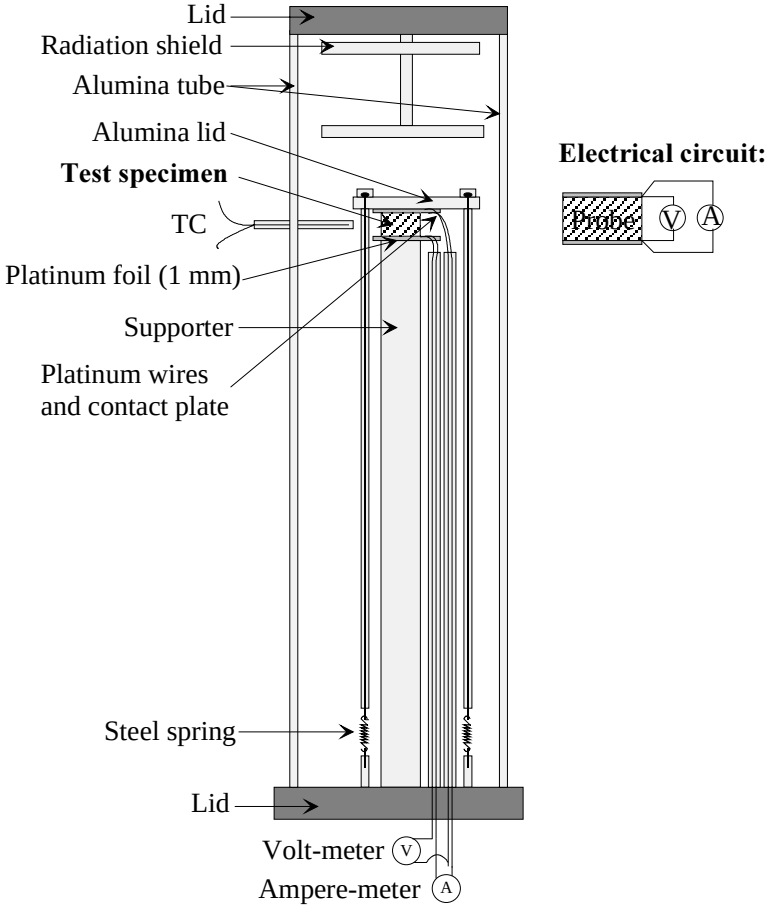

Figure 8-4: Apparatus used to measure conductivity by the two-points method. The test equipment was contained in a closed resistance heated furnace.

A HP 6032 A System Power Supply was used as current supply, and 0.1 A was constantly passing through the test probe during the tests. A Keithley 2000 Multimeter was measuring the voltage drop through the test probe every 10 seconds.

The contact surfaces of the test probe were sputtered with a micrometer-thin layer of platinum prior to the test to ensure proper contact between the sample and the external platinum circuit. By using platinum instead of, for example, gold one reduces the Peltier resistance caused between different materials. The melting point of gold (1063 ^{o}C) is also too close to the highest temperature chosen, *i.e*. 1050 ^{o}C.

Initially the electrical circuit through the furnace was shorted, and an experiment was run in the same way as with the cermet samples. The voltage drop in the circuit could be expressed as,

$$E_{\text{External circuit}} = 6.86 \cdot 10^{-7} \cdot T + 5.04 \cdot 10^{-4} \quad [V] \qquad T = {}^{o}C \qquad [8\text{-}4]$$

This voltage drop is negligible compared to the voltage drop across the cermet sample, and the only voltage drop not measured was the contact voltage between the sputtered platinum layer and the cermet. Thomson voltage drop caused by the temperature gradient in the outer circuit through the lower part of the furnace is generally low, and was neglected.

8.6 Results

Cermets with different contents of NiO and $NiFe_2O_4$ were produced, and their electric conductivity was measured in air. The results are shown in Figures 9-7 to 9-9 below.

The cermet probes were continuously heated 1 degree per minute from room temperature up to 1050 ^{o}C. It is important to ensure equilibrium within the probe at all times, hence the heating rate must not be too fast. For this reason the heating was interrupted at 600 ^{o}C and at 1050 ^{o}C for a few minutes, and the recorded conductivity was found to remain constant during these periods.

The result shown in Figure 8-5 was reproduced once, giving the same result. The conductivity measured shows a semi-conducting type of behaviour, since the conductivity increases with increasing temperature. As one can see, the heating and cooling curves (indicated by arrows) give similar values below 550 and above 1000 degrees. The rapid cooling between 600 and 1000 ^{o}C, which was difficult to control, caused the discrepancy between the conductivities measured during heating and cooling in this range. Therefore, the heating curve gives the best data of the conductivity of this cermet.

The stoichiometric cermet showed a maximum value of only 32 ± 2 S/cm at 1050 ^{o}C (see Figure 8-5), which is about 1/7 of the value Olsen (4), (5) found for the same material[1], but at 650–700 ^{o}C. No explanation can be given for this discrepancy, but the shape of Olsen's curve may indicate contact problems because of the extremely rapid conductivity change at 600 ^{o}C.

Compared to a traditional carbon anode, the cermet containing stoichiometric $NiFe_2O_4$ probably has too low conductivity to be used as an anode material.

[1] The only difference between the preparation of the two materials was the dispersing agent used. Olsen used oxidised fish oil, while the present material was made by using Geropon SDS (see Chaper 3).

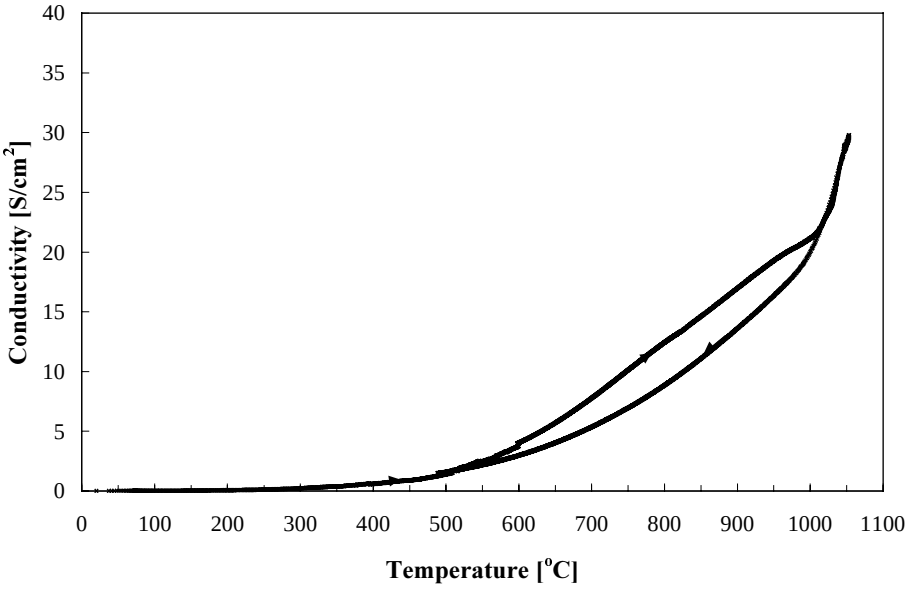

Figure 8-5: The conductivity measured for a stoichiometric $NiFe_2O_4$ cermet sample, mixed with 17% Cu and 3% Ni , as a function of temperature.

Alcoa (8) used a cermet with excess NiO in the ceramic phase. The most promising material they found was a cermet with 17% excess NiO and 17% Cu prior to sintering. This mixture with additional 3 wt% Ni (to make it comparable to Olsen *et al.*'s material (4), (5) was prepared and tested. The results are given in Figure 8-6.

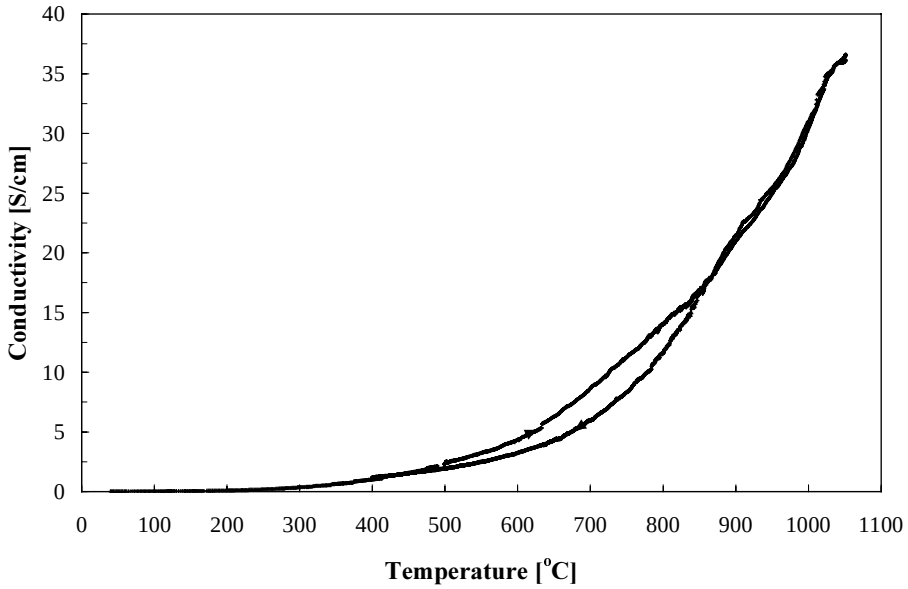

Figure 8-6: The conductivity measured for a cermet sample with 17% excess NiO in $NiFe_2O_4$, 17% Cu and 3% Ni, as a function of temperature.

Olsen *et al.* (4), (5) increased the NiO content beyond the Alcoa composition (8) (*i.e.* 23 % NiO) in an attempt to improve the material even more. Hence a similar mixture to that of Olsen *et al*., was made and tested. The results are given in Figure 8-7.

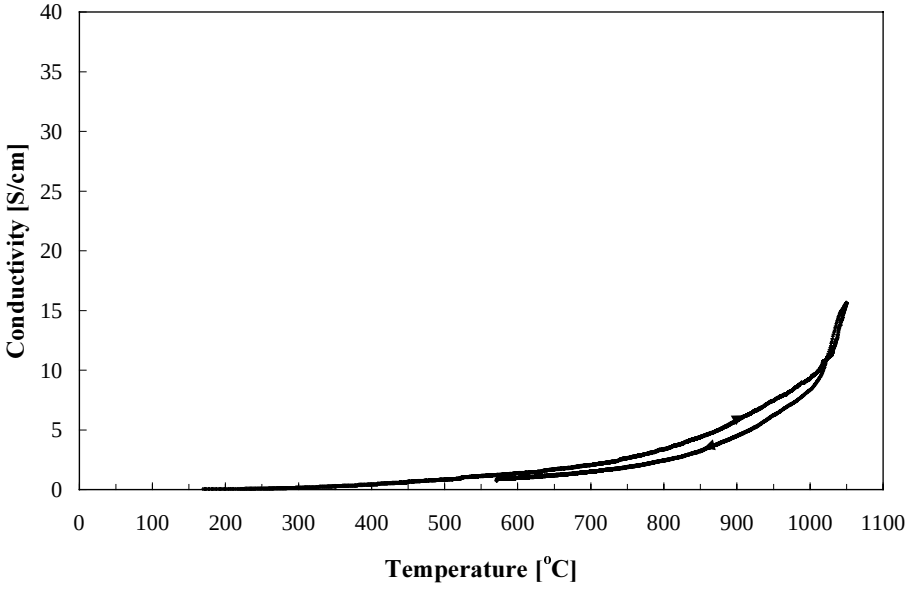

Figure 8-7: The conductivity measured for a cermet sample with 23% excess NiO in $NiFe_2O_4$, 17% Cu and 3%, as a function of temperature.

As one can see, the cermet containing 23 % NiO gave much lower conductivity than the one with only 17 % NiO. The conductivity data obtained for all the three samples are much lower than the values obtained by Olsen *et al.* (4), (5). Since NiO generally is considered to have low electrical conductivity, it should be reasonable to expect lower conductivity in cermets with increasing amounts of excess NiO, if the physical properties are comparable in these materials (*i.e.* microstructure, porosity *etc.*). However, Olsen *et al.* (4), (5) obtained a higher conductivity for the cermet with 23 % excess NiO (*i.e*. ~100 S/cm at about 1000 ^{o}C) than for the material with only 17 wt % NiO (*i.e.* 70 S/cm at about 1000 ^{o}C).

Since Alcoa (8) measured the conductivity of a substantial number of anode samples, and since some of Olsen's results are hard to explain, Alcoa's results appear to be the most reliable. The present results were reproducible and similar to those of Alcoa (8) (compare Figures 8-5 to 8-7 with Figures 8-2 and 8-3).

Hart *et al.* (14) measured the electrical conductivity of a $NiO\text{-}NiFe_2O_4$ cermet contain 21 wt% Cu and 4 wt% Ni prior to sintering. They measured the conductivity to be 170 S/cm at around 1000 ^{o}C, which was substantially higher than what was found for cermets without nickel, made by Hart *et al.* (14) and by Alcoa (8). The improvement was attributed to the influence of the added nickel on the metal phase, but no explanation was given for the mechanism involved (14).

Strachan *et al.* (15) produced a cermet containing 17 wt% excess NiO in a NiO-$NiFe_2O_4$ cermet with 25 wt% Cu, 3 wt% Ni and 1 wt% Al prior to sintering. These anodes yielded electric conductivities of about 410 S/cm at 950 ^oC, which is significantly higher than the conductivities obtained for NiO-$NiFe_2O_4$-Cu and NiO-$NiFe_2O_4$-Ni[2] cermets. The metal phase appeared to be continuously interconnected, which could account for the increased conductivity. However, the electrical conductivity increased with increasing temperature, suggesting that the conduction took place partly through the semi-conducting parts of the material. It was postulated that the aluminium reacts with the NiO and the $NiFe_2O_4$ phases by the following reactions:

$$2Al + 3NiO = Al_2O_3 + 3Ni \qquad [8\text{-}5]$$

and,

$$8Al + 3NiFe_2O_4 = 4Al_2O_3 + 3Ni + 6Fe \qquad [8\text{-}6]$$

Free alumina is probably not formed, but it rather goes into solid solution with the spinel.

As an alternative to using Al as a catalyst, Hart *et al.* (14) mixed 0.75 wt% Mg into the anode powder mix together with 21 wt% Cu and 3 wt% Ni. The result was a high-density anode with fine dispersion of copper, which was expected to give high electrical conductivity. The anodes were, however, not tested electrochemically and have not been found mentioned in later reports from Pacific Northwest Laboratory.

The electrical conductivity of $NiCr_2O_4$ was reported by Augustin *et al.* (17) to increase with increasing sintering temperature, and in an unspecified atmosphere it was found to be 2.70 S/cm at 1000 ^oC.

Augustin *et al*. (18) reported the electrical conductivity of pure $NiFe_2O_4$ to be 2.5 S/cm at 1000 ^oC. The highest conductivity was obtained for a sintering temperature of 1400 ^oC. At a sintering temperature of 1000 ^oC the conductivity was reduced to 0.3 S/cm in air at 1000 ^oC (19).

Augustin *et al.* (20), (21) reported the conductivity of $CoFe_2O_4$ to be 6.0 S/cm at 1000 ^oC. When the ferrite was mixed with 1 wt% niobium pentoxide to increase the density, the conductivity in an atmosphere of air was reduced to 4 S/cm at 1000 ^oC.

Chuanfu *et al.* (2) measured the conductivity of $NiFe_2O_4$ with excess NiO (made from approximately 48 wt% Fe_2O_3 and 52 wt% NiO) and with different amounts of copper. The electrical conductivity increased from 1.12 S/cm in pure $NiFe_2O_4$ to 31.2 S/cm in a $NiFe_2O_4$ material mixed with 20 wt% Cu at 1000 ^oC. A $NiFe_2O_4$ material similar to the one presently investigated was one mixed with 16 wt% Cu, which gave 6.90 S/cm at 1000 ^oC. Chuanfu *et al.* also investigated the effect of sintering temperature in the range 1000 – 1350 ^oC, and the highest conductivity was 20.6 S/cm obtained at 1000 ^oC for a

[2] NiO-$NiFe_2O_4$-Ni cermets form a continuos Ni rich metal phase in the cermet (16) in contrast to NiO-$NiFe_2O_4$-Cu materials that form distinct Cu rich metal grains in the cermet.

material sintered at 1200 ^{o}C. All the materials were sintered at the maximum temperature for 2 hours. The corresponding heating and cooling slopes were not reported.

Two $NiFe_2O_4$ cermet materials with 10 wt% Cu and 10 % Fe, showed very different conductivities (2). The one with copper was sintered at 1300 ^{o}C for 2 hours and obtained 5.38 S/cm, while the one with Fe was sintered at 1350 ^{o}C and obtained 83.3 S/cm at 1000 ^{o}C. The corrosion rates of materials with high iron contents have been found to be too high to be of interest for aluminium production (8).

Chuanfu *et al.* (2) attributed the wettability characteristics of the different compositions to play a mayor role with regard to conductivity. By adding yttrium oxide to the cermet matrix they improved the wettability between the copper metal phase and the oxide phases in the cermet, giving a finely dispersed and interwoven copper phase and a significantly higher conductivity as a result. By adding 2.7 wt% Y_2O_3, the conductivity of $NiFe_2O_4$ mixed with 10 wt% Cu increased to 833 S/cm at 1000 ^{o}C. Y_2O_3 was found in small amounts in the NiO phase and at the interface between the copper phase and the oxide phases. Pure Y_2O_3 is rather expensive compared to iron oxide and nickel oxide, and it has a rather low conductivity (*i.e.* 0.0069 S/cm at 1000 ^{o}C (2)). The high conductivity of these materials might therefore be attributed to a better inter-linking between the ceramic and the metal phases because of the Y_2O_3 present.

Some electrical conductivities of different materials have been compiled by Zhang *et al.* (22), which are summarised in Table 8–1.

Table 8-1: Electrical conductivity of different candidate anode materials for aluminium production, data compiled by (22).

Materials	**Electrical conductivity at 1000 ^{o}C [S/cm]**
$NiFe_2O_4$	0.77
$NiFe_2O_4$ + 0.05 SnO_2	1.7
Industrial Cryolite	2.5
$NiFe_2O_4$ + 0.05 TiO_2	3.3
$Ni_{0.9}Fe_{0.1}Fe_2O_4$	11
$NiFe_2O_4$ + 20 w/o Pd	71
$Ni_{0.5}Fe_{0.5}Fe_2O_4$	111
Industrial carbon anode	143
Fe_3O_4	200
SnO_2	500
Graphite	1000
Al(liquid)	41322

The values reported for carbon anodes and SnO_2 in Table 8-1 seem to be a bit high according to a data sheet from Dyson Refractories (23), which reports the conductivity of their Stannex Tin Oxide Electrodes to be only 133 S/cm at 1000 ^oC. Cryolite is an ionic conductor. "Industrial cryolite" has excess AlF_3, which makes it liquid at 1000 ^oC.

8.7 Concluding remarks

The electrical conductivity values found in the literature vary considerably. It seems like parameters such as:

- composition/additives
- particle sizes and distribution
- sintering conditions
- grain sizes/microstructure
- porosity
- morphology
- wettability

play a major role when it comes to the electrical conductivity of the materials, and since the materials tested in the literature were not identical, it seems to be very difficult to compare the available data.

8.8 References

(1) Sadoway, D.R., *A Material System Approach to Selection and Testing of Nonconsumable Anodes for the Hall Cell*, TMS, Light Metals 1990, pp. 403–407, 1990.

(2) Chuanfu, W., Guoxun, L., Shuling, Q., Aiqin, H and Guobin, L., *Effect of Adding Y_2O_3 in Cermet Electrodes on the Electrical Conductivities,* Rare Metals, vol. 11, no. 4, pp. 255-259, Oct. 1992.

(3) Solheim, A., Note, SINTEF Materials Technology, Norway, Dec. 1999.

(4) Olsen, E., *Nickel Ferrite and Tin Oxide as Anode Materials for Aluminium Electrolysis*, Dr.ing. (Ph.D.) thesis no 100, NTH, Trondheim, Norway, 1995.

(5) Olsen, E. and Thonstad, J., *Nickel ferrite as inert anodes in aluminium electrolysis – Part I Material fabrication and preliminary testing*, J. Appl. Electrochem., vol. 29, pp. 293-299, 1999.

(6) Kingery, W. D., *Introduction to Ceramics*, John Wiley & Sons, Inc., 4th ed., 1967.

(7) Richerson, D.W., *Modern Ceramic Engineering Properties, Processing and Use in Design,* Marcel Dekker, Inc., Chap. 2, 1982.

(8) Weyand, J.D., DeYoung, D.H., Ray, S.P., Tarcy, G.P. and Baker, F.W., *Inert Anodes for Aluminium Smelting Final Report*, Alcoa Center, DOE/CS/40158-20, Washington, USA, 1986.

(9) Ray, S.P., I*nert Anodes for Hall Cells*, Light Metals 1986, pp. 287-298, 1986.

(10) Van der Pauw, L.J., *A Method of Measuring the Resistivity and Hall Coefficient on Lamellae of Arbitrary* Shape, Philips Tech. Review, vol. 20, no. 8, pp. 220-224, 1958/59.

(11) Van der Pauw, L.J., *Deterination of Resistivity Tensor and Hall Tensor of Anisotropic Conductors*, Philips Res. Repts, vol 16, pp 187-195,1961.

(12) Goretzi, H., *Observations Using the Van der Pauw Method of Resistivity Measurements,* Munin Ruzicka, pp 85-95, 1972.

(13) Paulsen, F.W., Buitink, P. and Malmgran-Hansen, B., *Van der Pauw- and conventional 2-points conductivity measurements on YSZ-plates*, Athens, Greece, July 2^{nd}-5^{th}, pp. 1-11, 1991.

(14) Hart, P.E., Brenden, B.B., Davis, N.C, Koski, O.H., and Marschman, S.C., *Fiscal Year 1986 Annual Report, Inert Anode/Cathode Program*, Pacific Northwest Laboratory, PNL-6247, UC-95f, June, 1987.

(15) Strachan, C.M, Koski, O.H., Marschman, S.C., Brenden, B.B. and Davis, N.C., *Fiscal Year 1987 Annual Report, Inert Electrodes Program*, Pacific Northwest Laboratory, PNL-6746, UC-95f, Dec., 1988.

(16) Tarcy, G.P*., Corrosion and Passivation of Cermet Inert Anodes in Cryolite-type Electrolytes*, TMS, Light Metals 1986, pp. 309–320, 1986.

(17) Augustin, C.O., Prabheakaran, D. and Srinivasan, L.K., *Fabrication and characterization of $NiCr_2O_4$ spinel*, J. Materials Sci. Letters, vol. 12, pp. 383-386, 1993.

(18) Augustin, C.O., Srinivasan, L.K. and Srinivasan, K.S., *Inert Anodes for Environmentally Clean Production of Aluminium – Part I*, Bull. Electrochem., vol. 9, pp. 502-503, Aug.-Oct. 1993

(19) Augustin, C.O., *Sintering behaviour of NiO-Fe_2O_3 composites*, J. Materials Sci. Letters, vol.12, pp. 1786 - 1788, 1993.

(20) Augustin, C.O., Srinivasan, L.K., Srinivasan, K.S.and Desikan, P.S., *Studies on ferric oxide based anodes for aluminium production*, Bull. Electrochem., vol. 6, pp. 526-527, May 1990.

(21) Augustin, C.O., Srinivasan, L.K., Srinivasan, K.S.and Mani, A., *Structural and Electrical Properties of Cobalt Ferrite*, J. Mater. Sci. Technol., vol 12, pp. 417- 420, 1996.

(22) Zhang, H., De Nora, V. and Sekhar, J.A., *Materials Used in the Hall-Heroult Cell for Aluminium Production*, TMS, ISBN 0-87339-245-0, p. 91, 1994.

(23) *Stannex Tin Oxide Electrodes*, Data Sheet from Dyson Refractories, Baslow Road, Sheffield S17 3BL, England, 1991.

URN:NBN:no-6347

URN:NBN:no-6347

9 Conclusions and suggestions for further work

A thorough investigation has been performed on the behaviour of Ni, Fe and Cu oxide species in cryolite melts, and the solubility of these species was measured as a function of alumina content, NaF/AlF_3 molar ratio (CR) and temperature.

Both NiO and FeO form aluminates in the solid phase at high alumina activity. The alumina concentrations corresponding to the points of coexistence between FeO and $FeAl_2O_4$ and between NiO and $NiAl_2O_4$were determined to be 5.03 and 3.0 wt% Al_2O_3, respectively. In cryolite-alumina melts they are present as NiF_2 and FeF_2 with different numbers of associated "NaF's". Ni(II) forms Na_3NiF_5 in melts from CR 2 to 12. Fe(II) forms $NaFeF_3$ in acidic melts, and Na_3FeF_5 and some Na_4FeF_6 in basic melts.

Arrhenius plots showing the temperature dependence of the Ni(II) and Fe(II) solubilities in alumina-saturated cryolite gave the following partial molar enthalpy of dissolution: $\Delta\overline{H}^{o}_{NiAl_2O_4}$ = 248.2 kJ/mol and $\Delta\overline{H}^{o}_{FeAl_2O_4}$ = 64.8 kJ/mol.

Copper ions in solution show a complex behaviour since they form both fluorides and oxy-complexes in the melt. The extent of co-existence of Cu(I) and Cu(II) in the same melt is also considerable, varying with the amount of alumina present in the melt. Cu(I) forms CuF, especially at low alumina contents, while Na_5CuO_3 is formed with increasing alumina concentration. Cu(II) forms CuF_2 in decreasing amounts with increasing alumina concentration. The species that gave the best fit for the cupric oxy-complexes was $Na_{16}CuO_9$, and the amount increased with increasing alumina content.

Solubility measurements for CuO in alumina-saturated melts at CR 3.0 to 1.2 were carried out, and the results clearly show that the saturation concentration is dependent on both temperature and melt composition (*i.e.* CR). Interpolation of data from one temperature to another should, therefore, be made with caution.

Arrhenius plots showing the temperature dependence of the Cu(I) and Cu(II) solubilities gave $\Delta\overline{H}^{o}_{CuAlO_2}$ = 166.2 kJ/mol and $\Delta\overline{H}^{o}_{CuAl_2O_4}$ = 176.3 kJ/mol in alumina-saturated cryolite, and $\Delta\overline{H}^{o}_{Cu_2O}$ = 143.0 kJ/mol and $\Delta\overline{H}^{o}_{CuO}$ = 98.2 kJ/mol in cryolite.

The interpretations of the solubility measurements for the oxides of Ni and Fe gave conclusive and consistent results, while some of the results obtained for the Cu oxides are hard to explain. The mechanisms proposed at low alumina concentrations seem to be satisfactory, while there is still some uncertainty, both experimental and theoretical, for the high alumina range. More work is needed to find out what is happening with the copper aluminates.

Cermet anodes were prepared with a $NiFe_2O_4$-based oxide phase mixed with a ~20 wt% copper-rich metal phase. The electrical conductivity for these materials was measured as a

function of temperature, showing semiconductor behaviour from room temperature to 1050 ^{o}C. The highest electrical conductivity recorded was ~30 S/cm at 1000 ^{o}C, which is on the low side for use as an anode material for aluminium production.

After 48 hours of electrolysis there was no metal phase present in the outer 100 μm of the anode, not even pores indicating where the metal grains had been. A copper-rich phase was found in one of the anodes ~2 mm from the outer surface, and it is believed that copper diffuses out of the anode. The concentrations of Fe and Cu in the electrolyte were below the saturation concentrations, while the concentration of Ni was 3-4 times above. The dissolution mechanisms do not fit a first order mass-transport model, but can probably be explained by a controlled dissolution mechanism with some additional disintegration/ spalling of the anode material. Further work is needed to make any conclusion, and one needs correct solubility data for the anode constituents to make a proper evaluation of other anode materials. Perhaps the 1st order mass-transport model agrees for some materials, but based on the present results it seems untenable for cermet materials made of $NiFe_2O_4$ with a copper-rich metal phase.

The solubility of the oxides of Ni(II) and Fe(III) are very low for alumina-saturated melts, which make them promising candidates for inert anodes. However, if nickel aluminate, which is an insulator, is formed and grows on the anode surface it is a cause of concern. Fe(II) aluminate is not expected to be formed on the anode surface because of the high partial oxygen pressure, but it might be formed in the bulk of the electrolyte where the partial oxygen pressure is lower.

The solubility of Cu oxides in alumina-saturated cryolite is high with respect to the use of Cu-rich materials as an inert anode. A low-ratio melt (*i.e.* CR ~1.2) is more interesting for a copper-based long-life anode material. Even if this means one has to design a new type of cell to keep and operate the cell at alumina saturation, one might have to redesign the aluminium cells completely to find a technical solution that works properly with inert anodes.

Since the dissolution model seems to be more complex than what the simple Keller-Evans mass transport model predicts, one should investigate the anode reactions and kinetics more thoroughly. Electrochemical measurements like cyclic voltammetry and impedance measurements may give new information about the behaviour of these anode materials.

The concept of “inert” anodes has been known since Hall in the 1880s tried to make anodes that were inert to the aggressive environment in cryolite-based melts. Even if very little work was done on this fields for more than 60 years, the efforts made during the last 40 years have not resulted in an anode that is totally *inert*. Perhaps the time has come to realise that a totally inert anode material is not possible to find, and instead one should consider a way to handle a “slowly consumable” anode that still can yield high quality aluminium metal. This will only be feasible if it is developed a reliable, cost-effective method to adequately remove the relevant impurities from aluminium introduced by the dissolved anode material. One should, therefore, not test only the anode materials, but these materials in an overall concept where all the processes from primary aluminium production to the final product are considered.

Appendix

URN:NBN:no-6347

URN:NBN:no-6347

A Environmental considerations and the primary aluminium producers' contribution to the greenhouse effect

The globally averaged temperature of the air at the Earth's surface has warmed between 0.3 and 0.6 °C since the late nineteenth century (1). The four warmest years on record since 1860 have all occurred since 1990 (see Figure A-1). Evidence of global temperature increase since the nineteenth century includes the observed rise in sea level of 10 to 25 centimetres, the shrinkage of mountain glaciers, a reduction of northern hemisphere snow cover, and increasing sub-surface ground temperatures. Even the Arctic ice has decreased its thickness with 30 % the last 40 years according to the American Marine.

Data from a few locations can be used to trace temperatures even further into the past. Deep ice cores and North Atlantic deep sea sediments suggest that the recent warming stands out against a record of relatively stable temperatures over the past thousand years. The century-to-century variations of temperature have seldom approached the observed increase of global mean temperature of about 0.3 to 0.6°C over the last century. Data derived from measurements of tree rings suggest that global surface temperatures are now as warm as or warmer than at any time in the past 600 years.

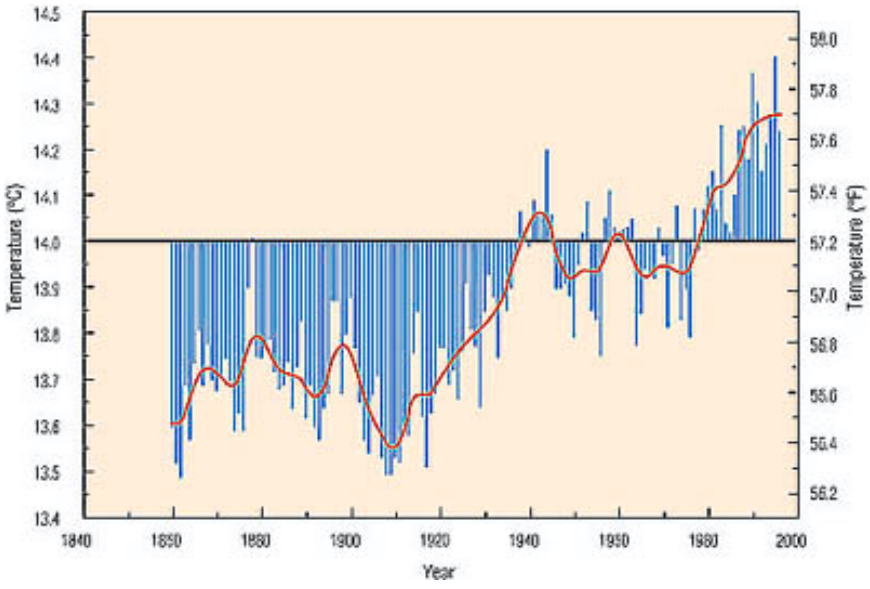

Figure A-1: Combined land surface air and sea surface temperatures 1861 to 1994 the last 150 years, from (1).

The United Nations Intergovernmental Panel on Climate Change (IPCC) estimated that the globally averaged surface temperature will increase by 1 to 3.5°C by the year 2100, with an associated rise in sea level of 15 to 95 cm. Warming in this range is cause for concern. These changes may lead to a number of potentially serious consequences. For example, mid- and high-latitude regions, such as much of the United States, Europe, and Asia, could experience an increase in the incidence of heat waves, floods, and droughts as the global climate changes. The impacts of such extreme events on human welfare as well as natural ecosystems could be significant. Apparently small global average temperature changes also led to large climate shifts in the past. Earth's average temperature increased by only about 5 degrees Celsius between the end of the last ice age and today, but much of the Northern Hemisphere went from being buried under thousands of feet of ice to being ice-free.

Because most greenhouse gases remain in the atmosphere for a long period of time, even if emissions from human activities were to stop, and the effects of accumulated past emissions may persist for more than a century before the atmospheric level of carbon dioxide approaches its pre-industrial level (1).

A1 The greenhouse effect

The Sun warms the Earth and is the source of energy for the climate system. However, the process by which this occurs is complicated. Only about half of the incoming radiation from the Sun is absorbed by the Earth's surface. About a quarter is absorbed by the atmosphere, and the remainder is reflected back into space by clouds, dust and other particulate substances without being absorbed, either by the surface or atmosphere (2). The energy absorbed by the Earth's surface is re-radiated to space as long-wave radiation. A fraction of this re-radiated energy is absorbed by so called greenhouse gases, *i.e.* water vapour, CO_2, methane, etc. When a greenhouse gas molecule absorbs long-wave energy, it heats up and radiates energy in all directions, including back down to the Earth's surface, which further warms the surface. This phenomenon is known as the greenhouse effect (3).

A1.1 The natural greenhouse effect

The sun's radiation, much of it in the visible region of the spectrum, warms our planet. On average, Earth must radiate back to space the same amount of energy, which it gets from the sun. Being cooler than the sun, Earth radiates in the infrared. (An object, when getting warmer, radiates more energy and at shorter wavelengths. On cooling, it emits less and at longer wavelengths, for example Lava.) The wavelengths at which the sun and the Earth emit are, for energetic purposes, almost completely distinct. Often, solar radiation is called short wave, whereas terrestrial infrared is called long-wave radiation (3).

Greenhouse gases in the Earth's atmosphere, while largely transparent to incoming solar radiation, absorb most of the infrared emitted by Earth's surface. The air is cooler than the surface, emission declines with temperature, so the air or, rather, its greenhouse gases emit less infrared upwards than the surface. Moreover, while the surface emits upwards only, the air's greenhouse gases radiate both up- and downward, so some infrared comes back

down. Clouds also absorb infrared well. Again, cloud tops are usually cooler and emit less infrared upwards than the surface, while cloud bottoms radiate some infrared back down. All in all, part of the infrared emitted by the surface gets trapped (3).

Satellites, viewing Earth from space, tell us that the amount of infrared going out to space corresponds to an `effective radiating temperature' of about –18 ^{o}C. At –18 ^{o}C, about 240 watts per square metre (W/m^2) of infrared are emitted (3). This is just enough to balance the absorbed solar radiation. Yet Earth's surface currently has a mean temperature near 15 ^{o}C and sends an average of roughly 390 W/m^2 of infrared upwards. After the absorption and emission processes just outlined, 240 W/m^2 eventually escapes to space; the rest is captured by greenhouse gases and clouds. The `natural greenhouse effect' can be defined as the 150 or so W/m^2 of outgoing terrestrial infrared trapped by Earth's pre-industrial atmosphere. It warms Earth's surface by about 33 ^{o}C (3).

Garden glasshouses retain heat mainly by lack of convection and advection. The atmospheric `greenhouse' effect, is, however, a misnomer since it is caused by absorption and re-emission of infrared radiation. Under clear sky, roughly 60-70 % of the natural greenhouse effect is due to water vapour (3), which is the dominant greenhouse gas in Earth's atmosphere. Next important is carbon dioxide, followed by methane, ozone, and nitrous oxide (4).

Clouds are not the same as water vapour: clouds consist of water droplets or ice particles or both. Under cloudy sky the greenhouse effect is stronger than under clear sky. At the same time, cloud tops in the sunshine look brilliantly white: they reflect sunlight. Globally and seasonally averaged, clouds currently exert the following effects: Outgoing terrestrial infrared trapped (warming) about 30 W/m^2, and solar radiation reflected back to space (cooling) nearly 50 W/m^2. The net cloud effect (cooling) is roughly 20 W/m^2 (3).

Earth's present reflectivity or albedo (whiteness) is near 0.3. This means that about 30 % or slightly over 100 W/m^2 of the sun's incoming radiation is reflected back to space, while roughly 240 W/m^2 or about 70 % is absorbed (3). Clouds cause almost half of Earth's current albedo, and perhaps 20 % of the natural greenhouse effect. Quantities involving clouds are hard to measure and may vary by a few W/m^2.

Globally averaged, the surface constantly gains radiative energy, whereas the atmosphere scores a loss. Sending up about 390 W/m^2, the surface absorbs roughly 170 W/m^2 solar radiation and over 300 W/m^2 infrared back radiation from greenhouse gases and clouds. The atmosphere, clouds included, radiates both up- and downward, altogether over 500 W/m^2. It absorbs roughly 70 W/m^2 solar radiation and 350 W/m^2 terrestrial infrared (3).

The surface's radiative heating and the atmosphere's radiative cooling are balanced by convection and by evaporation followed by condensation. When evaporating, water takes up latent heat; when water vapour condenses, as happens in cloud formation, latent heat is released to the atmosphere. The Greenhouse effect is visualised in Figure A-2.

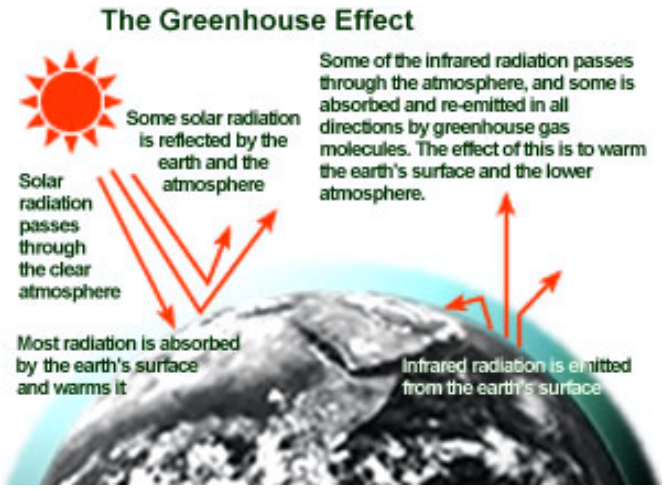

Figure A-2: The greenhouse effect, from (3).

The long-term balance of energy of the Earth and its atmosphere controls the climate. Incoming radiation from the sun, mainly in the form of visible light, is absorbed at the Earth's surface and in the atmosphere above. On average, absorbed radiation is balanced by the amount of energy returned to space in the form of infrared "heat" radiation. Greenhouse gases such as water vapour and carbon dioxide, as well as clouds and small particles (called aerosols), trap some heat in the lower part of the Earth's atmosphere. If there were no natural greenhouse effect, the average surface temperature would be about 34° colder than it is today (3).

Winds and ocean currents redistribute heat over the surface of the Earth. The evaporation of surface water and its subsequent condensation and precipitation in the atmosphere redistribute heat between the Earth's surface and the atmosphere, and between different parts of the atmosphere. An vertical representation of the atmosphere is shown in Figure A-3.

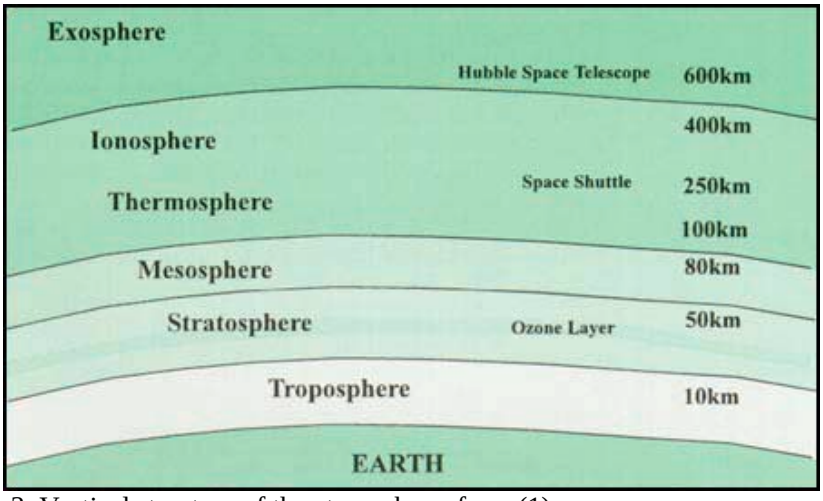

Figure A-3: Vertical structure of the atmosphere, from (1).

A1.2 Human contribution to greenhouse effect

Humanity is altering the energy balance of our planet by adding gases that absorb infrared radiation to the atmosphere, and thereby strengthening the greenhouse effect (4). The chief "greenhouse gases" are CO_2, methane, and nitrous oxide. Whenever oil, coal, gas, or wood are burned, carbon dioxide is released into the atmosphere. Approximately half of the CO_2 that is released is soon absorbed by the oceans or by increased plant photosynthesis. The other half remains in the atmosphere for many decades. As a result, the atmospheric concentration of CO_2 is increasing. The average concentration of carbon dioxide has increased from around 275 parts per million before the industrial revolution, to 315 ppm when precise monitoring stations were set up in 1958, to 361 ppm in 1996. This change has increased the amount of energy striking the Earth's surface by about 1.5 watts for every square meter of the Earth's surface. This increased energy is equal to about 1 percent of the energy in the sunlight that reaches the Earth's surface.

About two thirds of the current emissions of methane into the atmosphere result from cattle farming, rice paddies, landfills, coal mining, oil and gas production, and several other human activities. The other third comes from natural sources, particularly wetlands and termites. The total greenhouse effect from methane has increased by about 0.5 watts (0.3%) the energy striking each square meter of the Earth's surface. Several other gases collectively may have as much of a greenhouse effect as methane. Nitrous oxide (also known as "laughing gas") is released by the use of nitrogen fertilisers, the burning of wood, and some industrial processes. Higher levels of ozone, an urban pollutant, also add to the greenhouse effect. (The loss of ozone in the upper atmosphere tends to reduce the greenhouse effect.) Other gases with a greenhouse effect include methyl chloroform, carbon tetrachloride, and numerous halocarbons.

Humanity is also increasing the extent to which the atmosphere and the surface of the Earth reflect light back into space, which tends to cool the Earth. Changes in land use can change the reflectivity of the Earth's surface; tropical deforestation appears to be the most important change, but has only reduced the amount of sunlight absorbed by about 0.1 watt per square meter (5).

Changes in the reflectivity of the atmosphere, however, appear to have an impact that could be as great as the impact of carbon dioxide, albeit in the opposite direction. Most importantly, society is adding very fine particles and droplets known as aerosols. The most important aerosols are sulphates. Power plants that burn coal, as well as copper, lead, and zinc smelters, release sulphur dioxide, which reacts with water vapour in the atmosphere to form sulphates. Sulphates currently reflect enough light back into space to reduce the amount of energy striking the Earth's surface by somewhere between 0.5 and 1.5 watts per square meter. Unlike CO_2, methane, and other greenhouse gases, which remain in the atmosphere for decades or longer, most of the sulphates are removed by precipitation within a few weeks of being emitted. As a result, sulphates tend to be concentrated in the areas immediately downwind of major industrial areas.

A1.3 Argument used to explain why human-made greenhouse gases matter when water vapour is the most potent greenhouse gas

The Earth's surface temperature would be about 34 °C colder than it is now if it were not for the natural heat trapping effect of greenhouse gases like carbon dioxide, methane, nitrous oxide, and water vapour (3). Indeed, water vapour is the most abundant and important of these naturally occurring greenhouse gases. In addition to its direct effect as a greenhouse gas, clouds formed from atmospheric water vapour also affect the heat balance of the Earth by reflecting sunlight (a cooling effect), and trapping infrared radiation (a heating effect) (6), (7).

However, just because water vapour is the most important gas in creating the natural greenhouse effect does not mean that human-made greenhouse gases are unimportant. Over the past ten thousand years, the amounts of the various greenhouse gases in the Earth's atmosphere remained relatively stable until a few centuries ago, when the concentrations of many of these gases began to increase due to industrialisation, increasing demand for energy, rising population, and changing land use and human settlement patterns. Accumulations of most of the human-made greenhouse gases are expected to continue to increase, so that, over the next 50 to 100 years, without control measures, they will produce a heat-trapping effect equivalent to more than a doubling of the pre-industrial carbon dioxide level.

Increasing amounts of human-made greenhouse gases would lead to an increase in the globally averaged surface temperature. However, as the temperature increases, other aspects of the climate will alter, including the amount of water vapour in the atmosphere. While human activities do not directly add significant amounts of water vapour to the atmosphere, warmer air contains more water vapour. Since water vapour is itself a greenhouse gas, global warming will be further enhanced by the increased amounts of water vapour. This sort of indirect effect is called a positive feedback.

It has been suggested that as greenhouse gases accumulate, the atmospheric events that generate cumulus clouds in tropical areas would cause a drying rather than moistening of the upper layers of the troposphere (the lowest region of the atmosphere) (1). However, observations of the current atmosphere provide evidence for the conclusion that on a global scale, a warmed atmosphere will moisten and this will enhance greenhouse warming.

Clouds are another important factor in determining climate. The increased levels of water vapour in the atmosphere, as well as changes in temperatures and winds, will also cause changes in clouds that will alter the amount of energy from the sun that is absorbed and reflected by the Earth. At some locations the reflection will be enhancing and at others diminishing the warming due to greenhouse gases. Clouds closer to the earth's surface reflect sunlight, producing an overall cooling effect. Clouds higher up in the atmosphere however have the effect of trapping heat and warming the planet. The response of clouds to global warming is a major uncertainty in determining the magnitude and distribution of climate change.

A1.4 Gases and particles which contribute to the greenhouse effect

Natural events cause changes in climate (1). For example, large volcanic eruptions put tiny particles in the atmosphere that block sunlight, resulting in a surface cooling of a few years' duration. Variations in ocean currents change the distribution of heat and precipitation. El Niño events (periodic warming of the central and eastern tropical Pacific Ocean) typically last one to two years and change weather patterns around the world, causing heavy rains in some places and droughts in others. Over longer time spans, tens or hundreds of thousands of years, natural changes in the geographical distribution of energy received from the sun and the amounts of greenhouse gases and dust in the atmosphere have caused the climate to shift from ice ages to relatively warmer periods, such as the one we are currently experiencing.

A comprehensive assessment by the IPCC of the scientific evidence suggests that human activities are contributing to climate change, and that there has been a discernible human influence on global climate. Studies that aim to identify human influences on climate attempt to separate a human-caused climate-change factor (the signal) from the background noise of natural climate variability. Such investigations usually consist of two parts: detection of an unusual change, and attribution of all or part of that change to a particular cause or causes.

The concepts of detection and attribution may be understood in terms of a simple medical analogy. Measurement of a human temperature of 40 °C detects the presence of some abnormal condition or symptom, but does not in itself give the cause of the symptom. To attribute the symptom to an underlying cause often requires additional and more complex tests, such as chemical analyses of blood and urine, or even x-rays and CAT scans. Early work on climate-change detection examined changes in the globally averaged surface temperature of the Earth over the last century. Most studies of this type concluded that the observed increase of roughly 0.5 °C was larger than would be expected as a result of natural climate variability alone (1). Observed globally averaged temperature changes have also been analysed away from the Earth's surface. The observations used come from conventional weather observing instruments (radiosondes) and from satellites. As expected, because of the different factors affecting the variability of and persistence of temperatures at different altitudes, there are noticeable differences between short-term trends at the surface and those at higher altitudes. The record of temperatures away from the Earth's surface, which spans only the past 40 years compared with the much longer surface record, is too short for globally averaged values to provide any definitive information about the extent of human influences.

The further step of attributing some part of observed temperature changes to human influences makes use of climate models, which have been employed to estimate the climatic effects of a range of human-induced and natural factors. The human factors include recent changes in the atmospheric concentrations of both greenhouse gases and sulphate particles (called "aerosols") (1).

The atmospheric amounts of many greenhouse gases are increasing, especially that of carbon dioxide, which has increased by 30% over the last 200 years, primarily as a result of changes in land use (e.g., deforestation) and of burning coal, oil, and natural gas (e.g., in automobiles, industry, and electricity generation) (1). Carbon dioxide (CO_2) contributes to

more than 50 per cent of the increased greenhouse effect. If current trends in emissions were to continue, the amount of carbon dioxide in the atmosphere would double during the twenty-first century, with further increases thereafter. The amounts of several other greenhouse gases would increase substantially as well. The atmospheric CO_2 concentration the last 1000 years is shown in Figure A-4.

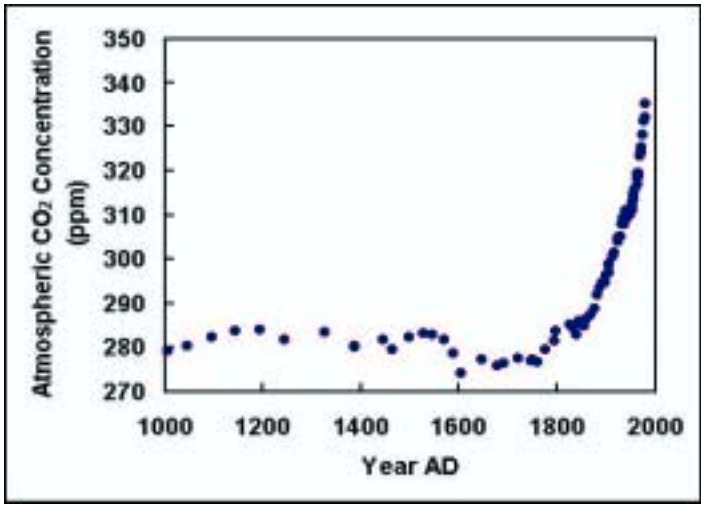

Figure A-4: Atmospheric CO_2 concentrations the last 1000 years, from (1).

The burning of coal, oil, and natural gas, as well as deforestation and various agricultural and industrial practices, are altering the composition of the atmosphere and contributing to climate change. These human activities have led to increased atmospheric concentrations of a number of greenhouse gases, including carbon dioxide, methane, nitrous oxide, chlorofluorocarbons, and ozone in the lower part of the atmosphere. The relative importance of these gases is shown in Figure A-5.

Carbon dioxide is produced when coal, oil, and natural gas (fossil fuels) are burned to produce energy used for transportation, manufacturing, heating, cooling, electricity generation, and other applications. The use of fossil fuel currently accounts for 80 to 85% of the carbon dioxide being added to the atmosphere.

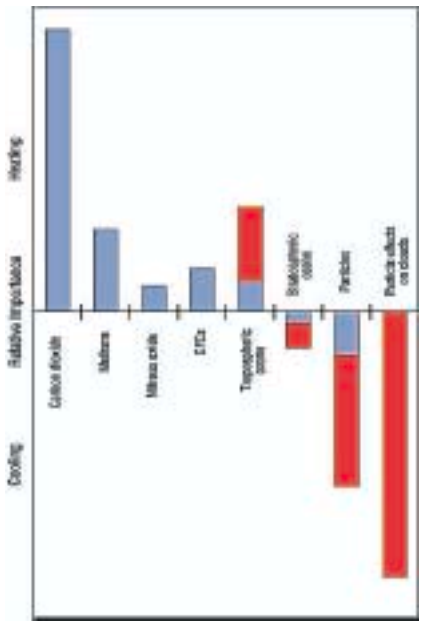

Figure A-5: Relative importance of the various greenhouse gases and small particles currently in the atmosphere from (1).

The bars extending above the horizontal line indicate a warming effect. Bars extending below the horizontal line indicate a cooling effect. The range of possible effects for these gases is indicated by the dark gray bars, *i.e.*, the effect is in the range of one end of the dark gray bar to the other. The impacts of tropospheric ozone, stratospheric ozone, and particles are quite uncertain.

Land-use changes, e.g., clearing land for logging, ranching, and agriculture, also lead to carbon dioxide emissions. Vegetation contains carbon that is released as carbon dioxide when the vegetation decays or burns. Normally, lost vegetation would be replaced by re-growth with little or no net emission of carbon dioxide. However, over the past several hundred years, deforestation and other land use changes in many countries have contributed substantially to atmospheric carbon dioxide increases. Although deforestation is still occurring in some parts of the Northern Hemisphere, on the whole, re-growth of vegetation in the north appears to be taking some carbon dioxide out of the atmosphere. Most of the net carbon dioxide emissions from deforestation are currently occurring in tropical regions. Land use changes are responsible for 15 to 20% of current carbon dioxide emissions.

Methane (natural gas) is the second most important of the greenhouse gases resulting from human activities. It is produced by rice cultivation, cattle and sheep ranching, and by decaying material in landfills. Methane is also emitted during coal mining and oil drilling, and by leaky gas pipelines. Human activities have increased the concentration of methane in the atmosphere by about 145% above what would be present naturally (3).

Nitrous oxide is produced by various agricultural and industrial practices. Human activities have increased the concentration of nitrous oxide in the atmosphere by about 15% above what would be present naturally (1).

Chlorofluorocarbons (CFCs) have been used in refrigeration, air conditioning, and as solvents. However, the production of these gases is being eliminated under existing international agreements because they deplete the stratospheric ozone layer. Other fluorocarbons that are also greenhouse gases are being used as substitutes for CFCs in some applications, for example in refrigeration and air conditioning. Although currently very small, their contributions to climate change are expected to rise (1).

Global Warming Potential (GWP) describes the relative importance of different greenhouse gases in comparison to CO_2. The GWP is described as CO_2-equivalents.

The present emission of CO_2 is six metric giga tonnes per year (1). Due to the decrease of emissions of fluorine-containing gases, the total emission of CO_2-equivalencies for example in Norway has remained rather stable, and has been fluctuating between 50 and 55 million tonnes per year since 1989 (see Figure A-6).

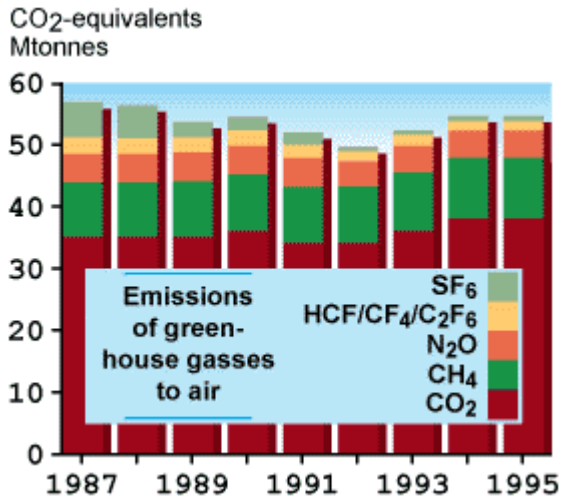

Figure A-6: The Norwegian emission of some greenhouse gases represented as CO_2-equivalencies, from (7).

Ozone in the troposphere (see Fig. A-3), *i.e.* in the lower part of the atmosphere, is another important greenhouse gas resulting from industrial activities (1). It is created naturally and also by reactions in the atmosphere involving gases resulting from human activities, including nitrogen oxides from motor vehicles and power plants. Based on current data, tropospheric ozone is an important contributor to the enhanced greenhouse effect. However, in part because ozone is also produced naturally, and because of its relatively short atmospheric lifetime, the magnitude of this contribution is uncertain.

Contrary to popular perception, the Antarctic ozone hole does not cause global warming. Instead, the global depletion of stratospheric ozone caused by CFCs and other gases have resulted in a small cooling effect (3).

Human activities, such as the burning of fossil fuels and changes in land use, have increased the abundance of small particles in the atmosphere. These particles can change the amount of energy that is absorbed and reflected by the atmosphere. They are also believed to modify the properties of clouds, changing the amount of energy that they absorb and reflect. Intensive studies of the climatic effects of these particles began only recently and the overall effect is uncertain. It is likely that the net effect of these small particles is to cool the climate and to partially offset the warming of increasing concentrations of greenhouse gases (1).

The accumulation of greenhouse gases in the atmosphere due to human activities may change the climate by enhancing the natural greenhouse effect, leading to an increase in the Earth's average surface temperature. This warming may be partially offset in certain regions where air pollution leads to high concentrations of small particles in the atmosphere that block sunlight (1).

A1.5 The sun's contribution to global warming

Global warming may not be caused by humanity's fossil fuel emissions, but could be due to changes in the Sun (8), (2). Research suggests that the magnetic flux from the Sun more than doubled this century. As solar magnetism is closely linked with sunspot activity and the strength of sunlight reaching Earth, the increase could have produced warming in the global climate.

The evidence for an increasingly energetic Sun comes from a new analysis of the magnetic field between the planets, carried out by scientists at the Rutherford Appleton Laboratory, near Oxford, UK (8). This magnetic field is caused by the Solar Wind, a stream of particles given off by the Sun which fills the solar system. The Solar Wind brings the Sun's magnetic field into space. Since 1964 the interplanetary magnetic field has increased in strength by 40%. Evidence from before the space age suggests that the magnetic field at present is 2.3 times stronger than it was in 1901 (8).

ICCP (5) does not doubt that the increased magnetic field results from a more energetic Sun. Their problem is that the effect of these increases on the Earth is unknown, but it might effect the global warming. The Sun's increased activity may have caused the Earth's global temperature to rise and in turn warmed the oceans. Warmer oceans absorb less carbon dioxide from the atmosphere. So a warmer Earth has more of the so-called greenhouse gases (9). Humanity's burning of fossil fuels may therefore not be the cause of global warming.

Measurements of the magnetic field are not the only evidence for the Sun's variable influence on the Earth. The planet went through a "little ice age" during the 17th Century, at a time when very few sunspots appeared on the surface of the Sun. The so-called "medieval maximum" was a period of warmer than average global weather in the 12th Century. Astronomers believe that the Sun was slightly brighter at that time (11).

According to an article in Science magazine (11) variations in solar output over the last century could have been large enough to affect some long-term trends. Global temperature rose sharply from about 1900 to 1940, and then levelled off until the 1970s. Then it began another warming spell, which has accelerated in this decade. In order to explain their results using solar effects alone, the authors found that their model had to be about six times more sensitive to changes in solar input than they thought realistic. The conclusion was that solar output alone is insufficient to explain the behaviour of the observed temperature data. But by contrast, they found that combining solar input with changes in greenhouse gas levels produced a more credible result. Their results imply that both anthropogenic (human-induced) activities and solar forcing have significantly affected global climate. The results "strengthen the confidence that there has been a discernible human influence on climate".

The amount and distribution of energy from the sun varies according to an 11 year sunspot cycle (12), (13) that can be traced in climate proxy records, but the magnitude of the effect is very small. The radiation difference in this cycle is about 1-2 W/m^2 at the outer atmosphere (12), which is only about 0.1 % of the total solar constant of 1367 W/m^2. The direct temperature effect of this heat variation has been estimated as only a few tenths of a degree (12).

Christensen *et al.* claim however that enhanced activity at the sun and the effect of cosmic radiation are the main reasons for the temperature increase on Earth (14). The variable activity of the sun will influence the development and amount of clouds. Christensen *et al.* claims that there is a correlation between the cosmic radiation from the sun and the cloud cowers on Earth. The temperature variations the last decades also seem to correlate with the activity of the sun. Christensen *et al.* concluded in 1998 that the total cloud-cower decreases with 3 percent from minimum to maximum sun activity, and in correlation with the decrease in cosmic radiation. In 1998 there were a lot of active sun storms created by magnetic sun spots, but they claim that the activity at the sun will decrease significantly the next century and actually cause a cooling effect on Earth. Christensen and co-workers think IPCC has underestimated how the sun affects the climate. Others (15) claim that an estimate indicates that the warming effect of solar variations since pre-industrial times is only about one-tenth as large as the warming effect of the greenhouse gas build up.

A1.6 The carbon cycle

The concern is not only to find out how the climate responds to a given concentration of a greenhouse gas, but also to try to predict what that concentration will be. The carbon cycle is quite complex, and it is no easy task to find out where all the CO_2 will go. Carbon is exchanged between many different "reservoirs", and it is important to find out how these different storage sites for carbon will react to a global warming.

In the short term, most of the human released carbon will end up in the atmosphere and, therefore, increase the greenhouse effect rapidly. (This is why the graphs from IPCC (5) show such steep curves for the CO_2 concentrations the next hundred years.) In the long

run, however, the ocean has an enormous potential for CO_2 uptake. Carbonate dissolved in sea-water and in sediments respectively results in the uptake of CO_2 through the following reactions (12), (16)

$$CO_{2(g)} \Leftrightarrow CO_{2(aq)} \quad [A\text{-}1]$$

$$H_2O + CO_{2(aq)} + CO^{2-}_{3(aq)} \rightarrow 2HCO^{-}_{3(aq)} \quad [A\text{-}2]$$

The source of $CO^{2-}_{3(aq)}$ is $CaCO_3$, $MgCO_3$ (and other carbonates) which mainly come from the sediments in the sea.

$$CaCO_{3(s)} \Leftrightarrow Ca^{2+}_{(aq)} + CO^{2-}_{3(aq)} \quad [A\text{-}3]$$

$$MgCO_{3(s)} \Leftrightarrow Mg^{2+}_{(aq)} + CO^{2-}_{3(aq)} \quad [A\text{-}4]$$

which have a finite solubility in sea water. The two following reactions help to balance the concentration of carbonate with water:

$$HCO^{-}_{3(aq)} + H_2O \Leftrightarrow H_3O^{+}_{(aq)} + CO^{2-}_{3(aq)} \quad [A\text{-}5]$$

$$H_2O \Leftrightarrow H_3O^{+}_{(aq)} + OH^{-}_{(aq)} \quad [A\text{-}6]$$

The sediments contain enough carbonate to take up all the CO_2 released to the atmosphere through human activity (17). The oceans contain about 50 times more carbon than the atmosphere. The oceans may take up to nearly 6 times more CO_2 at equilibrium and the photosynthesis of land biota may increase to 18 giga tons/year before the concentration of carbon in the oceans is doubled (three times the present emission) (17). This will however be a slow process, and the availability of the sedimented carbonate will influence the rate of the CO_2 uptake.

The largest amounts of energy coming in from the sun strikes the equatorial region of the earth (1). Only a modest amount strikes the area around the poles. About half the energy carried from the equator toward the poles is carried by the atmosphere. The remainder is carried by currents flowing in the oceans (1).

The *thermohaline circulation* is, put very simply, an ocean circulation loop where surface water sinks, follows a path deeper in the sea, and then returns to the surface streams again somewhere else. Dense, cold, salt-laden water sinks in the North Atlantic. This drives the "Ocean Conveyor Belt" (see Fig. A-7) that carries it under the Atlantic and Indian Oceans to resurface in the northern Pacific. The North Atlantic remains more salty because the general circulation of the atmosphere carries fresh water (as vapour) from the North Atlantic to fall as rain in the North Pacific (see Mackenzie (12) for further details). These underwater streams are enormous, and carry large quanta of $CO_{2(aq)}$ from the surface to the colder depths of the sea, which have a greater potential as a CO_2 reservoir. The CO_2 flux

from the atmosphere to the sea depends on the magnitude of the concentration gradient from the sea level down to the deep of the ocean. However, how much the oceanic circulation affects the CO_2 uptake is still unknown.

The concentration of CO_2 in the oceans is in steady state with the air above the surface, which is greatly influenced by the temperature and the circulation patterns in the sea. The atmosphere in contact with warm ocean-water contains more CO_2 than if it is in contact with cold ocean-water. This fundamental mechanism drives the adsorption close to the poles, and the desorption to the tropics. The question is, however, how much an increased heating of the sea contributes to a release of CO_2 from the sea with respect to CO_2 concentration in air . At present, the oceans are still mostly on a pre-industrial level (9).

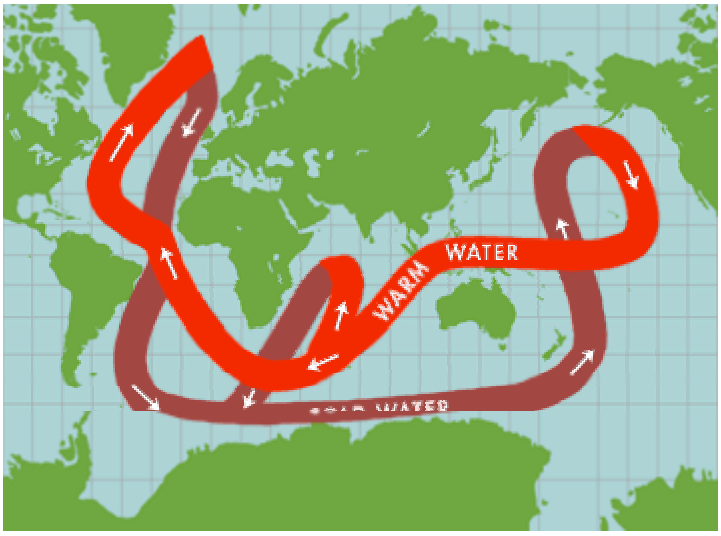

Figure A-7: The “conveyor belt” which shows the general flow pattern in the ocean (18).

Evidence for abrupt climate changes on millennial and shorter time scales is widespread in marine and terrestrial climate records (19). Rapid reorganisation of ocean circulation is considered to exert some control over these changes, as are shifts in the concentration of atmospheric greenhouse gases. Sudden changes in the Thermohaline circulation probably have profound consequences for the temperature distribution, at least in the northern and tropical Atlantic Ocean.

Because of all the natural sinks (e.g. trees, polar ice and deep-sea sediments) for CO_2, the released CO_2 does not lead to an irreversible accumulation, but has a definite life-time. A *half*-life time of 38 years has been suggested (20), which reduces the IPCC predictions for future CO_2 concentrations with as much as an order of magnitude. The IPCC models have been criticised from many scientists the last years, and some predicts that the 60% reduction demand will only lead to a temperature reduction of 0.005 degrees (21)!

The Artic ice covers, an area roughly the size of the United States, has a profound effect on heat exchange. Open water absorbs as much as 100 times more solar energy than ice (1). The amounts of ice also affect density, salinity and flow of seawater in much of the

Atlantic and elsewhere. In theory, a substantial change in ice extent could prompt severe alterations in ocean circulation, and hence in weather.

A2 How the greenhouse effect influences the living planet

The greenhouse effect may change the ecosystems and production patterns. It may be possible for global agricultural production to keep pace with increasing demand over the next 50-100 years if adequate adaptations are made, but there are likely to be difficulties in some regions. This conclusion takes into account the beneficial effects of carbon dioxide fertilisation, *i.e.*, given sufficient water and nutrients, plant growth will be enhanced by an increased concentration of carbon dioxide in the atmosphere. Changes in the spread and abundance of agricultural pests and the effects of climate variability were not reflected in this assessment. Regional changes in crop yields and productivity are expected to occur in response to climate change. There is likely to be an increased risk of famine, particularly in subtropical and tropical semi-arid and arid locations (1).

Climatic changes affect wind patterns and precipitation. Some areas are expected to receive more rain while other areas will become drier. Climate change is also likely to affect human infrastructure, including transportation, energy demand, human settlements (especially in developing countries), the property insurance industry, and tourism.

The maximum warming is expected to occur in the Arctic in winter. Night-time temperatures are expected to increase more than daytime temperatures. In general, there will probably be an increase in the number of very hot days at mid-latitude locations in summer, such as in most of North America, Europe, and parts of South America, with a decrease of very cold days in the same locations in winter.

Extreme events such as heavy rains and droughts are the most destructive forms of weather, and the frequency and duration of these events are likely to increase as the climate continues to change. Increases in the global averages of both evaporation and precipitation are expected. In winter at mid-latitudes, higher surface temperatures are expected to cause an increased portion of the precipitation to fall in the form of rain rather than snow. This is likely to increase both wintertime soil moisture and runoff, leaving less runoff for summer. In spring, faster snowmelt is likely to aggravate flooding. In the summer, increased heating will lead to increased evaporation, which could decrease the availability of soil moisture needed both for natural vegetation and agriculture in many places, and increase the probability of severe drought. Droughts and floods occur naturally around the world, for example in association with El Niño events, but are likely to become more severe, causing water management to become an even more critical problem in the future (1), (3).

The range of estimated warming of 1 to 3.5°C by the year 2100 (1) arises from uncertainties about the response of climate to the build-up of greenhouse gases and particles, as well as the total amount of future emissions of these gases. Factors such as estimates of human population growth, land use changes, life styles, and energy choices yield a range of plausible greenhouse gas emissions. For example, concerted efforts to reduce emissions of greenhouse gases would lead to a significantly lower projected temperature rise.

Scientific modelling produced has depicted a series of scare scenarios that *might* result from global warming:

- malaria and dengue fever could reach epidemic levels and spread farther from the equator
- Range of arable land expands south and north
- Soil drier due to higher evaporation rates, and deserts expand
- Rising waters (15 to 95 cm), the result from melting polar ice caps and water expansion from increasing warmth.
- Cloud cover increases and the circular flow of water will accelerate
- Hurricanes range farther north, south on warmer water, and can occur more frequently
- Levels of the greenhouse gas methane may increase
- Range of insects likely to expand
- Habitats for some animals shrink
- Increased CO_2 aids some plant growth

A3 The pre-historical climate

According to Mackenzie (12), the climate has changed considerably the last 180 millions of years. Conditions have apparently been mostly warmer than at the present, especially in the period before 10 millions years BC. Paleclimatic information (12) have shown that the Earth's climate has undergone many rapid changes in the past. Especially the last glacial period was dominated by large and abrupt changes. The Dansgaard-Oeschger cycles and the Heinrich ice rafting events are the most prominent features where the cycles of gradual cooling ended by very rapid warming. Temperature changes of the order of 10 degrees in as little as fifty years may have occurred. Corresponding CO_2 concentrations changed very little from the "Medieval Warm Period" to the "Little Ice Age", demonstrating that dramatic air temperature changes can occur without any change in atmospheric CO_2 (10).

The Holocene epoch (*i.e.* the last 10.000 years) has been extraordinary stable compared to earlier times (12). In the Greenland ice-cores(10), (22) it totally stands out from the other periods given data for in the 3030 meter long ice core. In other words, the climate in pre-historical times seems to have changed more rapidly than mankind has experienced the last centuries.

A4 The future climate

A4.1 Designing climate models to predict the future

Predictions of climate change are calculated by means of computer models that mathematically simulate the interactions of the land, sea, and air, which together determine the Earth's climate (1). The confidence in these models rests largely on their basis in accepted physical laws, their ability to describe many aspects of current climate accurately, and their skill at reproducing some of the important features of past climates.

Climate models are based on a wealth of scientific observations and well established laws of physics, including the laws of gravity and fluid motion, and the conservation of energy, momentum, mass, and water. It is this reliance on basic physical laws that lends high confidence to the prediction that a build-up of greenhouse gases will eventually lead to a significant alteration in the Earth's climate (1), (5).

Climate models have an ability to reproduce many of the observed features of the atmosphere and ocean (5). For the purposes of predicting the behaviour of the atmosphere for only a few days ahead, an atmosphere-only model, with no simulation of the ocean, can be used. This is the method employed in making short-term weather forecasts, whose relative accuracy demonstrates the ability of this sort of model to reproduce some of the important details of the atmosphere's behaviour.

While reliable weather forecasts can only be made for periods up to ten days, predictability for greater lengths of time can be obtained for averages of weather, *i.e.*, the climate. For example, with regard to longer periods (several years or more), climate models in which both the oceans and the atmosphere are represented, are able to simulate the main features of current climate and its variability, including the seasonal cycle of temperature, the formation and decay of the major monsoons, the seasonal shift of the major rain belts and storm tracks, the average daily temperature cycle, and the variations in outgoing radiation at high elevations in the atmosphere as measured by satellites. Similarly, climate models have reproduced many of the large-scale features observed in the ocean circulation (1).

It is possible for a model to simulate current climate, well but still fail in its prediction of climate change. So another test of models is to compare their simulations of earlier climates to historical data, including the climate of the past century. These efforts have been hampered by our imprecise knowledge of a variety of factors, including how humans have changed the amounts of small particles in the atmosphere and variations in the energy output of the sun (1).

Nevertheless, using estimates of some of these factors, climate models can reproduce many changes observed over the last century, including the global mean surface warming of 0.3 to 0.6 °C, the reduction in temperature differences between day and night, the cooling in the atmosphere above about 14 km, the increases in precipitation at high latitudes, the intensification of precipitation events in some continental areas, and a rise in sea level. Moreover, a climate model has correctly predicted broad features of the globally averaged surface cooling and subsequent recovery associated with the eruption of Mt. Pinatubo in 1991 (1).

Climate models can also be used in attempts to reproduce the main features of prehistoric climates, but this effort has been limited by the scarcity and the indirect nature of the evidence available from sediment cores, tree rings, preserved pollen, and ice core data used to infer earlier climates. Even so, the models have reproduced some of the general features of reconstructed past climates, such as the enhanced North African monsoon 6000 to 9000 years ago, and the approximate level of cooling during the last ice age.

A4.2 The validity of models predicting future climate changes

The major weakness of climate models is their reliance on approximations of some aspects of climate (1). It takes too much computer time, or is simply beyond the capacity of even supercomputers, to represent some of the key smaller-scale processes that affect climate. Even if adequate computers were available, scientists' understanding of the detailed physics of such processes is limited. So, some aspects of climate are approximated, based on a combination of physical laws, laboratory experiments, and direct observations of climate. For example, it is not possible to represent the details of the formation and dissipation of clouds. So, approximations are used. The approximation of cloud behaviour is a major source of uncertainty in climate models (9), (21).

In summary, the fact that models are based upon the known physical laws of nature and can reproduce many features of the current climate and some general aspects of past climates gives us increasing confidence in their reliability for projecting many large-scale features of future climate. However, there remains substantial uncertainty in the exact magnitude of projected globally averaged temperature rise caused by human activity, due to shortcomings in the current climate models, particularly in their representation of clouds. Furthermore, scientists have little confidence in the climate changes they project at the local level. Other uncertainties, not arising from specific limitations in the climate models, such as estimates of the rate of future greenhouse gas emissions, also restrict the ability to predict precisely how the climate will change in the future (1).

The agreements between the patterns of change predicted by models and those actually observed are due to similarities at large spatial scales, such as contrasts between the temperature changes in the northern and southern hemispheres or between different levels of the atmosphere (21). It is at these large scales that scientists have most confidence in model performance. More importantly, many of the results of these studies agree with our physical understanding of the climate system, and do not depend solely on numerical models or statistical techniques.

There are still uncertainties in these detection and attribution studies. These are due primarily to our imperfect knowledge of the true climate-change signal due to human activities, to our incomplete understanding of the background noise of natural climatic variability against which this signal must be detected, and to inadequacies in the observational record. Such uncertainties make it difficult to determine the exact size of the human contribution to climate change. Nevertheless, the most recent assessment of the science suggests that human activities have led to a discernible influence on global climate and that these activities will have an increasing influence on future climate.

Four lines of evidence have been claimed to prove that the recent build-up of carbon dioxide arises largely from human activities (1).

The nuclei of carbon atoms in carbon dioxide emitted by burning coal, oil, and natural gas (fossil fuels) differ in their characteristics from the nuclei of carbon atoms in carbon dioxide emitted under natural conditions. Coal, oil, and natural gas were formed deep underground tens of millions of years ago, and the fraction of their nuclei that were once radioactive has long ago changed to non- radioactive carbon. But the carbon dioxide emitted from natural sources on the Earth's surface retains a measurable radioactive

portion. As carbon dioxide has been emitted through fossil fuel combustion, the radioactive fraction of carbon in the atmosphere has decreased. Forty years ago scientists provided the first direct evidence that combustion of fossil fuels was causing a buildup of carbon dioxide and thereby diluting radioactive carbon in the atmosphere by measuring the decreasing fraction of radioactive carbon-14 captured in tree rings, each year between 1800 and 1950.

Secondly, scientists began making precise measurements of the total amount of carbon dioxide in the atmosphere at Mauna Loa, Hawaii, and at the South Pole in the late 1950s. They have since expanded their observations to many other locations. Their data show convincingly that the levels of carbon dioxide have increased each year world-wide. Furthermore, these increases are consistent with other estimates of the rise of carbon dioxide emissions due to human activity over this period.

A third line of evidence has been added since 1980. Ice buried below the surface of the Greenland and Antarctic ice caps contains bubbles of air trapped when the ice originally formed. Drilling deep into the ice has retrieved these samples of fossil air, some of them over 200.000 years old. Measurements from the youngest and most shallow segments of the ice cores, which contain air from only a few decades ago, produce carbon dioxide concentrations nearly identical to those that were measured directly in the atmosphere at the time the ice formed. But the older parts of the cores show that carbon dioxide amounts were about 25% lower than today for the ten thousand years previous to the onset of industrialisation, and over that period changed little.

The last line of evidence comes from the geographic pattern of carbon dioxide measured in air. Observations show that there is slightly more carbon dioxide in the Northern Hemisphere than in the Southern Hemisphere. The difference arises because most of the human activities that produce carbon dioxide are in the north and it takes about a year for northern hemispheric emissions to circulate through the atmosphere and reach southern latitudes.

However, CO_2 is released to the atmosphere by a variety of sources, and over 95% percent of these emissions would occur even if human beings were not present on Earth (1). For example, the natural decay of organic material in forests and grasslands, such as dead trees, results in the release of about 220 billion tons of carbon dioxide every year. But these natural sources are nearly balanced by physical and biological processes, called natural sinks, which remove carbon dioxide from the atmosphere. For example, some of the CO_2 dissolves in seawater, which is removed by plants as they grow.

As a result of this natural balance, carbon dioxide levels in the atmosphere would have changed little if human activities had not added an amount every year. This addition, presently about 3% of annual natural emissions, is sufficient to exceed the balancing effect of sinks. As a result, carbon dioxide has gradually accumulated in the atmosphere, until at present, its concentration is 30% above pre- industrial levels (1).

Direct atmospheric measurements of other human-produced greenhouse gases have not been made in as many places or for as long a period as they have for carbon dioxide. However, existing data for these other gases do show increasing concentrations of methane, nitrous oxide, and chlorofluorocarbons over recent decades. In addition, ice core

data are available for methane and for nitrous oxide that demonstrate that the atmospheric concentrations of these gases began to increase in the past few centuries, after having been relatively constant for thousands of years. Chlorofluorocarbons are absent from deep ice cores because they have no natural sources and were not manufactured before 1930 (1).

Clouds reflects sunlight cooling the Earth, but they also trap heat warming the Earth (23). Different clouds do more of one or the other depending on how bright and how high in the sky they are. The cloud's brightness is depending on their type and size of particles, their water content and form (liquid/ice) (23) and the temperature inside the clouds. Clouds closer to Earth's surface reflect sunlight, producing an overall cooling effect. As earlier mentioned, clouds higher up in the atmosphere have the effect of trapping heat and warming the planet. Where the extra moisture in the atmosphere ends up - high or low - could determine how much of an impact of global warming has on the environment.

Soupy components of air pollutants lower the surface tension on tiny wetted aerosol particles. This could make the particles more likely to turn into cloud drops through condensation of water vapour on their surfaces (24). This could lead to a larger number of clouds drops of smaller size. The upshot is that the clouds become more efficient reflectors of sunlight and thereby tend to cool the Earth's surface. Uncertainty remains, however, about how clouds form and how they affect the climate.

A5 How the primary aluminium production contributes to the greenhouse effect

The global industrial sector accounts for approximately 47% of energy related carbon dioxide emissions, and significant quantities of additional greenhouse gases are released as industrial process gases (25). Industrial emissions of Greenhouse gases was in 1996 lower than they were in the mid-1970s in most industrialised countries, and while absolute levels have grown in newly industrialising (developing) countries, the rate of growth has slowed and CO_2 emission per unit of Gross Domestic Product has dropped in most cases (25).

A5.1 The traditional Hall-Héroult technology with carbon anodes

The primary reaction for aluminium production with traditional carbon anodes can be expressed as

$$2Al_2O_3 + 3C \rightarrow 4Al + 3CO_2 \qquad [A\text{-}7]$$

CO_2 is released as a process gas from the oxidation of the carbon anode during electrolysis. Carbon emissions from this source are approximately 0.45 kg of carbon per kg of aluminium, which would imply a total release of 8.2 MT C, or 0.15% of global fossil fuel carbon in 1991 (25). Small amounts of CO are also produced, but most of the CO from modern cells is burned to CO_2 in separate burners before leaving the stacks (26), and the CO emissions are, therefore, small.

As we can see from the reaction scheme, CO_2 is a *by-product* (waste) in the aluminium production. Approximately 1.7 tons of CO_2 is produced per tonne primary aluminium produced. In 1994 the annual world production of aluminium was about 19 million tonnes

per year, the total CO_2 emission from the aluminium producers was 35-40 million tonnes per year (26).

The second class of important greenhouse gases from the aluminium process is the perfluorocarbons which are released occasionally. When the amount of the feedstock of alumina (Al_2O_3) gets below a critical value, two new greenhouse gases are produced during the so-called *anode effect*, *i.e.* $CF_{4(g)}$

$$Na_3AlF_{6(l)} + \frac{3}{4}C_{(s)} \rightarrow Al_{(l)} + 3NaF_{(l)} + \frac{3}{4}CF_{4(g)} \quad [A\text{-}8]$$

and small amount of $C_2F_{6(g)}$ (only 5-15 percent of the amount of CF_4 formed (26))

$$Na_3AlF_{6(l)} + C_{(s)} \rightarrow Al_{(l)} + 3NaF_{(l)} + \frac{1}{2}C_2F_{6(g)} \quad [A\text{-}9]$$

The *anode effect* is caused by inadequate process control, but continuous development of the technology has reduced the average anode effect frequency from 3 to 1 per day per cell (26). The lowest average anode effect frequency reported for a pot-room is below 0.1 per cell per day (26).

Tetrafluoromethane ($CF_{4(g)}$) and hexafluoroethane ($C_2F_{6(g)}$) were previously considered innocuous, because they are non-toxic to humans, animals and plant life, and they do not affect the stratospheric ozone depletion. However, these perfluorocarbon gases are characterised as powerful greenhouse gases, and they may, therefore, contribute to global warming. They are not absorbed on the alumina particle surface, and therefore they cannot be collected in the present gas cleaning system (*i.e.* dry scrubbers with alumina absorbent collecting HF).

The concentrations of these two gases in the atmosphere are extremely small, about 0.07 ppb for $CF_{4(g)}$ and about one tenth of that for $C_2F_{6(g)}$. In comparison, the atmospheric concentration of CO_2 is about 5 million times higher. $CF_{4(g)}$ is an extremely stable (inert) gas, which strongly absorbs infrared radiation at 7.8 μm, and therefore is capable of influencing the greenhouse effect (27),(28),(29). No natural sources have been identified, and the major anthropogenic source appears to be the electrolytic smelting of alumina to produce aluminium. Measurements of CF_4 concentrations in the atmosphere are reviewed, and these are combined with aluminium production rates to provide an estimate of 1.3-3.6 kg of CF_4 emitted per ton of aluminium produced for the period up to 1985 (27).

Aluminium production also requires large amounts of electrical energy, leading to the *total*[1] emission, of as much as 22 tons of carbon dioxide per ton of aluminium due to fossil fuel combustion in power plants. The present day contribution of hydroelectric power reduces this Figure to about 14 tons of carbon dioxide per ton of aluminium. An estimate of the CF_4 and CO_2 emitted in aluminium production during this same period (1900- 1985)

[1] Total emission also take into consideration the production of the raw materials like alumina (Al_2O_3) and carbon anodes, and the energy requirements of shipping the raw materials to the aluminium plants in the world.

indicates that the effect of CF_4 is about one-third of that of the CO_2 formed by aluminium production (27). However, the emission of fluorocarbons from modern aluminium electrolysis cells is much lower than previous estimates indicate, and this fact is considered when estimating potential long-term global warming effects of CF_4 and CO_2 from aluminium production (7).

Perfluorocarbons (PFCs), e.g. tetrafluoromethane (CF_4) and hexafluoroethane (C_2F_6), are greenhouse gases with a very high global warming potential in addition to an exceptionally long atmospheric lifetime. The range of estimates for perfluorocarbons vary from 0.6 to 2.5 kg per ton of aluminium for CF_4 and 0.06 to 0.25 for C_2F_6 (25). CF_4 can exist in the atmosphere for more than 10000 years, and has a global heating factor (30) (CO_2 equivalent factor) of 5100 (26) compared to CO_2. C_2F_6 has a global heating factor of 10000 (26). CF_4 has been estimated to contribute to 1.7% of the global warming potential during the 1980s (25). Reduction of CO_2 equivalents is possible by reducing the frequency and the duration of the anode effects. Dolin (31) has described the international efforts to reduce perfluorocarbon gases.

Perfluorocarbons are primarily formed during aluminium production, and since Norway is a major aluminium producer it seemed likely that PFC emissions would also be high. However, the emissions per tonne of aluminium from Norwegian production plants (see Figure A-8) seem to be much smaller than those reported from other countries.

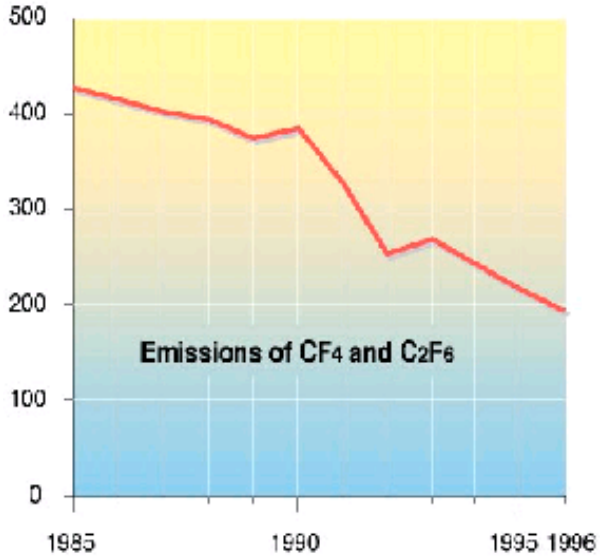

Figure A-8: Norwegian emissions of greenhouse gases, from (7).

On the basis of photoacoustic measurements carried out in 1992 by aluminium producers in Norway, emissions of PFCs in 1995 were calculated to be about 218 tonnes (27). Around 4% of the PFC emissions were estimated to be hexafluoroethane (C_2F_6), and the remainder was tetrafluoromethane (CF_4). From 1990 to 1995, emissions were reduced by 43%. This is explained by a reduction in emissions per produced unit from about 0.6 to 0.3 kg PFCs per tonne aluminium during the past 7-10 years (26). This is a result of improved process control and thereby reduced frequency of anode effects.

Carbon anodes are produced using petroleum coke, coal tar pitch and butts, which is materials from spent carbon anodes (32). These three ingredients are all by-products (waste products) of the petroleum industry, the coke-making industry and the aluminium industry, itself. According to Mannweiler and Keller (19) sulphur and vanadium levels in petroleum coke continuously increase, and inferior mechanical and physical properties of petroleum coke are observed. Pitch properties are changing too, and pitches with lower quinoline insoluble (see (32) for further details) content and higher melting points will come to the marked and will challenge the production of carbon anodes with consistent good quality.

A5.2 The new technology with inert anodes

The idea of using an inert anode is to replace the carbon anode with an inert anode material, and thereby eliminating the production of CO_2 as a by-product. Instead oxygen is produced according to the overall reaction:

$$2Al_2O_{3(l)} \rightarrow 4Al_{(l)} + 3O_{2(g)} \qquad [A\text{-}10]$$

It is, however, important to consider the total energy consumption in the two processes. By using electric power produced in coal-fired power plant, the total emission of CO_2 per tonne aluminium produced in the Hall-Héroult process is almost ten times (33) higher when hydroelectric power was used. If gas-fired power is used, the total emission of CO_2 is 4 times higher than if hydropower is used (see Table A-1). Lower energy consumption from cells with inert anodes, by decreasing the distance between the electrodes in the cells, is the main cause for a lower electric power consumption and therefore an overall smaller contribution to the CO_2 emission than for the existing Hall-Héroult cells (33).

Depending on the source from which electricity is drawn and the state of the art in molten salts, the primary energy consumption for the production of primary aluminium can vary by a factor of 3 (34). From 1960 to 2000 the energy-related CO_2 emissions vary by a factor of 5 from lignite power plants in 1960 to modern natural gas-combined cycle systems in 2000 (34). Since there is no *carbon* in an inert anode, neither will CF-gases be emitted from the electrolysis process.

Table A-1: Calculated specific CO_2 emissions from existing Hall-Héroult cells and possible future inert anode cells, and also from the corresponding electric energy production from three different types of power plants, from (26).

	Hall-Heroult cells:			Inert anode cells:		
CO_2 emmisions (t CO_2/t Al)	**Hydro power**	**Gas fired power**	**Coal fired power**	**Hydro power**	**Gas fired power**	**Coal fired power**
CO_2 from cells	1,7	1,7	1,7	0	0	0
CO_2 from electric power	0	6,2	15,4	0	4,8	12,0
Total CO_2 emissions	1,7	7,9	17,1	0	4,8	12,0

However, as Table A-1 indicates, the full environmental potential of inert anodes is not utilised except when electric energy consumed in the process comes from hydropower.

If the inert anode technology is met with success and is implemented, the aluminium industry will no longer need the by-products used to produce carbon anodes. What will then happen to these by-products is highly questionable, but they might be burned as fuel to generate electricity (and CO_2) with less efficiency than if it is used in an aluminium cell (35). If that happens, the argument that going to inert anodes saves CO_2 generation will be inherently specious (35).

A6 What humans can do to decrease the Greenhouse Effect

Climate change has the potential to alter many of the Earth's natural ecosystems over the next century. Yet, climate change is not a new influence on the biosphere, so why cannot ecosystems just adapt without significant effects on their form or productivity? There are three basic reasons (1).

First, the rate of global climate change is projected to be more rapid than ever to have occurred during the last 10000 years. Second, humans have altered the structure of many of the world's ecosystems. They have cut down forests, ploughed soils, used rangelands to graze their domesticated animals, introduced non-native species to many regions, intensively fished lakes, rivers and oceans, and constructed dams. These relatively recent changes in the structure of the world's ecosystems have made them less resilient to further changes. Third, pollution, as well as other indirect effects of the utilisation of natural resources, has also increased since the beginning of the industrial revolution. Consequently, it is likely that many ecosystems will not be able to adapt to the additional stress of climate change without losing some of the species they contain or the services they provide.

For millions of years, species have been shifting where they grow and reproduce in response to changing climate conditions. Over the next century, global warming could result in approximately one-third of the Earth's forested area undergoing major transitions in species composition. From the fossil record we have an indication of the maximum rate at which various plant species have migrated to more suitable areas; from 0.04 km/year for the slowest to 2 km/year for the fastest (1). However, the projected rate of surface temperature change in many parts of the world could require plant species to migrate at faster rates (1.5 to 5.5 km/year) (1). Thus, many species may not be able to move rapidly enough to prosper. These changes in vegetation and ecosystem structure may in turn give rise to additional releases of carbon into the atmosphere, further accelerating climate change.

Moreover, as the old vegetation dies in areas most affected by climate change, such as forests in northern latitudes, it is likely to be replaced by fast growing, often non-native species. These species commonly yield less timber, provide lower quality forage for domesticated animals, supply less food for wild animals, and furnish poorer habitat for many native animals. The prevalence of pest species, such as weeds, rats, and cockroaches, may also increase (1).

Humans actively and productively use and manipulate large portions of the land surface of the Earth, whether it will be for agriculture, housing, energy, or forestry. These practices have created a mosaic of different land uses and ecosystem types, resulting in fewer remaining large and contiguous areas of a single type of habitat than existed in the past. Therefore, it will often be difficult for plants and animals to move to a location with a more suitable climate even if a species was able to migrate quickly enough. This was not the case thousands of years ago, when ecosystems last experienced rapid climate change. Now, many of the world's ecosystems are essentially trapped on small islands, cut off from one another, only capable of travel over a limited and shrinking number of "bridges". As this increasingly occurs, more species are likely to be stranded in an environment in which they cannot survive and/or reproduce.

Further complicating the response of many of the Earth's terrestrial and aquatic ecosystems to climate change is the prevalence of stress from other disturbances associated with resource use. In the case of trees, for example, many species are already weakened by air pollution. Increased concentrations of carbon dioxide in the atmosphere will raise the photosynthetic capacity of many plants, but the net effect on ecosystem productivity is unclear, particularly when combined with higher air temperatures or where soil nutrients are limiting.

Among the ecosystems that are most likely to experience the most severe effects from climate change are those that are at higher latitudes, such as far northern (Boreal) forests or tundra. Also places where different habitat types converge, such as where grasslands meet forests, or forests give way to alpine vegetation, will be influenced. Coastal ecosystems are also at risk, particularly saltwater marshes, mangrove forests, coastal wetlands, coral reefs, and river deltas. Many of these ecosystems, already under stress from human activities, may be significantly altered or diminished in terms of their extent and productivity as a result of future climate change.

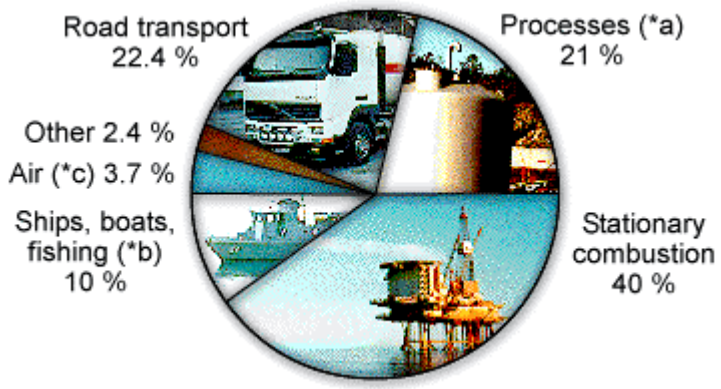

Figure A-9: Human-made CO_2-emission in Norway. *a: Emissions other than combustion, *b:International maritime transport excluded. *c: International flights excluded, from (7).

Human-made CO_2 emissions in Norway are shown in Figure A-9 as an example of where the emissions come from. Norway's provisional goal of stabilising CO_2-emissions at

1989-level (35.3 million tonnes) by the year 2000 will be difficult to reach, especially because of increased emissions from the petroleum sector. The more than 5 per cent increase during 1993-95 is mainly due to increased industry and petroleum production. In 1998 the air traffic alone contributed with almost 3 percent of the global emission of the greenhouse gases. It is now (1999) estimated (7) that the CO_2 goal will be exceeded by 19 percent.

A6.1 The Kyoto Protocol

As early as in 1896 the Swedish scientist, and Nobel Price winner of chemistry, Svante Arrhenius warned the world about CO and it's effect on the global temperature (36). The first time the greenhouse effect was discussed in modern time was, however, at UN's environmental conference in Stockholm in 1972, and in 1988 the Intergovernmental Panel of Climate Change (IPCC) was established.

In 1997 representatives from 166 countries met in Kyoto, Japan, to make a binding climate agreement for the industrial countries. 2000 scientists participated in the UN's IPCC, and agreed upon the fact that there were scientific evidence for claiming that human-made greenhouse gasses cause the global temperature to increase gradually. They also agreed that drastic actions have to be made to reverse the intensive human made greenhouse effect. On December 10th 160 of the nations reached an historic agreement on limiting emissions of carbon dioxide and other greenhouse gases. The Kyoto Protocol calls for the industrialised nations — the so-called Annex I countries – to reduce their average national emissions over the period 2008-2012 to 5.2 percent below 1990 levels (7), (2).

According to the Kyoto Protocol, Norway's emissions of greenhouse gases should not be more than one percent *higher* in the commitment period, 2008-2012, than in 1990. In practice, this means that Norway must reduce the emissions by about 6 percent from the 1996 level to meet its commitment (37). Without the introduction of new measures, emissions are expected to increase by 23 percent in the commitment period from 1990 to 2008-2012).

USA is pledged to reduce its emissions by seven percent below 1990, slightly less than the European Union and slightly more than Japan. The Protocol permits some industrialised nations to modestly increase their emissions and makes special provisions for the members of the former Soviet Bloc. None of the developing countries, including those with large and growing emissions, such as India and China, is required to limit its emissions. The "ultimate objective" is to stabilise "greenhouse gas concentrations in the atmosphere at a level that would prevent dangerous anthropogenic (human-induced) interference with the climate system.

The protocol is broader than previous agreements in that it includes all the major greenhouse gases and takes into account emission changes resulting from changes in forest and land use patterns. The Protocol also contains the elements of a program for international trading of greenhouse gas emissions. Such trading would employ market incentives to help ensure that the lowest-cost opportunities for emissions reductions are pursued (37).

The Kyoto agreement is a significant victory for advocates who have sought to convince world leaders to address climate change. It is intended to signal to governments, businesses, and households that limits will be placed on future emissions of greenhouse gases, and that now is the time to begin developing the necessary technologies. Advocates also express the hope that acceptance by industrialised countries of binding emission limits would make developing countries more willing to take emissions-limiting actions appropriate to their own circumstances (37).

A6.2 The primary aluminium production

It is important to notice that the environmental balance shows that aluminium is an environmentally friendly metal, even with the traditional Hall-Héroult technology. It is for example possible to reduce the consumption of engine fuel by replacing steel with aluminium in the transport section. The reduction of CO_2 these reductions represent corresponds to several times the production of CO_2 from the primary production of the same aluminium. However, since the primary production of aluminium requires a much electrical energy, the production of the necessary electrical energy must be considered. The total CO_2 emission is 14 tons of carbon dioxide per ton aluminium if hydroelectric power is used (as in Norway), instead of 22 tons if coal-power is used (27).

A major energy saving can be made by recycling aluminium. Generally, recycling may also reduce the amount of raw materials used and the environmental pollution problem caused by primary aluminium production. Reusing aluminium by remelting and casting requires only 5-8 percent (26) of the original energy input for aluminium produced from bauxite[2]. Thus, with respect to energy saving and conservation, recycling of aluminium is highly beneficial because about 95 percent of the energy is saved. Aluminium remelting also requires much less energy than steel remelting, so the potentials of energy savings are huge if more typical steel applications are replaced by aluminium. While *primary* steel, copper, glass and paper release approximately 4-5 times more CO_2 than the treatment of their secondary metal, primary aluminium production releases 40 times more than what is necessary for recycling (25). The recycling frequency for aluminium increases steadily, and for example in the USA 68% of the annual U.S. production of beverage cans (12% of the total aluminium production) was recycled (27).

The Norwegian aluminium industry contributes with 4 percent of the Norwegian CO_2 emission. "Prosessindustriens Landsforening" (PIL) estimated the total CO_2 emission from the primary aluminium industry in Norway to be 1.5 millions tons in 1990 (37). If the emissions of the perfluorocarbon-gasses are taken into account, the total emission is 4.7 million tons of CO_2-equivalents. However, from 1990 to 1995 the emissions were reduced with 35 percent. World-wide, the CO_2 emissions from aluminium production have been remained by 10 % in the past ten years (*i.e.* 1989-1999).

The Norwegian Government has proposed a minimum "Green Tax", a CO_2 tax of NOK 100 per tonne (38). The processing industry will, however, be compensated for the CO_2 tax by reducing the taxation of labour by nearly NOK 1.4 billion. The Governmental aim is both a cost-effective environmental policy and to shift the tax burden away from labour and towards environmentally harmful activities. The compensation scheme will be

[2] Bauxitt is the crude raw material for alumina (Al_2O_3).

retained to output of the products (tonnes of aluminium, ferro-alloys, carbides etc.). The compensation will be retained until the Kyoto Protocol is ratified by a sufficient number of countries. Thereafter the compensation will be gradually reduced until 2010, when it will be removed. However, the tax has not yet been imposed.

A new agreement was signed in 1998 where the Norwegian aluminium producers bind themselves to reduce the emissions of greenhouse gasses (*i.e.* CF_4 and C_2F_6) with 55 percent per tonne of aluminium produced in 2005 compared to 1990, which correspond to two millions tonnes of CO_2 per year (38). According to the Norwegian Department of the Environment (38) production of CO_2 equivalents by the industry was reduced with 35% from 1990 to 1995. (The agreement with the Norwegian process industry implies a 12% reduction of the total emission of greenhouse gases in Norway in 2005.) A complete reduction of the greenhouse gases CO_2, CF_4 and C_2F_6 is possible only if the development of a completely new technology with inert anodes (and cathodes) succeeds.

A6.3 The future CO_2 emission control for the process industry

A number of technical approaches to reduce CO_2 in the future are identified. CO_2 can be extracted from the exhaust with water-soluble amines (39). By allowing a counter flow of cooled exhaust and a mixture of amines and water, the amines react with the CO_2. The CO_2 can then be desorbed from the amines by heating. The CO_2 is then compressed from 1 to 64.5 bars mixed with water and cooled to 23 ^oC before it is injected into water-containing sandstone. The under-water rocks in the North Sea have a capacity of storing 1 billion tonnes of CO_2 each year for 700 years. The reservoirs in the North-Sea are capable to store all the CO_2 emissions from Europe for the next 600 years (40). Recent results from Statoil's Research Centre in Trondheim indicate that CO_2, which has been stored in the sandstone rocks, will stay there for several 10000 years (40). This application was originally meant for purifying gas from the Troll section of the North Sea oil fields, but could in principle also work for the CO_2 producing industry. By injecting CO_2 into the reservoirs, the viscosity of the crude oil decreases, which may cause as much as 20-50% higher production yields as a result. For the time being, the price for such a CO_2-removing installation is considered too high to be economically sustainable. The production costs of oil will increase with 30-100% if CO_2 separation is installed. Separation of CO_2 from the exhaust will also reduce the power efficiency significantly. Cost analysis do however show that gas power plants with CO_2 separation have a potential of competing with both wind power and hydro power plants (39).

CO_2 removal is also possible by a method called "de-carbonisation" (39), where crude gas is mixed with air and water steam. The carbon from the gas reacts with the oxygen from the water giving hydrogen (H_2), carbon monoxide (CO) and CO_2. The CO is converted to CO_2, which is removed from the hydrogen by separation under high pressure, and the hydrogen is then used as fuel in a power plant. Alternatively, oxygen can be used instead of air giving water steam and CO_2 as the combustion products. The water steam is then removed from the CO_2 upon cooling.

If the scientists working for the aluminium industry should not succeed in developing inert anodes, a reduction of the CO_2 emissions from the traditional Hall-Héroult cells could be possible by removing CO_2 with a scrubber system using the technology with amines

previously described. This purification method will, however, require much tighter cell constructions than what are presently used in order to keep the CO_2/air ratio in the outgoing gases as high as possible. The overall cost of a system for CO_2 removal and storage will probably be too high to be acceptable for the aluminium industry.

A7 Concluding remarks

There seems to be no question about the fact that the concentration of CO_2 in the atmosphere has increased during the last century, but scientists all over the world have different opinions about what causes the increased CO_2 concentration and what the effect of such an increase will be. Until the knowledge about the climate changes give conclusive results, mankind has decided to take precautions and reduce the emissions of potential greenhouse gases. Even if it turns out that our fear for future climate changes is groundless, the consequences of taking the wrong decision by doing nothing to reduce the emission of the greenhouse gases are too risky to be acceptable.

A8 References

(1) US Global Change Research Information Office, http://www.gcrio.org, Feb. 25th 1999.

(2) Bernstein, L.S., *The Science and Impact on Climate Change: Beyond the Rhetoric*, Mobile Corporation, http://www.mobil.no/cgi-bin, Sept. 1st 1999.

(3) EPA United States International Environmental Protection Agency, : http://www.epa.gov/globalwarming/climate/index.html, June 30th, 1999.

(4) IPCC report, *Climate Change 1994*, Radiative Forcing of Climate, Cambridge University Press, 1995, http://www.ipcc.ch.

(5) IPCC report, *Climate Change 1995 The Science of Climate Change,* Cambridge University Press, 1996, http://www.ipcc.ch.

(6) National Oceanic and Atmospheric Administration (NOAA), *Global Warming*, USA, http://www.ncdc.noaa.gov/ol/climate, July 1st 2000.

(7) United Nations Environment Programme, , Global Resource Information Database, Arendal, http://gaia.grida.no/prog/norway/soeno97/climate/, Jan. |4th 1998.

(8) BBC News, Sci/Tech, *Global Warming – is the sun to blame?*, http://news.bbc.co.uk/hi/english/sci/tech , June 3rd, 1999.

(9) Daly, J., *The Greenhouse Trap-why the Greenhouse Effect will not end Life on Earth*, ISBN 0-947-189-77-7, Bantam Books, Sydney, 1989.

(10) Johnson, S.J., *The Eem Stable Isotrope Record Along the GRIP Ice Core and its Interpretation,* Quaternary Research, no. 43, 1995.

(11) Kirkby, A., *Climate change - it's the sun and us,* Science Magazine, 27th Nov., 1998.

(12) Mackenzie, F.T., *Our Changing Planet,* 2nd ed., Prentice Hall, 1998.

URN:NBN:no-6347

(13) Landscheidt, T., *Solar Activity: A Dominant Factor in Climate Dynamics*, Schroeter Inst. Of Research in Cycles of Solar Activity, Nova Scotia, Canada, http://www.microtech.com.au/daly/solar, July 8th 1999.

(14) Klafstad, B.H., *Drivhuseffekten -en kostbar bløff*, Teknisk Ukeblad, vol. 145, no. 7, Norway, Feb. 1998.

(15) Environmental Defence Fund, *Global Warming: Myth vs. Fact*, http://www.edf.org/pubs/FactSheets , March 25th, 1999.

(16) Ahlbeck, J., *Increase of the Atmospheric Carbon Dioxide Concentration due to Ocean Warming*, Abo Akademi Univ., Finland, http://www.microtech.com.au/daly/oceanco2, July, 5th 1999.

(17) Nydal, G., *Globale Transportprosesser i Naturen*, Kompendium, Faculty of Physics, Mathematics and Computer Science, NTNU, Norway, 1990.

(18) Tenenbaum, D., *The Big Meltdown,* Univ. of Winsconsin-Madison, National Science Foundation, "The Whyfiles. Science Behind the News", http://whyfiles.news.wisc.edu/shorties/anta-ice.html, June 17th 1999.

(19) Mannweiler, U. and Keller, F., *The Design of a New Anode Technology for the Aluminium Industry,* JOM, pp. 15-21, Feb., 1994.

(20) Dietze, P., *Klimaschutz: Play Bach by Enquête – Falsche Zeitkonstanten und bis zum Faktor 8 überhöhte Reduktionsforderungen*, Fusion, vol. 16, no. 3, 1995.

(21) Daly, J.L., *Still Waiting for Greenhouse*, http://www.vision.net.au/~daly, Sept. 1st 1999.

(22) Dansgaard, W., *Evidence for General Instability of Past Climate from a 250k yr Ice Core Record*, Nature, vol. 364, 1993.

(23) Del Genio, A.D., Yao, M.-S., Kovari, W. and Lo, K.K.-W., *A prognostic cloud water parameterization for global climate models,* J. Climate, vol. 9, pp. 270-304, 1996, NASA Goddard Inst. For Space Studies, http://www.giss.nasa.gov/gpal/abstracts/1996.DelGenoYao.html, July, 1st 2000.

(24) Rohde, H., *Clouds and Climate*, Nature, vol. 401, pp. 223-225, 16th Sept., 1999.

(25) Moomaw, W.R., *Industrial emissions of greenhouse gases*, Energy Policy, vol. 24, no. 10-11 pp. 951-968, Oct.-Nov., 1996.

(26) Huglen, R. and Kvande, H., *Global Considerations of Aluminium Electrolysis on Energy and the Environment*, Light Metals 1994, pp. 373-380, 1994.

(27) Weston, R.E., *Possible greenhouse effects of tetrafluoromethane and carbon dioxide emitted from aluminium production*, Atmospheric Environment, vol.30, no. 16, pp. 2901-2910, Aug., 1996.

(28) Morris, R.A., Viggiano, A.A., Arnold, S.T. and Paulson, J.F., *Chemistry of atmospheric ions reacting with fully fluorinated compounds,* International J. of Mass Spec. and Ion Processes, vol. 149/150, pp. 287-298, 1995.

(29) Forrest, D. and Szekely, J., *Global Warming and the Primary Metals Industry*, JOM, vol. 43, no. 12, pp. 25-30, 1991.

(30) The United Nations Framework Convention on Climate Change, http://www.unfccc.de , Feb.26th, 1999.

(31) Dolin, E.J., *PFC Emissions Reductions: The Domestic and International Perspective*, Light Metal Age, vol. 57, no. 12, pp. 56-67, 1999.

(32) Marsh, H., Heintz, E.A. and Rodríguez, R., *Introduction to Carbon Technologies*, ISBN 84-7908-3174, University of Alicante, Spain, 1997.

(33) Kvande, H., *Inert Electrodes in Aluminium Electrolysis Cells*, Light Metals 1999, pp. 369-376, 1999.

(34) Briem, S., Alkan, Z., Quinkertz, R., Dienhart, M. and Kugeler, K., *Development of energy demand and energy-related CO_2-emissions in melt electrolysis for primary aluminium production*, ALUMINIUM, vol. 76, no. 6, pp. 502-506, 2000.

(35) Dewing, E.W., *Technical Working Group on Inert Anode Technology*, Am. Soc. of Mechanical Engineers', ASME International, CRTD, vol. 53, Appendix A-4, July, 1999.

(36) Charlson, R.J., *Giants' footprints in the greenhouse*, Nature, vol. 401, pp. 741-742, 21st Oct., 1999.

(37) Fjellanger, G., *Energy and Climate in an Environmental Context- "Norwegian Climate Change Policy Post Kyoto*, ODIN Ministry of the Environment (MD), Expo'98, Lisbon, Portugal, July 22nd. 1998.

(38) Press Release, *Norwegian Government proposes New Green Taxes*, ODIN Ministry of Finance and Customs (FIN), 18/98, April 23rd, 1998.

(39) Tønseth, S., *Når gass blir kraft*, GEMINI, no. 4, SINTEF, Norway, pp. 13-21, Dec. 1997.

(40) Abelsen, A, *Nå venter vi på energipolitikken,* Teknisk Ukeblad, vol. 47, no. 4, Norway, Jan. 2000.

URN:NBN:no-6347

B Emf data and solubility of Ni(II), Fe(II), Fe(III), Cu(I) and Cu(II) in cryolite-alumina melts

All the solubility data obtained and described in chapters 4–6 are presented as numbers in this appendix. The uncertainty in the presently obtained solubility data is generally higher than the numbers of the digits used in the tables implies, but are shown to separate pair of values that would be equal if the numbers of digits had been reduced.

B1 Solubility of Ni(II)

All the Ni(II) solubility data are obtained in a platinum crucible under an atmosphere of oxygen.

Table B1: Solubility of Ni(II) in cryolite at 1020 ^{o}C as a function of alumina concentrations.

wt% Al_2O_3 LECO	Alumina Activity	wt% Ni(II)	wt% Al_2O_3 LECO	Alumina Activity	wt% Ni(II)
0.47	0.001	0.319	2.26	0.041	0.133
0.89	0.005	0.243	2.68	0.058	0.137
0.91	0.005	0.191	3.34	0.090	0.088
0.96	0.006	0.239	3.68	0.109	0.083
1.05	0.008	0.156	5.03	0.195	0.026
1.05	0.008	0.153	5.19	0.207	0.027
1.13	0.009	0.233	6.26	0.291	0.021
1.13	0.009	0.171	6.65	0.323	0.017
1.26	0.012	0.161	8.20	0.466	0.011
0.79	0.004	0.245	8.81	0.526	0.013
1.59	0.019	0.166	12.12	1.000	0.006
2.07	0.034	0.178	12.16	1.000	0.007
2.24	0.040	0.079	12.16	1.000	0.008
2.24	0.040	0.105	13.02	1.000	0.006

Table B2: Solubility of Ni(II) in alumina-saturated cryolite as a function of temperature.

T [^{o}C]	1/T*10^{4} [K^{-1}]	wt% Ni(II)	T [^{o}C]	1/T*10^{4} [K^{-1}]	wt% Ni(II)
1040	7.62	0.0102	1000	7.85	0.0068
1040	7.62	0.0108	1000	7.85	0.0061
1030	7.67	0.0083	1000	7.85	0.0068
1020	7.73	0.0075	1004	7.83	0.0059
1020	7.73	0.0059	1004	7.83	0.0063
1020	7.73	0.0064	990	7.92	0.0053
1020	7.73	0.0061	980	7.98	0.0022
1000	7.85	0.0039	980	7.98	0.0040
1000	7.85	0.0067	980	7.98	0.0027

Table B3: Solubility of Ni(II) in alumina-saturated cryolite at 1020 ^{o}C as a function of molar ratio.

Molar Ratio	wt% Ni(II)	Molar Ratio	wt% Ni(II)
2.00	0.0010	3.00	0.0061
2.00	0.0012	4.00	0.0067
2.29	0.0045	5.00	0.0076
2.29	0.0025	5.00	0.0077
2.50	0.0058	8.00	0.0023
3.00	0.0075	8.00	0.0079
3.00	0.0059	12.00	0.0070
3.00	0.0064		

B2 Solubility of Fe(II)

All the Fe(II) solubility data are obtained in an iron crucible under an atmosphere of argon.

Table B4: Solubility of Fe(II) in cryolite at 1020 ^{o}C as a function of alumina concentrations.

Wt% Al_2O_3 LECO	Alumina activity	wt%Fe(II)	Wt% Al_2O_3 LECO	Alumina activity	wt%Fe(II)
2.69	0.058	4.174	5.20	0.208	2.299
2.96	0.071	3.539	5.22	0.209	2.395
2.98	0.072	3.849	5.58	0.236	2.037
3.02	0.073	3.498	5.90	0.261	1.703
3.02	0.074	3.427	7.17	0.369	1.117
3.04	0.075	3.610	8.06	0.452	0.843
3.06	0.075	3.477	9.26	0.572	0.837
3.33	0.089	3.188	9.79	0.628	0.598
3.64	0.106	3.348	11.19	0.781	0.457
4.05	0.130	3.155	11.21	1.000	0.315
4.08	0.132	3.269	11.21	1.000	0.309
4.28	0.145	2.603	13.13	1.000	0.308
4.81	0.180	2.324			

Table B5: Solubility of Fe(II) in alumina-saturated cryolite at 1020 ^{o}C as a function of molar ratio.

Molar Ratio	Wt% Fe(II)	Molar Ratio	Wt% Fe(II)
2.00	0.354	4.00	0.495
2.29	0.343	4.79	0.588
2.52	0.285	5.00	0.619
3.00	0.308	6.50	0.624
3.00	0.315	8.00	0.600
3.00	0.309		

Table B6: Solubility of Fe(II) in alumina-saturated cryolite as a function of temperature.

T [^oC]	$1/T*10^4$ [K^{-1}]	wt%Fe(II) Nat	T [^oC]	$1/T*10^4$ [K^{-1}]	wt%Fe(II) Synt	T [^oC]	$1/T*10^4$ [K^{-1}]	wt%Fe(II) New
981	7.97	0.242	981	7.97	0.253	980	7.98	0.262
987	7.94	0.267	990	7.92	0.267	990	7.92	0.273
998	7.87	0.295	1000	7.85	0.288	1000	7.85	0.297
1009	7.80	0.300	1011	7.79	0.303	1010	7.79	0.305
1020	7.73	0.315	1019	7.74	0.309	1021	7.73	0.316
1030	7.67	0.322	1030	7.67	0.318	1030	7.67	0.325
1040	7.62	0.346	1040	7.62	0.341	1041	7.61	0.352
1050	7.56	0.365	1050	7.56	0.360	1050	7.56	0.368

B3 Solubility of Fe(III)

All the Fe(III) solubility data are obtained in a platinum crucible under an atmosphere of oxygen by Diep (Ref. in chapter 5).

Table B7: Solubility of Fe(III) in cryolite at 1020 ^oC as a function of alumina concentrations, by Diep.

wt% Al_2O_3 added	Al_2O_3 Corrected for O in Fe_2O_3	Alumina activity	wt% Fe_2O_3	wt%Fe(III)
0	0.47	0.001	0.71	0.50
1	1.42	0.015	0.49	0.34
2	2.41	0.047	0.42	0.29
3	3.41	0.093	0.41	0.29
4	4.39	0.152	0.35	0.24
7	7.38	0.389	0.30	0.21
12	12.37	0.918	0.24	0.17

Table B8: Solubility of Fe(III) in alumina-saturated cryolite at 1020 ^oC as a function of molar ratio, by Diep.

Molar Ratio	wt% Fe_2O_3 (3 wt% Al_2O_3)	wt%Fe(III) (3 wt% Al_2O_3)	wt% Fe_2O_3 (Alumina sat.)	wt%Fe(III) (Alumina sat.)
2	0.27	0.19	0.15	0.10
2.5	0.30	0.21	0.22	0.15
3	0.41	0.29	0.26	0.18
4	0.39	0.27	0.27	0.19
6	0.37	0.26	0.24	0.17
10	0.23	0.16	0.19	0.13

B4 Solubility of Cu(I)

All the Cu(I) solubility data are obtained in a copper crucible under an atmosphere of argon.

Table B9: Solubility of Cu(I) in cryolite at 1020 ^{o}C as a function of alumina concentrations.

wt% alumina LECO	Alumina activity	wt% Cu(I) Natural	wt% Cu(I) Synthetic	wt% alumina LECO	Alumina activity	wt% Cu(I) Natural
0.41	0.001	0.362		4.16	0.137	0.216
0.42	0.001	0.346		5.14	0.203	0.219
0.53	0.001		0.328	5.46	0.227	0.233
0.55	0.002	0.327		8.03	0.449	0.242
0.86	0.005	0.245		8.15	0.461	0.254
1.30	0.012	0.230		9.11	1.000	0.301
1.35	0.014	0.267		9.99	0.649	0.273
2.91	0.068	0.218		10.66	0.722	0.296
3.84	0.118	0.216		12.01	0.876	0.304

Table B10: Solubility of Cu(I) in alumina-saturated cryolite at 1020 ^{o}C as a function of molar ratio.

Molar Ratio NaF/AlF_3	wt% Cu(I) Natural	Molar Ratio NaF/AlF_3	wt% Cu(I) Natural
2.29	0.354	4.00	0.305
2.52	0.287	5.00	0.325
3.00	0.271	6.50	0.295
3.00	0.279	8.00	0.289

Table B11: Solubility of Cu(I) in alumina-saturated cryolite as a function of temperature.

		No alumina addition				Alumina sat.
Temp		Wt% Cu(I)	Wt% Cu(I)	Temp		Wt% Cu(I)
[^{o}C]	1/T*10^{4}	Synthetic	Natural	[^{o}C]	1/T*10^{4}	Natural
1010	7.79		0.317	980	7.98	0.168
1010	7.79		0.288	980	7.98	0.175
1010	7.79	0.269		990	7.92	0.208
1020	7.73		0.327	1000	7.85	0.239
1021	7.73	0.328		1000	7.85	0.232
1030	7.67	0.346		1000	7.85	0.234
1040	7.62		0.397	1019	7.74	0.301
1044	7.59			1020	7.73	0.271
1045	7.59	0.400		1020	7.73	0.279
1050	7.56		0.462	1030	7.67	0.333
1050	7.56		0.447	1039	7.62	0.362

B5 Solubility of Cu(II)

All the Cu(II) solubility data are obtained in a platinum crucible under an atmosphere of oxygen.

Table B12: Solubility of Cu(II) in cryolite at 1020 ^{o}C as a function of alumina concentrations.

wt% alumina LECO	Alumina activity	wt% Cu(II) O_2	wt% Cu(II) Air	wt% alumina LECO	Alumina activity	wt% Cu(II) O_2	wt% Cu(II) Air
1.01	0.0070		0.926	6.48	0.309	0.371	
1.03	0.0073	0.915		8.01	0.447	0.366	
1.10	0.0085	0.883		9.26	0.572	0.302	
1.25	0.0114	0.787		11.51	0.818	0.363	
1.54	0.0181	0.681		12.7	0.957	0.404	
2.20	0.0386	0.559		12.91	0.982	0.418	
4.47	0.1569	0.485		13.06	1.000	0.449	
5.37	0.2203	0.394		13.06	1.000		0.441
5.79	0.2526	0.399		13.06	1.000	0.442	
5.90	0.2613	0.386		13.06	1.000		0.453

Table B13: Solubility of Cu(II) in cryolite as a function of temperature.

		No alumina				Alumina sat.	
Temp		Wt% Cu(II)	Wt% Cu(II)	Temp		Wt% Cu(II)	Wt% Cu(II)
[^{o}C]	1/T*10^{4}	Air	O2	[^{o}C]	1/T*10^{4}	Air	O2
1010	7.79	0.839		980	7.98		0.259
1011	7.79	0.853		982	7.97	0.283	
1011	7.79		0.884	1000	7.85		0.346
1015	7.76	0.908		1001	7.85	0.381	
1019	7.74		0.915	1010	7.79		0.402
1020	7.73	0.926		1020	7.73	0.441	
1020	7.73		0.883	1020	7.73		0.449
1021	7.73	0.947		1021	7.73	0.453	
1030	7.67	0.973		1021	7.73		0.442
1030	7.67		1.018	1029	7.68		0.503
1031	7.67		1.032	1030	7.67	0.511	
1038	7.63		1.027	1040	7.62	0.608	
1039	7.62	1.043		1040	7.62		0.613
1050	7.56		1.130	1050	7.56		0.650
				1050	7.56	0.642	

Table B14: Solubility of Cu(II) in alumina-saturated cryolite at 1020 °C as a function of molar ratio.

Molar Ratio NaF/AlF_3	wt% Cu(II) O_2	wt% Cu(II) Air	Molar Ratio NaF/AlF_3	wt% Cu(II) O_2	wt% Cu(II) Air
2.00	0.562		3.00		0.453
2.29	0.497		3.00		0.441
2.52	0.405		4.00	0.470	
3.00	0.449		5.00	0.449	
3.00	0.442		8.00	0.388	

Table B15: Solubility of Cu(I) and Cu(II) in cryolite at 1020 °C as a function of alumina concentration, and the necessary constants used to calculate the "pure" solubility in chapter 6-7.

wt% Al_2O_3	$a(Al_2O_3)$	wt% Cu(I) best fit	wt% Cu(II) best fit	$a_{Cu^{\cdot}} (p_{O2})^{1/4}$ Cu	$a_{Cu^{\cdot}} (p_{O2})^{1/2}$ O_2	K_1 [Cu(I)]	K_2 [Cu(II)]	Cu(I) [%]	Cu(II) [%]	Pure Cu(I) Wt%	Pure Cu(II) Wt%
1.0	0.007	0.282	0.904	0.0304	0.0200	8.15	37.04	87.86	81.96	0.248	0.741
1.5	0.017	0.256	0.735	0.0304	0.0200	7.53	29.21	89.45	79.50	0.229	0.584
2.0	0.032	0.240	0.639	0.0304	0.0200	7.13	24.81	90.43	77.67	0.217	0.496
2.5	0.050	0.228	0.575	0.0304	0.0200	6.84	21.92	91.12	76.21	0.208	0.438
3.0	0.073	0.220	0.529	0.0304	0.0200	6.62	19.85	91.64	75.00	0.201	0.397
3.5	0.098	0.213	0.494	0.0304	0.0200	6.44	18.28	92.05	73.96	0.196	0.365
4.0	0.127	0.217	0.466	0.0304	0.0200	6.61	16.70	92.87	71.63	0.201	0.334
4.5	0.159	0.217	0.443	0.0304	0.0200	6.65	15.52	93.38	70.00	0.202	0.310
5.0	0.193	0.223	0.424	0.0300	0.0200	7.04	14.17	94.31	66.82	0.211	0.283
5.5	0.230	0.230	0.408	0.0275	0.0200	8.03	12.35	95.95	60.59	0.221	0.247
6.0	0.269	0.236	0.393	0.0254	0.0188	8.98	11.94	96.74	57.07	0.228	0.224
6.5	0.311	0.241	0.381	0.0236	0.0163	9.89	13.48	96.88	57.70	0.234	0.220
7.0	0.354	0.246	0.370	0.0221	0.0143	10.79	15.07	97.00	58.27	0.239	0.215
7.5	0.399	0.251	0.366	0.0208	0.0127	11.69	17.15	97.03	59.47	0.244	0.217
8.0	0.446	0.256	0.366	0.0197	0.0113	12.57	19.66	97.01	60.99	0.248	0.223
8.5	0.495	0.260	0.366	0.0187	0.0102	13.46	22.29	96.99	62.34	0.252	0.228
9.0	0.545	0.264	0.366	0.0178	0.0093	14.35	25.03	96.98	63.56	0.256	0.232
9.5	0.597	0.268	0.366	0.0170	0.0085	15.23	27.88	96.97	64.67	0.260	0.236
10.0	0.650	0.271	0.366	0.0163	0.0078	16.11	30.83	96.97	65.68	0.263	0.240
10.5	0.704	0.275	0.366	0.0157	0.0072	16.99	33.88	96.97	66.61	0.267	0.244
11.0	0.760	0.278	0.366	0.0151	0.0067	17.86	37.02	96.96	67.46	0.270	0.247
11.5	0.817	0.281	0.366	0.0146	0.0062	18.73	40.25	96.96	68.25	0.273	0.250
12.0	0.874	0.285	0.383	0.0141	0.0058	19.55	46.63	96.75	70.46	0.275	0.270
12.5	0.933	0.288	0.408	0.0136	0.0054	20.35	54.79	96.46	72.92	0.277	0.297
13.0	0.993	0.290	0.432	0.0132	0.0051	21.13	63.66	96.17	75.08	0.279	0.325
13.1	1.000	0.291	0.435	0.0132	0.0051	21.23	64.78	96.14	75.32	0.280	0.328

"Cu(I) [%]" means the amount of Cu(I) present in a melt composition contained in a copper crucible. "Cu(II) [%]" means the amount of Cu(II) under an atmosphere of oxygen.

Table B16: Solubility of Cu(II) in alumina-saturated melts as a function of molar ratio. Data from Dalsbotten. (Ref. in Chapter 6.)

Molar Ratio	Temp	$1/T*10^4$	wt% Cu(II)
1.20	711	10.16	0.041
1.20	722	10.05	0.042
1.20	741.5	9.86	0.048
1.70	900.5	8.52	0.125
1.70	910.5	8.45	0.134
1.70	930.5	8.31	0.158
2.29	961.5	8.10	0.488
2.29	971	8.04	0.304
2.29	990	7.92	0.595

B6 Pictures of quenched melt samples taken from dissolved Cu(I) and Cu(II) in cryolite-alumina solutions

Figure B-1: Samples saturated with Cu_2O taken at 1020 ^oC from melts with 1) Synthetic cryolite[1], 2) unsaturated natural cryolite, 3) 0.25 wt% alumina, 4) 0.7 wt% alumina, 5) 1.25 wt% alumina, 6) 2.5 wt% alumina, 7) 4.0 wt% alumina, 8) 6 wt% alumina, 9) 10 wt% alumina, and 10) 13.1 wt% alumina added to natural cryolite melts.

Figure B-2: Samples saturated with CuO taken at 1020 ^oC from melts with 1) Natural cryolite, 2) 0.7 wt% alumina, 3) 1.25 wt% alumina, 4) 2.5 wt% alumina, 5) 5.0 wt% alumina, 6) 6.0 wt% alumina, and 7) 10.0 wt% alumina added to natural cryolite melts.

[1] Synthetic cryolite is a mixture of NaF and sublimated AlF_3

B7 Weight percent alumina versus alumina activity in cryolite at 1020 ^{o}C

Table B17: Weight percent alumina *versus* molar fraction and activity of alumina in cryolite at 1020 ^{o}C, calculations from Dewing and Thonstad (Ref. chapter 4).

wt% Al_2O_3	N (Al_2O_3)	a (Al_2O_3)	wt% Al_2O_3	N (Al_2O_3)	a (Al_2O_3)
1.00	0.020	0.007	7.50	0.143	0.399
1.50	0.030	0.017	8.00	0.152	0.446
2.00	0.040	0.032	8.50	0.161	0.495
2.50	0.050	0.050	9.00	0.169	0.545
3.00	0.060	0.073	9.50	0.178	0.597
3.50	0.069	0.098	10.00	0.186	0.650
4.00	0.079	0.127	10.50	0.195	0.704
4.50	0.088	0.159	11.00	0.203	0.760
5.00	0.098	0.193	11.50	0.211	0.817
5.50	0.107	0.230	12.00	0.219	0.874
6.00	0.116	0.269	12.50	0.227	0.933
6.50	0.125	0.311	13.00	0.235	0.993
7.00	0.134	0.354	13.06	0.236	1.000

B8 Emf data obtained and used to determine ΔG^{o} for $NiAl_2O_4$

Table B18: Emf data obtained for the determination of ΔG^{o} for $NiAl_2O_4$.

T [^{o}C]	T/K [K]	EMF cell [V]	Emf Mo-Ni [V]	ΔG^{o} $NiAl_2O_4$ [kJ/mol]
850	1123.15	1.182	-0.01213	-70.728
912	1185.15	1.255	-0.01321	-54.869
920	1193.15	1.267	-0.01335	-52.324
967	1240.15	1.324	-0.01417	-39.980
970	1243.15	1.323	-0.01423	-40.087
1020	1293.15	1.383	-0.01510	-27.076
1020	1293.15	1.380	-0.01510	-27.655

ΔG^{o} is given for the reaction: $NiO_{(s)} + Al_2O_{3(s,\alpha)} = NiAl_2O_{4(s)}$

B9 Emf data obtained and used to determine ΔG^o for $CuAlO_2$ and $CuAl_2O_4$

Table B19: Emf data obtained for the determination of ΔG^o for $CuAlO_2$.

Temp [^oC]	Temp [K]	Emf cell [V]	Emf Mo-Cu [V]	ΔG^o $CuAlO_2$ [kJ/mol]
750	1023.15	1.7296	-0.00764	-57.821
800	1073.15	1.7266	-0.00825	-55.277
850	1123.15	1.7101	-0.00885	-54.040
900	1173.15	1.7056	-0.00943	-51.652
950	1223.15	1.6976	-0.00998	-49.608
1000	1273.15	1.6910	-0.01050	-47.436
1020	1293.15	1.6886	-0.01070	-46.546
1023	1296.15	1.6882	-0.01073	-46.417

ΔG^o is given for the reaction: $0.5Al_2O_{3(s,\alpha)} + Cu_{(s)} + 1/4O_{2(g)} = CuAlO_{2(s)}$

Table B20: Emf data obtained for the determination of ΔG^o for $CuAl_2O_4$.

Temp [^oC]	Temp [K]	EMF cell [V]	EMF Mo-Pt [V]	ΔG^o $CuAl_2O_4$ [kJ/mol]
750	1023.15	2.2299	-0.01910	-66.210
800	1073.15	2.1985	-0.02083	-64.234
850	1123.15	2.1616	-0.02259	-62.789
900	1173.15	2.1314	-0.02438	-60.698
950	1223.15	2.1014	-0.02621	-58.588
1000	1273.15	2.0642	-0.02806	-57.175
1020	1293.15	2.0459	-0.02881	-56.941
1020	1293.15	2.0469	-0.02881	-56.844
1023	1296.15	2.0454	-0.02893	-56.689

ΔG^o is given for the reaction: $Al_2O_{3(s,\alpha)} + Cu_{(s)} + 1/2O_{2(g)} = CuAl_2O_{4(s)}$

B10 Stability diagrams for copper phases as a function of alumina activity

The following figures are based on thermodynamical data for the Cu phases present given by Jacob and Alcock (Ref. in chapter 6). Please note that the activities of alumina are given for 1020 ^{o}C in all the diagrams.

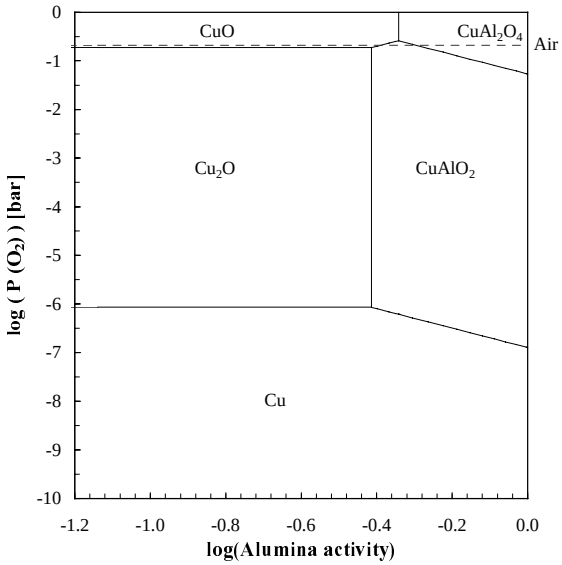

Figure B-3: Phase diagram showing the stability regions for Cu, Cu_2O, CuO, $CuAlO_2$ and $CuAl_2O_4$ at 1020 ^{o}C. The dotted line illustrates the partial pressure of oxygen in air.

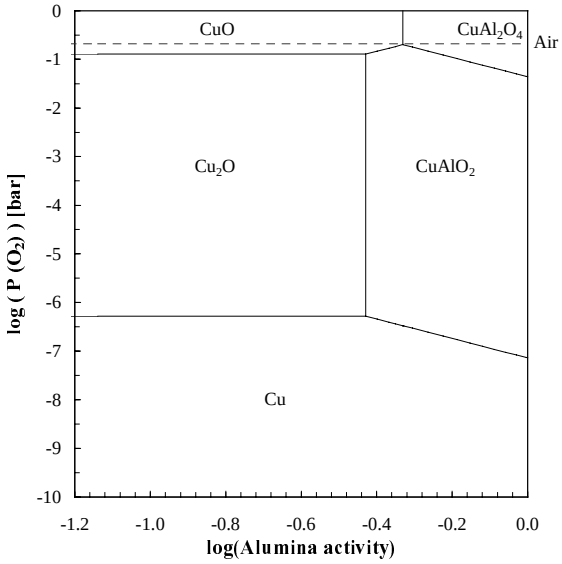

Figure B-4: Phase diagram showing the stability regions for Cu, Cu_2O, CuO, $CuAlO_2$ and $CuAl_2O_4$ at 1000 ^{o}C.

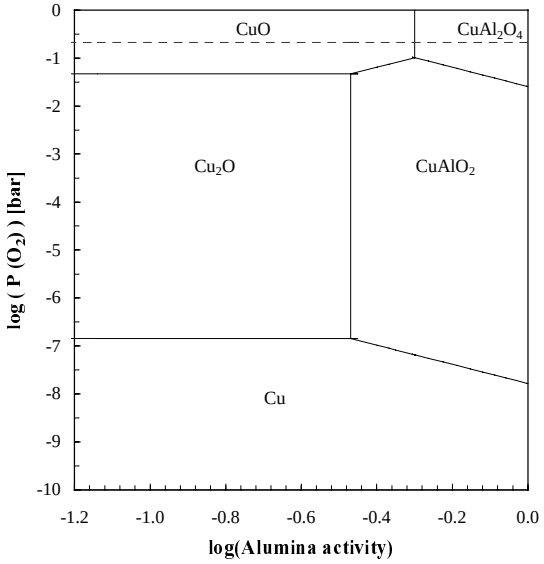

Figure B-5: Phase diagram showing the stability regions for Cu, Cu_2O, CuO, $CuAlO_2$ and $CuAl_2O_4$ at 950 ^oC.

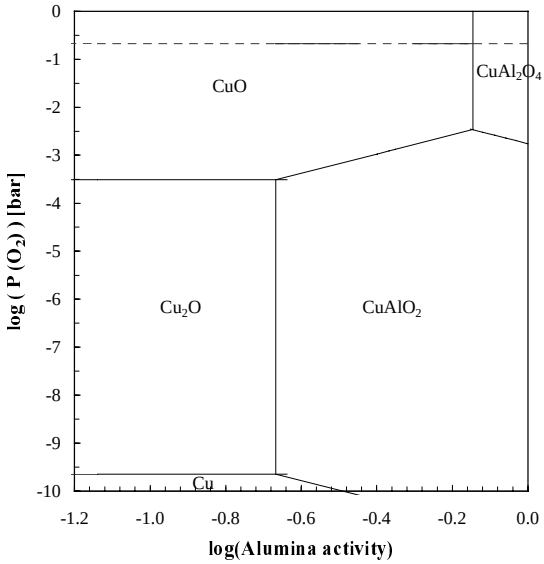

Figure B-6: Phase diagram showing the stability regions for Cu, Cu_2O, CuO, $CuAlO_2$ and $CuAl_2O_4$ at 750 ^oC.